UNIVERSIDAD EUROPEA DE MADRID

ESCUELA DE ARQUITECTURA, INGENIERÍA Y DISEÑO
DEGREE IN AEROSPACE ENGINEERING

BACHELOR'S DEGREE FINAL PROJECT REPORT

LIFTING SYSTEM REPLACEMENT FOR A HORIZONTAL STABILIZER

CARLOS DE LA CALLE MERCHÁN

Academic Year 2023/2024

TITLE: LIFTING SYSTEM REPLACEMENT FOR A HORIZONTAL STABILIZER

AUTHOR: CARLOS DE LA CALLE MERCHÁN

TUTOR: RAUL CARLOS LLAMAS SANDIN

DREGREE: AEROSPACE ENGINEERING

DATE: 09/06/2024

ABSTRACT

The fact of substituting the horizontal stabilizer of an aircraft appeared since the necessity of aviation to lower the weight of aircraft in order to generate fewer emissions as well as allowing the airlines to offer even cheaper flights so that to achieve a better accessibility to the aerospace sector for a bigger percentage of the population. This study will carry out not only the re-design of aircraft's tail but also, CFD (Computational Fluid Dynamics) analysis would be performed to see if this new configuration could be or not possible by the calculation of different performance parameters. Because of the climatological situation of the world, reducing the emissions and so making flights as efficient as possible constitute some of the key parameters to consider for the future of aircraft design; due to this, the design of this system was also performed considering these factors meticulously in addition to the investigation about the introduction of propfan engines to substitute the conventional jet engines.

Keywords: *Horizontal stabilizer, propfan engines, emissions.*

RESUMEN

El hecho de sustituir el estabilizador horizontal de un avión aparece de la necesidad de la aviación de bajar el peso de las aeronaves para generar menos emisiones además de permitir a las aerolíneas ofrecer vuelos aún más baratos para conseguir una mejor accesibilidad al sector aeroespacial para un mayor porcentaje de la población. Este estudio no sólo llevará a cabo el rediseño de la cola del avión, sino que también se realizará un análisis CFD (Dinámica de Fluidos Computacional) para ver si esta nueva configuración podría o no ser posible mediante el cálculo de diferentes parámetros de rendimiento. Debido a la situación climatológica del mundo, reducir las emisiones y así hacer que los vuelos sean lo más eficientes posible constituyen algunos de los parámetros clave a tener en cuenta para el futuro del diseño de aeronaves; debido a esto, el diseño de este sistema también se realizó considerando minuciosamente estos factores además de la investigación sobre la introducción de motores propfan para así sustituir los motores a reacción convencionales.

Palabras clave: *Estabilizador horizontal, motores propfan, emisiones.*

ACKNOWLEDGEMENTS

To begin with, I would like to express Raul Carlos Llamas Sandin, my lecturer and project supervisor, my sincere gratitude. The success of this project has been greatly due to his excellent recommendations, feedback and constant support throughout. In addition to this, my academic experience has been marked by his knowledge and support which has motivated me to aim for the excellence.

I am also exceptionally thankful of my family, who have been my biggest source of support during these years. Their constant support and strong faith in my talents have been essential to my academic success.

TABLE OF CONTENTS

FIGURE INDEX

CHAPTER 1. INTRODUCTION

PROBLEM APPROACH

Commercial aircraft are such complex vehicles which requires from a huge number of mechanisms as well as different complex structures. Making aircraft lighter has been one of the most important aspects in aviation through history, since the first jet commercial aircraft were designed. Through the time, aircraft have evolved as well as their design and materials used (due to the appearance of composite materials). Despite the gradual reduction on the weight since the beginning of aviation, during the last years weight on has been almost a fixed parameter depending on each family of aircraft which has not been able to be changed through the last years. Also, since the certification of aircraft has become more and more demanding with the years and that the rapid climate change, which is currently taking place, drastic changes on the configuration of commercial aircraft has become something almost impossible to achieve. Because of these reasons, the fact of performing a re-design was studied. This re-design at the tail of the aircraft will be intended to achieve several objectives in terms of weight reduction and will open different ways of avoiding issues with the certification in the way of placing some brand-new engines (more efficient) on the fuselage of the aircraft. This re-design would consist of the suppression of the horizontal stabilizer, of a commercial aircraft and the introduction of a new, original self-made concept. The study which will be carried out will include CFD (Computational Fluid Dynamics)- analysis in order to see if the final design would be able to replace a horizontal stabilizer as well as numerical calculations to validate the simulations. Also, a study about the possibility of changing the place where engines are attached would be made in order to study the possibility of reducing the C02 emissions emitted by the aviation industry as well as the fuel savings by the introduction of this new design.

1.1 PROJECT OBJECTIVES

This project will have a wide range of objectives as it introduces a brand-new design which cannot be compared with anything similar to it so, the following objectives will be covered during this project:

- Investigation about the operation of the horizontal stabilizer while being at cruise and take off. An investigation will be carried out to know more about how the horizontal stabilizer aerodynamics of a commercial aircraft. An estimation of the total weight of the horizontal stabilizer (including its wing box located in the tail cone) will be carried out so that to compare it with the weight of the proposed lifting system weight.

- Design of a lifting system to replace the horizontal stabilizer. The design will be carried out by using Adobe Illustrator (for a 2-dimensional design) and CATIA & Autodesk Inventor (for the 3-dimensional design). Also, hand-made drawings will be used as a starting point for its design.

- Numerical results about the new lifting system & conventional configuration. Some results were obtained during simulations such as lift and drag acting at the lifting system in order to compare it with the previous calculations. Also, a weight and flight range comparison will be carried out (results about these will be numerically achieved).

- Study about the implementation of unducted fan engines with the new configuration. The possibility of installing this type of engines would be studied as they are much more efficient and produce lower emissions than conventional engines.

- Conclusions about the possibility of introducing of this new lifting system and study the possibility of including propfan engines to substitute the conventional turbofan engines.

- Emission reduction & economic study between the three different configurations (conventional, lifting system and lifting system & propfan configurations).

1.2 GENERAL ANALYSIS

It is difficult to think about the possibility of substituting the horizontal stabilizer by a simpler device which would be lighter than the just mentioned as, since the beginning of aviation, the idea of having both a vertical and horizontal stabilizer was used. The main idea behind this new concept consisted of reducing the complexity and weight of manufacturing aircraft. Horizontal stabilizers need an internal structure composed by ribs, spars and stringers as it can be seen in figure 1; all of these structural components are necessary in order to sustain the aerodynamic forces acting at the horizontal tail plane but, all of them contribute to enhance the overall weight of the aircraft. Also, the fact that this component needs from a central joint or even a box (in case fuel needs to be also stored at the horizontal stabilizer) led to a potential increase of the weight of the aircraft as well as all the materials and manufacturing processes involving the assembly and integration of these components to finally obtain the desired product. Additionally, this change would involve advantages on the airport facilities due to the change on the aircraft's size.

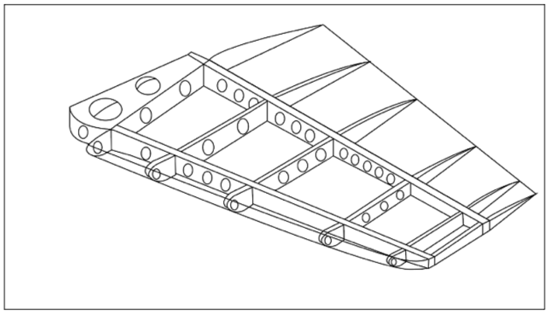

Figure 1. Internal structure from a section of a horizontal stabilizer

The expected results after the completion of this report would be to analyze the possibility of implementing this new design as well as considering the different possibilities this new concept would lead to the industry; not only in terms of weight reduction but also, how could it affect the aerospace industry in terms of material costs and reduction of the carbon dioxide emissions. Also, the implementation of propfan engines would be studied since, the re-design which would be carried out would lead to the possibility of using this type of engines which are already known to be much more efficient than the actual turbofan engines despite the descent in cruise speed which would suppose its implementation. The methodology used for this study would be simple, first an initial and preliminary design would be performed. Then, having completed the final design, a computational Fluid Dynamics study would be carried out with the purpose of comparing the results obtained in order to verify the effectiveness of this idea. Finally, some numerical calculations would be performed to compare some other parameters, such as the weight or range. Next, a study about the implementation of propfan engines would be done and to conclude, a comparison between the three mentioned configurations would take place.

1.3 POSSIBLE AFT FOR ITS IMPLEMENTATION

The fact that the design of this lifting system would be restricted to the range of aircraft which have not fuel tanks at their horizontal stabilizer, means that some aircraft such as the Airbus A330 or the Boeing 747-400 would not be capable of having this implementation on their fuselage but, considering that this brand-new system would be introduced on a future, it would be expected that different aircraft would be operating by that time. Because of this reason, the type of aircraft which would be more likely for the implementation of this system would consist of middle range aircraft with relatively long fuselages so that the system could be easier accommodated, carrying the highest number of passengers as possible since the descent in weight due to the introduction of the lifting system would enhance the performance of the aircraft allowing to have a lower weight of the aircraft's overall structure.

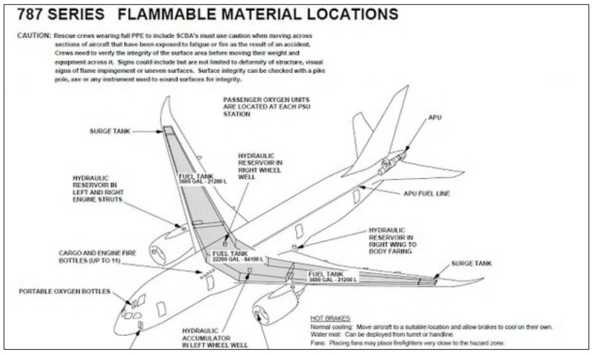

Figure 2. Boeing 787 Series fuel tanks distribution and location among its fuselage [1]

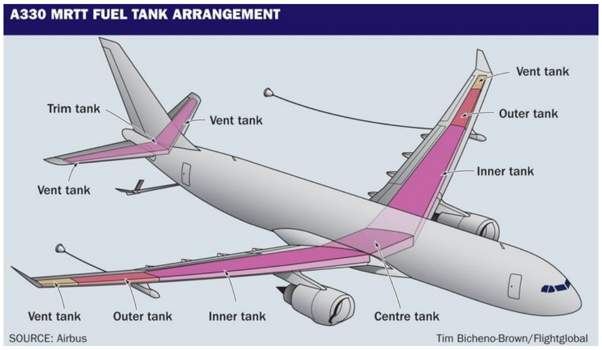

Figure 3. Airbus A330 MRTT fuel tanks distribution and location among its fuselage [2]

The introduction of this new lifting system would not only be focused on commercial aircraft, also, cargo aircraft could have this system in order to enhance their characteristics. Since aircraft developed for the transport of cargo, the lifting system could become even more determinant than using it on commercial aircraft. This would be due to the fact that as the maximum take-off weight on these aircraft is such higher compared to the previous ones, a reduction on the weight of the aircraft would become crucial. However, some problems could appear as the lift needed to be generated by the system would need to be potentially higher than the one at commercial aircraft and so a re-design of the lifting system would be needed by changing the dimensions of it. As the results which would be obtained from the simulations are not clear yet, the study would only consider commercial aircraft for its implementation.

1.4 AIRCRAFT SELECTION

The current brand-new lifting device would have the possibility of being implemented on a wide range of aircraft but, for the preliminary design which would take place during this report, a specific aircraft would be used as reference. The aircraft selected for the implementation of this system consisted of the Boeing 787-9"Dreamliner" (see figure 4). The Boeing 787 is a medium-sized, wide-body commercial aircraft which was developed by Boeing and whose operations started in 2009. It consists of a twin-aisle aircraft capable of accommodating between 217 and 323 people, depending on the family member; in this case, the 787-9 had the capacity of carrying up to 290 passengers. [27] [28]

Figure 4. Boeing 787-9 flying at cruise conditions [3]

The Boeing 787 can extend the flying range of big aircraft to mid-size planes while offering the airlines an exceptional low fuel consumption which allow it to have an extended range of about 7635-8786 nautical miles (around 14140 Kilometers) as well as being able to reduce the harmful emissions, and it uses 20% less fuel than any other aircraft of its size. The reason of choosing this aircraft instead, other is due to the fact that the Boeing 787-9 is a relatively modern aircraft in which, composite materials have been already introduced on a wide range of its structural components but, parallel to this, the A350 has very similar characteristics to the just mentioned Boeing 787-9 (as seen in table 1, a table about the comparison of both aircraft was performed in order to see the different specifications and so to clarify the decision of not continuing with the Airbus). The reason of not using the Airbus aircraft, was due to the fact that Boeing is having a wide range of problems among their company, and this would serve as a reason of trusting in innovative designs such as the one which is being presented. Note that Table 1 at ANNEX I show a comparison between the main characteristics of both aircraft. [27] [28]

CHAPTER 2. CONCEPTUAL DESIGN

The lifting system was initially designed having in mind these three basic concepts. The conceptual design consisted of a set of four venturi ducts along the exterior face of the cross-sectional area of the rear part of the fuselage; these ducts conceptually were designed to have a big entrance in order to try to collect all the possible air coming from the free stream, then the ducts were though to decrease their cross-sectional area to form a geometry similar to the previous mentioned (venturi ducts) so that the airflow would increase its velocity by accelerating the flow. The exit of these ducts would be designed to direct the air in different directions so that it would be able to create a lift or downforce forces on these directions. Also, the ducts were conceptually designed to have some mechanisms in order to let the air flow through them without creating almost any force which would lead to an increase in drag. These mechanisms were initially thought to be composed by some hydraulic systems which would be on charge of closing and opening the ducts depending on each specific situation. Also, an electric system would feed these hydraulics. However, the conceptual design could be better appreciated in the following sections of the report, where the initial arrangement of the new lifting system was conceptually designed.

2.1 CONCEPTUAL CONFIGURATION

The conceptual configuration of this brand-new system consisted of, as it was previously stated, on several venturi tubes acting for the acceleration of the flow in order to generate downforce or lift depending on each situation. As it can be seen from figures 12 and 13, the initial configuration only consisted of two sketches without any type of dimensions; being only focused on the main idea of the project.

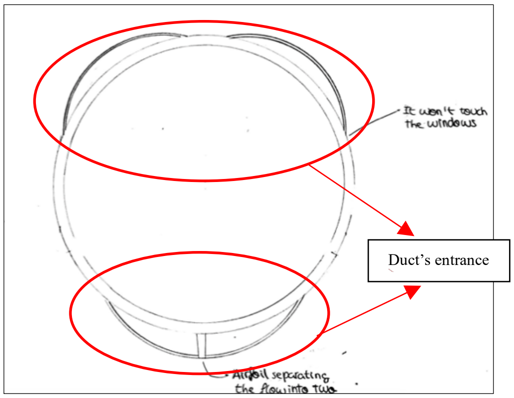

Figure 12. Cross sectional area of a Boeing 787-9 with the conceptual design of the lifting system

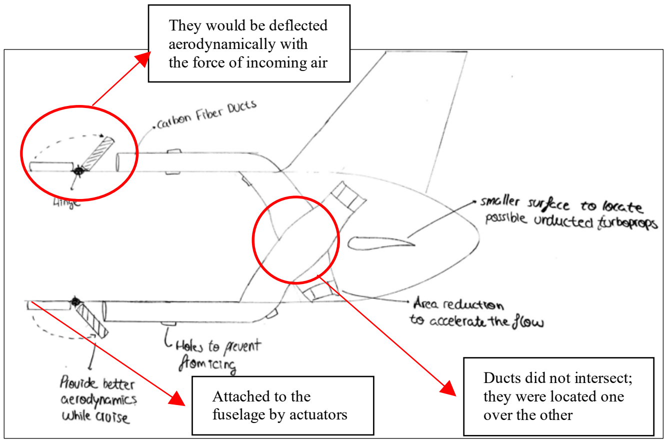

Figure 13. Side view of a Boeing 787-9 with the conceptual design of the lifting system

Initially, in the upper part of the fuselage two ducts were designed to be located symmetrically in respect the center of the fuselage meanwhile, in the lower part, a unique duct was designed to be divided into two different parts after the air has entered the duct. The reason of having only one duct instead of two was in order to gather the highest possible quantity of incoming air. As it can be depicted from the sketches, the space for windows was taken into account and the separation at the lower duct was carried out by the implementation of a wall with the shape of a symmetric airfoil (initially the idea was to use the NACA 0012) to separate the flow smoothly. It was also taken into account the hydraulic system which would consist of different "walls" in order to prevent the air coming into the ducts as well as some prevention of icing in case some water filters through the system while raining at lower altitudes and then getting to higher altitudes where, temperature dramatically descent leading the possible water located inside the tubes to start icing and create an additional weight and drag. To sum up, both ducts were crossing each other as it can be seen so that the internal hydraulic system on each of the ducts would direct the incoming airflow depending on the necessity on each moment.

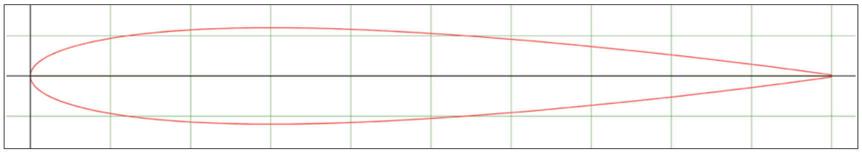

Figure 14. NACA 0012 Airfoil representation [13]

However, this design was only the initial one since, when going into the detail of the design, several problems arrived with this configuration and so the initial design suffered a huge amount of changes in order to make possible this lifting system to possibly work during the future simulations but, before going into the re-design of the concept, the initial configuration would be deeply explained for a better comprehension of the first idea which led to the beginning of this project. In order to perform this report, the airfoil selected for carrying out the studies, simulations… was decided to be the 2822 for the main wing; a transonic airfoil which is actually gaining momentum around the aerospace industry and the NACA 0012; a symmetric airfoil from the NACA family, was used for the horizontal and vertical stabilizers.

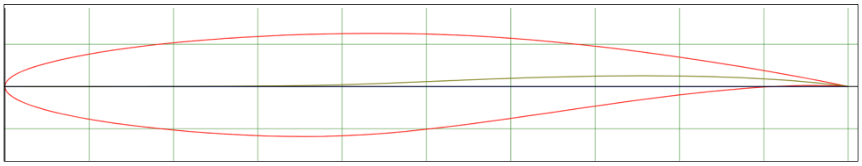

Figure 15. RAE 2822 Airfoil representation [14]

2.2 EXPLANATION OF THE INITIAL CONFIGURATION

The way in which the initial configuration was designed was relatively easy to understand. The air coming from the free stream would enter through the ducts; the air will follow the venturi ducts so that its direction will be able to change with the intention of generating the necessary aerodynamic forces depending on each situation. The air would first decelerate its velocity due to the increment in the cross-sectional area of the ducts and due to the previous contact of the air with the main wing which would lead to a boundary layer detachment and so a loss of the air's kinetic energy; this descent in velocity was intentionally created in order to prevent the flow from becoming supersonic and so creating shock waves in the interior of the ducts which could lead to severe structural and noise problems. Then, with the reduction of the cross-sectional area, the flow would accelerate and due to the curvature of the ducts, the accelerated flow will be deflected either upwards or downwards (note that the flow would not be completely deflected upwards or downwards since the necessary curvature for having that result would create severe issues as it would be seen during this report). The most difficult part of this initial configuration consisted of the area where both, the upper and lower ducts cross each other. Along this area, the air flowing through these ducts would cross each other creating vortices and so losing the sense of this lifting system. The way of avoiding this problem was to design a hydraulic system consisting of four plates with their respective hinges; each plate would be deflected or retracted depending on the route which the air must follow (for example, if it is necessary to create lift, the lower ducts would close their plates in order to not let the air flow through them while, the upper ducts would retract the plates allowing the air to flow through them).

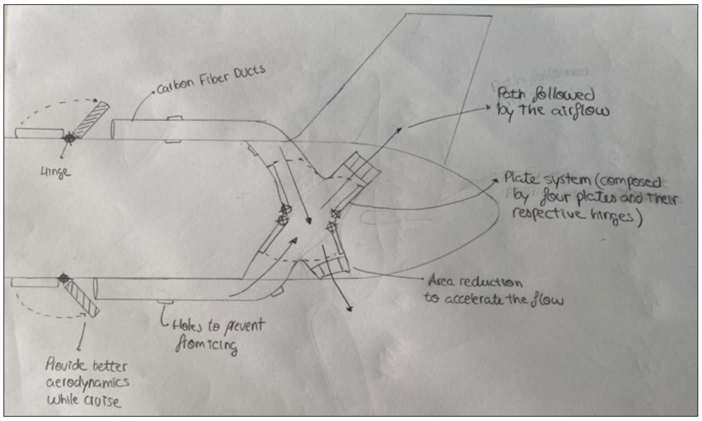

Figure 16. Lifting System conceptual design with its different components explained in more detail

Finally, in case of not needing to create either lift or downforce, both ducts would close their entrance leading the incoming flow to be slightly deflected and so avoiding as much drag as possible. This can be clearly seen in figure 16. However, the initial configuration of this system didn't take into account several aspects which, during the final design were needed to be changed such as the way in which both ducts are closed and a wide range of situations which were considered later on, after this initial configuration.

2.3 INITIAL INTERNAL STRUCTURE

At the beginning, the internal structure of the new lifting system was initially tough to be mainly composed by the same type of aluminum alloy used by almost every commercial aircraft. The fact that brand-new aircraft such as the Boeing 787-9 are being designed to be mainly composed by composite material led to the idea of using this type of materials for the whole structure [35]. Using composite materials is such complex in comparison with the use of aluminum alloys as a mold is needed as well as the matrix and the resin, a method to follow in order to let the resin cure and to create the component (there are several options such as Wet lay Up, Resin Transfer Molding, Prepeg process) [36] [37]

However, this new lifting system contain some complex shapes which won't be easy to manufacture meaning that some molds would be needed for its completion; in parallel to this, since an aluminum skin without any type of internal structure would be sufficient to ensure the system to withstand the high loads generated by the aerodynamic forces acting on this device, an internal structure was decided to be used. The structural configuration would consist of one aluminum layer of a thickness of about 8-9 millimeters which would be in direct contact with the exterior: in addition. This structure would dramatically enhance the mechanical properties of the whole system making it more rigid and so capable of withstanding the different aerodynamic loads parallel to what happens to the aircraft's fuselage. This aluminum structure would be supported by some internal frames similar to the ones which can be found at a conventional aircraft as seen in figure 17. This internal structure of frames was done being inspired from a conventional aircraft's fuselage [38]. However, as it would be seen later on at this report, this structure would change as a consequence of the appearance of carbon fiber in order to reduce the overall weight of the lifting system.

CHAPTER 3. PRELIMINARY & FINAL DESIGN

As it would be seen in the following chapters, during the preliminary design of the lifting system, a wide range of updates were introduced on its design. During this chapter, the updates would be mentioned and deeply studied in detail for a better comprehension of the reasons why these new updates were introduced to the lifting system design. Also, a final design would be provided with the conclusions extracted from the previous designs.

3.1 PRELIMINARY CONFIGURATION

Before starting with a deep explanation of the preliminary configuration, the preliminary design can be appreciated by looking at figures 18, 19 and 20 where the main views of the final design were represented in form of a CATIA model. In addition, ANNEX VI, contain the original planes from the Boeing 787-9 which were used as an initial guide to perform the preliminary design.

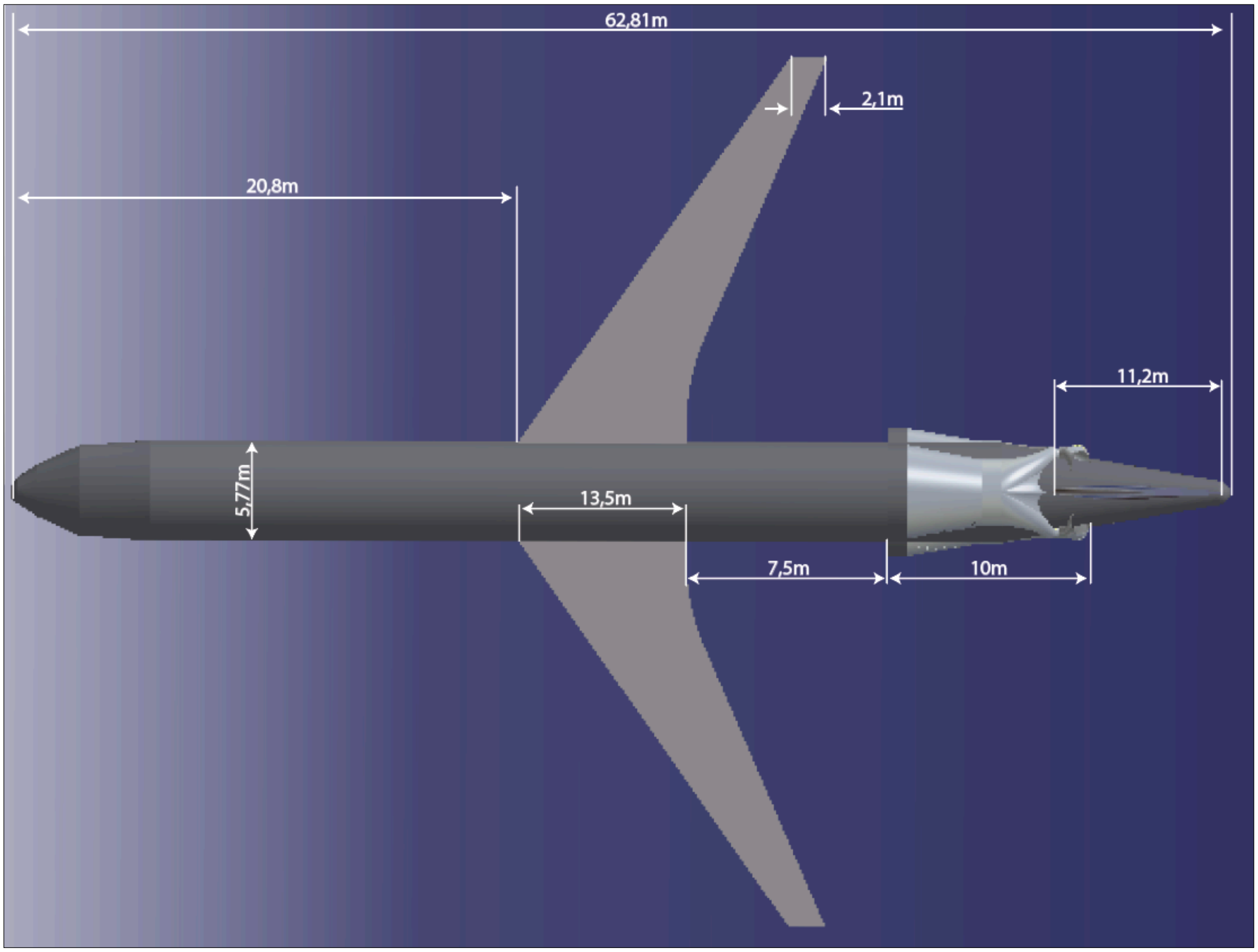

Figure 18. Upper view of the CATIA model including the lifting system

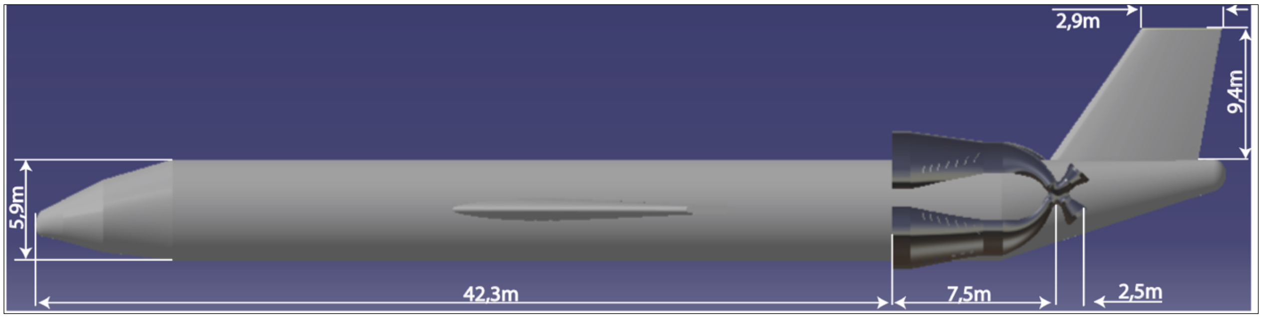

Figure 19. Side view of the CATIA model including the lifting system

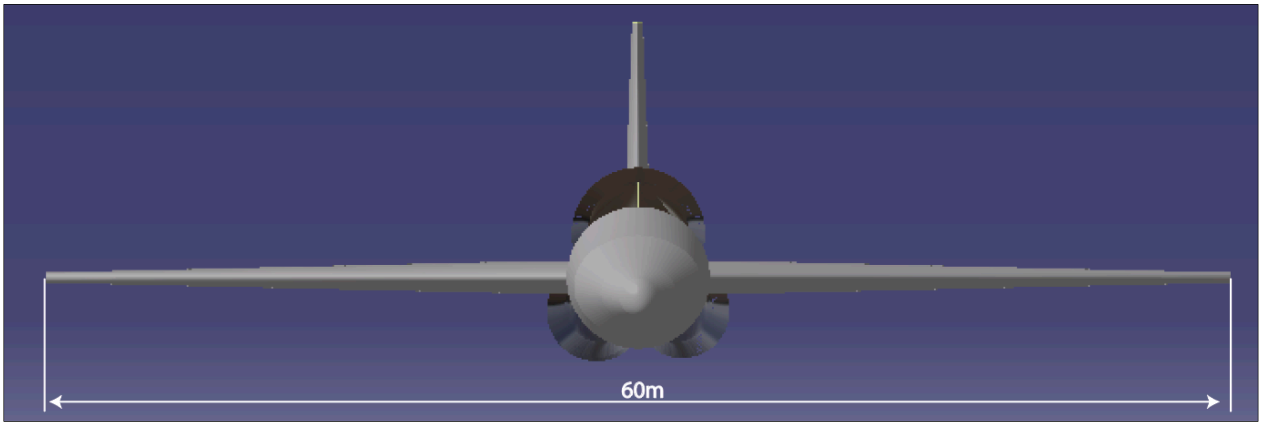

Figure 20. Front view of the CATIA model including the lifting system

The design of preliminary configuration of the lifting system introduced some updates in order to try to mitigate the problems which were found during the conceptual design state, and which would make the lifting system almost unacceptable to be used.

The first update corresponding to the conceptual design consisted of the better definition of the system itself. During the last step about its design, the fact about the position of the ducts while crossing each other wasn’t clear at all. The decision taken on this step consisted of crossing both ducts, instead of manufacturing one above the other so that they would have not cross each other. The main reason of crossing the ducts was because, if having one duct above the other, two additional problems with not a clear solution for them would have been needed to be faced up.

The first problem consisted of an increase in the effective cross sectional area of the lifting system; this increase in the area of the system could have cause interferences since the height of the aircraft would not be high enough to carry on the lifting system; this would have been a problem without no solution since, despite that problem would have been possible by the augmentation of the longitude of the landing gear, meaning that the whole design of the aircraft (the Boeing 787-9 in this particular case) would be needed to be changed.

The second problem which was presented with this configuration was the fact that, the air coming between both ducts, following the aircraft's fuselage would follow until it would face the "wall" corresponding to the plates of both ducts which will lead to a dramatic increase in the pressure drag while landing or taking off, but mostly while flying at cruise speed. Having this in mind, the best solution consisted of the connection of both ducts creating an intersection between them with an "X" shape as it can be clearly appreciated in figure 21. With the use of this configuration, it would be possible to avoid the problems which were involved with the augmentation of the landing gear's longitude but, the second problem about an increment in the pressure drag still to be a problem. In order to solve it, several possibilities were taken into account; one of the possibilities consisted of the design of an external surface covering the whole lifting system, by doing so the whole mechanism would be located below this surface and so a smooth surface would be obtained but on the other hand, another problem arises.

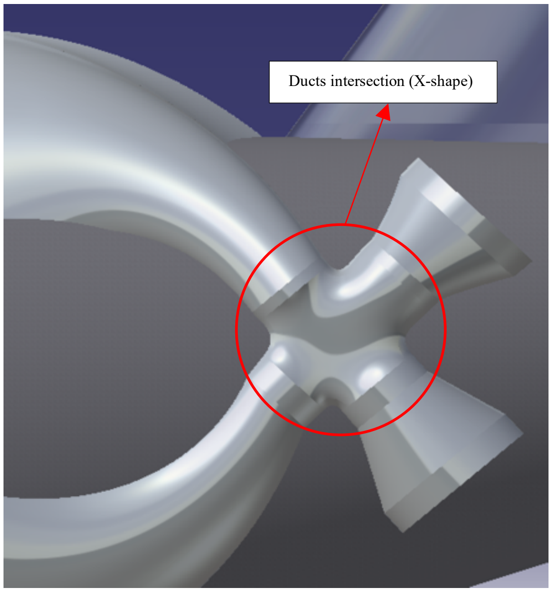

Figure 21. Lifting System duct intersection (X-shape) in detail represented (CATIA)

One of the main goals of the implementation of this new lifting system consisted of the overall weight reduction among other upgrades from a conventional aircraft but, if implementing an external plate acting as a surface, the weight would be significantly increased but not only that, also the accessibility to the interior of the mechanisms would be such difficult that the maintenance costs in order to sustain this system would become such high. Another possibility which was also though,

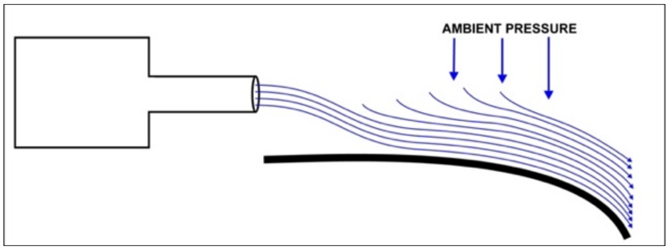

Figure 22. Coanda Effect concept explanation [16]

consisted of the implementation of an airfoil between the space generated by both ducts, similar to the ones formula 1 cars have, with the intention of generating wingtip vortices (vortices generated at the tip of surfaces due to lift which supposes an additional drag [39]) which, despite increasing the overall drag, this drag would be such smaller than the one generated without these devices; note that this idea wasn't finally carried out due to the increment of weight which would suppose the addition of these devices since, they would require from similar internal structures to the ones found in the wings, but at a much smaller scale.

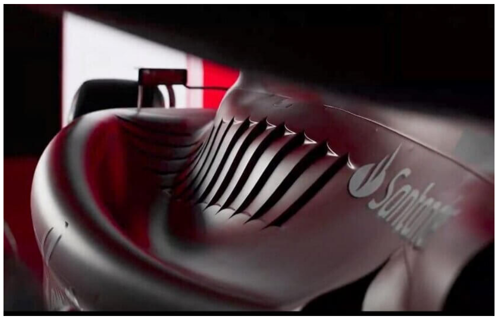

Figure 23. Ferrari F1 2023 with the air intakes seen in detail [17]

Additionally, another idea which was thought to be used consisted of the creation of some air intakes along the ducts so that the air flowing through the middle part between the ducts, would enter through this air intakes since most of the air would follow the curvature due to the Coanda effect which can be better understand by looking to figure 22, where it can be clearly appreciated how the ambient pressure pusses the air to the surface of the body which is being in contact with the air stream (the Coanda effect consists of the tendency of a fluid to stay attached to the surface of a body while the fluid is moving). [40] [41]

These intakes were initially thought to be located on diagonal direction so that the incoming air from the outside will flow into the ducts, meanwhile, the air flowing through the interior of the ducts would remain inside. The inspiration which led to this idea was taken from formula 1 cars (see figure 23), in the way they are designed to get the air flowing from the outside to get into the inside part of the car so that the internal components could lower their temperatures just by getting air in [42]. This idea was the one selected for the preliminary design and as it can be seen in figure 24, a total of six air intakes per duct were designed. Note that this number was almost randomly selected as well as its dimensions since later on, having done the simulations and

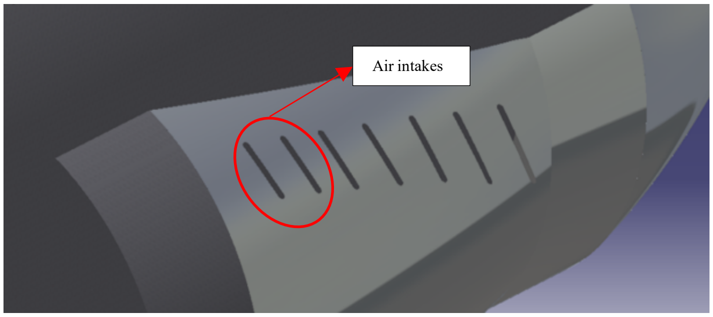

Figure 24. Lifting System air intakes seen in more detail (CATIA)

after got the pertinent results, the final number of intakes as well as their dimensions could change in order to try to maximize the aerodynamic efficiency of the system.

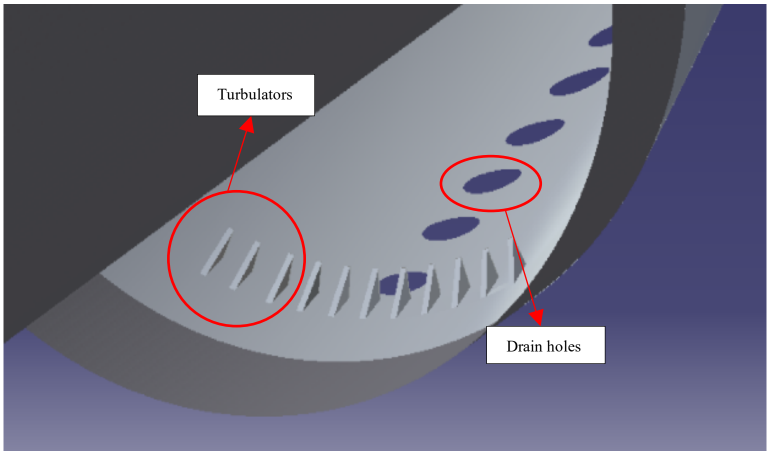

Figure 25. Lifting System turbulators and draining holes seen in detail (CATIA)

The last update which was introduced in the design was the implementation of internal turbulators (see on more detail in figure 25). A turbulator is a device which change the characteristics of the flow making its boundary layer more turbulent so that it prevents the boundary layer detachment by re-energizing the boundary layer [43]. However, that is not the only reason of using turbulators; for this case, the use of turbulators have been implemented as the speed of air after using them is increased; this could help the flow coming through the inside of the ducts to accelerate at some of its parts so that even more lift or downforce could be produced. As it happened with the air intakes, the number of turbulators was randomly selected as well as its position in the ducts (the amount of turbulators used for the designed consisted of a total of 11 turbulators per duct and the initial position selected was almost at the entrance of the duct since that area would be the easiest one to access in terms of maintenance). Note that the upper duct didn't use turbulator since, due to the separation of the internal flow into two different sub flows, the flow was not needed to be additional provided with more kinetic energy. [43]

To sum up, note that the "X" shape formed by the couple of ducts intersecting each other, a total of four "movable plates" would be implemented with their respective electric system which would allow them to be deployed or retracted depending on the direction on which the air is desired to be deflected. In addition to this, the dimensions corresponding to the ducts were chosen with the purpose of having the biggest possible duct entrances in order to gather the biggest possible amount of air (to accelerate a bigger quantity of air) taking into account the restriction on the dimensions of these ducts due to the dimensions of other elements such as the landing gears' height as well as the lift-off angle so that to avoid the collision of the lower part of the duct with the runway.

3.2 FINAL DESIGN

Having performed the conceptual and preliminary design, several parameters changed after a deep study of what it was previously stated. With all the changes updated, the engineering plans about the final design were done (they can be found at ANNEX IV). However, the final design can also be appreciated by looking at figures 26, 27 and 28 where the main views of the final design were represented. In addition, ANNEX I, contain the original planes from the Boeing 787-9 which were used as an initial guide to perform the final design.

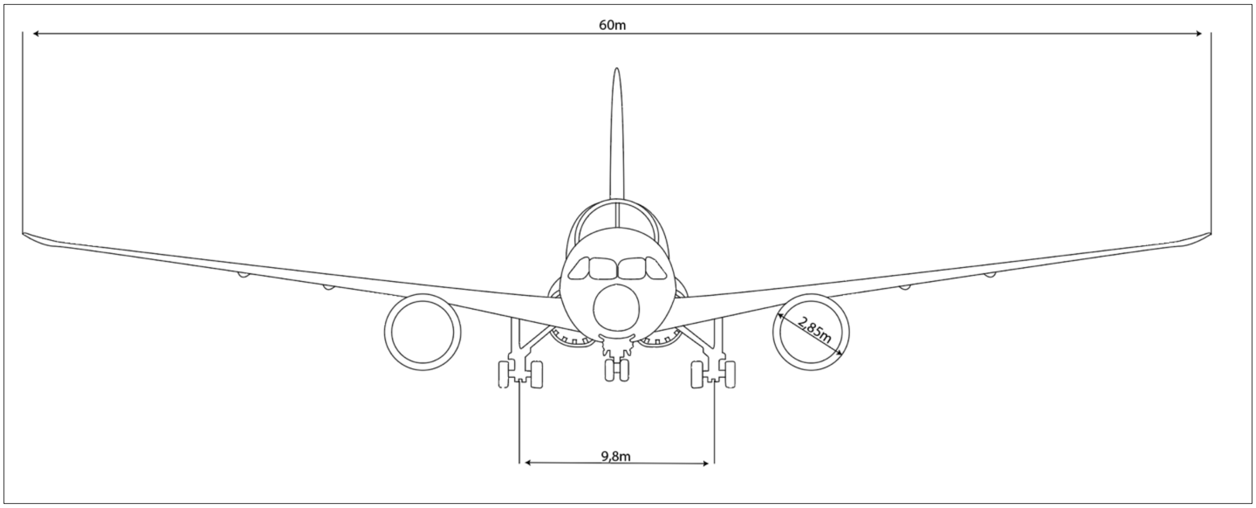

Figure 26. Front-view of the Boeing 787-9 with the definitive Lifting System configuration (Adobe Illustrator)

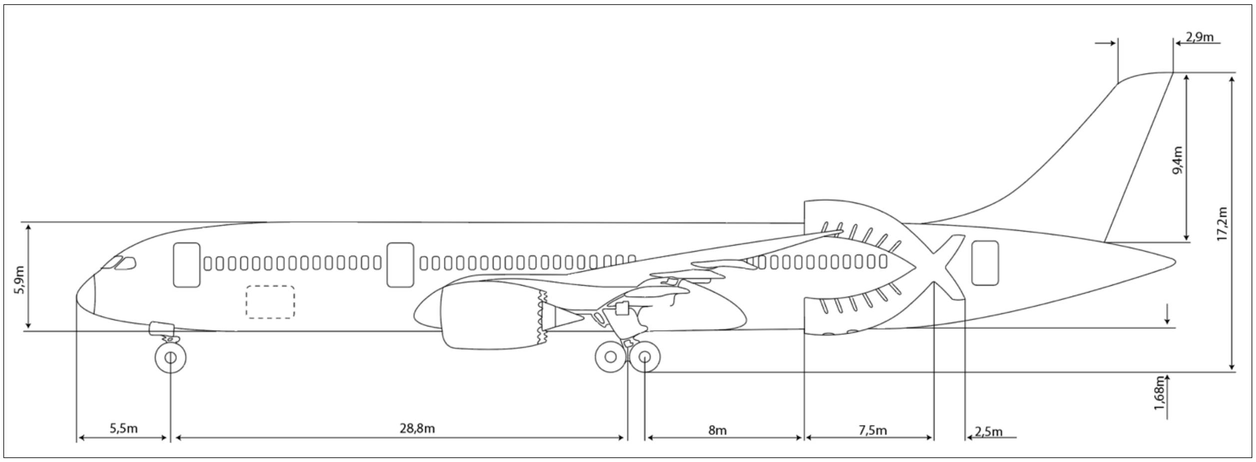

Figure 27. ide-view of the Boeing 787-9 with the definitive Lifting System configuration (Adobe Illustrator)

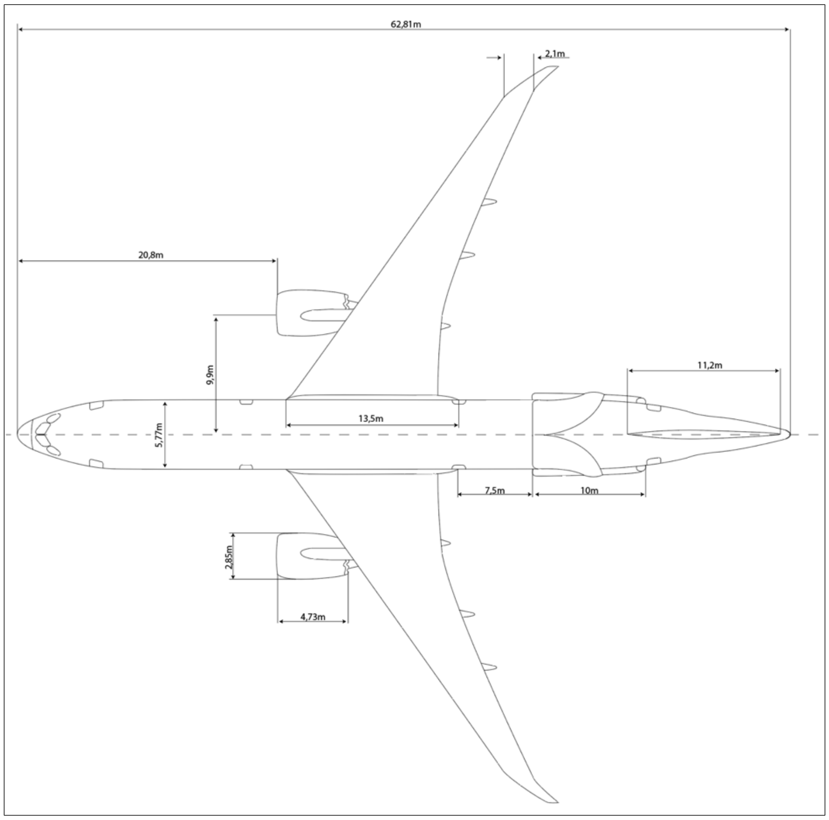

Figure 28. Upper view of the Boeing 787-9 with the definitive Lifting System configuration (Adobe Illustrator)

Having performed the preliminary design review, the final design was done taking into account the results which were obtained from the simulations which would be seen later on this report. The aim of the changes performed consisted of making the lifting system as simple as possible while reducing the overall weight of the system as much as possible and reducing the impact in drag while generating more lift or downforce when necessary. The first aspect to be changed consisted of the reduction of the number of drain holes [44] from six to two as well as reducing the diameter of these holes; the purpose of this change was given since the simulations with a total of six holes showed how a big amount of air flowing through the duct exit it through these holes (this would be seen at the simulations when, at the beginning they were done using 6 drain holes but, due to the negative results, the number of drain holes was changed up to 2 of them). Also, the position of them changed, they were relocated almost at the entrance of the duct since it consisted of the lowest point of the duct, where water would be more likely to be stagnant (this would be better seen during the simulations).

The next change performed during the final design was to provide the ducts with a more progressive inclination rather than the previous ducts (at the preliminary design) which were initially designed to obtain the highest possible lift and downforce respectively without taking into account the drag which would be generating the duct. During this final design the inclination was reduced (see figures 29 and 30) and as a result, the air followed easier the ducts and so, at the same time that the drag was reduced respect the previous design, an additional lift and downforce was created since a bigger quantity of air flowing around the ducts followed the desired shape (Coanda effect), despite the air was deflected on a less inclined direction which could be, at first, seen as a negative point (this would be seen later on in detail during chapter 3.8.1).

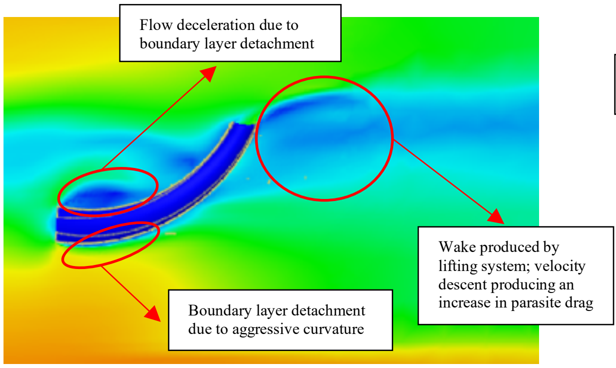

Figure 29. Initial design of the lower Lifting System duct generating downforce simulated at Autodesk CFD

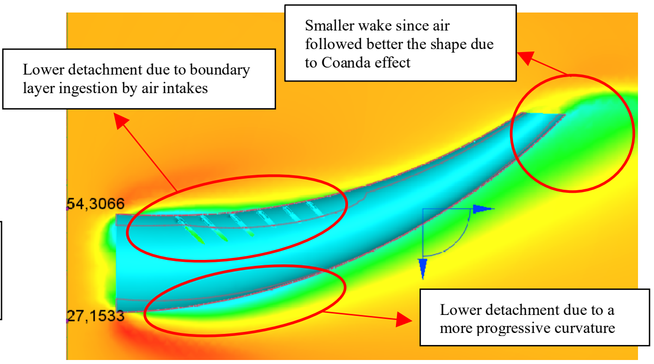

Figure 30. Final design of the lower Lifting System duct generating downforce at Autodesk CFD

Finally, the last features to be changed from the previous design consisted of the interior of the ducts. During the conceptual and preliminary design, the aircraft was supposed to have two external plates at the beginning of the ducts entrance in order to avoid as much as possible increments in either drag or downforce while flying at cruise. Due to the complexity of this system, which would require from much more weight in order to have two additional plates with enormous dimensions since these plates were supposed to cover the whole entrance to the duct but also, since they would be flat plates, the air would go around the plate and enter the duct and so the system would be a failure a simpler method was designed.

With the purpose of avoiding that system, similarly to the internal plates which were designed to deflect the air up or down, a third plate was designed as it can be in figure 31 so that thanks to the combination of the deflection of every plate the air could be directed into the free stream direction with even more velocity than before due to the mass conservation principle (explained during the previous chapter). The introduction of this system was considered since the drag generated by the lifting system while flying at cruise speeds would be such high that the overall efficiency of the aircraft would exponentially drop. This additional mechanism was finally designed, being inspired of formula 1 Drag Reduction System (explained at chapter 1). Similarly to how race cars reduce the drag at certain sectors of the tracks by opening their rear wing with the intention of letting the air flowing through it without being deflected, at the intersection between the ducts, an opening was designed to be open and closed by means of a system of radial actuators and plates (see figure 31). This system would redirect the air flowing through the interior of the ducts also, rearwards causing as a result, an acceleration of the flow since, as it was previously stated, the air would accelerate as the area at the exit would have been reduced such in comparison with the area at the entrance of the ducts. This acceleration of the flow could help to reduce the power of the engines while flying at cruise since this system would help the aircraft reaching higher velocities (despite this could cause an increment of the overall velocity of very low values, an extreme reduction of the engine's power through such high distances while the aircraft would be flying at cruise would help it to reduce emissions as well as reducing the fuel consumption and despite this reduction would be supposed to be such small, a small change for thousands of kilometers travelled per day could suppose an appreciable reduction of fuel consumed) and so

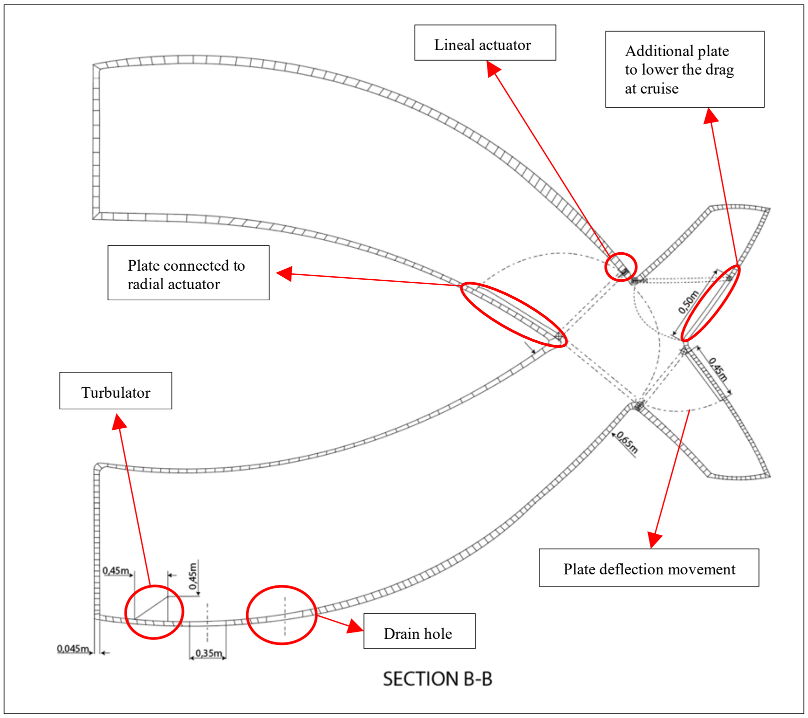

Figure 31. Side-view of the cross-sectional area of the ducts including the plate system (Adobe Illustrator)

reducing the overall drag in comparison with the previous case where this system was not though to be implemented. With all of these new implementations, the overall performance of the lifting system exponentially increased from the preliminary design. Note that the visual results of the differences which are being just explained can be clearly seen later during the simulations. Finally, a representation of the cross-sectional area of the final design can be seen at figure 32 where it can be appreciated the re-designed system of drain holes and turbulators as well as the separation wall located at the upper ducts to divide into two the flow and direct it to each of the ducts.

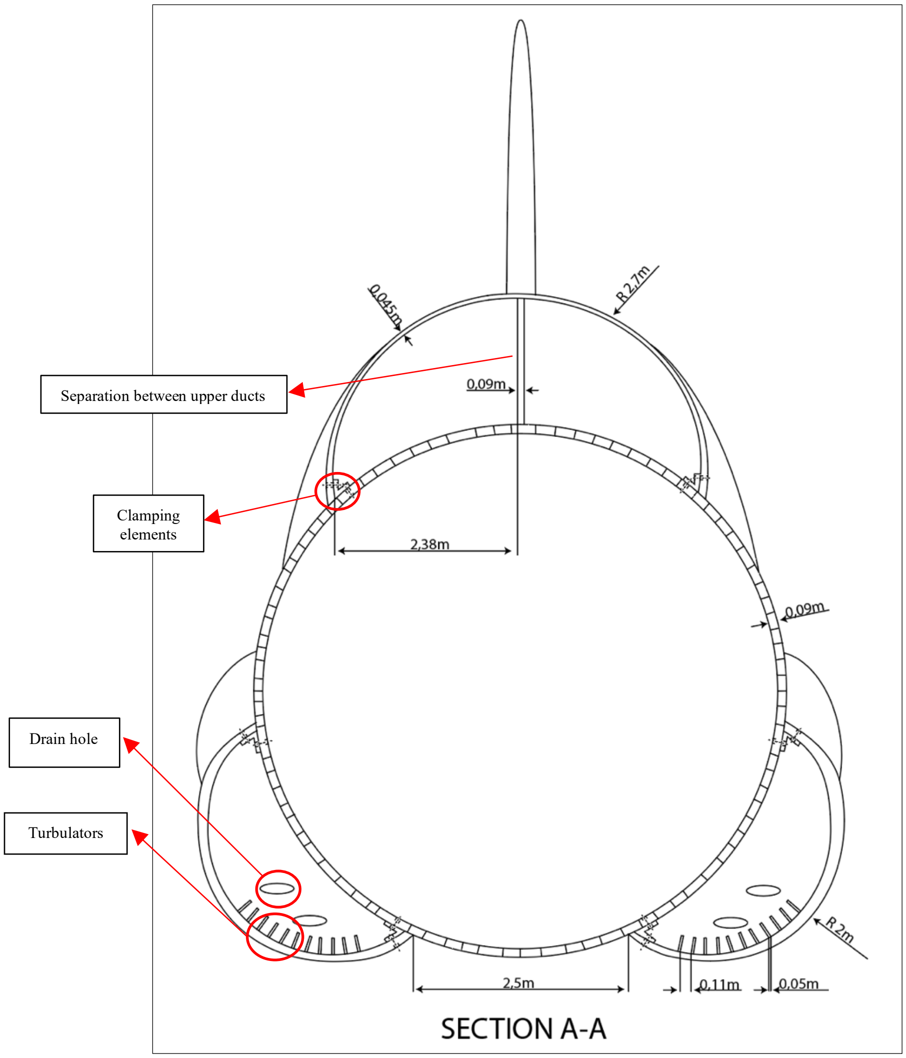

Figure 32. Front-view of the cross-sectional area of the Lifting System arrangement at the Boeing's 787-9 fuselage (Adobe Illustrator)

3.3 RE-DESIGN OF EMERGENCY DOORS POSITIONING

Every commercial aircraft has several emergency doors, which are located following the criteria imposed by the authorities; each emergency door must be separated at a maximum of around 60 ft meaning that almost every commercial aircraft whose fuselage is such long would need to have at least two type A doors at the same side of the aircraft (they have two type A doors; one at the front and one at rear part of the fuselage but also, two smaller doors are often located near the main wing in case of emergencies) [45]. The best manner to not have safety issues was to relocate the emergency door just after the lifting system so that every seat would be able to be kept (on the other hand, about two rows of seats would not have windows due to the lifting system introduction). Some other problems such as the ones involving the raise in noises generated by the new lifting system could also be determinant with its position but, initially, the position of the lifting system was supposed to be located at the same position as it has been just stated. Figure 33 represents the new position for the emergency door; as it can be clearly seen, the only difference from its conventional position is the elimination of the windows at two rows of the aircraft. Despite this, the tickets for these two rows could lower their prices as not having windows (since these rows would be the ones at the back of the aircraft their price could be even lower than usual so that the price could be more accessible to everyone) but also, more weight and maintenance could be saved since no windows would be needed at those positions.

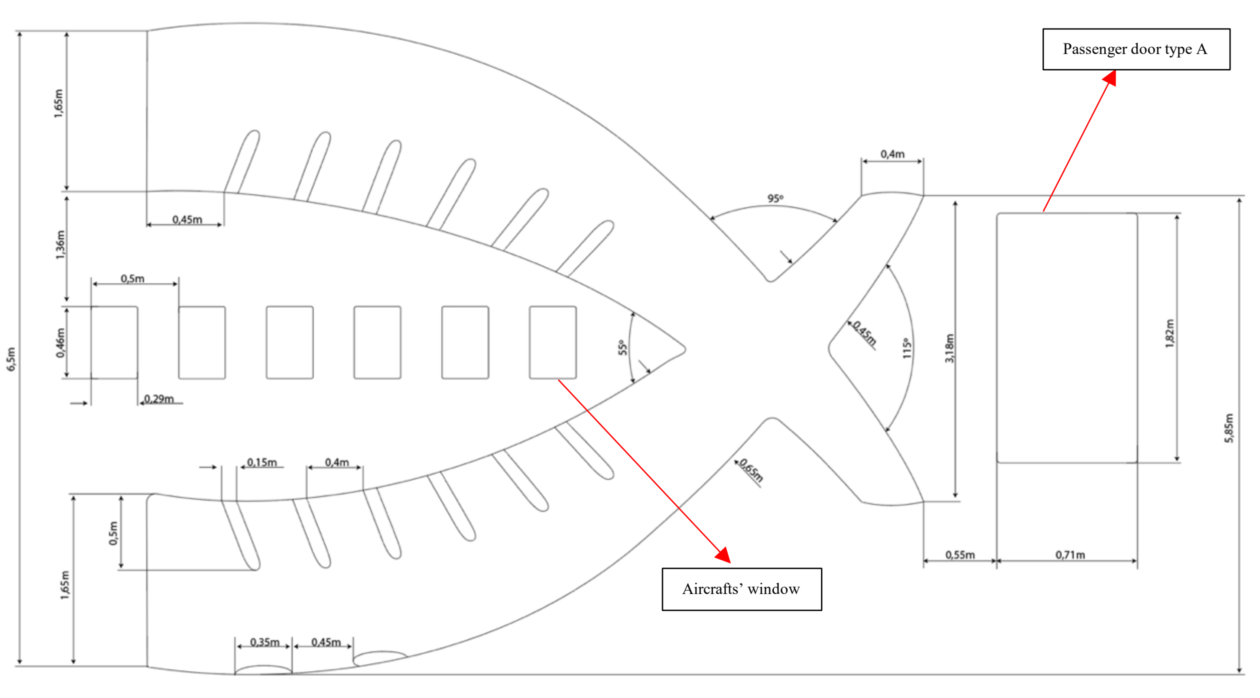

Figure 33. Side view of the duct system arrangement including the windows and rear passenger door positioning (Adobe Illustrator)

3.4 FINAL INTERNAL STRUCTURE

Despite during the first approach of the internal structure, the final structure was selected to be completely composed by carbon fiber. The main reason of not using the previous structure as it was initially though was due to the fact of the increment on the weight of the structure; since the main idea of this new lift device was to substitute the horizontal stabilizer by decreasing the weight of the whole system, using more materials than necessary will increase the weight of the aircraft as well as enhancing the manufacturing costs; for these reasons, the whole structure would be manufactured in carbon fiber with the addition of an aluminum honeycomb core with the purpose of increasing as much as possible, the mechanical properties of the lifting such as its hardness, toughness, plasticity and resistance to fatigue [46]. The carbon fiber selected for the development of the lifting system was decided to be the “Sandwich Panel- Aluminum 3.1lb/ft^3 Honeycomb Core (0.460’’)- Twill carbon Fiber Skins (0.02’’) – Matte/Matte – 48 x 48 x 0.500 inch” from the American company Rock West Manufacturing [47].

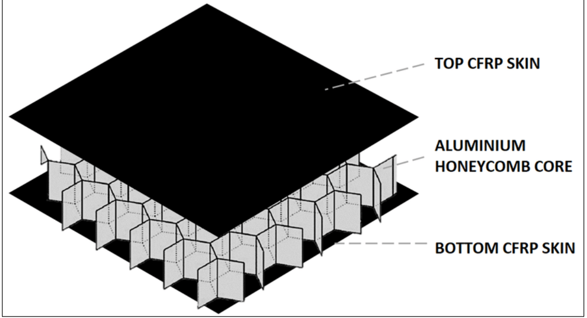

Figure 34. CFRP Sandwich structural arrangement with an aluminum core [18]

The main reason of using this type of carbon fiber instead other ones was due to the fact that it consists of a carbon fiber sheet exclusively made for aeronautical purposes; it has an aluminum honeycomb core which, allowing the structure to have a low overall density, a high strength-to-weight ratio, and a high stiffness-to-weight ratio. Having a sandwich structure also makes these materials capable of providing good thermal and acoustical insulation. Among the different dimensions and thicknesses which can be found at Rock West Manufacturing, the selected one for the manufacturing of the lifting system was decided to be of a thickness of 12,7 millimeters and the carbon fiber rolls which would be bought would consist of the biggest ones offered by this web page: 1219 x 1219 mm (in the following chapter, the number of carbon fiber rolls needed for the development of the lifting system would be calculated) [47]. However, this lifting system would be attached to the fuselage by means of rivets; for doing so, the number of necessary rivets might be calculated but, this was not performed since there are too many parameters which would not be reliable enough in order to take into considerations those calculations. About the mechanical properties of this type of carbon fiber, by looking at ANNEX XIX, it can be appreciated its main properties. Note that the plates for the air deflection would be manufactured using this same carbon fiber.

For the development of the composite structure, an RTM (Resin Transfer Molding) method would be needed to be used meaning that, a mold of the lifting system must be done in order to follow this process. Despite its difficulty, this won't generate many problems since after having the molds, the rest of the steps would be relatively easy. Despite the avoidance of corrosion since using composite materials, other problems could arrive even if using carbon fiber [48]. During rainy days, large quantities of water could enter inside the ducts, most of it would be able to be expelled because of the shape of the lifting system but, in other cases, some water could be stored among the ducts. In case this happens, when getting to higher altitudes, and due to the dramatic decrease of temperatures the remaining water could freeze and this would cause two main problems: the first one is that the weight of the aircraft would increase and so the additional efficiency obtained with this new lifting system would reduce and could make this option not as efficient as it could be, the second problem would consist of the unbalance of the aircraft; the formation of ice in one side of the aircraft would partially obstruct the duct in which the ice would have formed; that's to say that the tube where this would be happening would not be able to accelerate the flow as much as the rest of ducts which would not be affected by the ice and so, not desirable movements would be obtained as a response. In order to avoid this problem, it was decided to locate some holes with the purpose of draining the water which could get inside the ducts. These drain holes consisted of holes open to the exterior. They were strategically located so that in case of having water inside the ducts, the remaining fluid would be expelled through these cavities (as it was just seen at the final design, the position and number of holes would change).

To sum up, it is expected that during future reports, a deep study about the possibility of substituting these materials which have been just mentioned by others with similar mechanical properties such as the young modulus or rigidity but, with the intention of being more sustainable will be carried out so that the processes which would involve its manufacturing processes would be less harmful with the environment than if performing the manufacturing processes to obtain carbon fiber or aluminum.

3.5 HYDRAULIC SYSTEM

The hydraulic system of the new lifting system would work parallel to the electrical system, since both need from the other to perform their functions. During previous chapters on this report, the hydraulic system has been slightly described but, during this chapter, it would be explained with higher details. As it was previously mentioned, the lifting system would consist of a set of three ducts at the entrance (one in the upper part of the fuselage, which is then divided into two parts, and two ducts in the lower part) and four ducts at the exit. For an easier comprehension of the hydraulic system, the study of them would be carried out by separating them on two different zones: the entrance and the middle section & exit (figure 35).

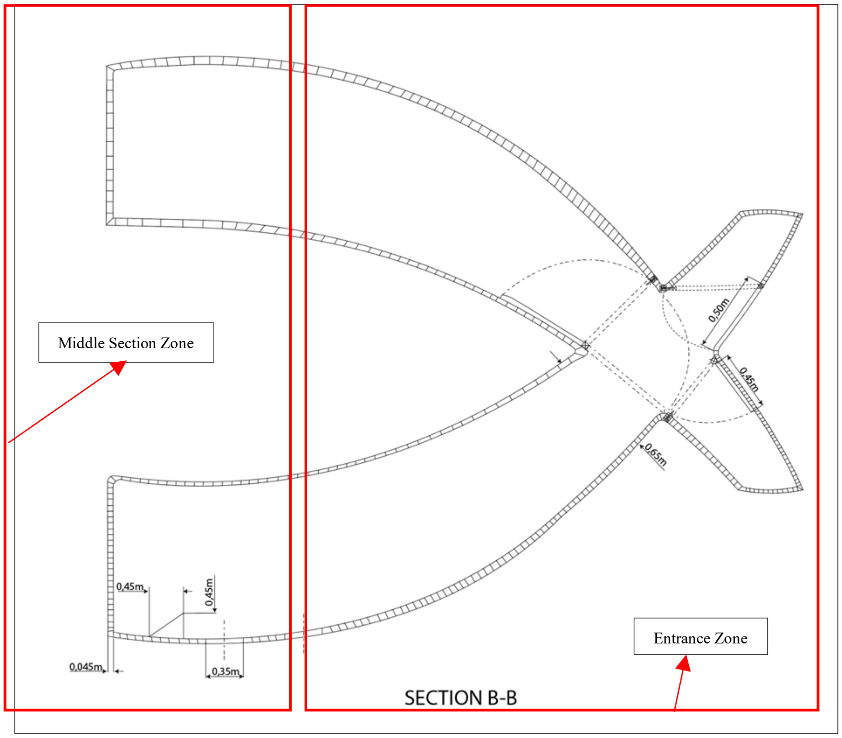

Figure 35. Lifting System cross-sectional area division into entrance and middle & exit sections (Adobe Illustrator)

At the entrance, non-hydraulic system components would be found. Despite during the initial designs, as it could be seen before at the first sketches, the first idea was to design some external plates to "close" the ducts; the purpose of these plates was to deflect them while flying at cruise so that most of the drag generated by the lifting system would be avoided but, this would be a problem since the plates needed for doing so would need to have such big dimensions that the overall weight would exponentially increase as well as the hydraulic and electric system associated to these plates to allow their movement. Instead of these plates, another solution was found to not create large quantities of drag while flying at cruise; a system similar to the DRS, (explained at the beginning of the report, used by the formula 1 cars in order to decrease as much as possible the drag) which would be later on explained into detail. At the middle section of the lifting system, the air entering through the entrance of the ducts would reach the X cross-section at this section, two plates would be found with the intention of redirecting the flow wherever the purpose of the motion is set (this can be clearly seen in figure 35). Each of these plates would be controlled by their own system of actuators; each plate would be connected by a pin, an actuator and a hinge, inserted at the carbon fiber structure; every time the system detects that a duct needs to redirect either downwards or upwards the incoming air, a signal would be sent to the hydraulic system of each plate would be able to deflect its position by rotating around the hinge by means of the radial actuator located on each plate; when the plates reached put the final position (closing a duct), the plate would be secured by a lineal actuator. For example, in case that the aircraft needs to increase its altitude, the ducts pointing upwards (lower ducts) would close their plates so that all the incoming flow would be exclusively directed downwards and so an additional lift would be created (this example can be clearly seen in figure 35). Additionally, in the middle section another plate was located. The aim of this plate is to direct the flow in the free stream direction and so, reducing the overall drag. The hydraulic system involving this plate would have the same components and way of working as in the two previous plates. Note that the actuators selected consisted of linear actuators which would extend their pin inside the plate to block their movement or subtract their pin from the plate to allow the movement of the plate by means of the hinge where they are connected to; the rotation of the plates would be carried out by means of a radial actuator for each of the plates (three radial and three lineal actuators in total). For the specifications of both actuators, see ANNEXES XVII and XVIII.

Figure 36. Lineal Actuator [19]

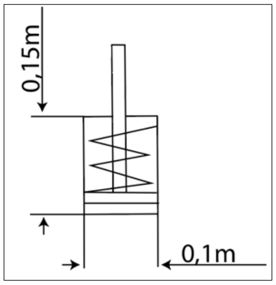

Figure 37. Lineal actuator representation (Adobe Illustrator)

Figure 38. Radial Actuator [20]

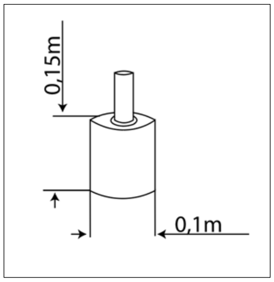

Figure 39. Radial Actuator representation (Adobe Illustrator)

3.6 OVERALL INTEGRATION ON THE EMPENNAGE

Before starting with the simulations, the first step was to create the full geometry of the aircraft and the brand-new lifting system. As it was previously stated, the aircraft chosen as reference consisted of the Boeing 787-900; in order to start with the three-dimensional model, the dimensions corresponding to this aircraft were used to create the model, taking into account almost every single external element except for the landing gear as well as the horizontal stabilizer. The first step was to create the geometry corresponding to the fuselage, for performing it, several tools and technics were used with the purpose of recreating as similar as possible the nose and end part of the Boeing 787-900 since the geometry at those areas involved complex techniques. The next step consisted of the definition of the main wing as well as the engines; during this step and since for the wing design of the aircraft has an unknown airfoil distribution, for this example a transonic airfoil (RAE 2822) was selected. The reason of using these airfoils among the rest was due to the fact that transonic airfoils are directly related with the laminar flow at wings during flights which means that these types of airfoils are supposed to be more efficient than conventional airfoils; for this reason they are considered to be the type of airfoils which would be used in a near future and because of that, the RAE 2822 airfoil was selected to carry out this study. Despite the advantages of the just mentioned airfoil, the vertical stabilizer of the aircraft was designed by using a NACA 0012 airfoil; the reason of this is that the RAE 2822 is an asymmetric airfoil which could cause some issues during flight since more lift would be generated and so a yaw moment would appear in one of the directions but, if using symmetrical airfoils such as the NACA 0012 this problem could be avoided. [49][50][51]

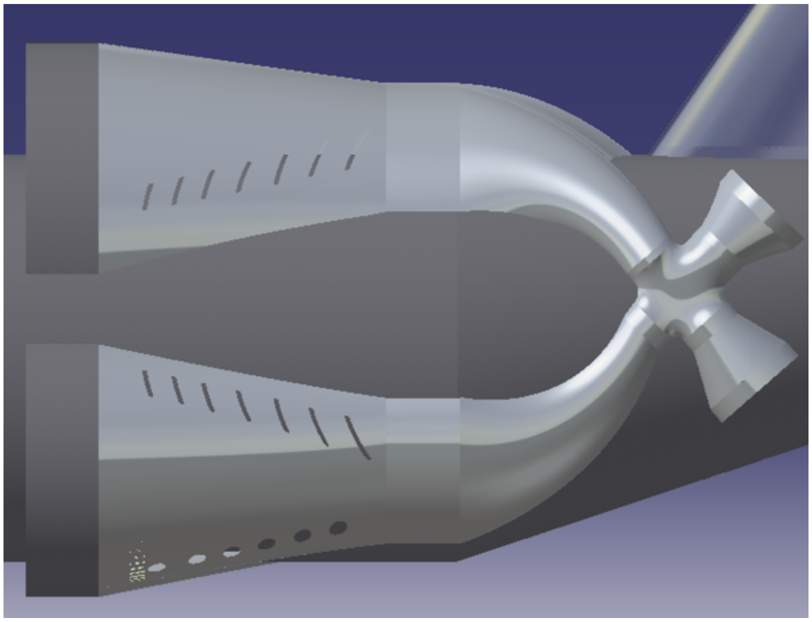

Figure 40. Side-view of the Lifting System (CATIA)

The following step consisted of the three-dimensional modelling of the lifting system. Due to the high complexity of the body, the system was designed performing several steps. At first, three sections were created (at the beginning of the duct, at the X cross-sectional area and at the end of the duct). The dimensions of these areas were previously stated considering the calculations performed in order to estimate the total surface area so that the lifting system with the purpose of knowing how much the overall weight of the lifting system would be as well as the costs related with the materials which would be calculated later on, at this report. At this point, and space was reserved for the location of the emergency doors since the lifting system could interfere on its position (this problem was already solved on the previous points during this report). Having already created the previous geometry, the following step consisted of generating the air intakes (similar to the ones used in Formula One cars) as well as the draining holes at the lower part of each of the ducts. The X section where both ducts are crossing each other was the most difficult part to design since there were multiple interferences and a wide range of tools were needed to use for the proper completion of the geometry. Finally, the new lifting system integration was done at the empennage of the aircraft as seen in figure 40; notice that different skins were given to each component of the aircraft for a better visual understanding. The structure was then transferred to Ansys for the pertinent preparation of the geometry and mesh for the required simulations, which would be covered in the following points over this report. However, as it would be seen later, despite the whole aircraft structure was already done in CATIA, due to a wide range of errors due to some inconsistencies which appeared when transferring the geometry from one program to the other, the final geometry which was decided to be used during the simulations consisted only of the new lifting system.

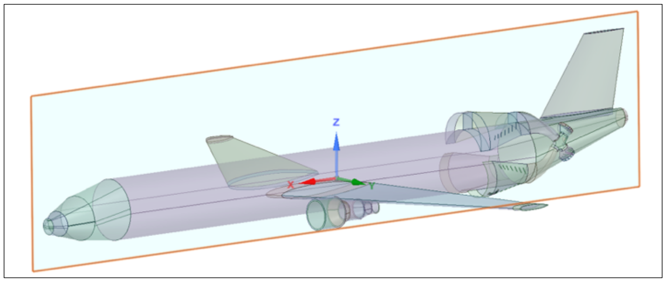

Figure 41. Boeing 787-9 with Lifting System configuration represented in Ansys Workbench

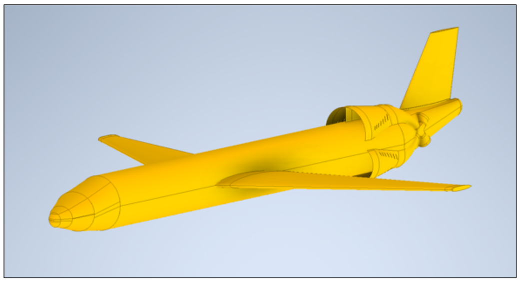

Figure 42. Boeing 787-9 with Lifting System configuration represented in Autodesk CFD

Despite what it was previously stated, several errors were found during the simulations in Ansys; due to the extremely complex geometries used for the completion of the lifting system and the tools used during this process in CATIA, it was almost impossible to obtain a mesh without errors and so the simulations at Ansys were not possible to be done. After a deep study about the different tools which can be used for fluid simulations and using all of them, the tool at which simulations were done consisted of the "Autodesk CFD"; however, the geometry done in CATIA was incompatible with this program and so, the easiest solution was to replicate the previous geometry at "Autodesk Inventor" and so having all the different information at the same environment (Autodesk environment). The advantages of this program with respect Ansys were that, despite it also gave geometry issues, the mesh which could be generated at this program supposed a dramatic increment of the mesh's quality since, in comparison with the 300,000 nodes which Ansys students version, Autodesk CFD allowed enormous quantities of nodes, being able to reach around a million of nodes and so having an incredible mesh quality if comparing it with Ansys. Note that the same geometry was replicated at Autodesk Inventor, as it was previously stated. However, even with Autodesk CFD failures continued due to the complex geometry of the lifting system. The geometry was repeated for several times and even when imperfections in the geometry were removed, problems continued during the simulations. The way in which these problems were solved were by simplifying such the geometry by simulating both ducts, the upper and lower ones separately from each other. By doing so, the geometry was so simplified that the simulations were able to be done. Also, the additional parts which were previously planned to be added to the ducts (turbulators) were not able to be simulated with the hole geometry and so, for ensuring that the mentioned devices could be able to work correctly, the geometry relative to the new lifting system was simulated aside from the rest of the geometry (not including the complete aircraft). This means that the results won't be such precise to what it was initially thought but, as it was the unique way of solving every issue related to the CFD, simulations were performed as it has been just explained; however, not only simulation were done, also calculations were carried out later on, in order to compare the results and see if there exists a correlation between the results. Note that during Autodesk CFD Simulations, the engines and landing gear were not taken into account for obtaining a more precise mesh at the lifting system; the final geometry of the aircraft with the lifting system included can be seen at ANNEX VII. Note that at figures located at the Annexes, engines were included but due to several errors in the geometry, the engines were finally deleted; also, as it can be seen in figure 41, this geometric model had a total of 7 air intakes and 6 drain holes but both numbers corresponding to these components were finally changed as it was previously stated.

3.7 SIMULATIONS & METHODOLOGY USED

As it was previously stated, simulations were finally done at Autodesk CFD. This software is relatively simple in comparison with other CFD software's. The first step consisted of replacing possible geometries which could interfere during the simulations. Then, an external "enclosure or box" which consists of the control volume was stated. This control volume had a bigger dimension than the aircraft itself [52]. Since it consisted of the control volume and the lifting system is tough to work upwards or downwards to generate the previously mentioned lift or downforce, the control volume was given a bigger dimension on that both directions but also, the sides were given certain distance from the tip of the wings in order to avoid the wing tip vortices to be perturbed (As its own name says, wing tip vortices refers to the vortices generated at the tips of the aircraft wings; these type of vortices are generated due to the difference of pressure existing between the lower and the upper sides of the wing) [53]. This pressure difference is what allows the aircraft to generate the lift but, when going to the tips, the air below the wing, whose pressure is much higher than the air above it tries to decrease that gradient in pressure by moving from the lower to the upper side to compensate that difference. This movement of air at the tips is the responsible for generating the so-called wingtip vortices so, as a conclusion, these vortices would always be generated while flying, despite it helps to generate lift, it creates large quantities of induced drag.

Having done the enclosure, the next step consisted of setting the boundary conditions for the simulations. These boundary conditions were assigned to both the geometry and the enclosure; for the geometry, the materials used were selected (as it was already stated carbon fiber was supposed to be the main material but, due to the fact that carbon fiber wasn't able to be chosen, aluminum alloy was selected instead; note that the results won't suffer noticeable changes due to this change) as well as the material of the enclosure which was selected to be air (note that the air inside the enclosure was assumed to be incompressible and inviscid since, if giving it compressibility and viscosity the program was not able to run correctly the simulation as it has several limitations due to the fact that a free trial was being used). Also, for each of the faces of the enclosure, a boundary condition was provided; for the frontal enclosure face, an initial air

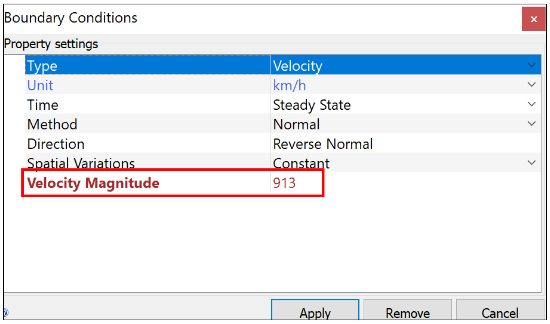

Type	Velocity
Unit	km/h
Time	Steady State
Method	Normal
Direction	Reverse Normal
Spatial Variations	Constant
Velocity Magnitude	913

Figure 43. Autodesk CFD boundary condition about the incoming freestream velocity

speed of 913 km/h was given due to the fact that the simulations would be firstly run at ideal cruise conditions, for the back face, a pressure gradient was selected so that the air would be forced to travel from the inlet to the outlet part of the enclosure; finally, for the rest of faces a function called slip/symmetry was selected with the purpose of making them "invisible for the program" while running the simulations. [54]

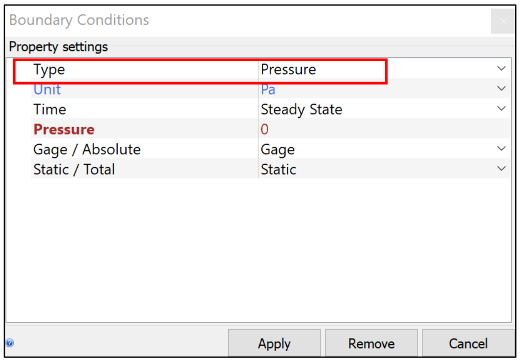
Boundary Conditions

Property settings

Type	Pressure
Unit	Pa
Time	Steady State
Pressure	0
Gage / Absolute	Gage
Static / Total	Static

Figure 44. Autodesk CFD boundary condition about the pressure at the end of the control volume

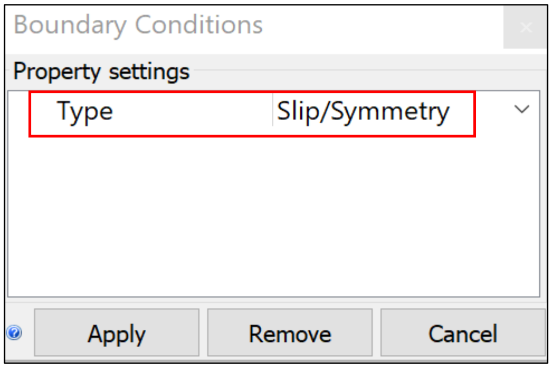
Boundary Conditions

Property settings

Type: Slip/Symmetry

Figure 45. Autodesk CFD boundary condition about slip/symmetry (acting as invisible boundaries)

The last step consisted of the creation of the mesh. The mesh was automatically generated to have an initial number of nodes but, since that number was too small to generate a realistic mesh, some refinements were used to improve it such as decreasing the growth rate or increasing the minimum number of nodes per surface with the purpose of improving as much as possible the mesh. Note that every simulation had the same number of nodes for a better comparison between each of them. During the steps involving the mesh development, some conditions were stated such as taking into account the turbulences of the flow as well as using SST-K omega turbulence model in order to later on solve the simulations (the common SST k-ω turbulence model is composed by two equations from the eddy-viscosity model. The shear stress transport (SST) formulation offers the best of the two options. The employment of a k-ω formulation in the inner sections of the boundary layer makes the model directly useable all the way down to the wall through the viscous sub-layer, hence the SST k-ω model may be applied as a Low-Re turbulence model without any additional damping function) [55] [56].

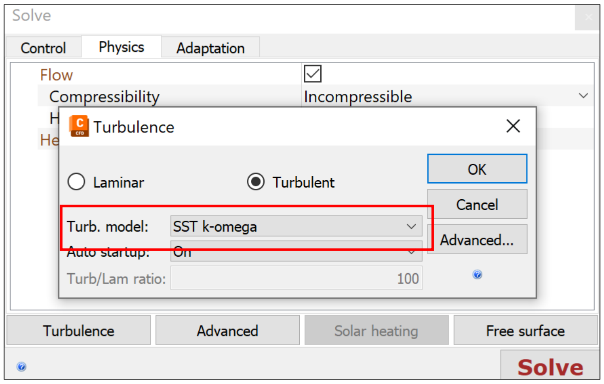
Solve

Flow ☑

Compressibility: Incompressible

Turbulence

○ Laminar ● Turbulent

Turb. model: SST k-omega

Auto startup: On

Turb/Lam ratio: 100

Figure 46. Autodesk CFD turbulence model used (SST-k omega)

3.7.1 SIMULATION RESULTS

As it was previously stated, a wide range of simulations were done for ensuring the most accurate results which would be later, compared with the results obtained from performing the respective theoretical calculations. Note that these simulations were done at ideal cruise & take-off and landing conditions (incompressibility and cruise speed coming directly frontwards to the aircraft, despite simulations with air coming from the sides were also performed). However, some concepts may be summarized before going through the results for a better comprehension of those.

Boundary layer

When an object moves through a fluid, the molecules near the object are perturbed and so forced to move around it. Aerodynamic forces are generated when the fluid interacts with an item; the magnitude of these forces is determined by the shape of the component, its speed, the mass of the fluid traveling around it, as well as the compressibility and viscosity [57].

As the fluid flows around the component, the molecules closest to the surface adhere to it. The molecules just above the surface are slowed down when they collide with the molecules on the surface and so, they slow down the flow which is found above them. The further from the surface, the fewer collisions by the air molecules with the aircraft's surface can be found. This creates a gradient of velocity moving from almost zero airspeed (at the surface) until the free stream velocity (at the free stream, far from the surface); this is known as boundary layer [58] [59]. The displacement thickness is determined by the Reynolds number, which is the ratio of inertial to viscous forces. [60]

$$\textbf{Reynolds Number} = \frac{\rho * V * L}{\mu}$$

The Reynolds number determines whether the boundary layer is laminar (the flow seemed to follow a consistent direction despite being perturbed by an object), transient (state between laminar and turbulent regimes which is not clearly defined) or turbulent (the flow seemed to be disordered and so it don't follow a consistent path). The boundary layer separates from the body, and this results in a completely different shape that the studied structure. This occurs due to the fact the flow near the boundary has a small amount of energy (compared to the free stream) and is more easily influenced by pressure changes. Flow separation, also known as boundary layer detachment, is the cause of wing stall at high angles of attack as well as the increment in drag due to the increase in drag. [61] [62]

Adverse Pressure Gradient

An adverse pressure gradient takes place when static pressure rises in the direction of the flow. This is crucial for boundary layers. Increasing fluid pressure increases the fluid's potential energy, resulting in lower kinetic energy and slowdown the flow. Because the fluid in the inner section of the boundary layer moves slower, it is more influenced by the growing pressure gradient. For a significant enough pressure rise, this fluid may reduce to zero or even become reversed, resulting in flow separation. This has important aerodynamic repercussions because flow separation considerably changes the pressure distribution throughout the surface, affecting lift and drag characteristics. Turbulent boundary layers are more capable of sustaining an unfavorable pressure gradient than laminar boundary layers. The most efficient way of mixing when the turbulent boundary layer carries the kinetic energy from the regime where the air has more momentum to the low momentum regime at the surface of the body which is being studied and so the boundary layer detachment which would occur in case of having a laminar flow would be avoided. As it can be seen in figure 47, the adverse pressure gradient is represented along the regimes through which the air flow is flowing. At the left part of the figure, the regime seemed to be laminar meaning that, as it is represented, no adverse pressure gradient can be found. However, when increasing the Reynolds number (moving from the left to the right of the figure), the regime would become transient at so some separation could be found (figure "c") and finally, when reaching the turbulent regime, where the highest number of Reynolds number are found (figures "d" and "e") and so, the adverse pressure gradient can be clearly seen due to the detachment of the boundary layer which is being generated. [63] [64]

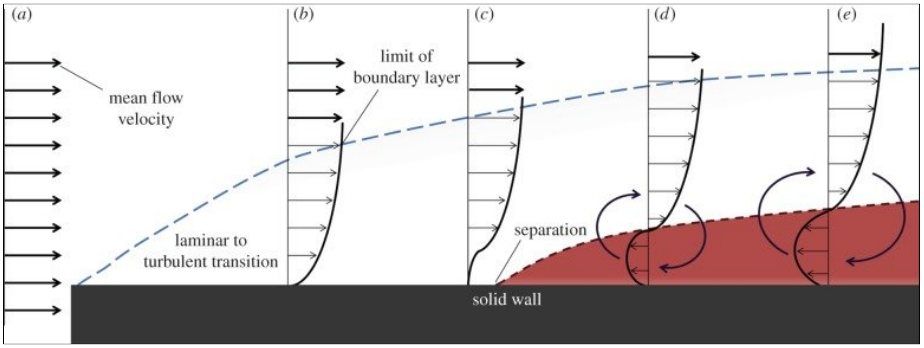

Figure 47. Adverse pressure gradient representation in an initial laminar regime [21]

Conventional configuration (with the horizontal stabilizer)

During the first simulation, the original Boeing 787-9 was replicated at Autodesk Inventor, meaning that the horizontal tail plane was also included at this geometry (the engines and landing gear were not represented with the intention of obtaining a mesh of higher quality; this happened for every simulation performed). As it can be appreciated at figures 48, the air speed distribution through the aircraft seemed to be such uniform. At the nose of the aircraft, the stagnation point can be depicted where, it can be appreciated how, the velocity decreased exponentially. The stagnation point is the point where the velocity of the local flow is almost 0 [66]; that is the reason why at this regime, the color of the velocity distributions turns into a green/blue color, since the velocity has decreased to almost 0 km/h. The flow then starts accelerating (suction peak: point of lowest pressure [66]) since the velocity at the stagnation was null; that explains the red color which can be found at both sides of the fuselage just after the stagnation point. Since the cruise speed of the aircraft is such high, the Reynolds number regime at which the aircraft is supposed to be flying would correspond to a turbulent regime, meaning that the flow would become turbulent. Also, due to the friction of the fuselage with the air (parasite drag) [67], the air would slow down at the regions near the fuselage and would go faster while getting far from it due to the lack of friction (boundary layer detachment). As it was previously stated, because of this phenomenon, an adverse pressure gradient would be formed since the appearance of the fuselage's friction would lead to some frictional forces pointing in the direction of the movement of the aircraft meanwhile the air far from the surface would continue with its direction, opposite to the aircraft's one. Finally, the aircraft tails seem to create a huge wake just after it, since the air would be divided by the vertical tail plane and so an empty space would be created just after the vertical stabilizer which would lead into a descent in the velocity since an enormous, induced drag would be created. [68]

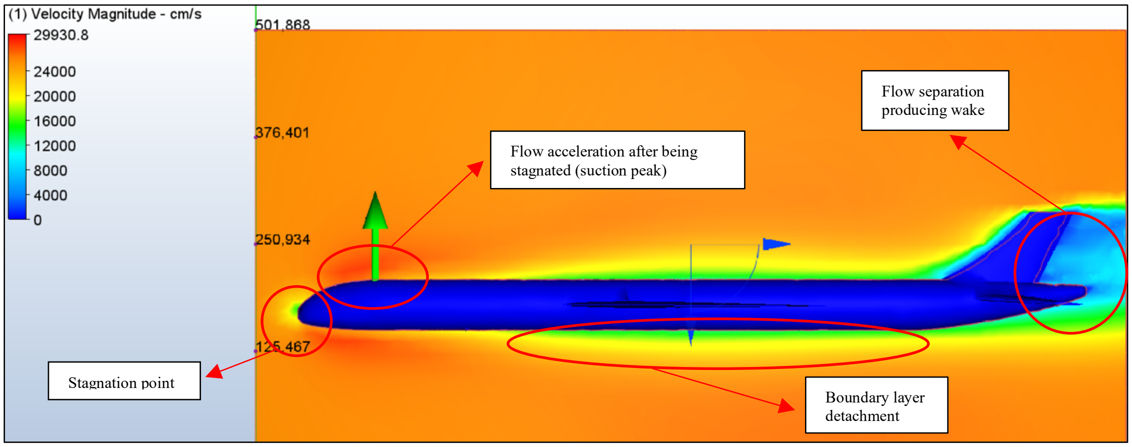

Figure 48. Velocity distribution (Z-axis) of the Boeing 787-9 with conventional configuration (including the horizontal stabilizer)

Also, it can be appreciated how the disturbances created by the main wing would affect the horizontal stabilizer; this is not the best distribution of the lifting surfaces since it can be seen how the boundary layer detachment affects the horizontal stabilizer. This means that it could partially enter to stall on a relatively easy manner in case of performing certain maneuvers. Figure 49 also represents the velocity distribution among the wing and the horizontal stabilizer. The stagnation points at both lifting surfaces can be clearly seen as in the previous figure, as well as the descent in velocity due to the empty space lead by the wake of the wings. Notice that the disturbances in velocity produced by the main wing on the horizontal stabilizer were not such important due to the separation between both of them.

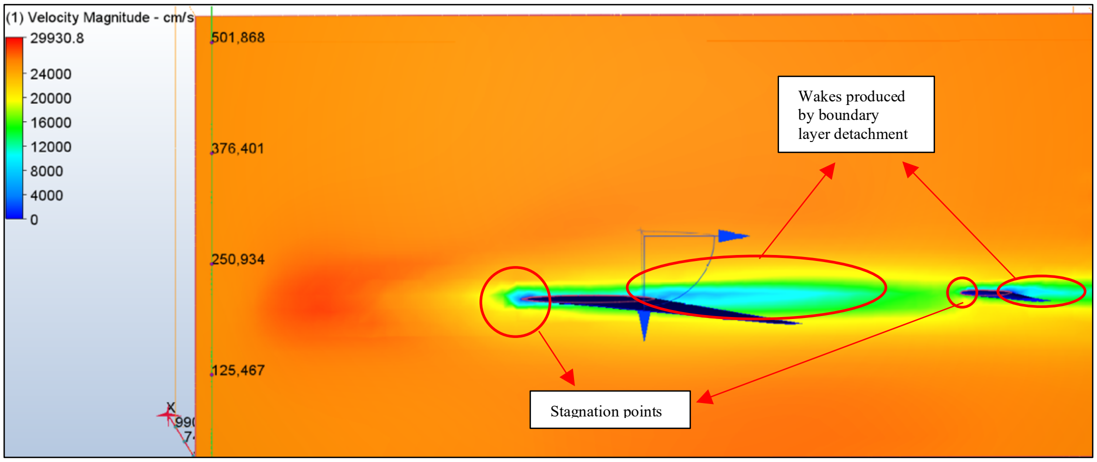

Figure 49. Velocity distribution (Z-axis) in detail at the main wing and horizontal stabilizer of the Boeing 787-9

For a better comprehension of what it has been just explained, the simulations were represented using cylindrical vectors in order to clearly represent the vectors' path. As it was done with the previous figures, at figure 50, it can be appreciated how the detachment of the flow would affect the horizontal stabilizer. Note that this detachment would not be such remarkable since the number of vectors used during the representation was not big enough with the intention of still seeing the horizontal tail plane.

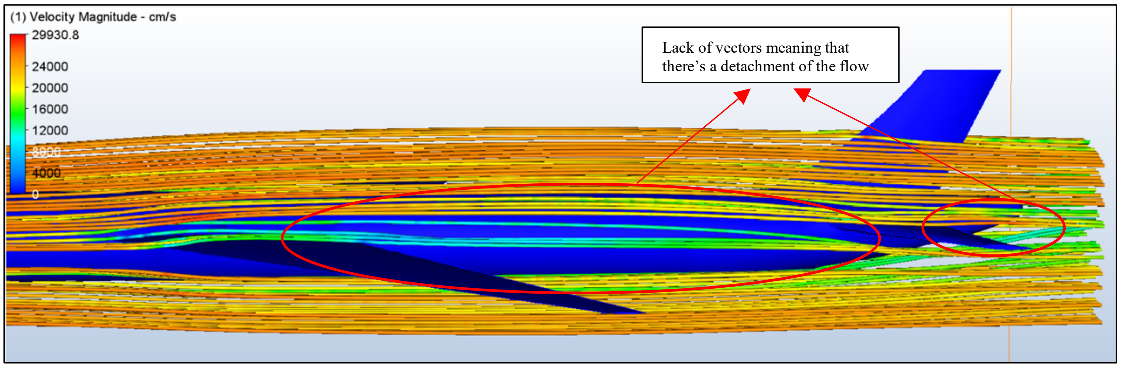

Figure 50. Vectorial representation of the velocity distribution (Z-axis) for the Boeing 787-9 with the horizontal stabilizer

Aircraft without horizontal stabilizer

The objective of this specific simulation was not to realize about the aerodynamics around the aircraft without the rearwards lifting devices; instead, it was simulated with the intention of obtaining numerical data in order to compare it with the conventional display of the Boeing 787 and the new Boeing 787 with the lifting system included. However, since the simulations were needed to be done, it is interesting how the air flows around the aircraft without these devices, as it is seen in figures 51 and 52.

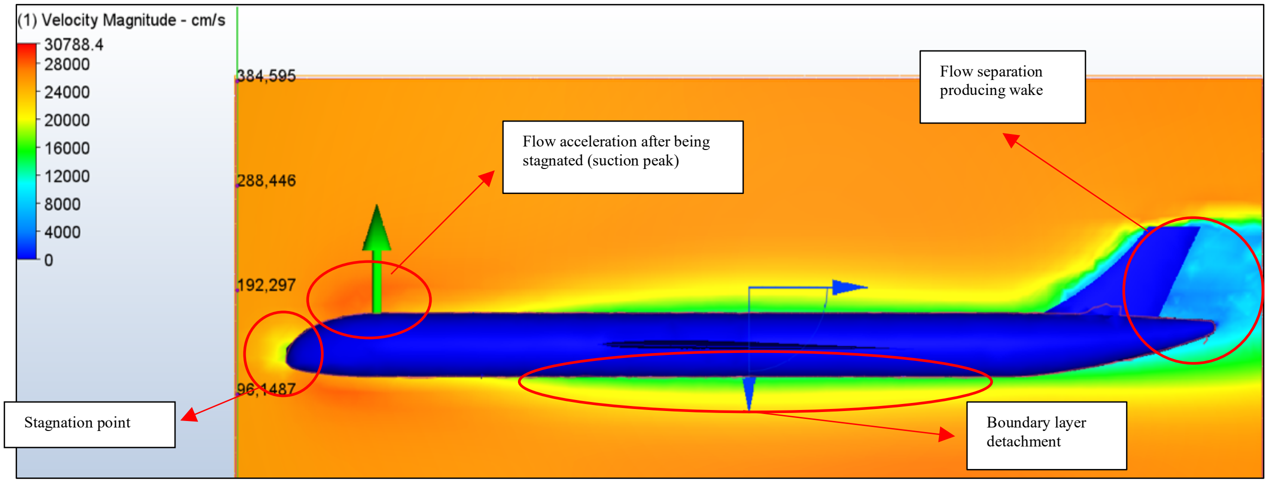

Figure 51. Velocity distribution (Z-axis) of the Boeing 787-9 without Lifting System & horizontal stabilizer

As it was done during the previous subparts, the air flow was also represented using vectors to clearly see the path followed by the air. It can be noticed how the air would become more laminar without any component at the rear part since no lifting system would be disturbing the air.

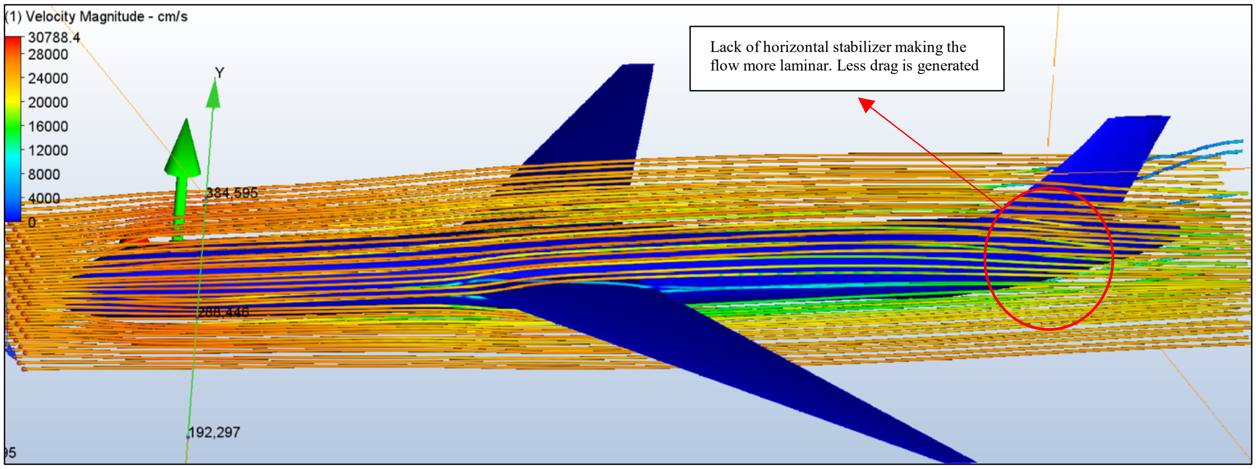

Figure 52. Vectorial representation of the velocity distribution (Z-axis) for the Boeing 787-9 without Lifting System & horizontal stabilizer

Aircraft with the lower duct generating downforce (preliminary design approach)

As it has been explained through the report, the predictions made before performing this simulation consisted of the generation of downforce due to the redirection of the air performed by the upper pointing duct. This geometry suffered significant changes from the first simulation done until the definitive one, since the initial simulations (as seen in figure 53) showed that the lifting system generated even a greater wake than before, located at the rear part of the aircraft. This would suppose an increase in the induced drag which would be generated, as well as severe turbulences which could affect the vertical stabilizer of the aircraft due to the generation of an adverse pressure gradient (vortices would be generated) which could affect the aircraft performance. However, note that due to the change in the number of nodes for each simulation, the final results could differ; this explains the sooner boundary layer detachment at the upper part of the fuselage in comparison with the previous simulations.

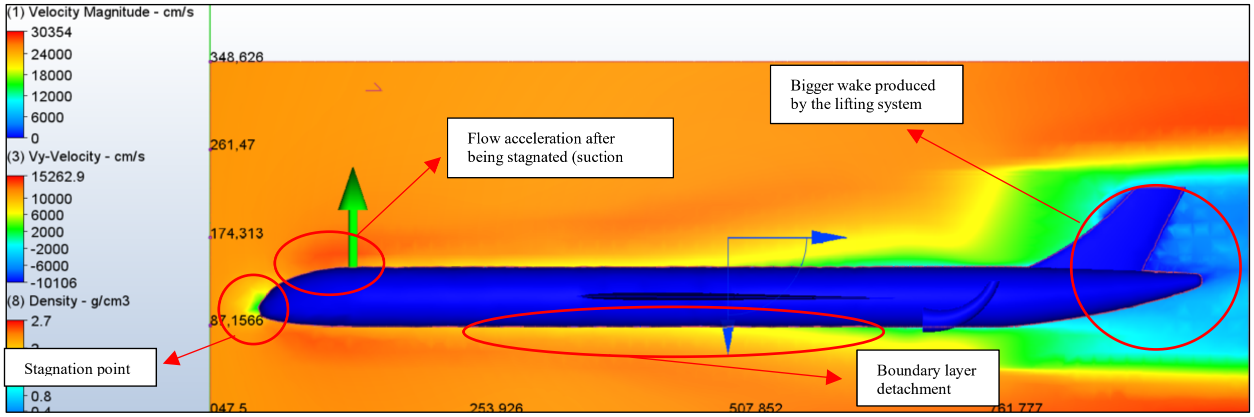

Figure 53. Velocity distribution (Z-axis) of the Boeing 787-9 with initial Lifting System

As seen in figure 53 where the initial approach was simulated, an enormous wake appeared just after the aircraft, exponentially increasing its induced drag due to the generation of vortices led by the boundary layer detachment. The first figure shows the wake generated by the aircraft's structure itself meanwhile, the figure below represents the wake generated by the lifting system (only the upper pointing duct). The severity of that increment of the induced drag led to the idea of introducing the previously mentioned elements in order to help to reduce this type of drag (turbulators, air intakes and draining holes). Despite the drag generated was such enormous, the system was able to be simulated and so, it was concluded that the lifting system worked correctly; this can be clearly seen in figure 54, where it can be appreciated how the air, which have lost part of its kinetic energy after travelling through almost the whole fuselage, the air is being accelerated inside the duct and the increment in airspeed at the outlet of the duct (as seen in the legend of every figure, red color represents the air travelling at high speeds meanwhile the blue color represents the air travelling at low speeds). This increment in the velocity of the air across the duct was able to be clearly seen in figure 55, where a graph at which the vertical velocity (Y-axis) depending on the selected coordinates was constructed. Note that distance was specified in centimeters, since the model of the aircraft was designed in millimeters in order to get a higher quality mesh. On the other hand, the figure 56, representing the horizontal velocity (Z-axis) which was also constructed, show the descent in horizontal speed across the ducts.

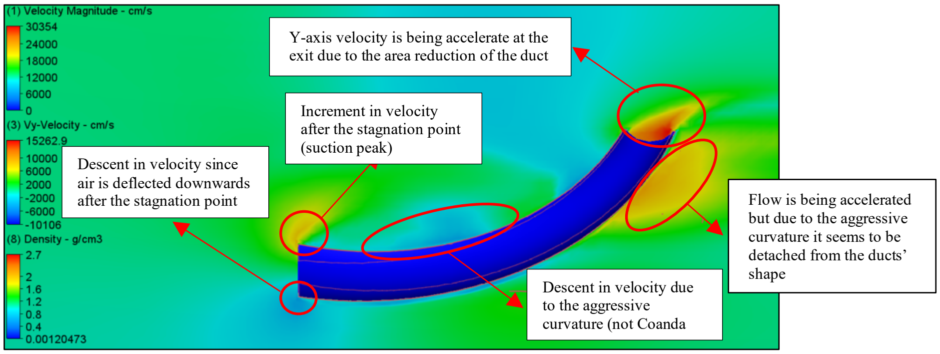

Figure 54. Velocity distribution (Y-Axis) through the initial design of the lower duct generating downforce

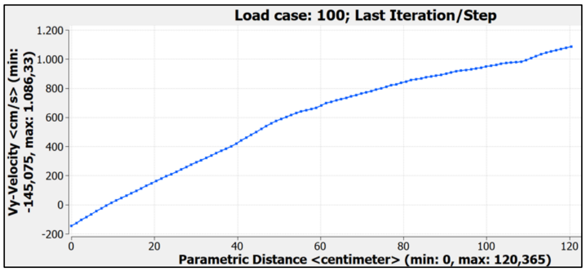

Figure 55. Vy-Velocity vs. Parametric distance graph for the simulation of the lower duct generating downforce while cruise

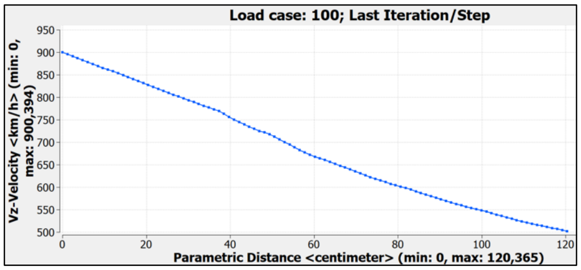

Figure 56. Vz-Velocity vs. Parametric distance graph for the simulation of the lower duct generating downforce while cruise

To sum up, the static pressure as well as the turbulent kinetic energy in order to validate the previous figures. Figure 57 represents the turbulent kinetic energy present at the entrance and exit of the duct; as it can be appreciated from this graph, the kinetic energy has increased through the duct and that is due to the fact that the velocity has increased. Since the kinetic energy can be represented as $\text{Kinetic Energy} = \frac{1}{2}\text{mv}^2$; as the mass would be almost the same as at the entrance of the duct (neglecting the air coming from the intakes and the air flowing across the drain holes) due to the conservation of mass and velocity would have increased as it was just stated before; as kinetic energy increases with the square of the velocity, it can be seen how the kinetic energy would grow following a parabola as it is appreciated in figure 58. About the static pressure, the graph could lead into doubts since it is already known that, when pressure drops means that the velocity of the fluid would increase since the streamlines became closer to each other (this can be proved by the Bernoulli's principle which was previously stated and explained). In this case, this is what happens but, the velocity which needs to be taken into account is the velocity in the Z-axis.

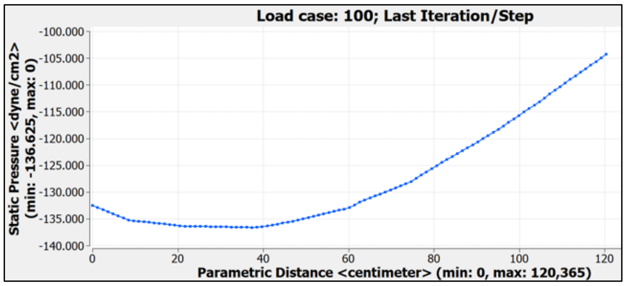

Figure 57. Static Pressure vs. Parametric distance graph for the simulation of the lower duct generating downforce while cruise

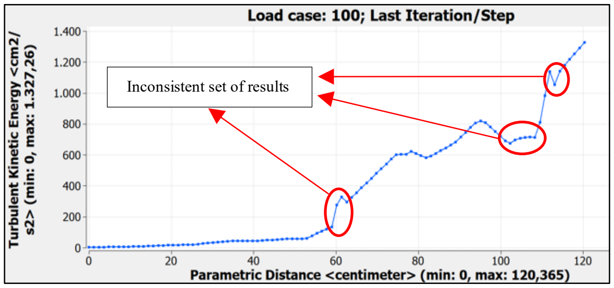

Figure 58. Turbulent Kinetic Energy vs. Parametric distance graph for the simulation of the lower duct generating downforce while cruise

For even a better comprehension of what was happening to the air flowing around the lifting system, the simulation was represented in many other ways as it can be appreciated in figure 58, in order to see in a more exact way how the air was flowing through the system as well as the clear air detachment existing through the system.

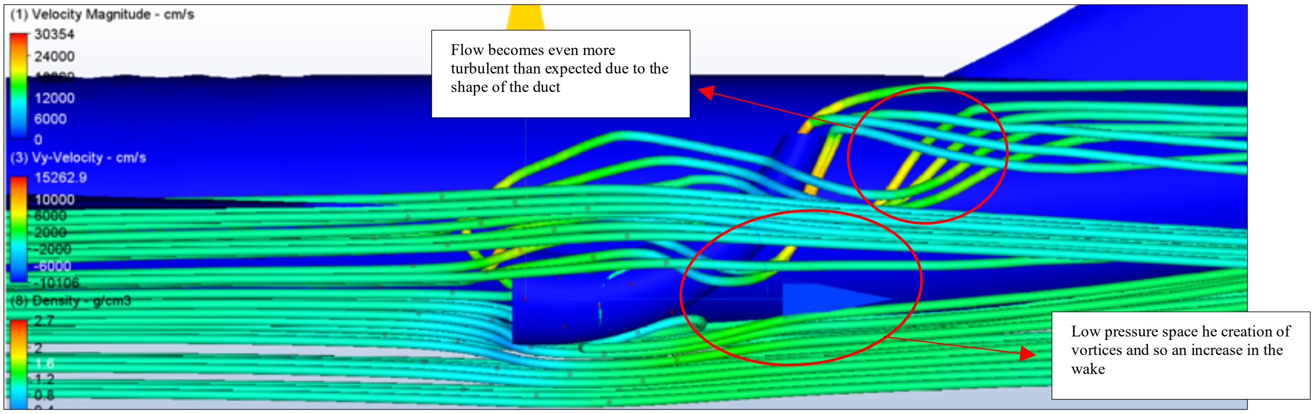

Figure 59. Vectorial representation of Vy-velocity distribution for the initial design of the duct generating downforce while cruise

This detachment can be seen to be mainly caused by the empty space generated just after the duct. The surrounding areas are full of air molecules meaning that the air would go to the regions where empty spaces of air molecules, are created; this led into the generation of vortices and boundary layer detachment. Also, figure 60, showed the poor optimization of the duct's geometry during this simulation. The wake produced by the main wing collided directly with the duct, creating even more drag apart from the enormous wake which is also being generated at the rear part of the duct as it was previously commented.

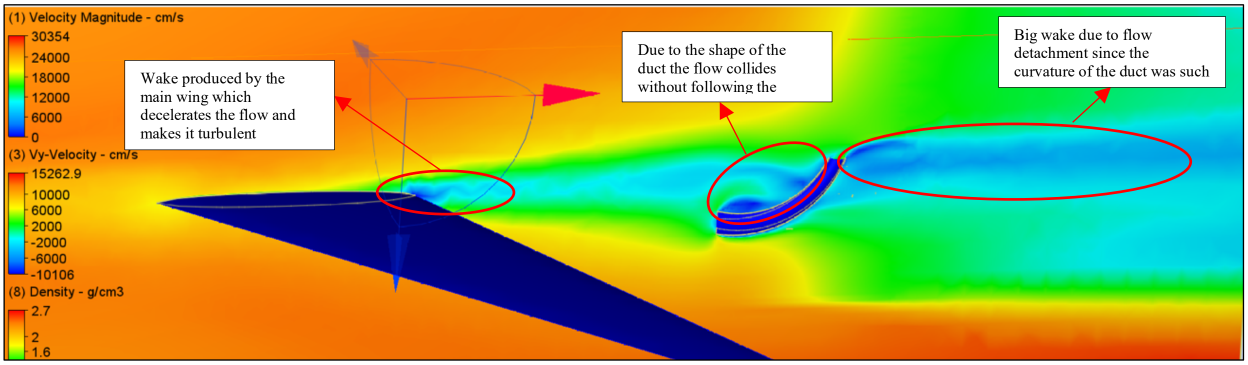

Wake produced by the main wing which decelerates the flow and makes it turbulent

Due to the shape of the duct the flow collides without following the

Big wake due to flow detachment since the curvature of the duct was such

Figure 60. Vy-velocity distribution in detail for the initial design of the lower duct generating drag

After this, a second simulation was performed with the implementations commented before as well as a clear change in the geometry of the lifting system in order to reduce the detachment seen before as well as including the drain holes and air intakes. However, turbulators were decided to be not included in these simulations since the mesh accuracy was not precise enough to detect the presence of the turbulators. Note that finally, a simulation taking exclusively into account the lifting system was done with the intention of seen how the presence of turbulators would affect the airflow as well as for a better understanding about the use of the air intakes and draining holes.

Aircraft with the lower duct generating downforce (final design approach)

As it was just stated, a new simulation was carried out with the intention of improving the aerodynamic results obtained just before. Figure 61 seems to be almost the same since it corresponds to the velocity distribution in the Z-axis, but it can be appreciated, at the rear part of the figure, how the wake generated by the aircraft decreased since the previous simulation. This means that the overall drag would be expected to have descent with respect the initial design used.

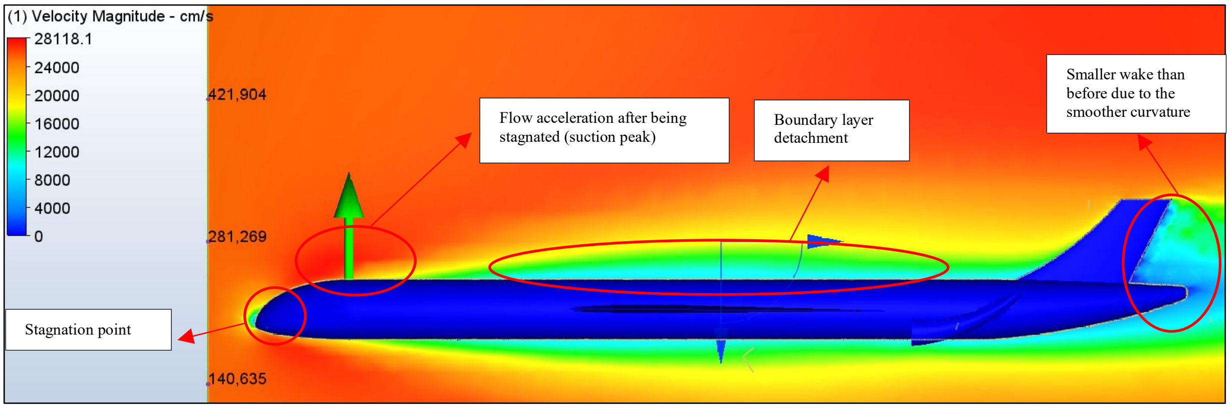

Flow acceleration after being stagnated (suction peak)

Boundary layer detachment

Smaller wake than before due to the smoother curvature

Stagnation point

Figure 61. Velocity distribution (Z-axis) of the Boeing 787-9 with final Lifting System configuration

As it can be appreciated from figure 62, the duct continued accelerating the flow after the re-design. The main goal of this new design of the duct consisted of making the curves smoother as possible in order to avoid the big turbulences obtained at the previous simulations; this meant to reduce the boundary layer detachment obtained before meanwhile obtaining an acceleration in the Y-axis similar to the one obtained at the previous simulations.

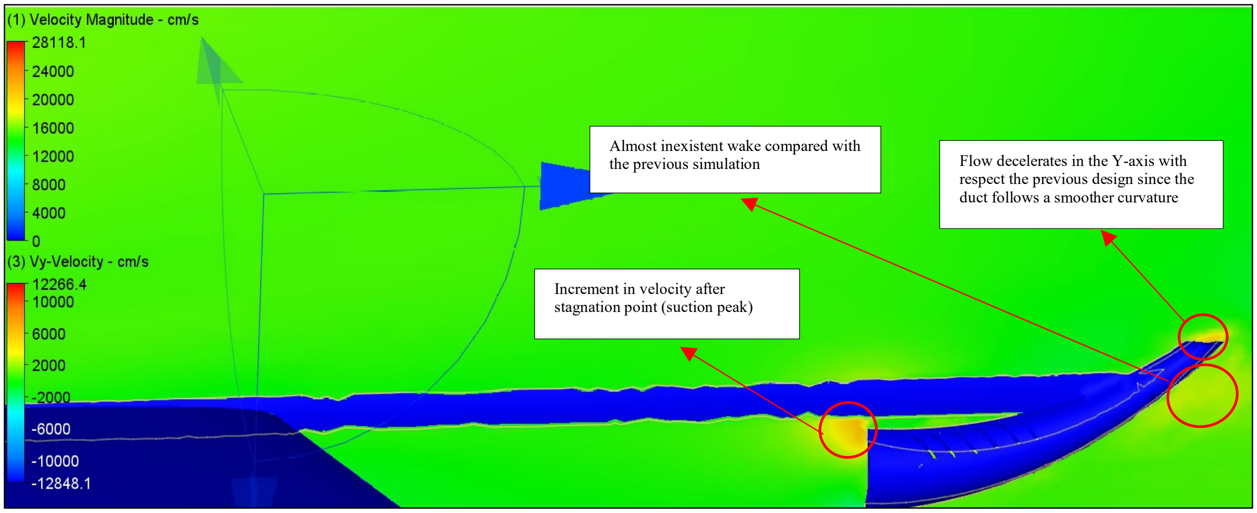

Almost inexistent wake compared with the previous simulation

Flow decelerates in the Y-axis with respect the previous design since the duct follows a smoother curvature

Increment in velocity after stagnation point (suction peak)

Figure 62. Velocity distribution (Y-Axis) through the final design of the lower duct generating downforce

The same study was carried as before where several points (from the entrance until reaching the exit of the duct) were chosen in order to obtain several graphs representing numerically the results seen at the figures about the velocity components, static pressure and kinetic energy. As it can be appreciated from figures 63 and 64, the value for the Y-axis velocity have turned slightly smaller than in the previous simulations; the main reason for this was that the re-designed lifting system introduced a duct with less inclination than before and so the velocity components have changed as seen in figure 63 where it can be clearly seen how, as increasing the Y-axis velocity, the X-axis velocity was parallel decreasing to compensate the change in the absolute velocity.

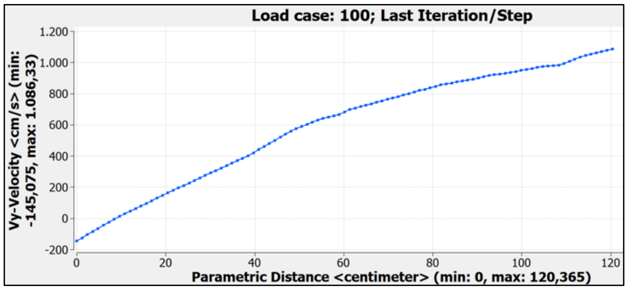

Figure 63. Vy-Velocity vs. Parametric distance graph for the simulation of the lower duct generating downforce while cruise

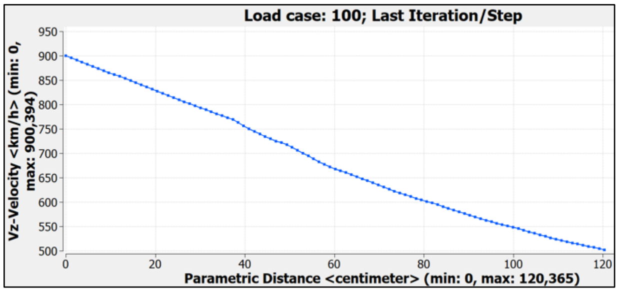

Figure 64. Vz-Velocity vs. Parametric distance graph for the simulation of the lower duct generating downforce while cruise

As it was done before, an analysis of the static pressure and kinematic energy was carried out. From both figures (65 and 66), it can be appreciated how the kinematic energy has also decreased due to the overall descent in the velocity and on the opposite, the static pressure has increased with respect to the previous simulations.

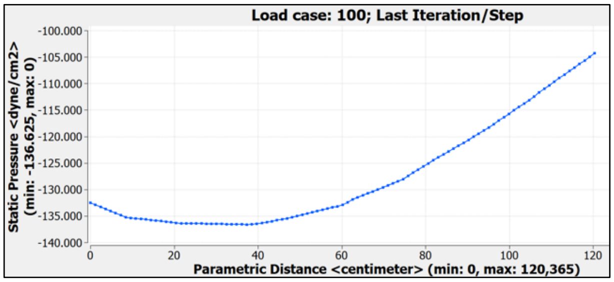

Figure 65. Static Pressure vs. Parametric distance graph for the simulation of the lower duct generating downforce while cruise

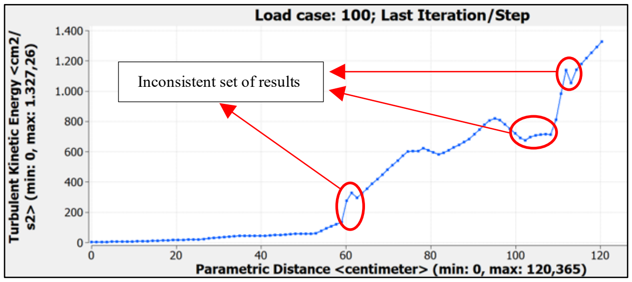

Inconsistent set of results

Figure 66. Turbulent Kinetic Energy vs. Parametric distance graph for the simulation of the lower duct generating downforce while cruise

This change in the geometry showed incredible results after simulations, as seen in figure 67, where the flow followed the curve described by the duct (which was the main goal of the re-design). Due to this, the turbulences which were obtained before were almost mitigated since the air was able to follow the new geometry due to the descent in the inclination of the ducts, avoiding the higher-pressure differentials which were formed in the previous model. In addition, due to the air following the duct's shape due to the Coanda effect (explained in previous chapters), this would also help to increase the overall downforce of the system.

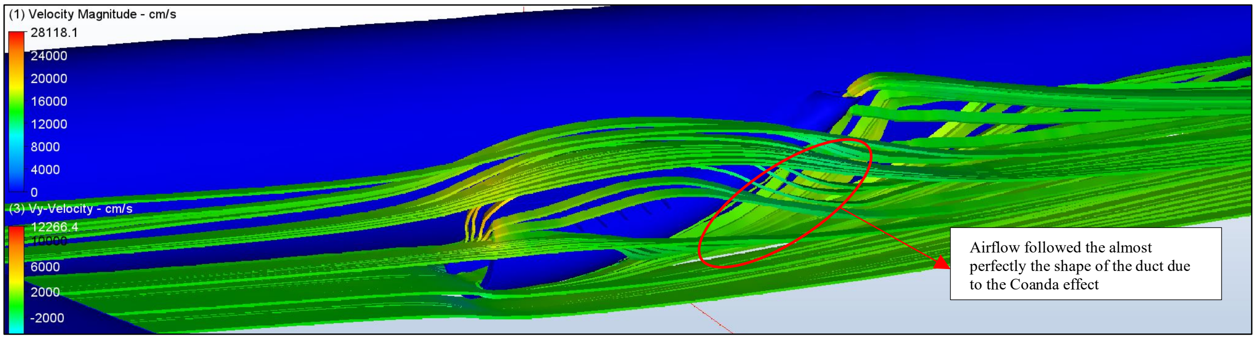

Airflow followed the almost perfectly the shape of the duct due to the Coanda effect

Figure 67. Vectorial representation of velocity distribution (Y-Axis) for the final design of the lower ducts of the Lifting System generating downforce

Also, the path followed by the airflow was represented by the use of cylindrical vectors for a better comprehension. Figure 68 shows the interaction between the main wing and the lifting system; since the duct is located at the rear part of the wing, it helped the duct to dissipate the air which would be flowing around the duct and so lowering the drag created by the duct by partially deflecting the air, which would potentially create turbulences, to the sides of the duct.

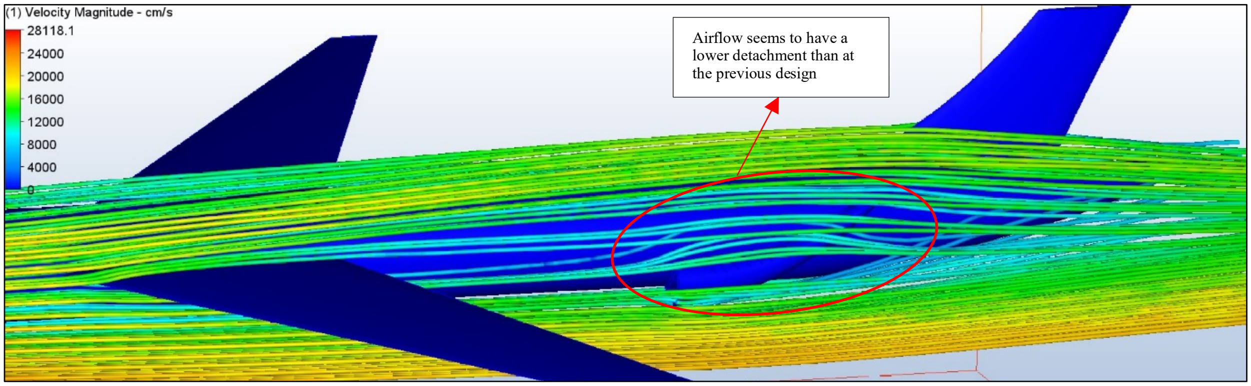

Figure 68. Vectorial representation of velocity distribution (Z-Axis) for the final design of the lower ducts of the Lifting System generating downforce

In addition to this, figures 69 and 70 represent the flow in the Z and Y axis respectively in order to demonstrate the flow homogeneity through the regime located just before the inlet of the ducts. As it can be seen at both graphs, the tendency of the air is to increment its speed in both axis; this is due to the fact that, after the air goes through the main wing, the flow stops having friction with the wing's surface as well as having no more turbulences due to the boundary layer detachment and so velocity increases.

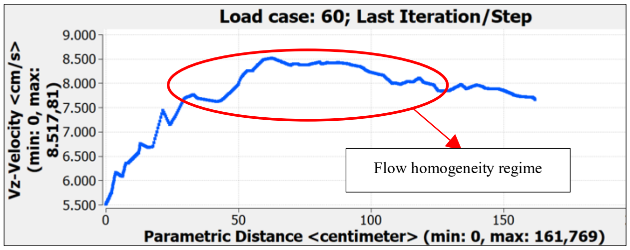

Figure 69. Vz-Velocity vs. Parametric distance (at the region before entering the duct) graph for the simulation of the lower duct generating downforce while cruise showing flow homogeneity

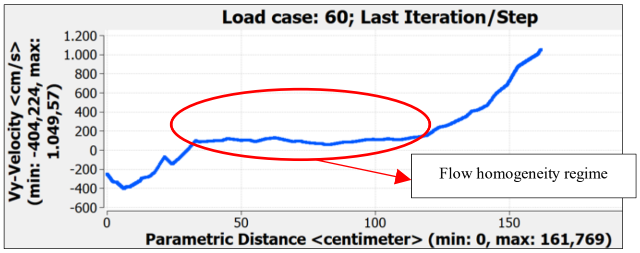

Figure 70. Vy-Velocity vs. Parametric distance (at the region before entering the duct) graph for the simulation of the lower duct generating downforce while cruise showing flow homogeneity

Note that during these simulations, the air intakes as well as the drain holes were introduced but, due to the small dimensions and the limited mesh accuracy, the behavior of these elements was not determinant for the simulations. In order to perform a study about the behavior of the just mentioned elements, they were analyzing these elements at the end of the rest of simulations.

Aircraft with the upper duct generating lift (final design approach)

The next simulation consisted of analyzing the duct which would generate the necessary lift at each circumstance. For performing these simulations, the same procedure as for the previous ones was used. Figure 71 shows in more detail how the duct would affect the incoming flow.

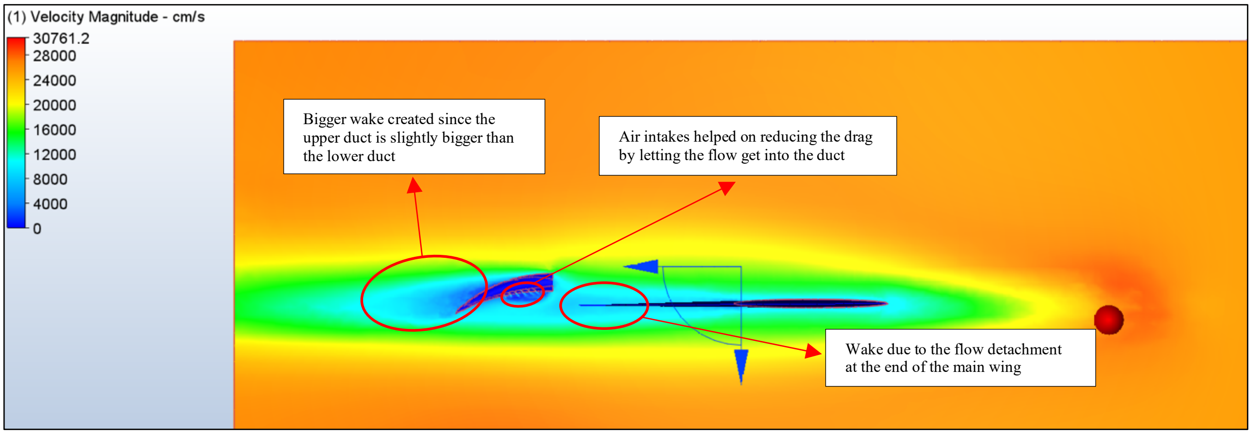

Figure 71. Vectorial representation of velocity distribution (Y-Axis) for the final design of the upper ducts of the Lifting System generating lift

As it can be appreciated, as well as for the previous duct, some turbulences are seemed to be created at the rear part of the duct, however, due to the shape of the duct, most of the air flowing through the upper part of the duct would follow that shape and despite the turbulences generated due to the boundary layer detachment, a big quantity of air would be deflected downwards and so the overall lift of the lifting system would be able to increase.

The velocity distribution in the Y-axis was represented as seen in figure 72, where, since the duct is generating lift, the velocity obtained at the exit of the duct would be pointing downwards. Due to this, the color at the exit is represented with blue color instead red, because the direction of the air flowing through the duct would be following the negative direction at the Y-axis.

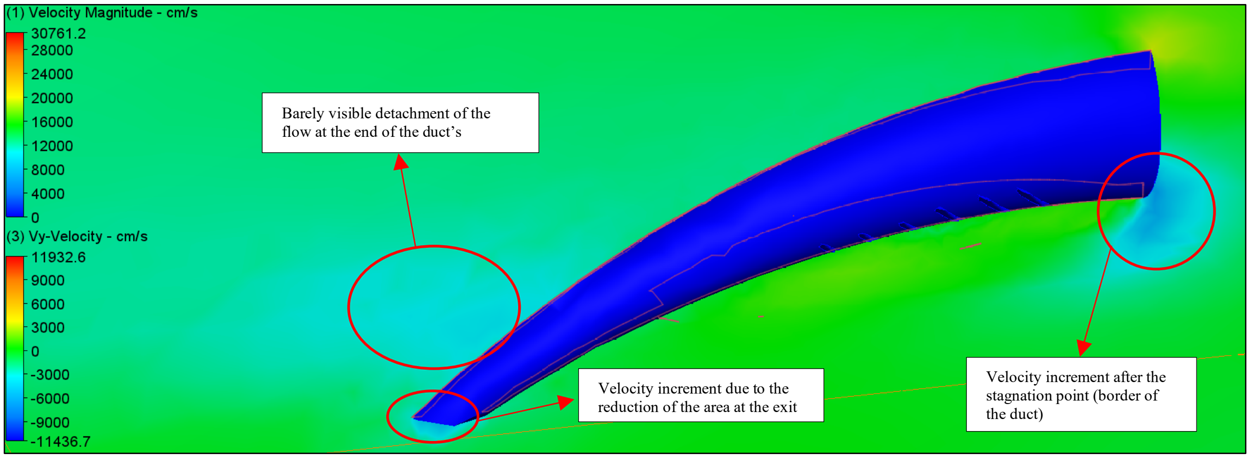

Figure 72. Velocity distribution (Y-Axis) for the final design of the upper ducts of the Lifting System generating lift

The same study was carried as it was done during the previous simulations, where a set of points (from the entrance up to the exit of the duct) were chosen in order to obtain several graphs representing numerically the results seen at the figures about the velocity components, static pressure and kinetic energy. As it can be appreciated from figures 73 and 74, the value for the Y-axis velocity reduces as the air moves through the duct; this doesn't mean that the overall vertical velocity has been reduced. This descent in the graph represents that, as the air was moving opposite to the positive orientation of the Y-axis during the simulations, the Y component reduced its value despite its absolute value has increased as it happened with the lower duct. Also, parallel to what happened previously, the air flowing along the Z-axis seemed to decrease its speed due to the interaction of the fluid with the aircraft.

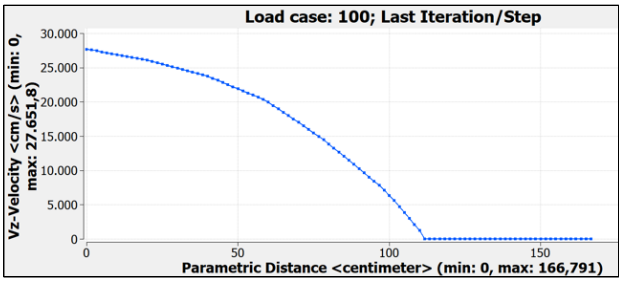

Figure 73. Vz- Velocity distribution vs. Parametric distance graph for the simulation of the lower duct generating downforce while cruise

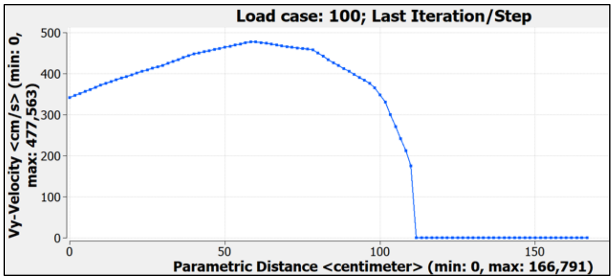

Figure 74. Vy-Velocity distribution vs. Parametric distance graph for the simulation of the lower duct generating downforce while cruise

As it was done before, an analysis of the static pressure and kinematic energy was carried out. From both figures (75 and 76). Despite the same graphs for the previous simulations, in this case the results obtained were not consistent enough. As it can be appreciated the kinetic energy of the air flowing through the duct appear to start increasing but, suddenly it dramatically decreased. This descent is supposed to be produced by some inconsistencies during the simulations, since the expected curve was consisted of an increasing parabola (as in the previous simulations).

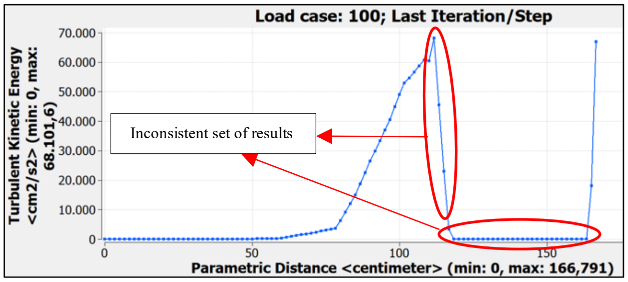

Figure 75. Turbulent Kinetic Energy vs. Parametric distance graph for the simulation of the lower duct generating downforce while cruise

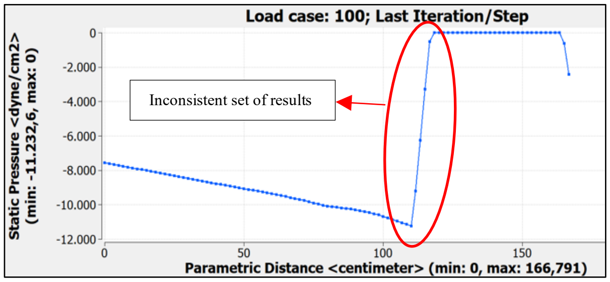

Figure 76. Static Pressure vs. Parametric distance graph for the simulation of the lower duct generating downforce while cruise

However, the result at the exit seems to be consistent despite the results obtained just before the interval shown in red color. Something similar happened with the static pressure which, despite that, it was supposed to increase as the overall velocity increased. The way in which it rise was not the consistent since a parabola was also expected; also, the way in which static pressure decreases at the end of the graph does not make sense as it would be supposed to continue growing.

Aircraft configuration without lifting system and horizontal stabilizer tilted 20º

Having analyzed the aircraft in cruise conditions, the following simulations were done in order to know more about the behavior during lift-off. For performing the simulation, the aircraft was tilted 20º simulating a situation of lift-off; figure 77 shows the velocity distribution in the Z-direction.

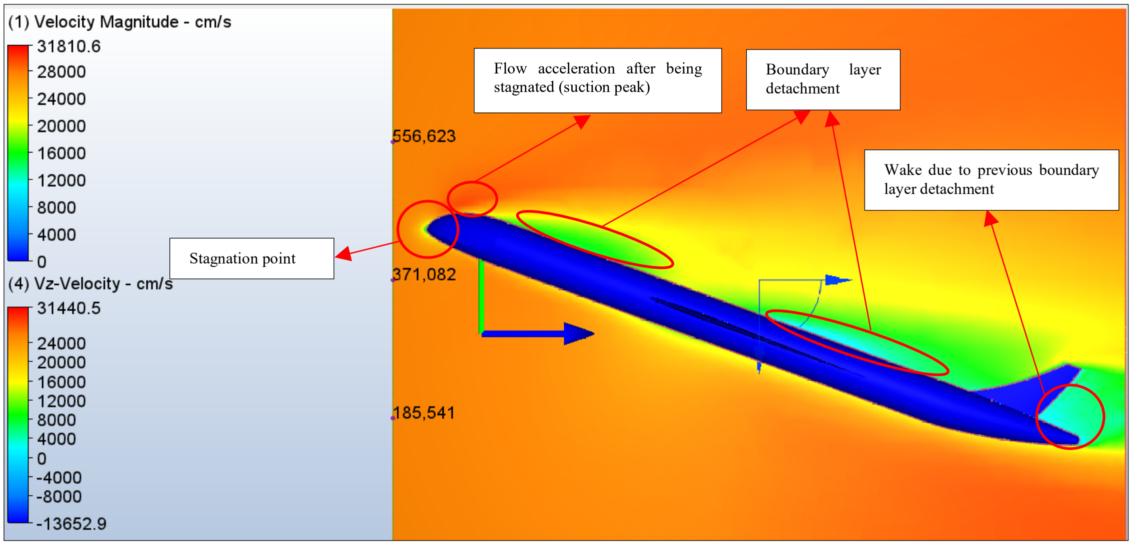

Figure 77. Velocity distribution (Z-axis) of the Boeing 787-9 tilted 20º without Lifting System & horizontal stabilizer

As it can be appreciated from the velocity distribution, air comes from the free stream to the aircraft. When reaching the aircraft, the air slows down at the aircraft's nose, the stagnation point. After that, an acceleration can be seen (suction peak), before the air starts detaching from the aircraft's surface (boundary layer detachment). However, the wake generated behind was not such big as the wake which would be seen in future simulations for the rest of cases being studied. Also, the pressure coefficient distribution was represented as it can be appreciated in figure 78.

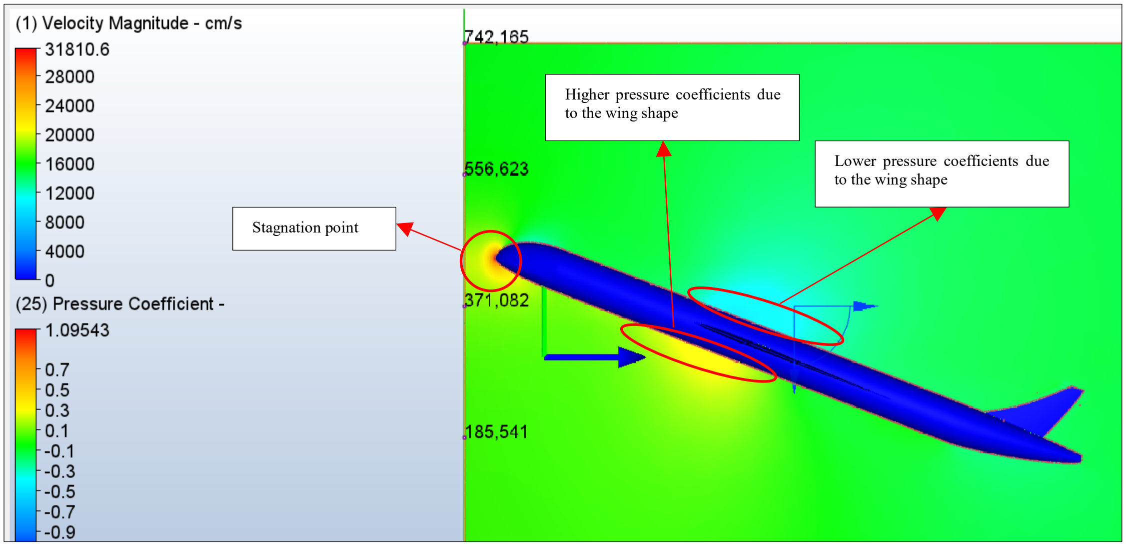

Figure 78. Pressure coefficient distribution of the Boeing 787-9 without Lifting System & horizontal stabilizer

This representation was performed since, as it was no lifting system, there was not a single area of the aircraft to be deeply studied and so a global pressure distribution analysis was carried out. As it can be seen, the area below the aircraft seems to have higher levels of pressure than above it. The reason of this is due to the generation of lift, meaning that at this angle of attack, the aircraft would be generating lift.

Aircraft conventional configuration (with horizontal stabilizer) tilted 20º

The following simulation consisted of almost the same as the previous one but, for this particular case, the aircraft had its conventional configuration (including the horizontal stabilizer). This was done in order to perform the future calculations about the range for each aircraft model (by knowing the lift and drag generated by each aircraft configuration). Figure 79 represents the velocity distribution in the Z-axis.

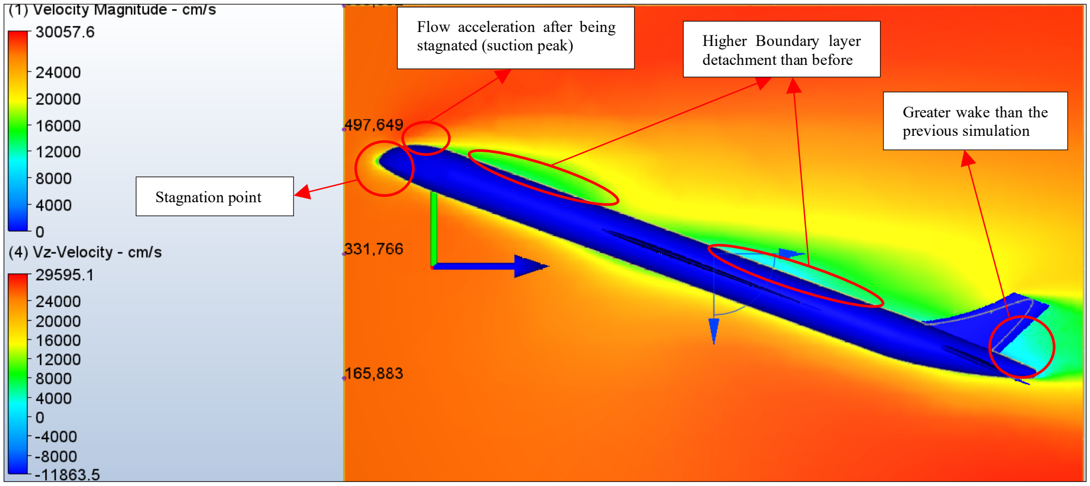

Figure 79. Velocity distribution (Z-axis) of the Boeing 787-9 with conventional configuration (with horizontal stabilizer)

If comparing it with the previous simulation, it can be appreciated how at the rear part of the fuselage, the wake generated became bigger due to the introduction of the horizontal stabilizer, which caused a bigger boundary layer detachment meanwhile the rest of the aircraft seemed to be kept almost the same as before. Also, the pressure coefficient distribution was represented in figure number, despite it was almost the same as before. However, the pressure distribution among the horizontal tail plane would help the aircraft to have higher lift since, as well as the main wing, they deflect the air downwards.

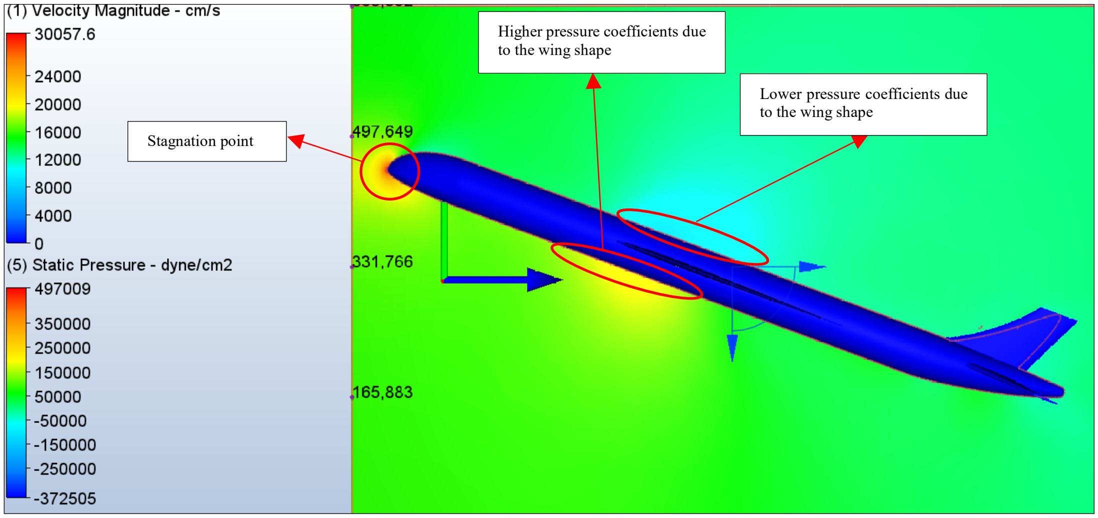

Figure 80. Pressure coefficient distribution of the Boeing 787-9 with conventional configuration (with horizontal stabilizer)

Aircraft with the upper duct generating lift with the Boeing 787-9 tilted 20º

The same simulation was carried out as before but for the upper duct which was the one generating lift. These simulations were focused on the behavior of the lifting system when performing such maneuvers requiring this tilt angles. As it was done during the previous simulations, figure 81 shows the velocity distribution in the Y-direction for the whole aircraft. The rest of parameters involving the boundary conditions remained unchanged for a better comparison of both cases.

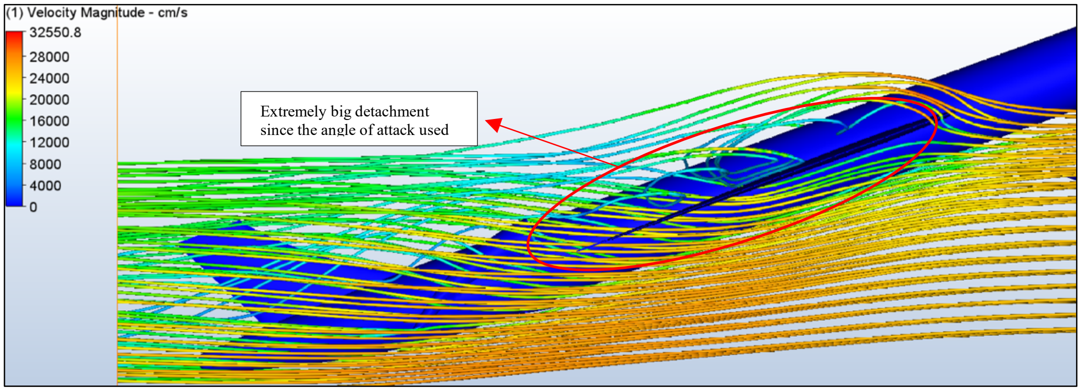

Figure 81. Vectorial representation of the velocity distribution (Z-axis) of the Boeing 787-9 tilted 20º with final Lifting System configuration generating lift

Also, figure 82 represents the velocity distribution in a different manner. As it happened during the simulations where the aircraft was not tilted, the velocity distribution showed that the duct was generating lift since, the velocity at the entrance of the duct was lower than the one at its exit. This could be counterintuitive since the color distribution is representing that at the exit of the duct the velocity is represented in blue color meaning that it would be a low velocity but, this is due to the fact that the velocity which is being represented consists of the Y-axis velocity; that's to say that the velocity at the exit is increasing in the negative Y-axis meaning that, meanwhile the absolute velocity is increasing, the relative one seems to be decreasing.

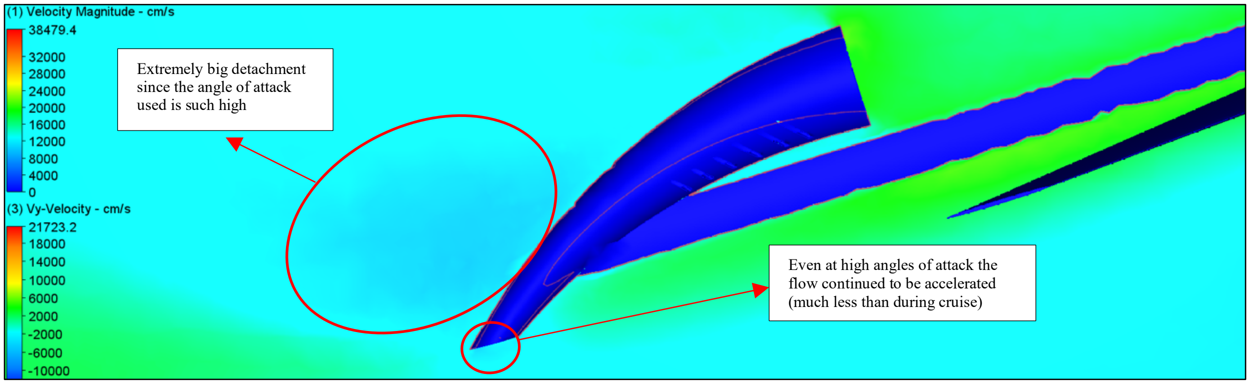

Figure 82. Velocity distribution (Y-axis) of the Boeing 787-9 with final Lifting System configuration generating lift

The same study was carried as it was done during the previous simulations, where two points (one at the entrance and one at the exit of the duct) were chosen in order to obtain several graphs representing numerically the results seen at the figures about the velocity components, static pressure and kinetic energy. As it can be appreciated from figures 83 and 84, the value for the Y-axis velocity reduces as the air moves through the duct; this doesn't mean that the overall vertical velocity has been reduced. This descent in the graph represents that, as the air was moving opposite to the positive orientation of the Y-axis during the simulations, the Y component reduced its value despite its absolute value has increased as it happened with the lower duct. About the Z-axis, the velocity seems to increase; this does not have any sense, meaning that at this point the simulation could not be representative due to some failures causing these inconsistencies.

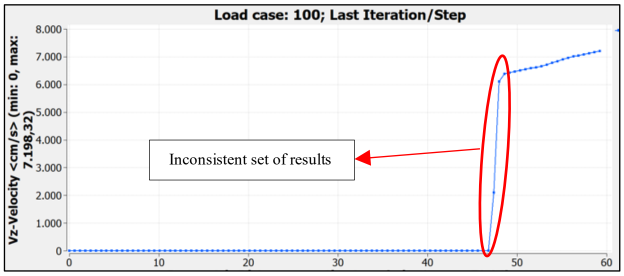

Figure 83. Vz- Velocity distribution vs. Parametric distance graph for the simulation of the lower duct generating lift while taking-off

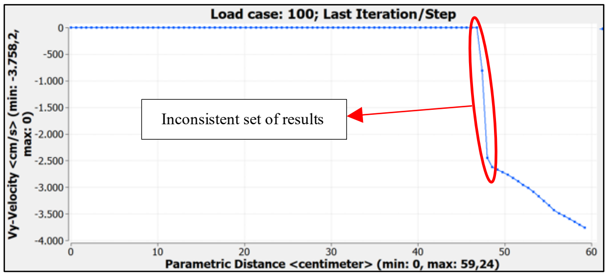

Figure 84. Vy- Velocity distribution vs. Parametric distance graph for the simulation of the lower duct generating lift while taking-off

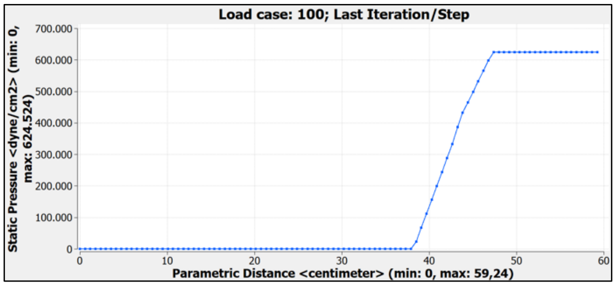

Figure 85. Static Pressure distribution vs. Parametric distance graph for the simulation of the lower duct generating lift while taking-off

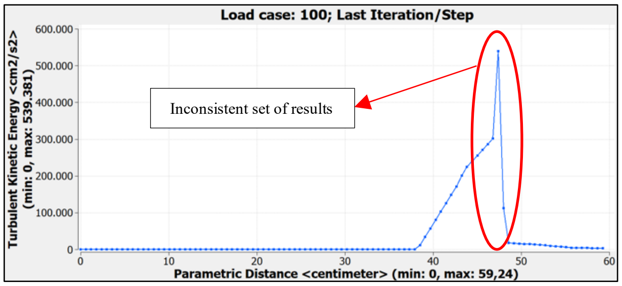

Figure 86. Turbulent Kinetic Energy distribution vs. Parametric distance graph for the simulation of the lower duct generating lift while taking-off

As it was done before, an analysis of the static pressure and kinematic energy was carried out. From both figures (85 and 86). Despite the same graphs for the previous simulations, in this case the results obtained were not consistent enough. As it can be appreciated, the kinetic energy of the air flowing through the duct appear to start increasing but, suddenly it dramatically decreased. This descent is supposed to be produced by some inconsistencies during the simulations since the expected curve was consisted of an increasing parabola (as in the previous simulations); however, the result at the exit seems to be consistent. About the static pressure results, they seem to be such consistent, since the pressure increment was progressively achieved in spite of what happened in the previous simulation. In addition to this, figures 87 and 88 represent the flow in the Z and Y axis respectively in order to demonstrate the flow homogeneity through the regime located just before the inlet of the ducts. As it can be seen at both graphs, the tendency of the air is to increment its speed in both axis; this is due to the fact that, after the air goes through the main wing, the flow stops having friction with the wing's surface as well as having no more turbulences due to the boundary layer detachment and so velocity increases. However, some inconsistencies can be appreciated at figure 88; this could be due to the fact that points to build up the graph were chosen manually so if choosing not exactly the points through the flow, this could lead into an inconsistency.

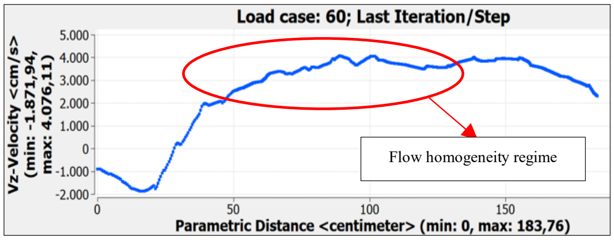

Figure 87. Vz-Velocity vs. Parametric distance (at the region before entering the duct) graph for the simulation of the upper duct while take-off showing flow homogeneity

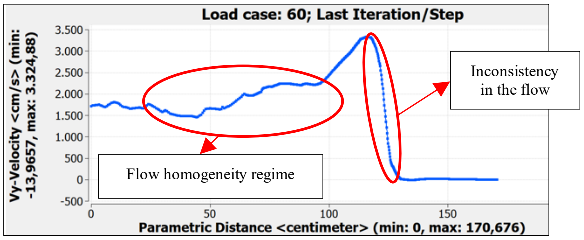

Figure 88. Vy-Velocity vs. Parametric distance (at the region before entering the duct) for the simulation of the upper duct while take-off showing flow homogeneity

Complete aircraft with the ducts closed and the rear aperture (similar to the DRS)

In this case the simulation for this particular case, was performed taking into account cruise conditions such as in the previous simulations. Exactly the same parameters as in the simulations, including cruise conditions were used. For this particular case, the only image taken from the simulations consisted of the Z-axis velocity distribution was used as seen in figure 89.

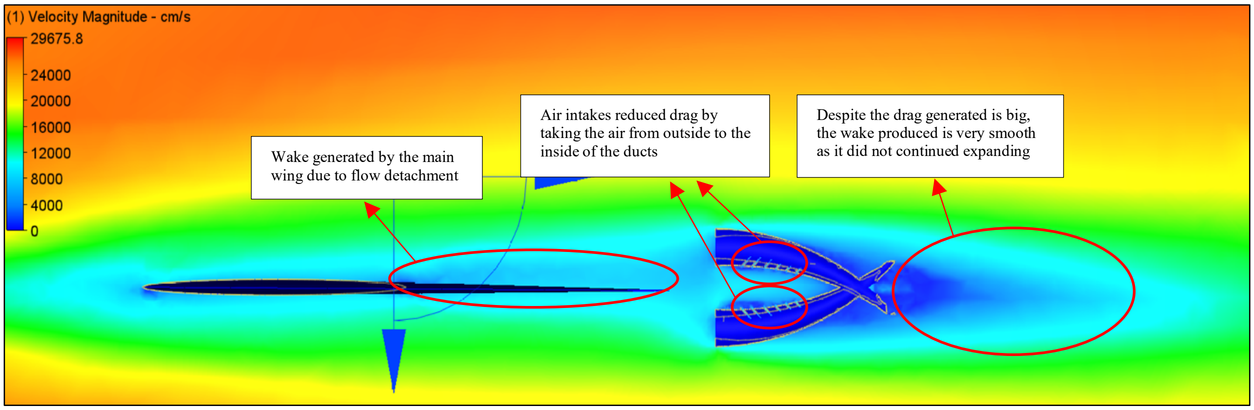

Figure 89. Velocity distribution (Z-Axis) with ducts closed and rear plate opened (as DRS) while cruise

The main reason of only considering this velocity distribution was due to the fact that the aperture would be only operating at cruise conditions and the only purpose of using it would be to decrease the wake as it can be appreciated in figure 89, with respect the rest of simulations as well as reducing the effect of lift / downforce and drag. However, since the aperture was such small, results were so inconsistent that were not even taken into account. These results can be seen, even clearly at figure 91, where a graph was obtained for the values of the velocity in the Z-axis. As it can be appreciated, the velocity increased substantially after going through the ducts, however, this increment was supposed to be lower since, some inconsistencies were detected when analyzing the graphs due to that sudden increment in speed. To validate these results the static pressure graph was also represented and, as it can be seen pressure decreased while velocity increased. Despite this, (the same inconsistency that happened for the velocity distribution took place) a sudden descent in pressure can be appreciated due to some inconsistencies while performing the simulations.

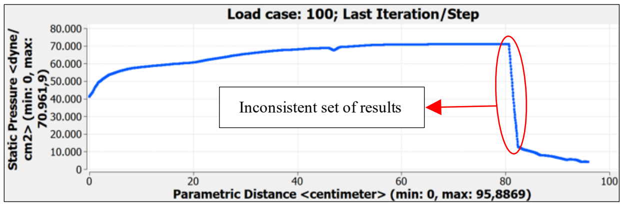

Figure 90. Static Pressure vs. Parametric distance graph for the simulation of both ducts closed and rear plate opened (as DRS) while cruise

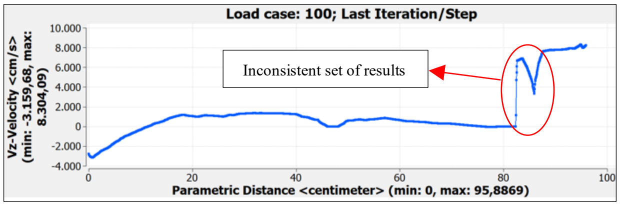

Figure 91. Vz-velocity vs. Parametric distance graph for the simulation of both ducts closed and rear plate opened (as DRS) while cruise

In addition to this, figures 92 represent the flow in the Z-axis, in order to demonstrate the flow homogeneity through the regime located just before the inlet of the ducts. As it can be seen at the graph, where the tendency of the air is to increment its speed in both axis; this is due to the fact that, after the air goes through the main wing, the flow stops having friction with the wing's surface as well as having no more turbulences due to the boundary layer detachment and so velocity increases

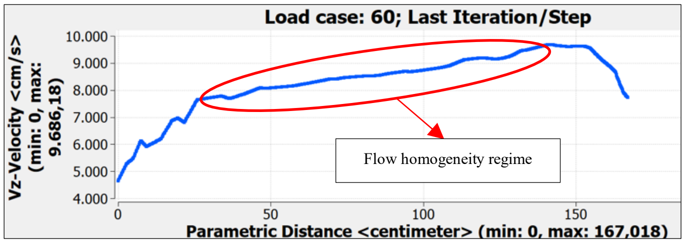

Flow homogeneity regime

Figure 92. Vz-Velocity vs. Parametric distance (at the region before entering the duct) graph for the simulation of the upper duct while cruise with the DRS open showing flow homogeneity

Duct in detail with draining holes and air intakes

Finally, a simulation of the duct was exclusively carried out in order to appreciate in a clear manner, the way in which air behaves among the ducts. Also, by performing this kind of simulations more in detail, the way in which the drain holes as well as the air intakes work together could be clearly seen. As it can be appreciated, figure 93 represents the velocity distribution among the Z-axis where it can be differentiated to the wake produced by the duct, due to the boundary layer detachment.

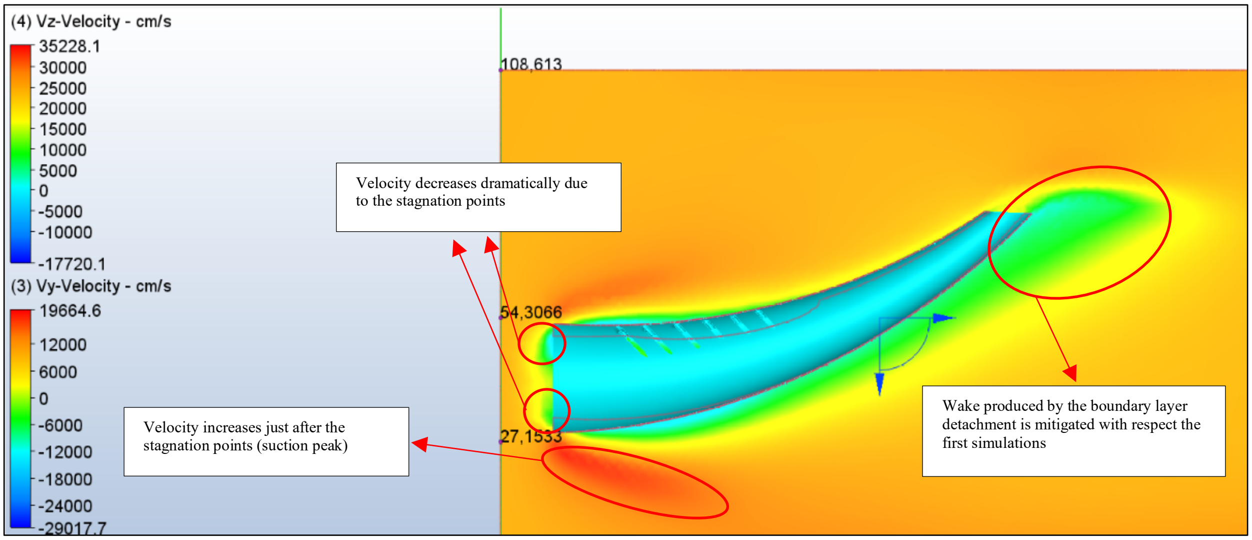

Velocity decreases dramatically due to the stagnation points

Velocity increases just after the stagnation points (suction peak)

Wake produced by the boundary layer detachment is mitigated with respect the first simulations

Figure 93. Velocity distribution (Z-Axis) lower duct generating downforce (final configuration) in detail with drain holes and air intakes

The air intakes allowed the lifting system to have a reduction of the boundary layer detachment in the upper part of the duct as it can be seen at the same figure. That's to say that the overall drag could be potentially reduced at that area. However, the wake produced at the lower part of the duct due to the detachment could be an issue since drag seems to be such high at that region. Also, this increment of boundary layer detachment at the lower part could be risen by the location of too many drain holes (more than necessary) so that a bigger amount of air than expected could be travelling out of the duct as the pressure inside is such big in comparison of the pressure at the exterior due to the difference in absolute velocities.

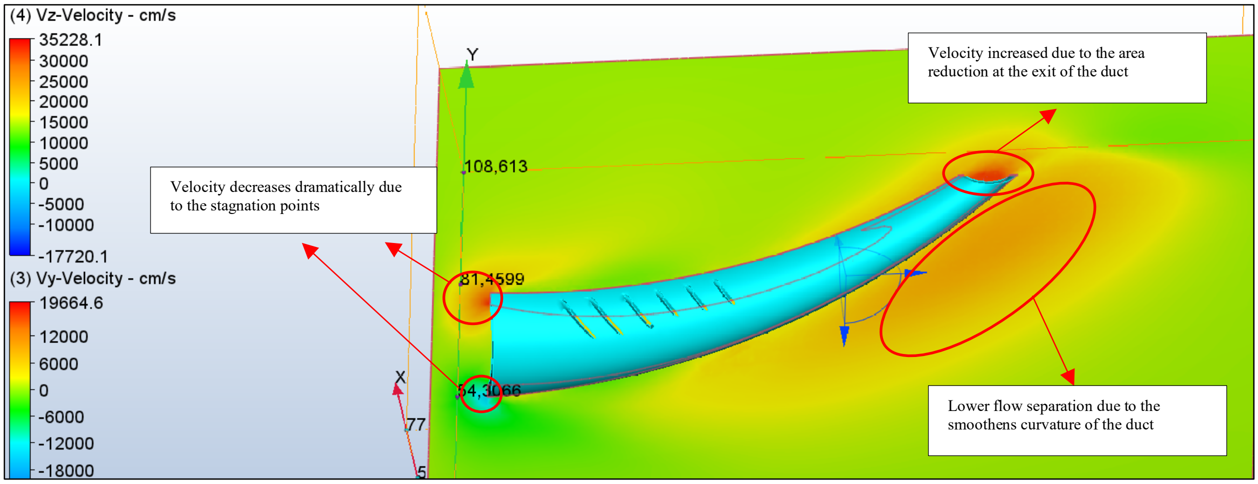

Velocity increased due to the area reduction at the exit of the duct

Velocity decreases dramatically due to the stagnation points

Lower flow separation due to the smoothens curvature of the duct

Figure 94. Velocity distribution (Y-Axis) lower duct generating downforce (6 drain holes configuration) in detail with drain holes and air intakes

As it was already done during previous simulations, the velocity distribution in the Y-axis was represented in figure 94, where it can be clearly seen the acceleration of the flow inside the duct. For a better comprehension of the results obtained, some graphs (figures 95 and 96) were plotted in order to see the behavior of the air through the duct. However, the static pressure simulation presents some errors since, the static pressure should decrease while increasing the velocity but, due to some inconsistencies, meanwhile the Z-axis velocity remains almost unchanged, the static pressure dropped exponentially.

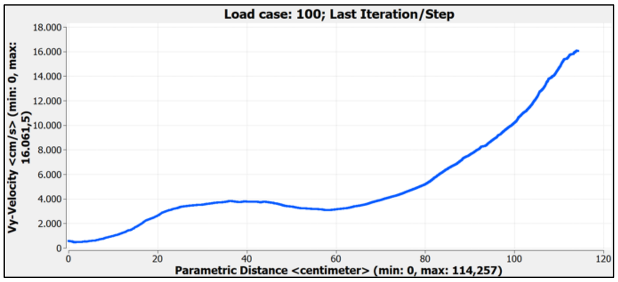

Figure 95. Vy-velocity vs. Parametric distance graph for the simulation of lower duct in detail (6 drain holes configuration)

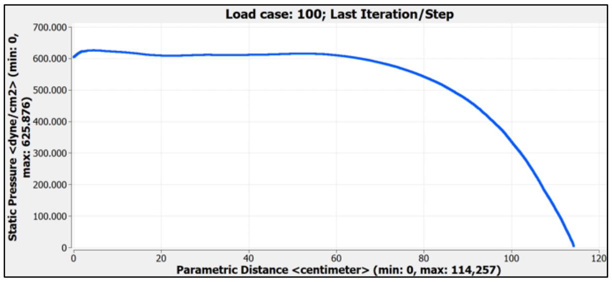

Figure 96. Static Pressure vs. Parametric distance graph for the simulation of lower duct in detail (6 drain holes configuration)

To sum up, the duct was tried to be optimized by reducing the number of draining holes with the purpose of reducing the massive boundary detachment at the lower part of the duct. The holes were decided to be reduced from 6 to 2 draining holes. These holes were located at the beginning of the duct since, if water gets into the duct, due to the shape of the lifting system, it will get stuck at the entrance where the duct has a downwards cavity shape. The result of the reduction of the drain holes can be seen appreciated in the figures 94 and 97 where the detachment is seemed to be reduced with respect to the version with the 6 draining holes.

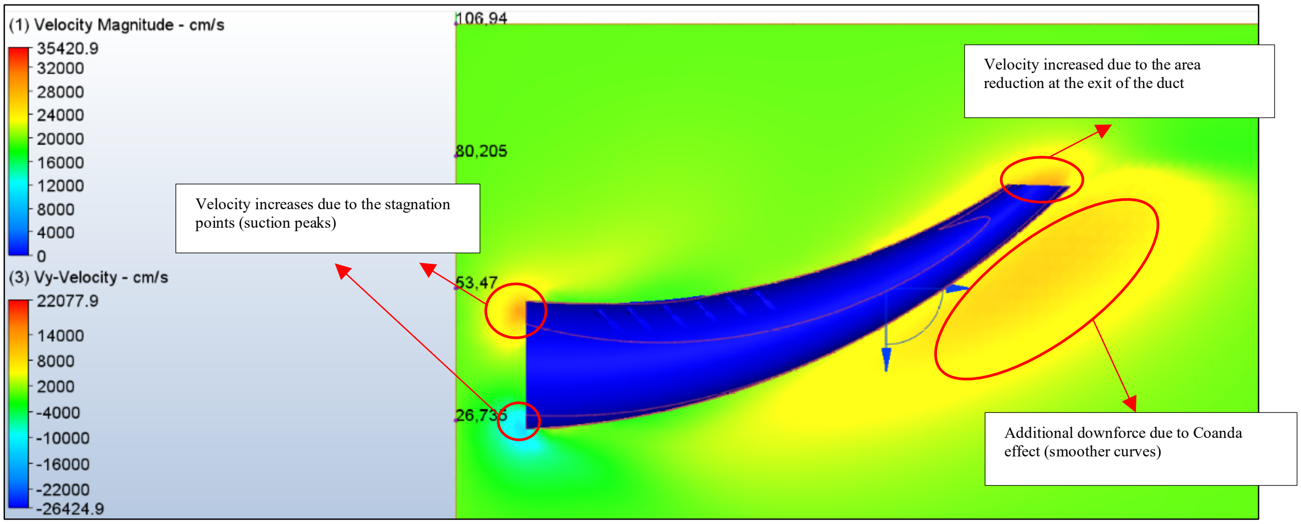

Figure 97. Velocity distribution (Y-Axis) lower duct generating downforce 2 drain holes configuration) in detail with drain holes and air intakes

Also, the reduction of the draining holes allowed to get a higher velocity among the duct; this could be clearly appreciated at figures 98 and 99 where the velocity in the Y-axis and the static pressure were represented. Exactly the same happened as before, where, despite the Y-axis velocity results made sense, the static pressure dropped exponentially while the Z-axis velocity was slightly reduced (meaning that some inconsistencies in the static pressure took place).

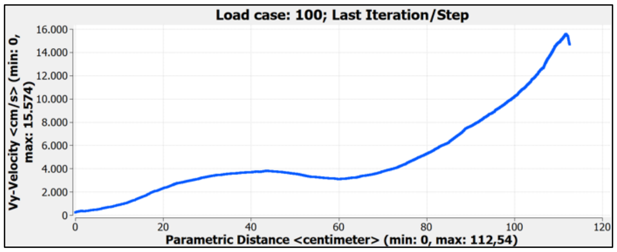

Figure 98. Vy-velocity vs. Parametric distance graph for the simulation of lower duct in detail (3 drain holes configuration)

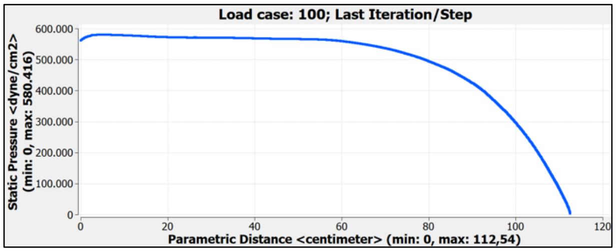

Figure 99. Static Pressure vs. Parametric distance graph for the simulation of lower duct in detail (3 drain holes configuration)

Having performed all the previous simulations for different cases, results were obtained for each of these simulations. These results were written on an Excel in order to facilitate the comparison of the results. The Excel tables can be seen at the ANNEXES IX-XVI (located at the end of the report); most of the results provided such consistent results meanwhile, on the other hand, some of them provided inconsistent results which would not be considered for the calculations performed on following chapters. Overall, every result obtained must be treated carefully since, even some of them were consistent, the mesh used for every simulation was of around 1 million nodes and, despite the numbers obtained were such big in comparison with other CFD software's such as Ansys Student, a mesh with much higher quality would be necessary for the abstinence of more accurate results. Note that no dihedral angle was given to the main wing and also, the engines were not represented during the simulations. The main reason was to avoid errors during the simulations but also, engines are such separated from the wing root that due to the limited mesh generated, it was supposed that the appearance of engines would have been almost not perceptible during the simulations. About the dihedral angle, since the results from these simulations were taken as percentages instead of pure numbers (this was decided since most users from this program stated that the results obtained were not representative instead treating them as percentages), using or not dihedral angle at the main wing was supposed not to have massive changes for the performance of the lifting system. To sum up with this chapter, some graphs were carried out with the purpose of obtaining a better comparison between each of the simulations performed. [69]

CHAPTER 4. FLIGHT MECHANICS

During this chapter, several theoretical calculations will be carried out, taking into account the results obtained from the simulations performed during the previous chapter. These calculations are supposed to differ from the real results which could be obtained after manufacturing the lifting system. Also, a comparison between the implementation of this system and the conventional configuration will be done at each section.

4.1 WEIGHT ESTIMATION

To perform an estimation of the weight for the lifting system is something complex since several issues might appear while performing the manufacturing of the system. Setbacks such as locating wrongly the carbon fiber, wrong riveting of the lifting system to the fuselage and tolerances at the carbon fiber dimensions would be assumed to appear while its manufacturing. Despite this, a theoretical calculation of the weight estimation for the lifting system would be performed in order to compare it with the weight estimated for the horizontal stabilizer of the Boeing 787-9. The first step to calculate the weight of the lifting system consisted of selecting the type of material which would be used; this was performed during previous chapters, and the carbon fiber selected consisted of double-sided high strength carbon fiber sheet. Once having the material selected, the gross weight per carbon fiber roll of (1219,2 x 1219,2 mm) was of about 1,484 Kg [70]. In order to calculate the whole weight of carbon fiber, the number of rolls needed would be needed to be calculated and for doing so, calculating the area of carbon fiber needed for the whole system of ducts was needed to be calculated. To obtain the area of the lifting system, the following drawing was performed for a better understanding; figure 100 represents one of the lower ducts in a planar way. This means that if taking the duct and unrolling it as if it was a cylinder, the result is the truncated cone seen below.

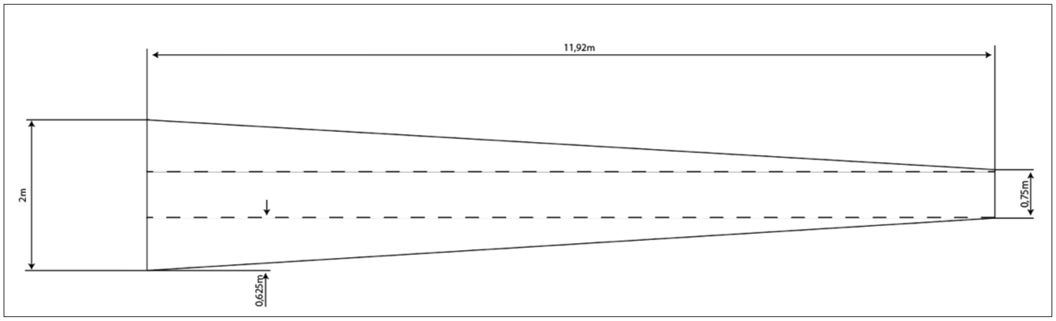

Figure 100. Upper view of one of the lower duct's planar surface (Adobe Illustrator)

The dimensions seen in the figure were obtained from the aircraft engineering plans previously presented. However, the dimension corresponding to 11,92 meter was calculated by using the Pythagorean theorem formula. Since the ducts', length was of 10 meters (see it in figure 102) and the height of 6,5 meters (see it in figure 101), the diagonal which would approximately correspond to the side seen in the figure above was obtained (11,92 meters).

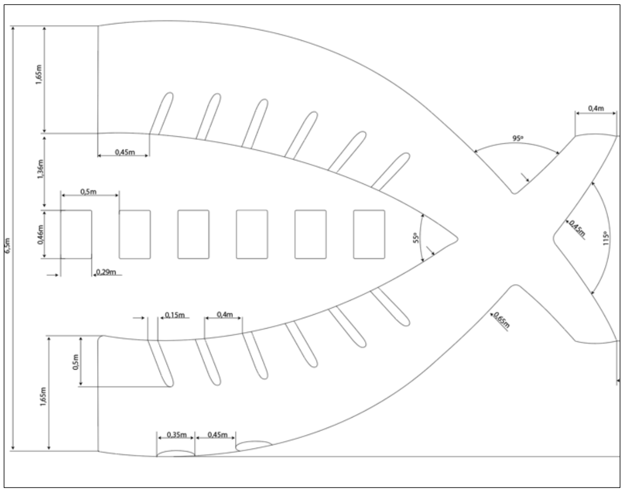

Figure 101. Side view of the Lifting System arrangement (Adobe Illustrator)

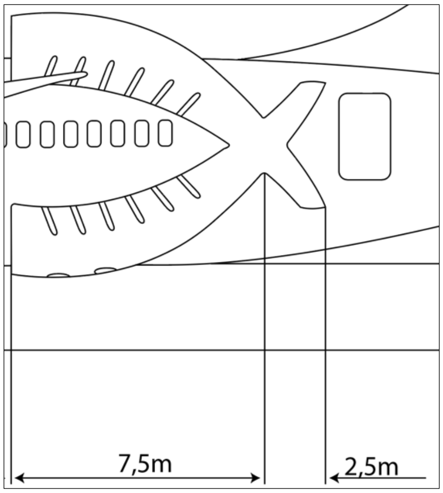

Figure 102. Positioning of the Lifting System and passenger's rear door (Adobe Illustrator)

For the lower ducts, the calculations involving the area resolution were the following ones:

Figure 100 was divided into the upper and lower triangles as it can be appreciated, and into the rectangle at the middle of the truncated cone.

- For the area corresponding to the lower duct:

$$A_{\text{rectangle}} = \text{base} * \text{height} = 0{,}75 * 11{,}92 = \mathbf{8{,}84\ m^2}$$

$$2 * A_{\text{triangle}} = \frac{\text{base} * \text{height}}{2} = \frac{0{,}75 * 11{,}92}{2} * 2 = \mathbf{8{,}94\ m^2}$$

$$\mathbf{A_{lower\ duct}} = 2 * A_{\text{triangle}} + A_{\text{rectangle}} = \mathbf{17{,}78\ m^2}$$

Note that the area of the triangle is multiplied by 2 since there are a total of 2 triangles.

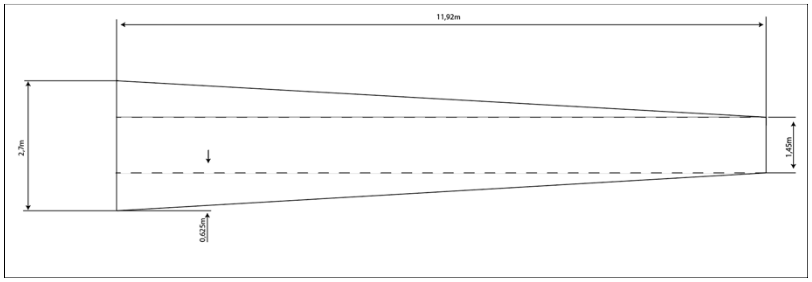

Figure 103. Upper view of the component which attaches the Lifting System to the aircraft's fuselage

Also, the area corresponding to the component involved in joining the lifting system and the fuselage, (see it in figure 103) which would be made of the same material, was needed to be calculated.

- For the area corresponding to the joint of the ducts to the fuselage:

$$\mathbf{A_{joint}} = base * height = 0{,}625 * 11{,}92 = \boldsymbol{7,45\ m^2}$$

This means that the total area for the lower duct would be:

$$\mathbf{A_{Lower\ ducts}} = 2 * \mathrm{A_{lower\ duct}} + 4 * \mathrm{A_{joint}} = \mathbf{65,36m^2}$$

The next step consisted of calculating the area for the upper ducts (see in figure 103); the area corresponding to these ducts was calculated in the same manner as for the lower ducts.

- For the area corresponding to the lower duct:

$$\mathrm{A_{rectangle}} = \mathrm{base} * \mathrm{height} = 1{,}45 * 11{,}92 = \mathbf{17,28\ m^2}$$

$$2 * \mathrm{A_{triangle}} = \frac{\mathrm{base} * \mathrm{height}}{2} = \frac{0{,}625 * 11{,}92}{2} * 2 = \mathbf{7,45m^2}$$

$$\mathrm{A_{upper\ duct}} = 2 * \mathrm{A_{triangle}} + \mathrm{A_{rectangle}} = \mathbf{24,73\ m^2}$$

Note that the area of the triangle is multiplied by 2 since there are a total of 2 triangles.

Also, the area corresponding to the component involved in joining the lifting system and the fuselage was the same as for the lower ducts:

$$\mathbf{A_{joint}} = \mathrm{base} * \mathrm{height} = 0{,}625 * 11{,}92 = \mathbf{7,45\ m^2}$$

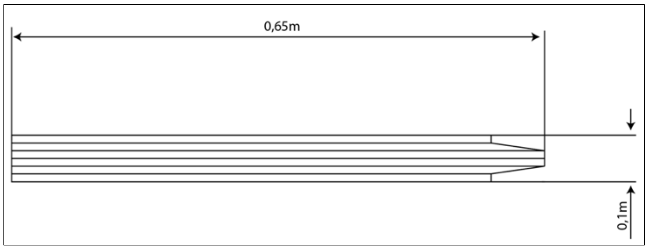

Figure 104. Upper view of one of the upper duct's planar surface

This means that the total area for the upper duct would be:

$$\mathbf{A}_{\textbf{Upper ducts}} = 2 * \mathrm{A}_{\text{lower duct}} + 4 * \mathrm{A}_{\text{joint}} = \mathbf{79,26m^2}$$

The total area of the lifting system is of: $\mathbf{A}_{\textbf{total}} = \mathrm{A}_{\text{Upper ducts}} + \mathrm{A}_{\text{Lower ducts}} = \mathbf{144,62\ m^2}$

Taking into account the information obtained from the fabricant of the carbon fiber selected, since the weight (in kilograms) for each square meter was estimated to be of about 3,43 kg/m^2 the total weight for the carbon fiber could be now performed. [70]

$$\textbf{Weight}_{\textbf{ducts}} = 3{,}43 * 144{,}62 = \textbf{496, 04 Kilograms}$$

In addition to this, the weight corresponding to the actuators, internal plates and electrical installation must be taken into account. [71] [72]

- For weight estimated for the actuators (rotatory and lineal):

$$\textbf{Weight}_{\textbf{actuators}} = 3 * \text{Weight}_{\text{lineal actuators}} + 3 * \text{Weight}_{\text{lineal actuators}}$$

$$\textbf{Weight}_{\textbf{actuators}} = 3 * 24{,}7 + 3 * 30{,}6$$

$$\textbf{Weight}_{\textbf{actuators}} = \textbf{165, 9 Kilograms}$$

- For weight estimated of the plates (made of the same carbon fiber as the ducts). For its calculation, figure number represents the shape of the plates, however, notice that the length of each of the plates was different (0,65m; 0,5m; 0,45m):

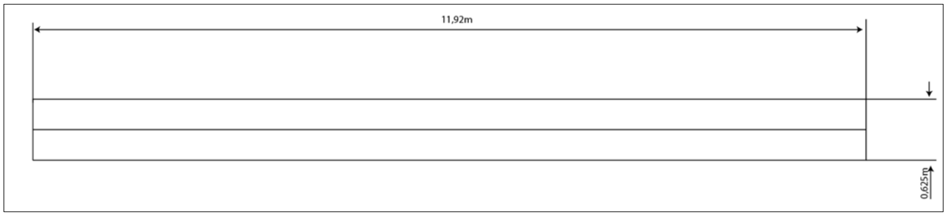

Figure 105. Upper view of one of the internal plates surface

$$\mathbf{Area_{plates}} = 0{,}65 * 0{,}1 + 0{,}5 * 0{,}1 + 0{,}45 * 0{,}1 = \mathbf{0{,}16\ m^2}$$

$$\mathbf{Weight_{plates}} = 0{,}16 * 3{,}43 = \mathbf{0{,}5488\ Kilograms}$$

- For the weight of the electrical system (taking into account the rivets and pins), a weight of around **100 kilograms** was estimated.

$$\mathbf{Weight_{Lifting\ System}} = \mathbf{662{,}48\ Kg}$$

Now, in order to compare the weight of the lifting system with the weight of the horizontal stabilizer, the weight corresponding to the HTP needed to be calculated. For doing so, the following formula was used:

$$\mathrm{Weight_{HS}} = 5.25\mathrm{S_{He}} * 0.8 * 10^{-6} * \frac{\mathrm{N_{ultimate}} * \mathrm{b}^3 * \mathrm{TOW} * MAC_W\sqrt{\mathrm{S_{He}}}}{\left(\frac{\mathrm{t}}{\mathrm{c}}\right) * \cos^2(\Lambda) * \mathrm{l_{H*}S_{Hg}}^{1.5}}$$

Where:

$\mathbf{S_{He}}$ Is the exposed area of the horizontal stabilizer (already known: **19,81*0,562= 11,13m²**).

$\mathrm{N_{ultimate}}$ Is the ultimate load (**1.5**).

b Is the wingspan (already known: **60m**).

TOW Is the take-off weight (already known: **128.850 kg**).

$\boldsymbol{MAC_W}$ Mean Aerodynamic Chord (already known: **4,468m**).

Λ Is the swept angle (already known: **32º**).

$\mathbf{L_H}$ Distance from the center of gravity to the aerodynamic center of the tail.

$\mathbf{S_{Hg}}$ Gross horizontal tail area (already known **77,34m²**).

$\mathbf{t/c} = \mathbf{0{,}562}$ (Already known)

$$\mathbf{L_H} = \mathbf{24{,}8} + \frac{\mathbf{3}}{\mathbf{4}}(\mathbf{11{,}2}) + \frac{\mathbf{1}}{\mathbf{3}}(\mathbf{5{,}8}) = \mathbf{35{,}13\ meters}$$

$$\mathrm{Weight_{HS}} = 5{,}25 * 11{,}13 * 0.8 * 10^{-6} * \frac{1{,}5 * 60^3 * 128850 * 4{,}468\sqrt{11{,}13}}{0{,}562 * \cos^2(32) * 35{,}13 * 77{,}34^{1.5}}$$

$$\mathbf{Weight_{HS}} = \mathbf{3063{,}04Kg}$$

As it can be appreciated from the results, the lifting system would be capable of ensuring **around a 462 % of weight reduction** in comparison with a conventional horizontal stabilizer. As well as the weight comparison between the conventional and the aircraft including lifting system, the economic viability of this new design would be a crucial factor in case of thinking at its future manufacture. However, since it was almost impossible to know about the economic factors involving the salaries for workers as well as the price corresponding to the necessary processes for working with carbon fiber, only a comparison between the price for the materials would be carried out.

In the case of the conventional aircraft, the horizontal stabilizer is composed of a wide range of materials and internal mechanisms. For this study, the main material used at the horizontal stabilizer was assumed to be composed by aeronautical aluminum, steel and CFRP composites (same material which would be used for the lifting system). As it can be depicted from figure 106, the leading edge of the horizontal stabilizer was entirely composed by aluminum (in specific aluminum 2024) while, the middle part was composed by the CFRP material and the rear part (where it can be found the elevator system) was made up of steel to provide a greater strength to the high-lift device located at this area: the elevator. The elevator consists of a principal flight control surface that directs an aircraft's lateral movement (known as pitch). The majority of aircraft have two elevators, situated on the trailing edge of each side of the horizontal stabilizer. For the economic calculations about the materials used first, an estimation about the Boeing 787-9 horizontal's stabilizer area was carried out [73]. For getting the resultant area of the horizontal stabilizer, the following calculations were performed:

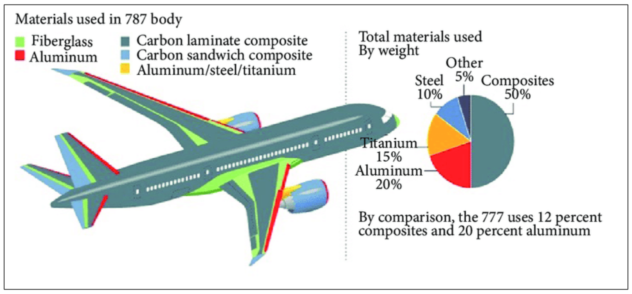

Figure 106. Main materials used for the manufacturing of the Boeing 787 [22]

$$Volume\ coefficient_{HPT} = \frac{S_t * L_t}{S_w * mac}$$

Where:

- S_t Stands for the surface of the horizontal stabilizer.
- L_t Stands for the distance between the aerodynamic center of the wing and the HTP.

- S_w Stands for the surface of the main wing.
- mac Stands for the mean aerodynamic chord of the main wing.
- W_f Stands for the weight of the fuselage.

To estimate the horizontal tail plane volume coefficient the following table was used:

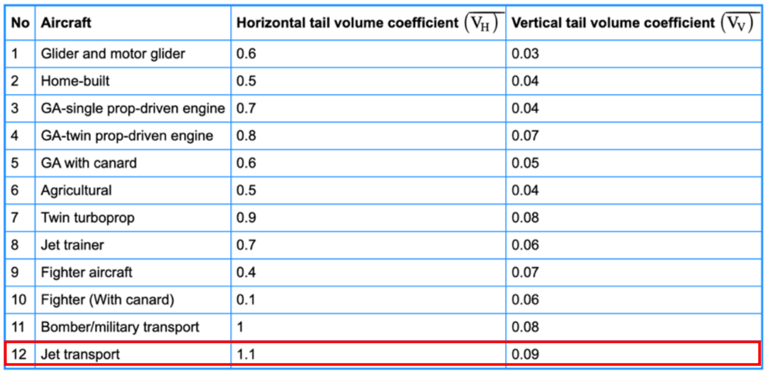

No	Aircraft	Horizontal tail volume coefficient $(\overline{V}_H)$	Vertical tail volume coefficient $(\overline{V}_V)$
1	Glider and motor glider	0.6	0.03
2	Home-built	0.5	0.04
3	GA-single prop-driven engine	0.7	0.04
4	GA-twin prop-driven engine	0.8	0.07
5	GA with canard	0.6	0.05
6	Agricultural	0.5	0.04
7	Twin turboprop	0.9	0.08
8	Jet trainer	0.7	0.06
9	Fighter aircraft	0.4	0.07
10	Fighter (With canard)	0.1	0.06
11	Bomber/military transport	1	0.08
12	Jet transport	1.1	0.09

Table 1. Horizontal & Vertical Tail volume coefficients for different aircraft depending on their configuration [23]

As it can be seen from table 2, since the Boeing 787-9 refers to a jet transport, the corresponding estimated horizontal tail volume coefficient would be of 1.1. Having already the volume coefficient, and taking into account that the rest of parameters, were already known, the horizontal stabilizer surface was able to be calculated:

$$\lambda = \frac{C_{tip}}{C_{root}} = \frac{3{,}33}{5{,}77} = \mathbf{0.5777 meters} \text{ (Already known)} \quad S_w = \mathbf{361\ m^2} \text{ (Already known)}$$

$$\text{mac} = \text{Chord}_{\text{Root}} * \frac{2}{3}\left(\frac{(1+\lambda+\lambda^2)}{(1+\lambda)}\right) = \mathbf{4{,}65 meters} \qquad Volume\ coefficient_{HPT} = \mathbf{1{,}1}$$

$$L_t(\text{distance between the aerodynamic center}) = 4{,}468 + 4{,}46 + 18{,}91 = \mathbf{27{,}83\ meters}$$

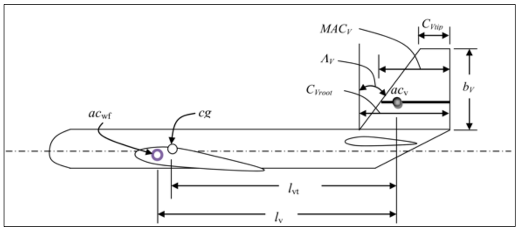

Figure 107. Boeing 787-9 scheme of the different distances between centers of gravity, mean aerodynamic chords and aerodynamic centers [24]

$$1{,}1 = \frac{S_t * 27{,}83}{361 * 4.65} \qquad HTP_{surface} = \mathbf{66{,}35m^2}$$

The result was assumed to be correct since usually, the horizontal stabilizer's area is around the 15-20% (18,46%) of the main wing area.

By dividing the device into two different parts as it was seen in figure 96, the area for each sub-element of the horizontal tail plane was able to be estimated:

- The area composed by CFRP material was of about **53,32 m2** (an 80% of the total area).
- The area composed by aluminum 2024 was of about **13,33 m2** (a 20% of the total area).

Considering the price per square meter of these materials, which were:

Lifting System

- The price per square meter for CFRP material was of about **1.828,79 euros**. Since the area for the lifting system, which was previously calculated, was of 144,62 m2, the estimated cost of the CFRP material would be of around **177.985,56 euros**.

Horizontal Stabilizer

- The price per square meter for aluminum was of about **3599,2 euros**. Since the area for the horizontal stabilizer was previously calculated (53,08 m2 only taking into account the aluminum part), the total costs would be of around **191.045,53 euros.**
- The price per square meter for CFRP material was of about **1.828,79 euros**. Since the area for the horizontal stabilizer was previously calculated (13,27 m2 only taking into account the aluminum part), the total costs would be of around **24.268,04 euros.**

Note that the price and other information from the materials selected can be found at ANEX XVII. Having performed the calculations, the total amount of money in terms of materials invested in the manufacturing of the Boeing's 787-9 horizontal stabilizer was of **215.313,57 euros** while the lifting system would have a cost of **177.985,56 euros**. This calculation only took into account the main material, meaning that the internal structure of the horizontal stabilizer including the elevator mechanism as well as the elements inside the lifting system such as the actuators were not taken into account. Having this in mind, manufacturing the lifting system would suppose a descent in costs (purely costs in terms of materials used) of around **37.328,01 euros**, which represents a descent of the **17,33%** of the material costs. If considering the rest of parameters such as actuators, ribs, spars, electrical system, machinery and labor, since machinery for CFRP material was already necessary for the manufacture of the horizontal tail plane, the overall costs would be expected to have a similar difference (around 30-35%) as the one obtained for the costs of materials.

4.2 DRAG ESTIMATION

Estimating the drag generated by the lifting system would be almost impossible without the previous performance of several simulations of this brand-new system. The methodology used in order to perform the following calculations consisted of first, running several simulations with the purpose of obtaining results corresponding to the original aircraft (aircraft including the horizontal stabilizer and without lifting system). Then, the re-designed aircraft (including the lifting system) would be simulated in order to obtain several results as it was done in the previous case. As Autodesk CFD software is known to be not very consistent about the numerical results it generates, a comparison between the results obtained at both cases was decided to be carried out so that the comparison between drag (which is the main purpose of this chapter) generated at both cases would be able to be carried out.

4.2.1 DRAG ESTIMATION AT CRUISE

As it was explained during chapter 3.7.1, these simulations were done taking into account the average cruise velocity corresponding to the Boeing 787-9 (913 km/h) at ideal conditions (incompressible flow) since the software was not optimized enough to provided consistent results from compressible flow simulations. Note that the tables including the different results directly obtained from the simulations can be found at ANNEXES IX-XVI; also, note that the Y-Axis meanwhile the horizontal one corresponded to the Z-Axis.

As ideal conditions were assumed while performing the simulations, the drag was assumed to be equal to the thrust (steady and level flight); this model was used in order to obtain simplified results. Note that this assumption would not be possible during the tilted aircraft simulations. The results from this simulation were:

$$\mathbf{F_{Z\ (cruise\ without\ HTP\ \&\ \mathit{lifting\ system})}} = \mathbf{2884,58\ Newtons}$$

$$\mathbf{F_{Z\ (\mathit{lifting\ system}\ "\mathit{one\ side}")}} = \mathbf{3437,5\ Newtons}$$

$$\mathbf{F_{Z\ (L.S\ )}} = \mathbf{F_{Z\ (L.S\ "1st\ side")}} - \mathbf{F_{Z\ (cruise\ without\ HTP\ \&\mathit{L.S})}} + \mathbf{Force_{Z\ (L.S\ "2nd\ side")}}$$

$$\mathbf{F_{Z\,(L.S\ configuration)}} = \mathbf{3437,5 - 2884,58 + 3437,5 = 3990,42\ Newtons}$$

$$\mathbf{F_{Z\,(conventional\ configuration)}} = \mathbf{3888,21\ Newtons}$$

As it can be appreciated from the results, an increase of drag took place after the introduction of the lifting system. **The drag increased around a 2,62%**, note that this increment in drag was already known to happen due to the loss of aerodynamic efficiency. However, due to the loss in weight, the overall efficiency would be expected to be higher than with the conventional configuration.

4.2.2 DRAG ESTIMATION AT TAKE-OFF

As it was explained during chapter 3.7.1, these simulations were done taking into account the average take-off velocity corresponding to the Boeing 787-9 (260 Km/h) at ideal conditions (incompressible flow) since the software was not optimized enough to provided consistent results from compressible flow simulations. Note that the tables including the different results directly obtained from the simulations can be found at ANNEXES IX-XVI; also, note that the vertical axis corresponded to the Y-Axis meanwhile the horizontal one corresponded to the Z-Axis. The results from this simulation were:

$$\mathbf{F_{Z\,(cruise\ without\ HTP\ \&\ \mathit{lifting\ system})}} = \mathbf{2933,3\ Newtons}$$

$$\mathbf{F_{Z\,(\mathit{lifting\ system}\ "\mathit{one\ side}")}} = \mathbf{3408,12\ Newtons}$$

$$\mathbf{F_{Z\,(L.S\,)}} = \mathbf{F_{Z\,(L.S\ "1st\ side")}} - \mathbf{F_{Z\,(cruise\ without\ HTP\ \&\mathit{L.S})}} + \mathbf{Force_{Z\,(L.S\ "2nd\ side")}}$$

$$\mathbf{F_{Z\,(L.S\ configuration)}} = \mathbf{3408,12 - 2933,3 + 3408,12 = 3882,94\ Newtons}$$

$$\mathbf{F_{Z\,(conventional\ configuration)}} = \mathbf{3659,03\ Newtons}$$

As it can be appreciated from the results, an increase of drag took place after the introduction of the lifting system. **The drag increased around an 6,11%**, note that this increment in drag was already known to happen due to the loss of aerodynamic efficiency. However, due to the loss in weight, the overall efficiency would be expected to be higher than with the conventional configuration.

4.3 LIFT ESTIMATION

Estimating the lift generated by the lifting system would be almost impossible without the previous performance of several simulations of this brand-new system. The methodology used in order to perform the following calculations consisted of first, running several simulations with the purpose of obtaining results corresponding to the original aircraft (aircraft including the horizontal stabilizer and without lifting system). Then, the re-designed aircraft (including the lifting system) would be simulated in order to obtain several results as it was done in the previous case. As Autodesk CFD software is known to be not very consistent about the numerical results it generates, a comparison between the results obtained at both cases was decided to be carried out so that the comparison between lift (which is the main purpose of this chapter) generated at both cases would be able to be carried out.

4.3.1 LIFT ESTIMATION AT CRUISE

As it was explained during chapter 3.7.1, these simulations were done taking into account the average cruise velocity corresponding to the Boeing 787-9 (913 km/h) at ideal conditions (incompressible flow) since the software was not optimized enough to provided consistent results from compressible flow simulations. Note that the tables including the different results directly obtained from the simulations can be found at ANNEXES IX-XVII; also, note that the vertical axis corresponded to the Y-Axis meanwhile the horizontal one corresponded to the Z-Axis. The results from this simulation were:

$$\mathbf{Force_{Z\,(cruise\ without\ HTP\ \&\ \mathit{lifting\ system})} = 2605,43\ Newtons}$$

$$\mathbf{Force_{Z\,(\mathit{lifting\ system}\ "\mathit{one\ side}")} = 3028,2\ Newtons}$$

$$\mathbf{F_{Z\,(L.S\,)} = F_{Z\,(L.S\ "1st\ side")} - F_{Z\,(cruise\ without\ HTP\ \&\mathit{L.S})} + Force_{Z\,(L.S\ "2nd\ side")}}$$

$$\mathbf{F_{Z\,(L.S\ configuration)} = 3028,2\ - 2605,43 + 3028,2 = 3450,97\ Newtons}$$

$$\mathbf{F_{Z\,(conventional\ configuration)} = 3207,26\ Newtons}$$

As it can be appreciated from the results, an increase of drag took place after the introduction of the lifting system. **The lift increased around a 7,59%**, note that this increment in lift was already known to happen due to the lower ducts pointing almost in upwards direction.

4.3.2 LIFT ESTIMATION AT TAKE-OFF

As it was explained during chapter 3.7.1, these simulations were done taking into account the average cruise velocity corresponding to the Boeing 787-9 (260 km/h) at ideal conditions (incompressible flow) since the software was not optimized enough to provided consistent results from compressible flow simulations. Note that the tables including the different results directly obtained from the simulations can be found at ANNEXES IX-XVI. Before looking the table mentioned above, remember that during the simulations, the vertical axis corresponded to the Y-Axis meanwhile the horizontal one corresponded to the Z-Axis. The results were:

$$\mathbf{Force_{Z\,(cruise\ without\ HTP\ \&\ \mathit{lifting\ system})} = 2551,43\ Newtons}$$

$$\mathbf{Force_{Z\,(\mathit{lifting\ system}\ "\mathit{one\ side}")} = 2852,25\ Newtons}$$

$$\mathbf{F_{Z\,(L.S\,)} = F_{Z\,(L.S\ "1st\ side")} - F_{Z\,(cruise\ without\ HTP\ \&\mathit{L.S})} + Force_{Z\,(L.S\ "2nd\ side")}}$$

$$\mathbf{F_{Z\,(L.S\ configuration)} = 2852,25\ - 2551,43 + 2852,25 = 3153,07\ Newtons}$$

$$\mathbf{F_{Z\,(conventional\ configuration)} = 2996,62\ Newtons}$$

As it can be appreciated from the results, an increase of drag took place after the introduction of the lifting system. **The lift increased around a 5,22%**, note that this increment in lift was already known to happen due to the lower ducts pointing almost in upwards direction.

4.4 MANEUVERABILITY

The necessity of mobility in commercial aircraft, such as the Boeing 787-9 Dreamliner, cannot be overemphasized. It has a direct impact on safety, operational efficiency, and the passenger experience. Improved mobility allows for faster reactions to unfavorable conditions, which optimizes flight routes, reduces fuel consumption, and ensures passenger comfort. Technological developments, such as fly-by-wire controls, improve aircraft agility and dependability. As aviation advances, emphasizing flexibility is critical to the future of air travel, defining safer, more efficient, and pleasurable experiences for passengers worldwide.

4.4.1 SIDE MANEUVERING

Because of this, maneuverability is something such important to take into account; during this report, the maneuvers involving taking and lading off have been deeply explained into detail. Side maneuvering is one of the most important things to take into account during aircraft design. The lifting system would not interfere during side maneuvers since the rudder's (the rudder is the movable integrated at the vertical stabilizer) [74] dimensions were kept the same so that it was not necessary to change nothing in relation with the vertical stabilizer meaning that the side maneuvering for the aircraft with the lifting system would remain almost unchanged. However, in case of the free stream velocity coming from one of the sides of the aircraft while flying at cruise could suppose an increment in drag since not all the incoming air would get into the ducts but, thanks to the air intakes among the ducts, part of the air could enter by them as well as by the principal entrance and as well as before accelerate partially the flow (at this case the acceleration would be less than if flying towards the free stream velocity).

In order to clearly see the adverse effects which would cause a cross wind [75] while flying at cruise were also studied by performing the pertinent simulations with the main purpose of gathering the data to see the difference in lift and drag with respect to the rest of cases. Note that this simulation was decided to be included in this chapter since it is directly related to it.

Figure 108 shows the velocity distribution for the case in which the aircraft would be at cruise conditions with the free stream flow coming sidewards (during this simulation, the air is coming with a deviation of 15º).

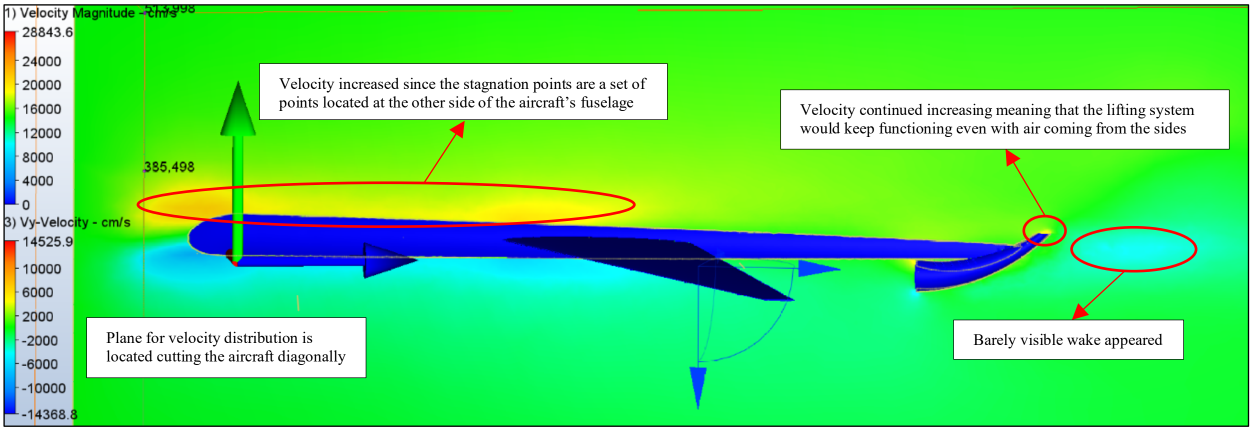

Velocity increased since the stagnation points are a set of points located at the other side of the aircraft's fuselage

Velocity continued increasing meaning that the lifting system would keep functioning even with air coming from the sides

Plane for velocity distribution is located cutting the aircraft diagonally

Barely visible wake appeared

Figure 108. Velocity distribution (Z-Axis) when the free stream velocity comes with an angle of 15º sidewards (the plane representing the velocity distribution was tilted to observe better the distribution of velocity)

During this simulation, the unique result to be focused at, consisted of the velocity in the Y-axis (vertical axis). This was due to the fact that the main goal of performing this simulation, consisted of ensuring if the lifting system would have a good performance while having cross wind or not. Also, a couple of graphs (see figures 109 and 110) were built from the simulation performed; these graphs represent the velocity in the vertical direction and the static pressure among the lower duct respectively.

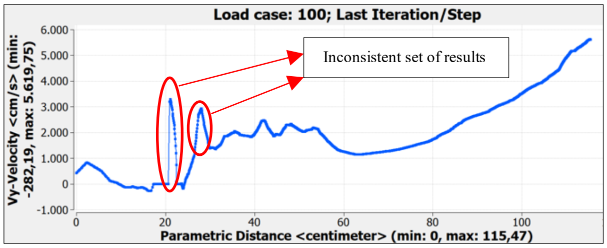

Inconsistent set of results

Figure 109. Vy-velocity vs. Parametric distance graph for the simulation in which air comes from 15º sidewards

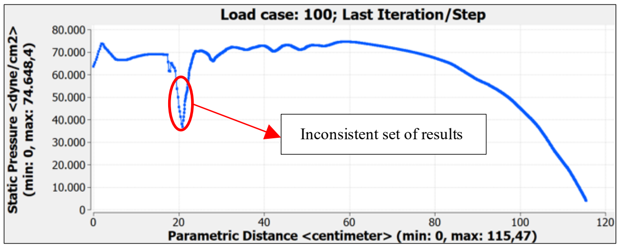

Inconsistent set of results

Figure 110. Static Pressure vs. Parametric distance graph for the simulation in which air comes from 15º sidewards

As it can be depicted from the graphs, the vertical velocity continued increasing even when the air came from the side of the aircraft with a deflection of 15º meaning that the lifting system would continue creating lift or downforce respectively. However, to understand the static pressure graph, an additional graph was needed. Figure 111 represents the velocity in the Z-axis, this velocity is directly related with the static pressure as it happened in the rest of simulation.

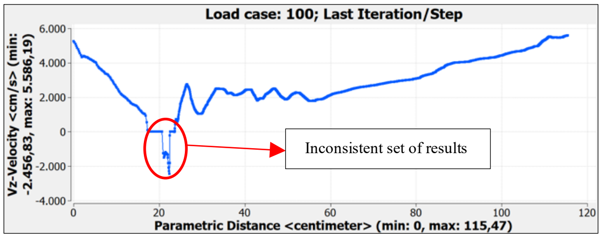

Inconsistent set of results

Figure 111. Vz-velocity vs. Parametric distance graph for the simulation in which air comes from 15º sidewards

As it can be seen, the velocity in the Z-axis is maintained almost constant through the aircraft. However, this result seems to be wrong since, due to the Bernoulli principle, when the velocity increases the static pressure would also increase but, in this case, the static pressure seems to have exponentially decreased while the velocity in the Z-axis has slightly decreased. This means that the results in terms of pressure would not be well calculated; these inconsistencies could be given by internal failures in the software during the simulations.

4.4.2 CLIMB & DESCENT MANEUVERING

With respect to the climb and descent maneuvers, they would slightly change with respect to the conventional configuration of the Boeing 787-9. After the introduction of the lifting system, the distance to the floor would have been reduced; this led the aircraft to be capable of performing the lift-off at almost similar angles of attack as seen in figure 112. Despite the angle for lift-off has slightly decreased with respect to the conventional configuration, due to the curvature of the aircraft's fuselage at the rear part, this descent in the distance from the runway to the lifting system would be almost insignificant. The best way of seen it is with figure 112, where it can rotate with an angle of attack of around 15-20 degrees, the first part of the aircraft on being in contact with the pavement would continue being the lower part of the rear fuselage. This means that the lifting system would not suppose a problem during this type of maneuvers, and so the same runways as before would still being used.

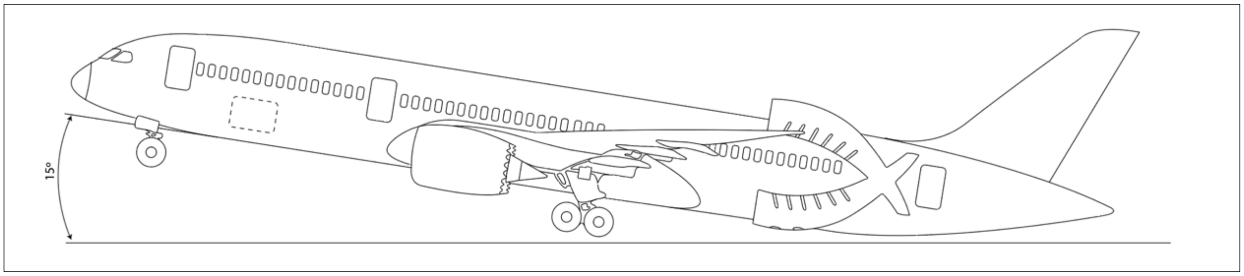

Figure 112. Boeing 787-9 with Lifting System configuration showing the maximum climb angle without touching the runway (Adobe Illustrator)

In addition, it during landing and taking-off, the lower ducts (generating downforce) could be though to have not a particular reason for its use but, the main use of this lower ducts would be to compensate the rest of forces acting through the aircraft and so to compensate the moments generated. However, the aircraft's stability would be entirely controlled by the on-board computer.

CHAPTER 5. ENVIRONMENTAL STUDY

In order to improve aviation technology, it is essential to understand the link between innovation in technology and environmental sustainability. As the aerospace sector seeks for innovation, the need to reduce its environmental impact becomes more and more evident. According to the International Air Transport Association (IATA), worldwide air traffic is expected to increase up to four times by 2037, placing the aviation industry at an important point where it must service rising demand while reducing its environmental effect [76]. The necessity of integrating these approaches becomes one of the main goals of Agenda 2030, the United Nations' strategy for sustainable development. [77]

Figure 113. 17 Sustainable development goals for 2030 [25]

Agenda 2030 includes seventeen Sustainable Development Goals (SDGs) but, in this case, the chapter would be focused on goal 13: Climate Action is central to this framework. Highlighting the need of reducing greenhouse gas emissions and improving resistance to climate change. In the context of aviation, carrying out this goal requires a change towards a cleaner, greener technology and operational processes. [78]

5.1 EMISSIONS REDUCTION (I)

The re-design of traditional aircraft design seems to be an efficient way for emissions reduction. A possible innovative technique is the elimination of horizontal stabilizers, an activity that is not limited to aerodynamic innovation but also connects well with the larger objective of reducing the emissions. Horizontal stabilizers, which are commonly made of aluminum and other materials, are not just aerodynamic devices but also contribute significantly to the aircraft's structural weight [79]. By avoiding the building of these stabilizers, aircraft manufacturers could achieve significant savings in both materials use as well as the associated emissions.

The effects go further to the aircraft's structure since it would include the whole manufacturing process. The production of horizontal stabilizers demands complex industrial processes, going from material extraction and manufacturing to assembly and integration (all of these results in energy consumption and emissions). By avoiding the fabrication of certain components, the aerospace industry may reduce its environmental impact at the point of manufacture. Furthermore, the removal of horizontal stabilizers would have effects through the supply chain, resulting in savings in energy consumption and emissions. Aluminum, which is an essential component in conventional stabilizer building, is known for its energy-intensive extraction and processing. By reducing demand for aluminum and other structural elements, aircraft manufacturers may achieve significant reductions. Also, the removal of horizontal stabilizers would have positive results in terms of fuel economy and pollution reduction. Aerodynamic drag, which is the factor which dramatically reduces the fuel efficiency, could be reduced and so the thrust and fuel consumption during the flight would be also decreased. In addition to the direct emissions reductions achieved from material reduction, the removal of horizontal stabilizers results in additional environmental benefits since the reduced structural complexity would lead to simpler manufacturing processes, lowering energy consumption and emissions in industrial facilities. Because of these reasons, the lifting system could a greater solution in order to reduce the emissions since, due to the descent in the quantity of material used as well as the reduction of the aircraft weight which would lead into an improved overall efficiency while flying since the efficiency of the aircraft is directly linked to its weight. However, it is important to remark that, despite the processes involving the carbon fiber treatment are less sustainable than the ones involving aluminum, since the aircraft's weight could be dramatically lowered as seen in the previous chapter, the overall reduction of emissions would be on favor of replacing the horizontal stabilizers for the lifting system.

Figure 114. Flight route distance from Los Angeles - London Heathrow [26]

In order to demonstrate how the lifting system would be able to lower the emissions, a study about the difference in range which would suffer the aircraft by the implementation of the lifting system was carried out. For a better comprehension, the route "Los Angeles – London Heathrow" was used as an example; note that it consists of one of the most frequent flights done by the aircraft chosen and that the flight distance between both destinations is of **8754,67 Km** [80]. Having this initial analysis into account, an analytical study was carried out with the purpose of comparing the fuel consumption for the actual configuration of Boeing 787-9 with the new configuration for the aircraft (including the lifting system). Before starting with the calculations, several data were needed:

Engines

As it is already known, the engines used by the Boeing 787-9 are either the Rolls-Royce Trent 1000 or the General Electric GEnx- but for this study, the engines manufactured by Rolls-Royce were selected [81]. The necessary data from the engines selected consisted of the following points:

- Maximum thrust generated by the engines (at Mean Sea Level): **265,3–360,4 kN.** [81] [82]
- Specific Fuel Consumption (SFC): **0.506 lb/hr/lbf** which is equivalent to **1,37 g/kN/s**. [81] [82]

Weights

Information about the total weight and thrust of the aircraft was needed:

- Maximum Take-Off Weight of the Boeing 787-9 is of **254.700 Kg.** [83]
- The Fuel Capacity of the Boeing 787-9 is of **126.372 Kg**. [83]

Having the necessary data, calculations were able to be performed. To calculate the range of the aircraft for each of the cases, the Breguet Equation was used [84]:

$$Range = \frac{Velocity}{SFC} * \frac{C_L}{C_D} * Ln\left(\frac{W_{Start\ of\ cruise}}{W_{end\ of\ cruise}}\right)$$

The first step to calculate the range by using this equation consisted of estimating the aerodynamic efficiency of the aircraft ($\frac{C_L}{C_D}$). However, the lift to drag ratio cannot be calculated without already knowing the range of the aircraft; because of this, the aerodynamic efficiency was assumed to have a value of 20 ($\frac{L}{D} = 20$). This factor was chosen being based on an article published by the University of British Columbia [86]. Also, the different weights appearing at the Breguet Equation were able to be calculated with the data gathered:

$$\mathbf{W_{Start\ of\ cruise}} = \text{Maximum Take Off Weight} = \mathbf{254.700\ Kg}$$

Taking into account that airlines are forced to fill the fuel tanks with at least the fuel necessary to keep flying an additional time of 1 hour and knowing that the **fuel consumption** of the aircraft chosen, was of about **5400 Liters of fuel per hour (**equivalent to 600L per 100 Km**)** [87], it means that the aircraft must arrive to its destination with at least 5400 Kg of fuel remaining for these calculations, this quantity of fuel was approximated to **6000 Kg**).

$$\mathbf{Fuel\ burnt} = \frac{8.759{,}67 * 600}{100} = \mathbf{52.528{,}02\ Kg\ of\ fuel\ burnt}$$

$$\mathbf{Additional\ fuel = 5400\ Kg\ of\ fuel}$$

This means that the weight at the end of cruise could be now calculated:

$$\mathbf{W_{End\ of\ cruise}} = \mathrm{W_{Start\ of\ cruise}} - (\text{Fuel burnt} + \text{Additional fuel})$$

$$\mathbf{W_{End\ of\ cruise}} = 254.700 - (52.528{,}02 + 5400) = \mathbf{196.771{,}98\ Kg}$$

Having already calculate all the necessary parameters, the range was able to be calculated with the Breguet Equation (velocity at cruise was assumed to be of 913 Km/h during the simulations):

$$\mathrm{Range} = \frac{\mathrm{Velocity}}{\mathrm{SFC}} * \frac{C_L}{C_D} * \mathrm{Ln}\left(\frac{W_{\mathrm{Start\ of\ cruise}}}{W_{\mathrm{end\ of\ cruise}}}\right) = \frac{253{,}61}{1{,}37 * 10^{-4}} * 20 * \mathrm{Ln}\left(\frac{254.700 * 9{,}81}{196.771{,}98 * 9{,}81}\right)$$

$$\mathrm{Range} = 9.553.536{,}29 \text{ meters} = \mathbf{9553{,}53\ Kilometers}$$

Now, the estimation for the maximum range with the lifting system integrated would be calculated:

Lift over Drag Ratio

Due to the fact that the lift and drag changed while flying at cruise due to the introduction of the lifting system (lift increased a 7,59% and drag increased a 2,62%) a different Lift over Drag ratio (L/D) would be obtained:

$$\frac{L}{D_{\mathrm{old}}} = 20 \text{ which could be represented as } \frac{20}{1}$$

$$\frac{\mathbf{L}}{\mathbf{D_{new}}} = \frac{20}{1} = \frac{20 + (20 * 0{,}0759)}{1 + (1 * 0{,}0262)} = \frac{21{,}252}{1{,}0281} = \mathbf{20{,}96}$$

Weights

The overall weight of the aircraft also changed as it was demonstrated during the previous chapter, where the weight of the horizontal stabilizer was stated to be of around 3063,04 Kg meanwhile the weight according to the lifting system would be of about 596,58 Kg. The new total weights were now calculated:

$$\mathbf{W_{difference}} = 3063{,}04 - 596{,}58 = \mathbf{2466{,}46\ Kg}$$

$$\mathbf{W_{Start\ of\ cruise\ new}} = 254.700 - 2466{,}46 = \mathbf{252.233{,}54\ Kg}$$

$$\mathbf{W_{End\ of\ cruise\ new}} = 196.771{,}98 - 2466{,}46 = \mathbf{194.305{,}52\ Kg}$$

Having already calculate all the necessary parameters, the range was able to be calculated with the Breguet Equation as it was already done at the previous case (velocity at cruise was assumed to be of 913 Km/hr during the simulations):

$$\mathrm{Range} = \frac{\mathrm{Velocity}}{\mathrm{SFC}} * \frac{C_L}{C_D} * \mathrm{Ln}\left(\frac{W_{\mathrm{Start\ of\ cruise}}}{W_{\mathrm{end\ of\ cruise}}}\right) = \frac{253{,}61}{1{,}37 * 10^{-4}} * 20{,}96 * \mathrm{Ln}\left(\frac{252.233{,}54 * 9{,}81}{194.305{,}52 * 9{,}81}\right)$$

$$\mathrm{Range} = 10123962{,}12\ \mathrm{meters} = \mathbf{10.123{,}96\ Kilometers}$$

This means that for the same amount of fuel, the conventional Boeing 787-9 would have a range of 9553,53 kilometers meanwhile the one with the lifting system would have a range of 10.123,96 kilometers. This would suppose an **increment in range of 570,43 kilometers** (increment of a **5,97%)** for this particular flight route. This increment in the range could be transposed into a descent in the fuel burned. As it was stated before, the fuel consumption of the B787-9 was of 600 Liters per 100 kilometers (however, this fuel consumption would also change with the introduction of the lifting system but, for this analysis it would be assumed to keep the same). With this information, the amount of fuel saved for the flight Los Angeles – London Heathrow could be calculated:

$$\mathbf{Fuel\ saved} = \frac{600}{100} * 570{,}43 = \mathbf{3422{,}59\ Liters\ of\ fuel}$$

The amount of fuel saved due to the introduction of the lifting system on the aircraft would be of 3422,59 liters. Taking the price of fuel at the departure airport (Los Angeles), the price found for jet A fuel (from Atlantic aviation) was found to be of 9,43$ (8,74 euros) per 100LL (this information can be seen in ANEX XVIII). [88]

$$\mathbf{Economic\ fuel\ savings} = 3422{,}59 * \frac{8{,}74}{100} = \mathbf{299{,}13euros}$$

A total of **299,13 euros are expected to be saved** during cruise for this flight route. However, these savings would be much higher since it does not take into account the moment of taking off and lading where the lifting system would be expected to perform its best and so dramatically reducing this economic savings in fuel.

CHAPTER 6. FURTHER POSSIBILITIES

In spite of the main idea which has been developed during this report, an additional idea was developed in order to enhance the idea of replacing the horizontal stabilizer for the mentioned lifting system. This idea consisted of the installation of propfan (also known as unducted fan) engines. A propfan, also known as an open rotor engine, open fan engine, or unducted fan, is a kind of aircraft engine that is similar to both the turboprop and the turbofan but have several differences from both which makes them unique. The design aims to combine the speed and performance of a turbofan with the fuel efficiency of a turboprop. A propfan is often constructed with numerous short, highly twisted blades, similar to the fan in a turbofan engine. As a result, the propfans are known to be classified as unducted fans or an ultra-high-bypass turbofans.

Several studies were carried out years ago involving the usage of this type of engines; these studies showed the dramatic increase in the efficiency of these engines with respect to the conventional ones. During this chapter, a conceptual design would be carried out in order to combine the previous aircraft configuration (including the lifting system) with these types of engines. Note that, since the main purpose of this project consisted of the introduction of the lifting system, no simulations or three-dimensional models were performed; only the engineering plans as well as the pertinent calculations were carried out.

6.1 POSSIBILITY OF PROPFAN ENGINE INSTALLATION

The reason for not continuing with these studies was due to the fact that the propfans were needed to be located at the rear part of the aircraft. That supposed an important problem in terms of safety and regulations since the engines were needed to be structurally integrated with the horizontal and vertical stabilizers which meant that in case of engine failure the aircraft would face up a severe situation without no control surfaces except for the ones located at the main wing. However, this position of the engines would allow the manufacturers to build up propfans of enormous dimensions which would turn into a dramatic increase of the overall efficiency; not only that, the main wing would be free from the engines meaning that, despite the loads acting at the wings would turn higher than before, the wing would create even more lift and much less parasitic and induced drag due to the elimination of the engines which supposed an obstacle for the air coming to the wings. Having in mind the previous design of the lifting system and taking into account some additional changes which would be seen during this chapter, propfans became an option since, not only the horizontal stabilizer could be eliminated but also, thanks to the additional changes, also the vertical stabilizer could be subtracted from the aircraft. Taking as reference the previous design; the new one was performed with the purpose of also generating the forces which were previously done by the rudder located at the vertical stabilizer. This was possible thanks to an additional system of movable surfaces, which were designed to be inspired by how the SpaceX's Starship uses its grid fins to re-direct the flow and orient the spaceship at each moment. Before entering into the detail of how these movable plates would function, figures 115, 116 and 117 showed the drawing plans for the propfan aircraft, with the lifting system (engineering plans at ANNEX V):

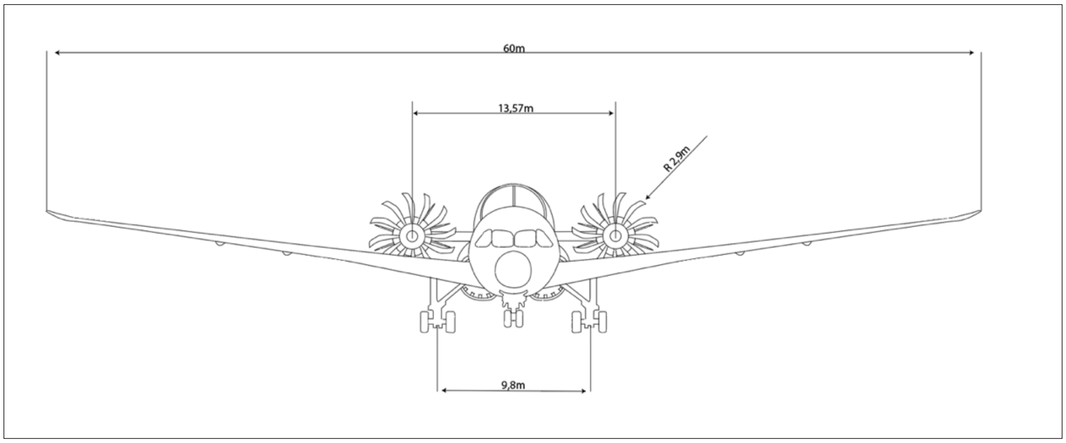

Figure 115. Front-view of the Boeing 787-9 with the propfan & Lifting System configuration (Adobe Illustrator)

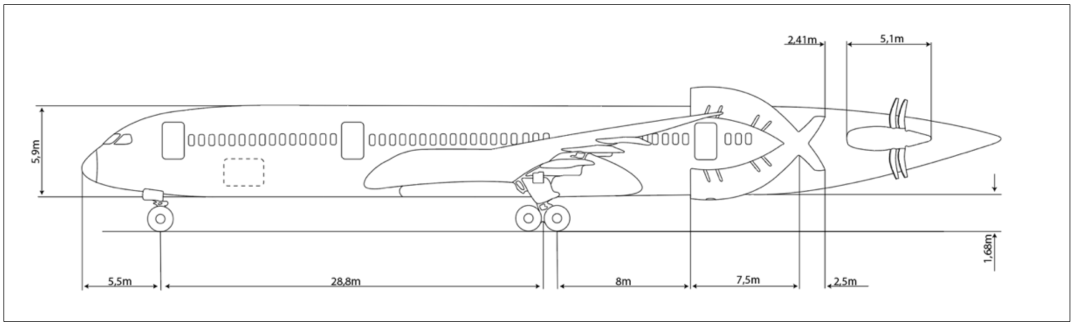

Figure 116. Side-view of the Boeing 787-9 with the propfan & Lifting System configuration (Adobe Illustrator)

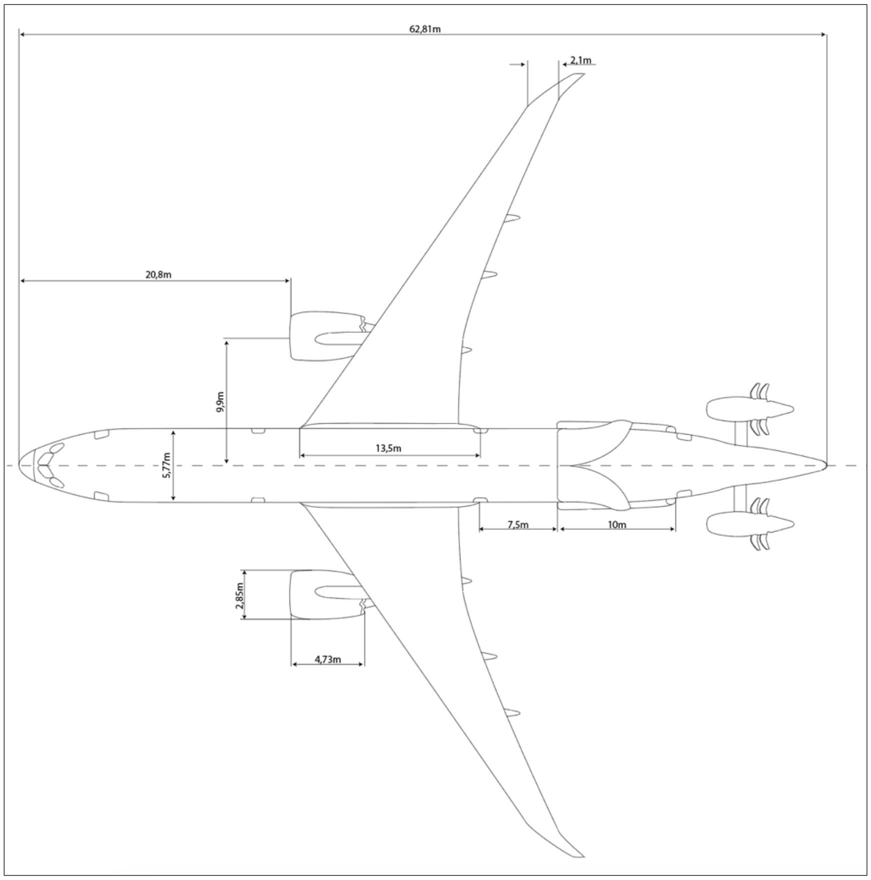

Figure 117. Upper view of the Boeing 787-9 with the propfan & Lifting System configuration (Adobe Illustrator)

In addition to these drawing plans, a perspective 3-dimenisonal drawing was performed with the purpose of understanding better the functioning of the design (see figure 118).

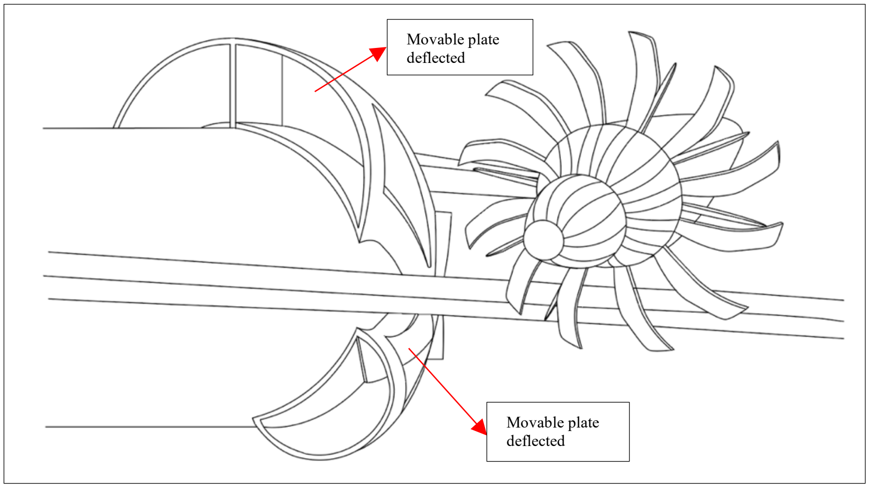

Figure 118. Detailed view of the Propfan & Lifting System configuration with the lateral movable plates deflected to the inside of the ducts (Adobe Illustrator)

Having in mind the drawing plans for the new aircraft concept, it can be appreciated the similarity between the older and the new concept. As it can be depicted from the plans, the detail which have allowed to eliminate the vertical stabilizer and so changing the whole configuration consisted of the movable plates located at the sides of each of the duct. The purpose in the design of these plates consisted of deflecting the air sidewards the aircraft as the rudder does. In case the aircraft needed to perform any yaw movement, the movable plates would rotate thanks to the radial actuators located inside the walls of the ducts. Radial actuators would allow the movement of the plates (which are part of the duct's wall; they are integrated on it) into the interior of the duct, just as if a simple door opens and closes. The plate would close the duct, and so an opening would appear at the side of the duct. This opening would allow the air to flow sidewards and thanks to the Newton's third law (action & reaction), a yaw movement would be created without the necessity of having a vertical tail in the aircraft. For performing the design of the movable plates, two different types of plates were designed depending on the ducts, at which they would be located at. For the upper ducts, the design used would be the one represented in figures 119 and 120 meanwhile for the lower ducts, the design used would be the one represented in figures 121 and 122.

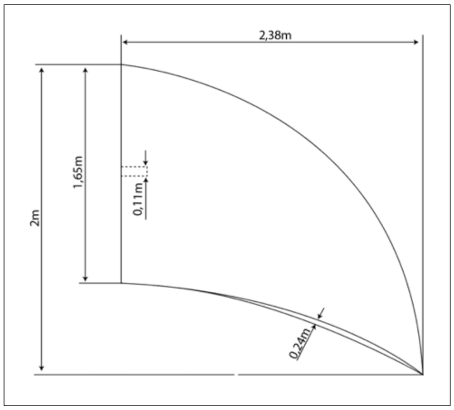

Figure 119. Movable plate corresponding to the upper duct at rest position

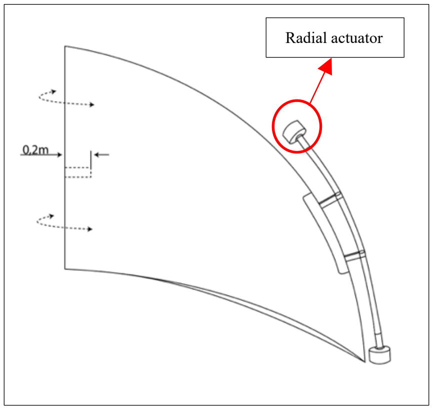

Figure 120. Movable plate corresponding to the upper duct rotating due to the radial actuators

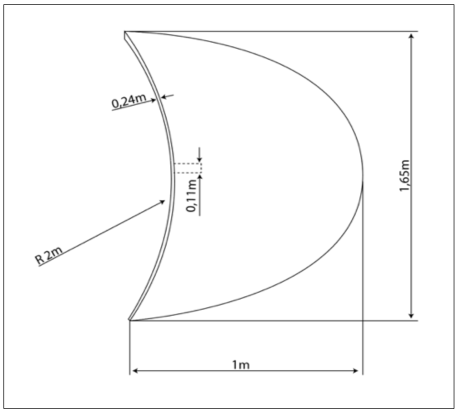

Figure 121. Movable plate corresponding to the lower duct at rest position

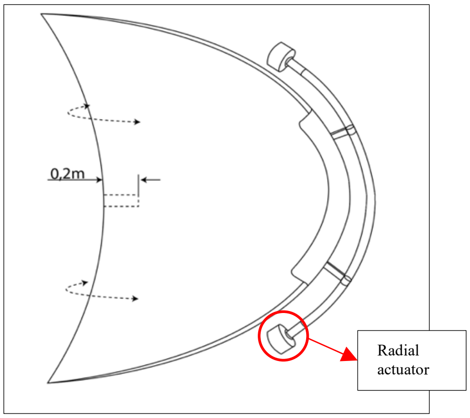

Figure 122. Movable plate corresponding to the lower duct rotating due to the radial actuators

As it can be depicted from the design, the first drawing of each plate corresponds to a side view of the plates. This view would be the one as if the plate would be disassembled from the duct's wall while at the other two figures, the mechanism for each type of plate could be seen. This mechanism consists of a cylindrical bar connected to two radial actuators which would be on charge of rotating the plates; this rotation would be allowed by the small plates connecting the cylindrical tube to the plate itself. The movement of the plates which has been just described can be appreciated even better in figure 123, where an upper view of the lifting system was performed. As it can be appreciated the movable plates would not deflect totally, they would deflect up to a certain angle (60º) so that de air would follow smoothly its path to the gap created by the deflection of the plate.

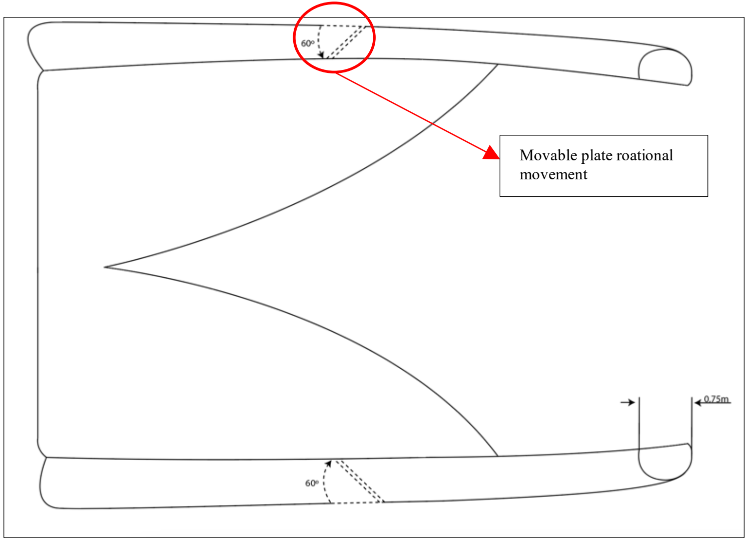

Figure 123. Upper view of the Lifting System with the movable plates being deflected inwards (Adobe Illustrator)

Note that the system of plates described in the previous chapter, which was located inside the ducts continued the same as the new designed only contemplate the introduction of these movable plates. However, some changes in the cross-section of the lifting system were needed due to the appearance of the radial actuators as well as an additional actuator which would be located at the fuselage of the aircraft; these actuators would be on charge of blocking the movement of the plates due to the high velocities reached by the air inside the duct. These lineal actuators would enter into a hollow located inside the plates as it was seen in figure 120 and 122 Its position in the cros-section of the aircraft could be clearly appreciated in figure 124. Note that the dimensions of the lineal actuators were decided taken into account the space width of the different walls among the aircraft and the lifting system. However, this design presented a negative

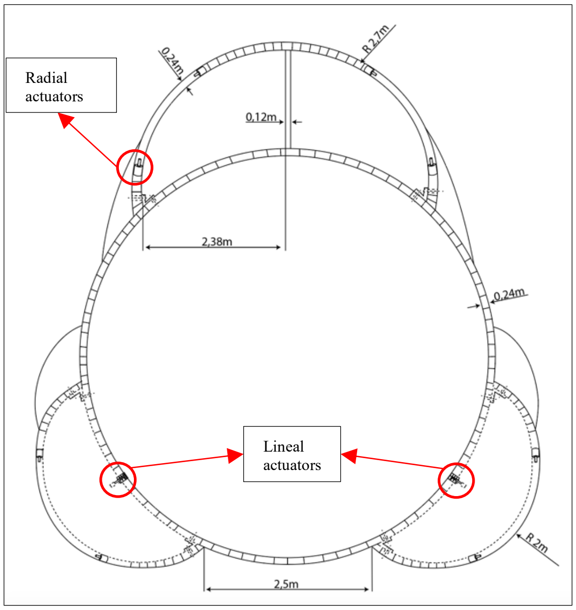

Figure 124. Cross-sectional area of the Lifting System including the radial & lineal actuators positioning (Adobe Illustrator)

point, the air intakes presented during the previous design would not fit completely at this design. Because of the system of movable plates, two of the six air intakes located at the ducts of the lifting system would interfere; the solution was eliminating these air intakes and so the final design would only have four air intakes (see figure 124). This could lower the overall performance of the system but, this would be numerically calculated in future reports. Not only that, also a re-design in the passenger's door and aircraft windows was needed to be performed as it was previously made for the other design. This re-location of the aircraft's rear door could be seen in figure 125. As it was stated at the beginning of the chapter, the main idea of this re-design was though to allow the introduction of the propfan engines. This type of engines was known to be more efficient at the rear part of the aircraft instead at the wing (propfan engines need to have such a big diameter to reach greater efficiencies; since commercial aircraft have kind of low wings, the diameter of this type of propellers would need to be such small that using turbofans was the best option. The only manner of using propfans on actual commercial aircraft with low wings was to locate the engines at the rear part of the fuselage) but, due to the fact of the proximity of the engines to the vertical and horizontal stabilizers, the use of propfans was discarded. However, this re-design has allowed to eliminate both components, the vertical and horizontal tail planes and so the engines could be allowed to be located at the rear part of the fuselage; this can be clearly seen in figure 126. This new position of the engines was the cause of re-locating the passenger door.

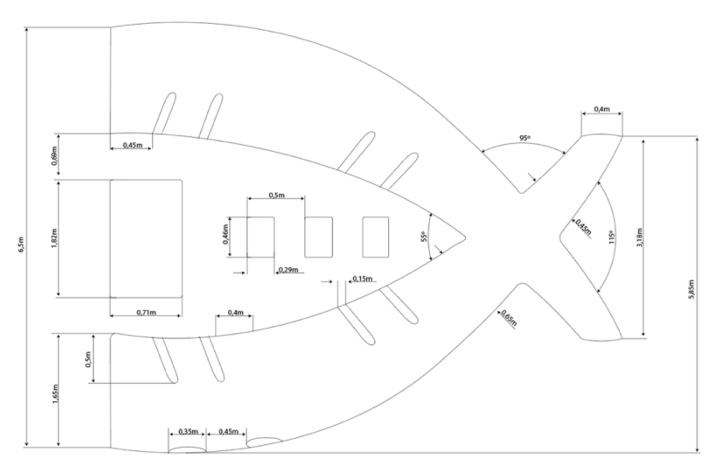

Figure 125. Side view of the Lifting System & rear passenger door arrangement for the Propfan & Lifting System configuration (Adobe Illustrator)

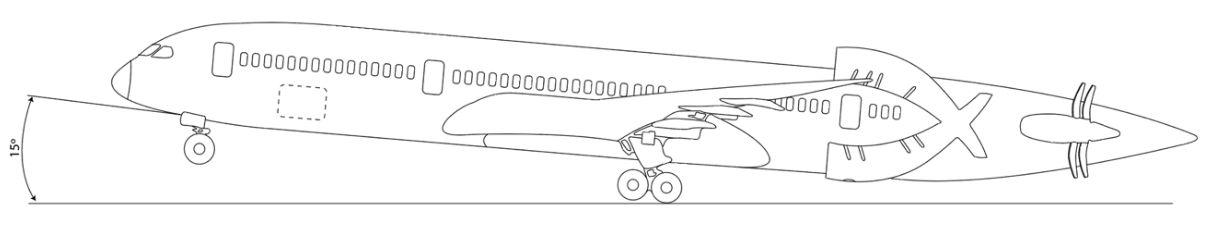

Figure 126. Boeing 787-9 with Propfan & Lifting System configuration showing the maximum climb angle without touching the runway (Adobe Illustrator)

6.2 EMISSIONS REDUCTION (II)

As it was done during the previous chapter, calculations involving the inclusion of the propfan engines could be performed with the purpose of comparing the previous aircraft design and the propfan design (both including the lifting system). In order to perform the pertinent calculations, the following data was gathered:

Propfan Engines

The propfan engine selected consisted of the General Electric GE36 propfan; the reason of using these engines was simply because a wide range of specifications were public for this engine model so that no data was needed to be assumed. Several specifications were gathered from these engines:

- Maximum thrust generated by the engines (at Mean Sea Level): **265,3–360,4 kN.** [88]
- Specific Fuel Consumption (SFC) at cruise: **0.49 lb/(lbf·h) or 1,33 g/kN/s**. [88]
- Cruise speed: 800 km/h (**222,22 m/s**). [88]

Before being able to calculate the range, since the vertical tail would be eliminated as well as it happened to the horizontal one, the weight of the vertical stabilizer was needed to be calculated. To calculate the vertical tail plane surface, the following equation was used:

$$\text{Volume coefficient}_{\text{VPT}} = \frac{S_f * L_f}{S_w * b}$$

Where:

- S_t Stands for the surface of the horizontal stabilizer.
- L_f Stands for the distance between the aerodynamic center of the wing and the horizontal tail plane.
- S_wStands for the surface of the main wing.
- b Stands for the wingspan of the main wing.

The Volume coefficient estimated was of about 0,09 [89]. Since the rest of the parameters were already known, the surface was able to be calculated:

$$S_w = \mathbf{361\ m^2} \qquad b = \mathbf{60\ meters} \qquad \text{Volume coefficient}_{\text{HPT}} = \mathbf{0.09}$$

$$\mathrm{L_f(distance\ between\ aerodynamic\ centers)} = \frac{1}{3}(11{,}2) + 10 + 7{,}5 + \frac{3}{4}(13{,}5) = \mathbf{31,35m}$$

$$0.09 = \frac{\mathrm{S_f} * 31{,}35}{361 * 60} \qquad \mathrm{VTP_{surface}} = \mathbf{62,18m^2}$$

Having calculated the surface area, the weight of the vertical stabilizer was able to be estimated:

$$\mathrm{Weight_{VS}} = 2.62\mathrm{S_{VS}} * 1.5 * 10^{-6} * \frac{\mathrm{N_{ultimate}} * \mathrm{b}^3 * (8 + 0.44\frac{\mathrm{TOW}}{\mathrm{S_{Wg}}})}{\left(\frac{\mathrm{t}}{\mathrm{c}}\right) * \cos^2(\Lambda)}$$

Where:

$\mathrm{S_{VS}}$ Is the wetted area of the vertical stabilizer (**9,4*0,567=5,32m2**).

$\mathrm{N_{ultimate}}$ Is the ultimate load (**N=1,5**).

b Is the wingspan (**60 meters**).

TOW Is the take-off weight (**128850 Kg**).

$\mathrm{S_{Wg}}$ It is the wing area (**361m2**).

Λ Is the swept angle (**32º**).

$$\frac{\mathrm{t}}{\mathrm{c}} = \mathbf{0.562}$$

$$\mathrm{Weight_{HS}} = 2.62 * 5{,}32 * 1.5 * 10^{-6} * \frac{1.5 * 60^3 * (8 + 0.44\frac{128850}{361})}{0.562 * \cos^2(32)}$$

$$\mathbf{Weight_{VS} = 2741,78Kg}$$

As it can be appreciated from the results, the lifting system in addition with the propfan engine implementation would be capable of ensuring **around a 513,43% of weight reduction** in comparison with a conventional horizontal stabilizer. To calculate the range of the aircraft for each of the cases, the Breguet Equation was used:

$$Range = \frac{Velocity}{SFC} * \frac{C_L}{C_D} * Ln\left(\frac{W_{Start\ of\ cruise}}{W_{end\ of\ cruise}}\right)$$

Since the aerodynamic efficiency (L/D) was not possible to be calculated and taking into account some research [90] which located the finesse of propfan engines between 25-30, for this specific case, an L/D of 25 would be assumed (same example for LAX- London Heathrow would be calculated).

$$\mathbf{W_{difference}} = \text{VTP} + \text{HTP} - \text{Lifting System} = 3063{,}04 + 2471{,}78 - 596{,}58 = \mathbf{4938,24\ Kg}$$

$$\mathbf{W_{Start\ of\ cruise\ new}} = 254.700 - 4938{,}24 = \mathbf{249.761,76\ Kg}$$
$$\mathbf{W_{End\ of\ cruise\ new}} = 196.771{,}98 - 4938{,}24 = \mathbf{191.833,74\ Kg}$$

$$\text{Range} = \frac{\text{Velocity}}{\text{SFC}} * \frac{C_L}{C_D} * \text{Ln}\left(\frac{W_{\text{Start of cruise}}}{W_{\text{end of cruise}}}\right) = \frac{222{,}22}{1{,}33 * 10^{-4}} * 25 * \text{Ln}\left(\frac{249.761{,}76 * 9{,}81}{191.833{,}74 * 9{,}81}\right)$$

$$\text{Range} = 11.022.381{,}18 \text{ meters} = \mathbf{11.022,38\ Kilometers}$$

This means that for the same amount of fuel, the conventional Boeing 787-9 would have a range of 9553,53 kilometers meanwhile the one with the lifting system would have a range of 11.022,38 kilometers. This would suppose an **increment in range of 1.468,85 kilometers** (increment of a **15,37%)** for this particular flight route. This increment in the range could be transposed into a descent in the fuel burned. As it was stated before, the fuel consumption of the B787-9 was of 600 Liters per 100 kilometers (as it was done for the previous example) [87]. With this information, the amount of fuel saved for the flight Los Angeles – London Heathrow could be calculated:

$$\mathbf{Fuel\ saved} = \frac{600}{100} * 1468{,}85 = \mathbf{8813,1\ Liters\ of\ fuel}$$

The amount of fuel saved due to the introduction of the lifting system on the aircraft would be of 8813,1 liters. Taking the price of fuel at the departure airport (Los Angeles), the price found for jet A fuel (from Atlantic aviation) was found to be of 9,43$ (8,74 euros) per 100LL (this information can be seen in ANEX XX). [88]

$$\mathbf{Economic\ fuel\ savings} = 8813{,}1 * \frac{8{,}74}{100} = \mathbf{770,26\ euros}$$

A total of **770,26 euros were expected to be saved** during cruise for this flight route. However, this savings would be much higher since it does not take into account the moment of taking off and lading where the lifting system would be expected to perform its best and so dramatically reducing this economic savings in fuel.

Having performed all the calculations involving the emissions reduction now, it would be possible to estimate the reduction of C02 emissions which would take place for each of the cases studied. This comparison was carried out taking into account the flight Los Angeles – London Heathrow (as it was previously stated) and for its estimation, an online calculator (IATA calculator) [91] was used to turn the range reduction obtained into CO2 emissions. Note that this calculator worked with range and number of passengers as inputs, since it assumed a standard aircraft model meaning that, these results could present some approximation errors. For the same quantity of fuel (including the reserve fuel) each configuration was provided with its range; this range was introduced in the online calculator and the results for the CO2 emissions where the following ones depending on the number of passengers (for the Boeing 787-9 there exist three configurations: for 222, 283 and 389 passengers):

- For 222 passengers and the route Los Angeles – London Heathrow:
  - **Conventional configuration** produced around **101.023,3 Kg of CO2.**
  - Aircraft **with Lifting System** produced around **88.857,2 Kg of CO2.**
  - Aircraft **with Lifting System & Propfan** produced around **76.922,6 Kg of CO2.**

- For 283 passengers and the route Los Angeles – London Heathrow:
  - **Conventional configuration** produced around **128.782 Kg of CO2.**
  - Aircraft **with Lifting System** produced around **113,273 Kg of CO2.**
  - Aircraft **with Lifting System & Propfan** produced around **98.059,1 Kg of CO2.**

- For 389 passengers and the route Los Angeles – London Heathrow:
  - **Conventional configuration** produced around **177.018,4 Kg of CO2.**
  - Aircraft **with Lifting System** produced around **155.700,4Kg of CO2.**
  - Aircraft **with Lifting System & Propfan** produced around **234.788 Kg of CO2.**

CHAPTER 7. CONCLUSIONS

Over the last years, aviation has evolved with the implementation of the fly-by-wire systems however, the necessity of reducing the emissions has come to reality and recent studies about the use of hydrogen aircraft have found extremely severe difficulties for its storage and use. At this point, the idea of designing a lifting system to replace a crucial heavy component as the horizontal stabilizer came up to achieve what aerospace engineers have desired during the last decades, a notable reduction of the aircraft's weight. As it can be appreciated through this report, the lifting system introduction would suppose an enhancement not only in terms of economy, but also it would suppose a game changer in the future of aviation due to the notable reduction of emissions. The use of the lifting system would allow aircraft manufacturers to lower the weight of the Boeing 787-9 (this system could be also introduced among a wide range of different aircraft) up to a 1,2%. Not only that, also the introduction of the lifting system would increase the range of the aircraft if comparing it with its conventional configuration, and so decreasing the costs in terms of fuel and the emissions generated. This difference in weight and range between the three variants being studied (conventional, lifting system and lifting system & propfan engines) can be appreciated in figure 127 and 128.

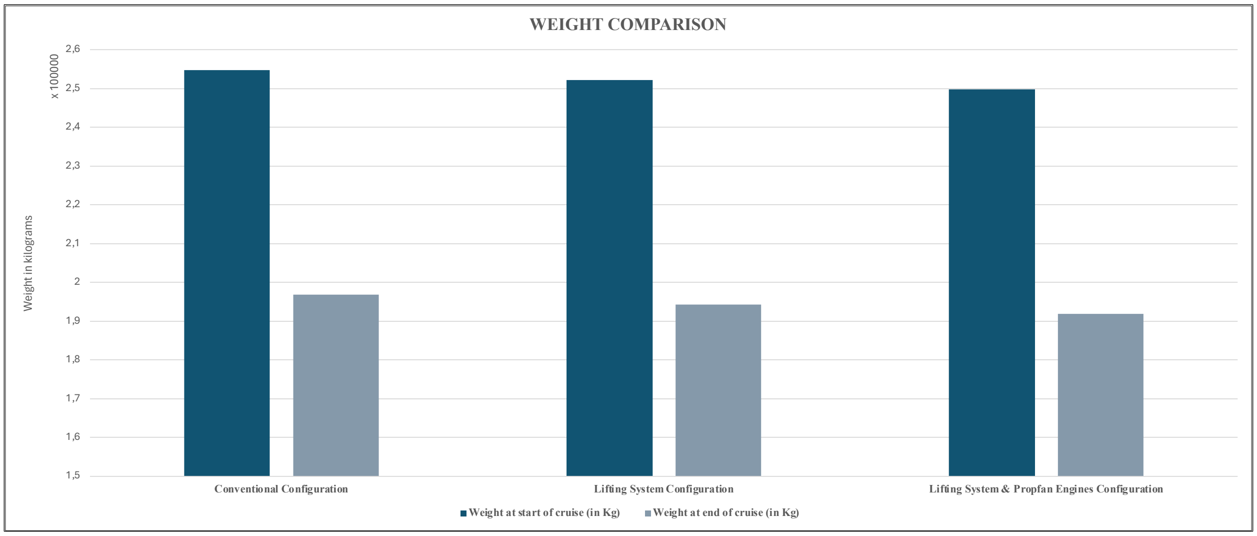

Figure 127. Weight comparison (in Kilograms), between the three configurations: conventional configuration, Lifting System configuration and Lifting System & Propfan Engines configuration which have been studied, at the start and the end of cruise

For the case of range comparison, the example previously stated was used as reference (necessary fuel for the flight from Los Angeles – London Heathrow):

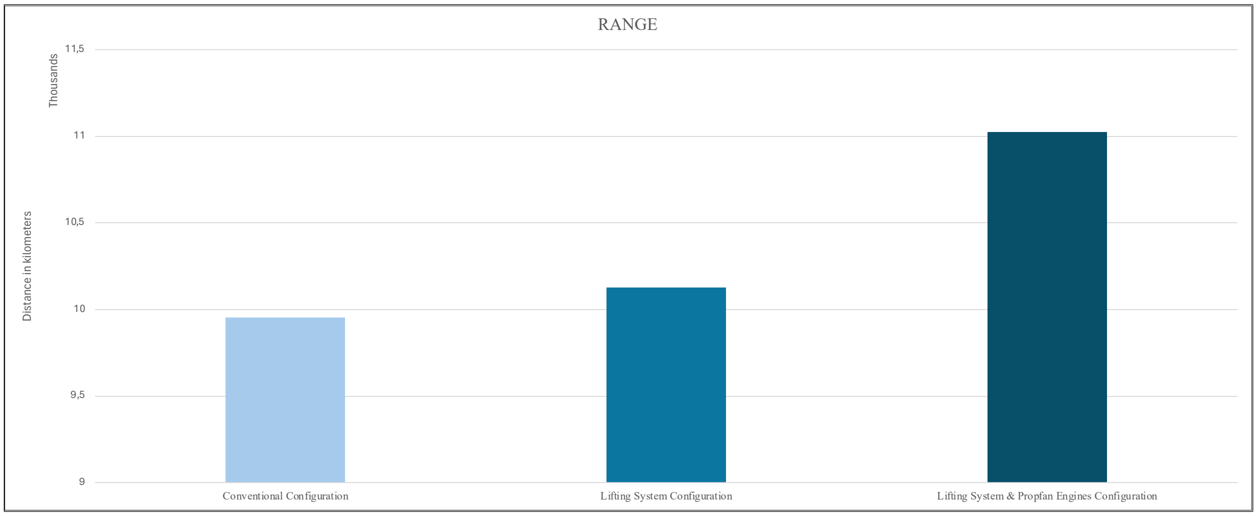

Figure 128. Range comparison (in thousands of kilometers), between the three configurations: conventional configuration, Lifting System configuration and Lifting System & Propfan Engines configuration, assuming cruise conditions

As it has been covered, the lifting system also leads to the possibility of implementing the already mentioned propfan engines. These engines are presented as one of the best positioned candidates to substitute the turbofan engines which are actually in use. It is well known that aircraft manufacturers such as Airbus or Boeing are looking forward for hydrogen engines but, due to the extremely high complexity and logistics involving them, its implementation results such difficult that nowadays, the turbofans are still being used and there are no signs of short-term changes. However, its implementation would lead to a remarkable reduction in the carbon footprint produced by aircraft, as it has been demonstrated and can be clearly appreciated in figure 129.

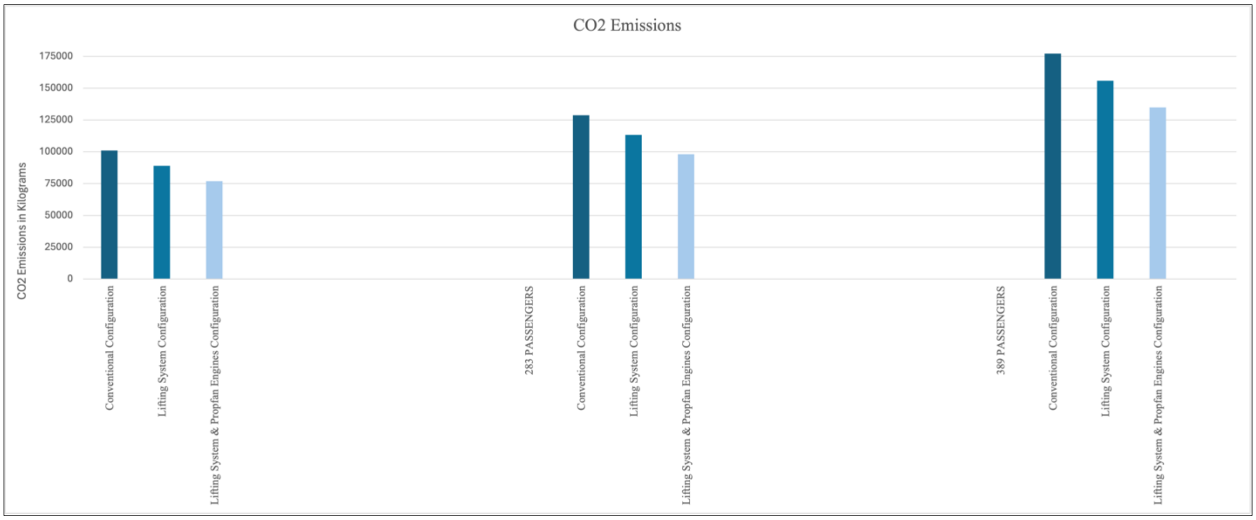

Figure 129. CO2 Emissions comparison (in Kilograms), between the three configurations: conventional configuration, Lifting System configuration and Lifting System & Propfan Engines configuration for three different Boeing 787-9 passenger configurations (222, 283 and 389)

Despite the velocities reached by these engines were slightly lower than the turbofans; due to the weight reduction of a 1,99%, the price per ticket flight would decrease and so more this would turn people who nowadays cannot afford to pay for a flight trip, the opportunity of doing. This means that the aeronautical industry in terms of commercial flights would be able to become more accessible for everyone. During the example of a Boeing 787-9 flying from Los Angeles – London Heathrow, a descent in costs due to fuel savings (only during cruise so, even higher savings would be expected) can be seen in figure 130, which as well, represented the annual economic savings for an airline such us Norse Atlantic Airlines, which operates this flight five times per week. As a result, taking into account only this particular flight route, savings could go up to 72.000 euros (if using the lifting system configuration) or up to 185.000 euros (with the implementation of the lifting system & propfan engines) annually.

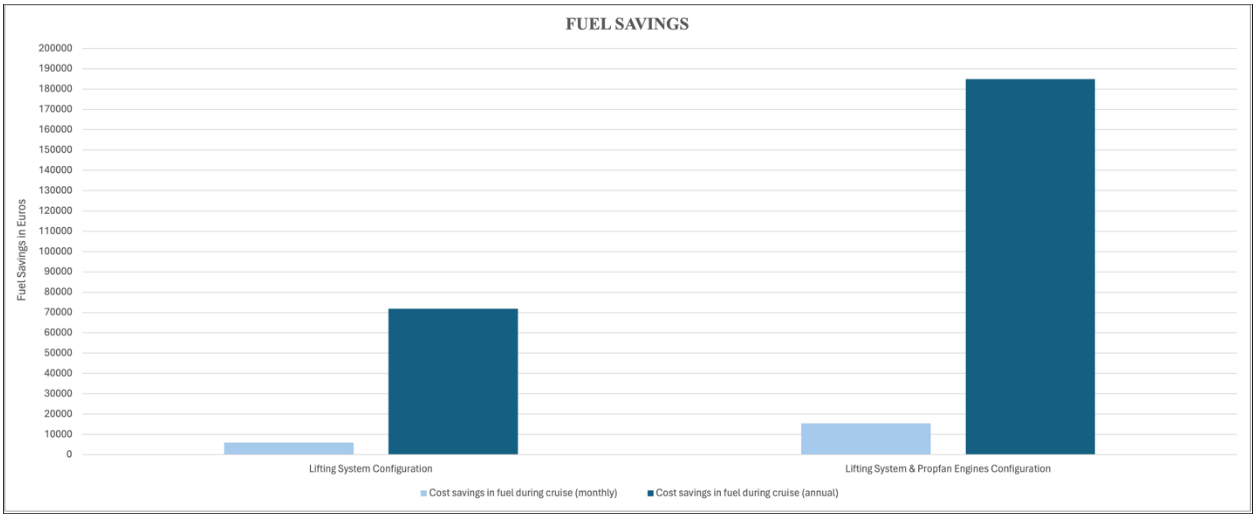

Figure 130. Fuel Savings comparison (in euros), between the three configurations: conventional configuration, Lifting System configuration and Lifting System & Propfan Engines configuration, considering the descent suffered due to the replacement of the horizontal

Also, the emission would decrease due to the dramatic increment in range leading to the idea to start using this aircraft configuration instead looking for hydrogen commercial aircraft (however, flight times would be higher than the actual ones due to the descent in the cruise speed).

As a conclusion, the lifting system seems to be a well-positioned candidate to lower emissions & and annual costs to airlines. However, due to the assumptions taken during the numerical calculations, as well as the relatively "poor" mesh accuracy during the simulations and the problems involving them such as the fact that the performance of the turbulators were not able to be simulated due to the problems with the CFD program, this project should be taken as a first approach for the creation of the lifting system. In order to get results of higher fidelity to reality, a wide range of simulations should be carried out with better mesh accuracy as well as wind tunnel tests to validate the simulations; also, the accuracy in weight should be improved after manufacturing it for the first time since problems such as tolerances or human errors while performing the necessary processes to the carbon fiber. Also, the principal purpose of this new system which consisted of weight reduction was not as efficient as it was though at the beginning. The study has showed a weight reduction of between the 1-2% but, despite this number could be treated as if it has slightly reduced, during this chapter, it can be appreciated how both the C02 emissions and operating costs for airlines would dramatically decrease.

This means that, it is not necessary to introduce massive changes in order to get acceptable results. Only by decreasing the overall weight by a 1-2%, the rest of parameters dramatically decreased meaning that the best way of reducing emissions is to enhance the aircraft’s characteristics periodically even if these changes are considered almost imperceptible, since, as it can be depicted from this report, even the smallest upgrade can lead to noticeable improvements.

ANNEXES

ANEX I

COMPARISON BETWEEN BOEING 787-9 & AIRBUS A350-900

	Boeing 787-9	Airbus A350-900
Passengers	294	348
Range (Kilometers)	Around 14,140 Km	Around 15,372 Km
Length (meters)	63m	66,80m
Wingspan (meters)	60m	64,75m
Height (meters)	17m	17,05m
Engine	GEnx-1B/Trent 1000	Rolls-Royce Trent XWB

Table 2. Comparison between the main specifications of the Airbus A350-900 and the Boeing 787-9 [4] [5]

ANEX II

BASIC AERODYNAMIC CONCEPTS

BASIC CONCEPTS

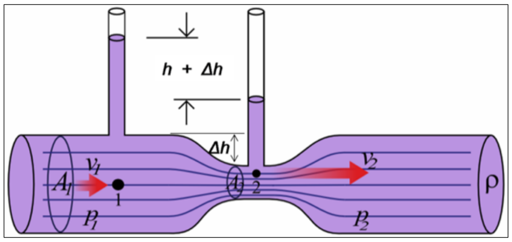

Figure 5. Duct with smaller cross-section at its middle part to explain Bernoulli's Principle [6]

The idea of designing a brand-new lifting system which would be able to substitute the horizontal stabilizer of an aircraft was initially though by being inspired by some of the aerodynamic systems which can be found on a formula 1 car. They way cars redirect the flow coming from the free stream was the main source of inspiration but, to understand the root of this lifting system, it would be necessary to get into the detail on three basic aerodynamic concepts.

LIFT AND DOWNFORCE

Formula 1 cars use the aerodynamics of the air coming to them with the purpose of reducing the drag as much as possible as well as generating a certain amount of downforce. Downforce can be defined as a lift force acting on a downwards direction; this aerodynamic feature allows the cars to go faster while maintaining a high level of grip. This downforce is obtained by deflecting the air downwards and so producing the named as downwash effect (the downwards deflection of an airflow) [29]; this is achieved by locating airfoils flipped with respect to the airfoils used for the aircraft in aviation (see figure 5 and 6).

As it can be appreciated, a simulation was done on Ansys with the same airfoil, on the left figure, the airfoil represented had a positive camber meaning that it would generate lift in upwards direction (it can be seen how the air is deflected downwards as well as having a differential of pressure between the upper and lower sides where the higher pressure is found at the lower side and lower pressure at the upper side), meanwhile, in the right figure, the airfoil represented had a negative camber meaning that it would generate lift in

downwards direction (it can be seen how the air is deflected upwards as well as having a differential of pressure between the upper and lower sides where the higher pressure is found at the upper side and lower pressure at the lower side).

VENTURI EFFECT

Having deflected the air downwards, Formula 1 cars redirect part of that deflected incoming flow through the lower part of the vehicle; this part is well known as flat bottom. This flat bottom is formed by several channels which use the venturi effect; this effect consists of a reduction of the cross-section area of a channel through which a fluid is flowing meaning that, the fluid will experience an increase in velocity due to the conservation of mass meanwhile the static pressure will decrease due to the Bernoulli's principle (see figure 4). Note that this principle is only applicable to incompressible fluids (not air), so they are only used to explain this effect. [30] [31]

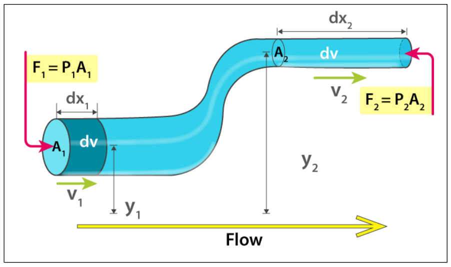

Figure 6. Duct with different cross-sectional areas in order to understand the Bernoulli's Principle [9]

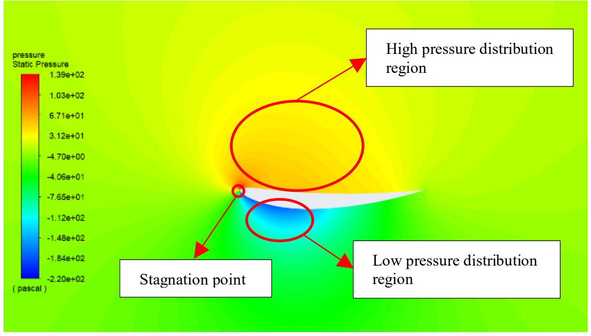

Figure 7. Airfoil simulation at Ansys fluent generating downforce [7]

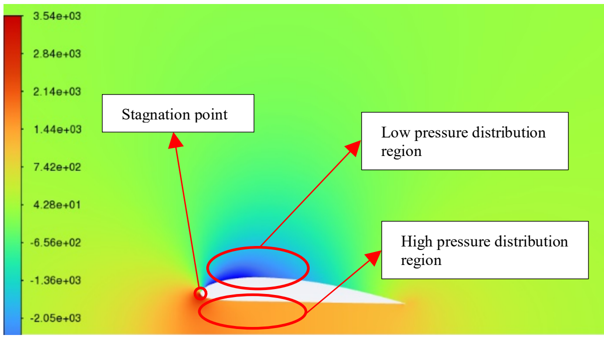

Figure 8. Airfoil simulation at Ansys Fluent generating lift [8]

As it can be seen in figure 8, by having in mind this venturi duct diagram, both the conservation of mass as well as the Bernoulli' principle can be easier explained. The blue lines crossing from one side of the duct to the other are representing the streamlines of the fluid; while the fluid is moving at the entrance and the end of the duct (where the cross-sectional is bigger), the streamlines are separated meaning that the flow would be moving slowly. [30] [31]

On the other hand, at the central part of the duct, where the cross-sectional area gets smaller, it can be appreciated how the streamlines start concentrating meaning that at that region, the velocity of the fluid would have increased. This explains the mass conservation equation which was previously represented since, at ideal conditions, the mass of fluid entering the duct would be the same that the mass coming out of the duct; parallel to this, the Bernoulli principle also explains that in the regimes where the fluid is moving slower, the pressure would be higher that on the regimes where the fluid has higher kinetic energy but, as Bernoulli is only applicable for inviscid and incompressible fluids among other wide range of assumptions, it would not be really useful to explain how the lifting system would work. For a better comprehension of both, the Bernoulli and mass conservation principles, they would be derived as it can be appreciated just below: [30] [31]

- **Bernoulli Principle:**

Assume the fluid to be incompressible, frictionless, and inviscid; having in mind these assumptions the Bernoulli principle could be demonstrated: [30] [31]

Due to the assumptions made, the energy associated to the fluid will be conserved:

$$\mathrm{Work} = \mathrm{Force} * \mathrm{Displacement}$$

$$\mathrm{dW} = \mathrm{F_1 dx_1} - \mathrm{F_2 dx_2} = \mathrm{P_1 A_1 dx_1} - \mathrm{P_2 A_2 dx_2} = \mathrm{P_1 dV} - \mathrm{P_2 dV} = (\mathrm{P_1} - \mathrm{P_2})dV$$

Since the fluid will also have kinetic energy due to its movement:

$$\mathrm{Kinetic\ Energy} = \frac{1}{2}\mathrm{m_2}v_2^2 - \frac{1}{2}\mathrm{m_1}v_1^2 = \frac{1}{2}\rho dV(v_2^2 - v_1^2)$$

$$\mathrm{Potential\ Energy} = m_2 g h_2 - m_1 g h_1 = \mathrm{g}\rho dV(h_2 - h_1)$$

$$\mathrm{Energy} = \mathrm{Kinetic\ Energy} + \mathrm{Potential\ Energy}$$

$$(\mathrm{P_1} - \mathrm{P_2})dV = \frac{1}{2}\rho dV(v_2^2 - v_1^2) + \mathrm{g}\rho dV(h_2 - h_1)$$

$$\mathbf{P_1} + \frac{\mathbf{1}}{\mathbf{2}}\boldsymbol{\rho v_1^2} + \boldsymbol{g\rho h_1} = \mathbf{P_2} + \frac{\mathbf{1}}{\mathbf{2}}\boldsymbol{\rho v_2^2} + \boldsymbol{g\rho h_2}$$

- **Mass conservation principle:**

The conservation of mass principle stands that for a given control volume, the mass of fluid entering that volume would be the same as the mass of the fluid going out of the control volume. [32] [33]

$$\mathrm{m}_1\,(Inlet) = \mathrm{V}_1 * \rho_1 \qquad \mathrm{m}_2\,(Outlet) = \mathrm{V}_2 * \rho_2$$

Due to the mass conservation principle, the inlet and outlet mass must be equal so:

$$\mathrm{m}_1\,(Inlet) = \mathrm{m}_2\,(Outlet)$$

$$\mathbf{V_1 * \rho_1 = V_2 * \rho_2}$$

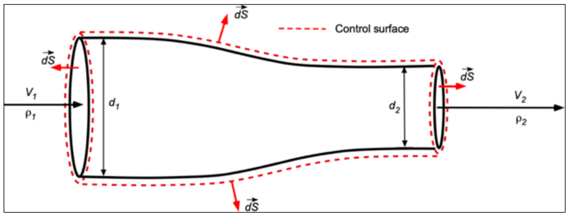

Figure 9. Duct with different cross-sectional area to understand the Mass Conservation Principle [10]

DRAG REDUCTION SYSTEM (DRS)

This system is the last one between the car and the free stream; it is located at the rear wing of the formula 1 cars and its main intention is to reduce the drag while the car doesn't need to generate large amounts of downforce (see figure 10 and figure 11). This mechanism opens the rear wing and creates an empty space by which the air goes through and so exponentially reducing the overall drag. In the same way formula 1 cars accelerate the airflow using venturi channels, the lifting system was designed to use this type of channels to direct the incoming airflow in order to generate lift of downforce depending on each situation. Also, a similar system to the drag reduction system was implemented in the design so that while flying in cruise the drag could be lowered by only having some movable surfaces similar to the technology just mentioned. [34]

Figure 10. Red Bull Racing F1 car's rear wing with the DRS system open [11]

Figure 11. Red Bull Racing F1 car's rear wing with the DRS system closed [12]

ANEX III

ORIGINAL DIMENSIONS OF THE BOEING 787-9

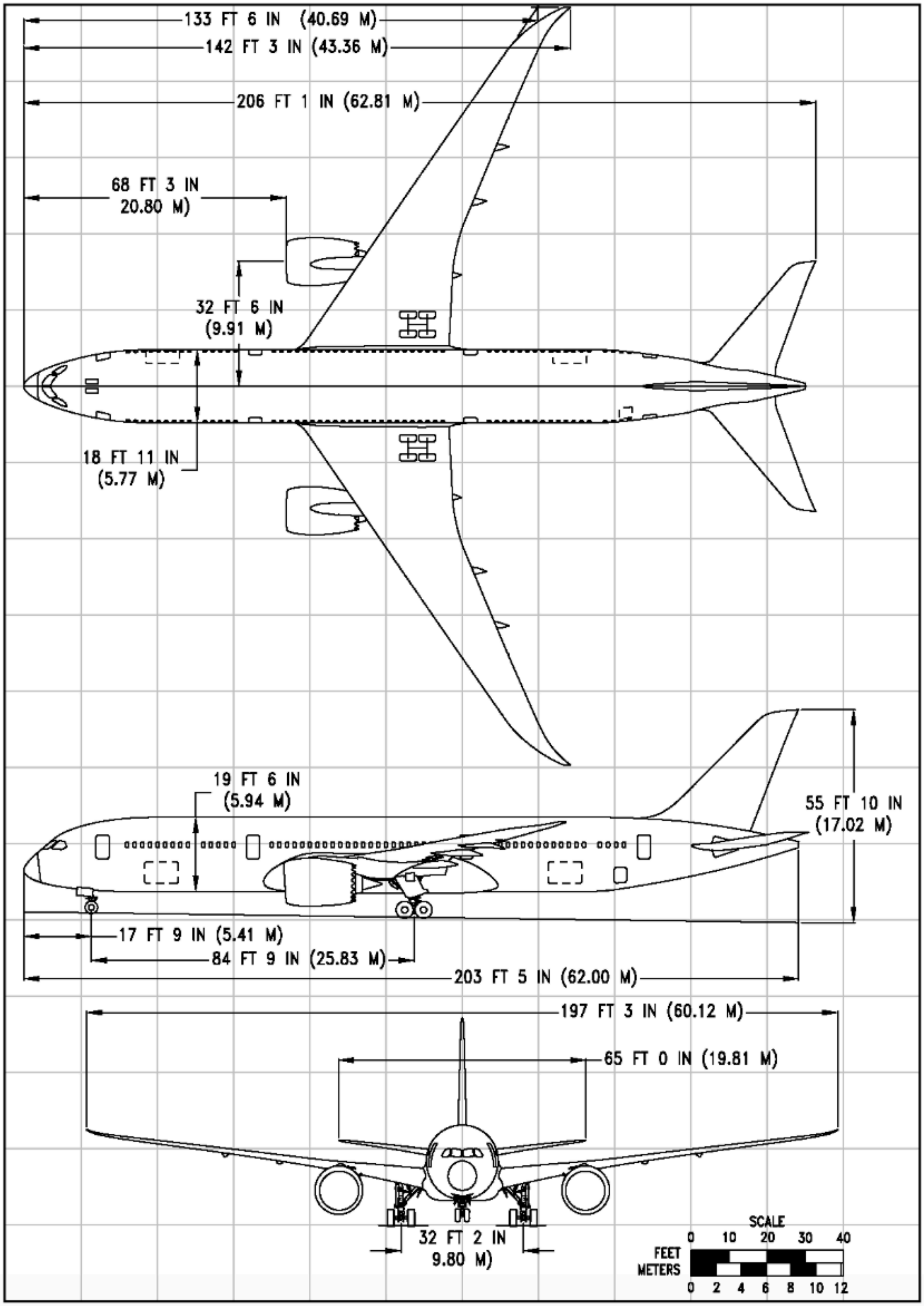
133 FT 6 IN (40.69 M)
142 FT 3 IN (43.36 M)
206 FT 1 IN (62.81 M)
68 FT 3 IN
20.80 M)
32 FT 6 IN
(9.91 M)
18 FT 11 IN
(5.77 M)
19 FT 6 IN
(5.94 M)
55 FT 10 IN
(17.02 M)
17 FT 9 IN (5.41 M)
84 FT 9 IN (25.83 M)
203 FT 5 IN (62.00 M)
197 FT 3 IN (60.12 M)
65 FT 0 IN (19.81 M)
32 FT 2 IN
9.80 M)
SCALE
FEET
METERS
0
10
20
30
40
0
2
4
6
8
10
12

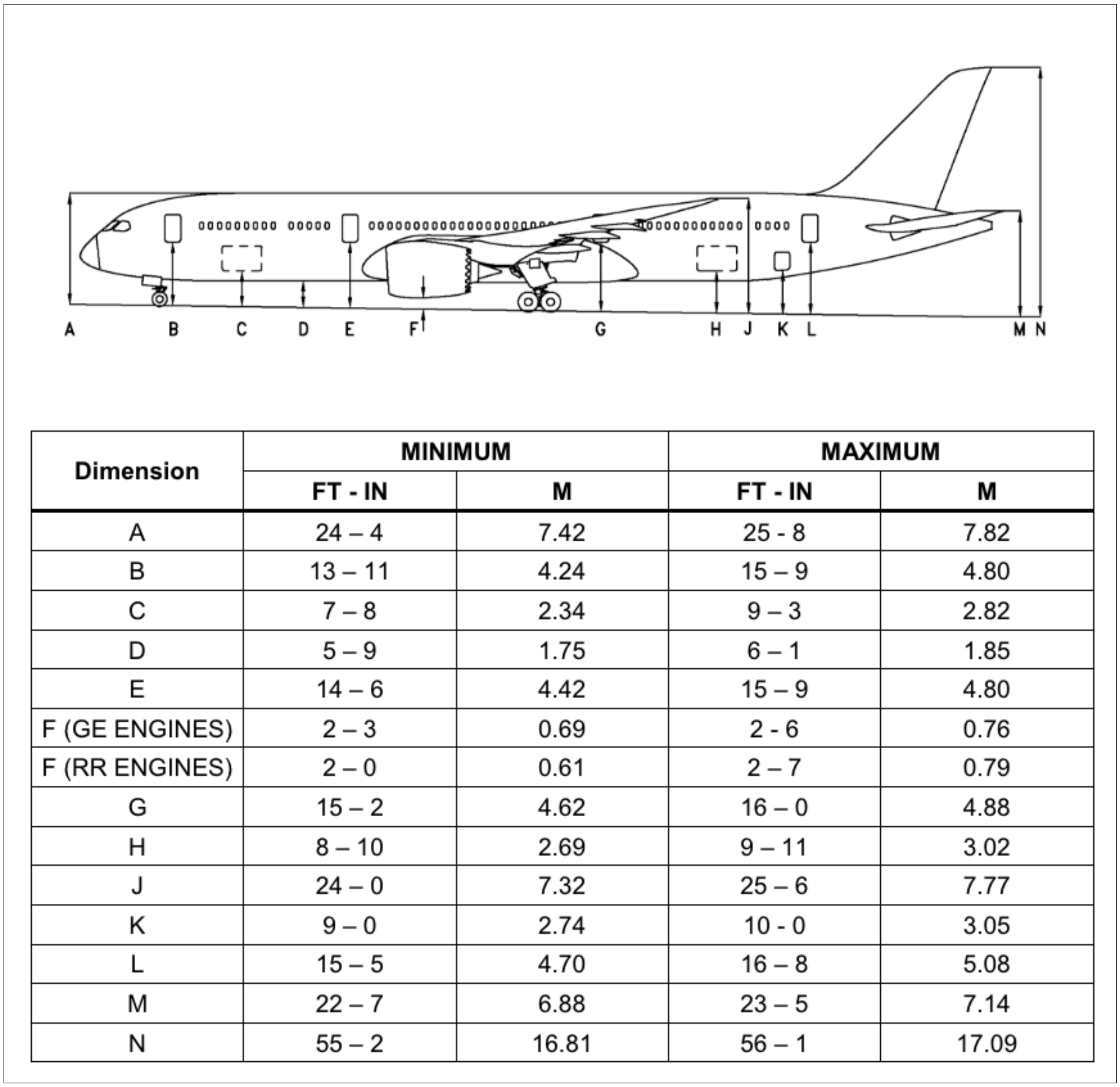

Dimension	MINIMUM		MAXIMUM	
	FT - IN	M	FT - IN	M
A	24 – 4	7.42	25 - 8	7.82
B	13 – 11	4.24	15 – 9	4.80
C	7 – 8	2.34	9 – 3	2.82
D	5 – 9	1.75	6 – 1	1.85
E	14 – 6	4.42	15 – 9	4.80
F (GE ENGINES)	2 – 3	0.69	2 - 6	0.76
F (RR ENGINES)	2 – 0	0.61	2 – 7	0.79
G	15 – 2	4.62	16 – 0	4.88
H	8 – 10	2.69	9 – 11	3.02
J	24 – 0	7.32	25 – 6	7.77
K	9 – 0	2.74	10 - 0	3.05
L	15 – 5	4.70	16 – 8	5.08
M	22 – 7	6.88	23 – 5	7.14
N	55 – 2	16.81	56 – 1	17.09

ANEX IV

ENGINEERING PLANS OF BOEING 787-9 WITH LIFTING SYSTEM CONFIGURATION

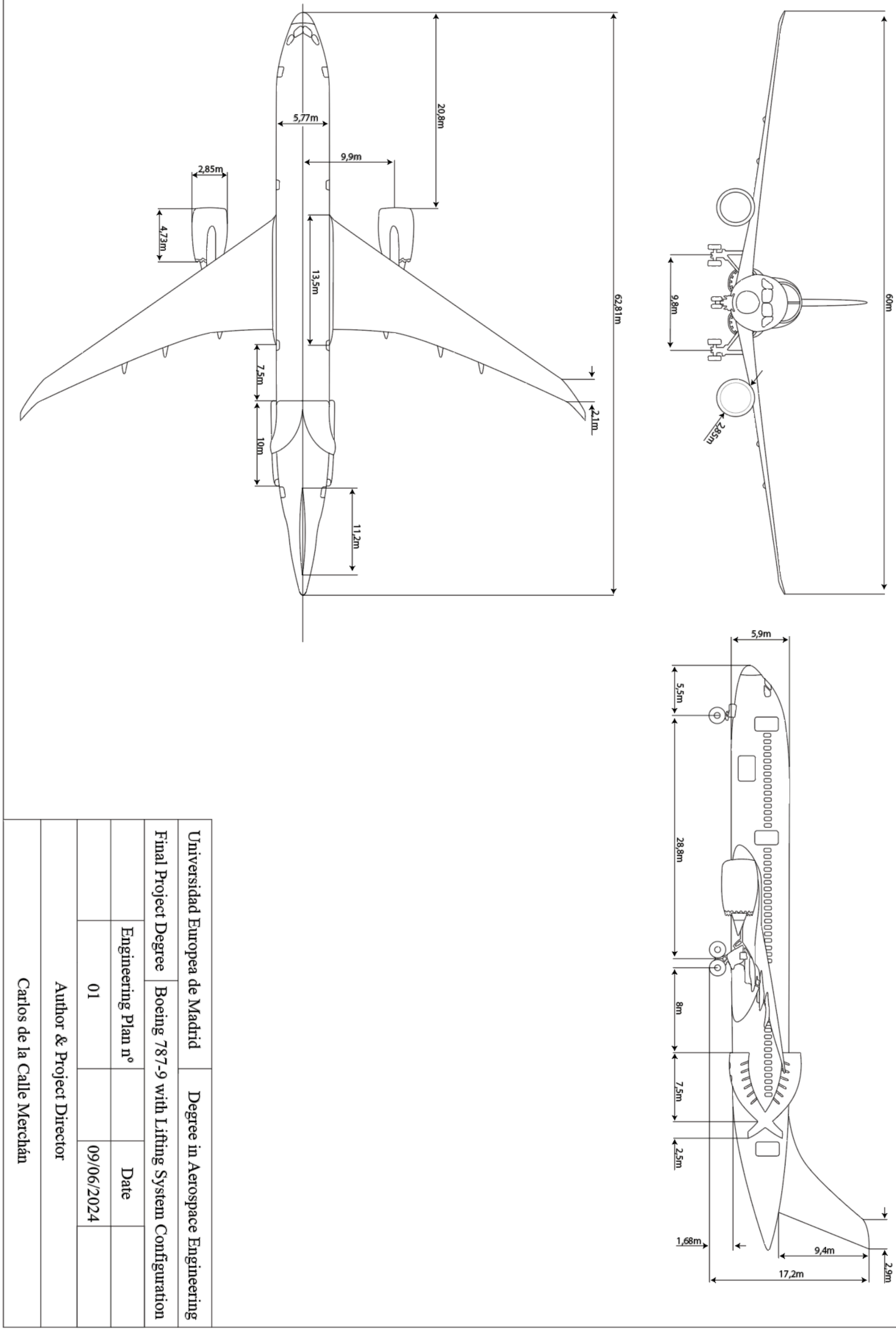

Universidad Europea de Madrid	Degree in Aerospace Engineering
Final Project Degree	Boeing 787-9 with Lifting System Configuration
Engineering Plan nº	Date
01	09/06/2024
Author & Project Director	
Carlos de la Calle Merchán	

ANEX V

ENGINEERING PLANS OF BOEING 787-9 WITH PROPFAN CONFIGURATION

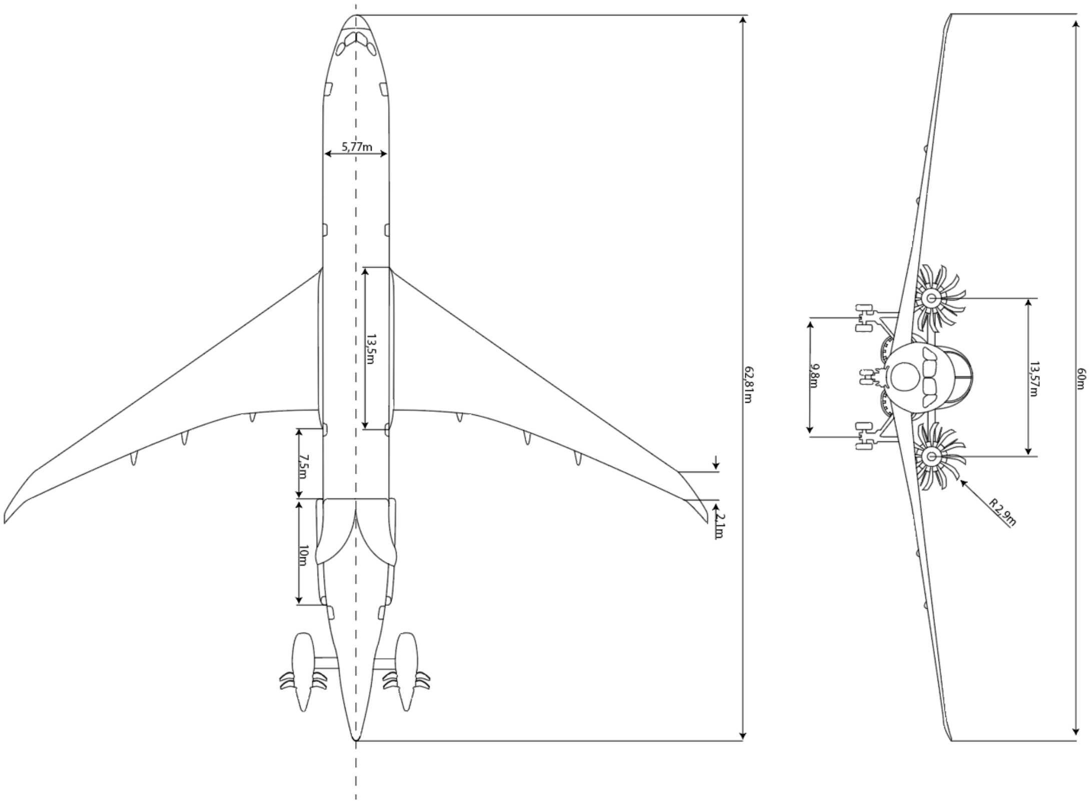

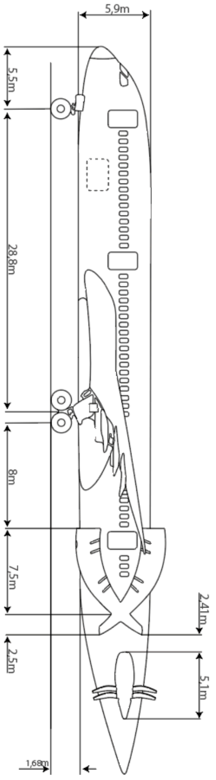

Universidad Europea de Madrid	Degree in Aerospace Engineering
Final Project Degree	Boeing 787-9 with Propofan Configuration
Engineering Plan nº	Date
02	09/06/2024
Author & Project Director	
Carlos de la Calle Merchán	

ANEX VI

CATIA THREE-DIMENSIONAL MODEL

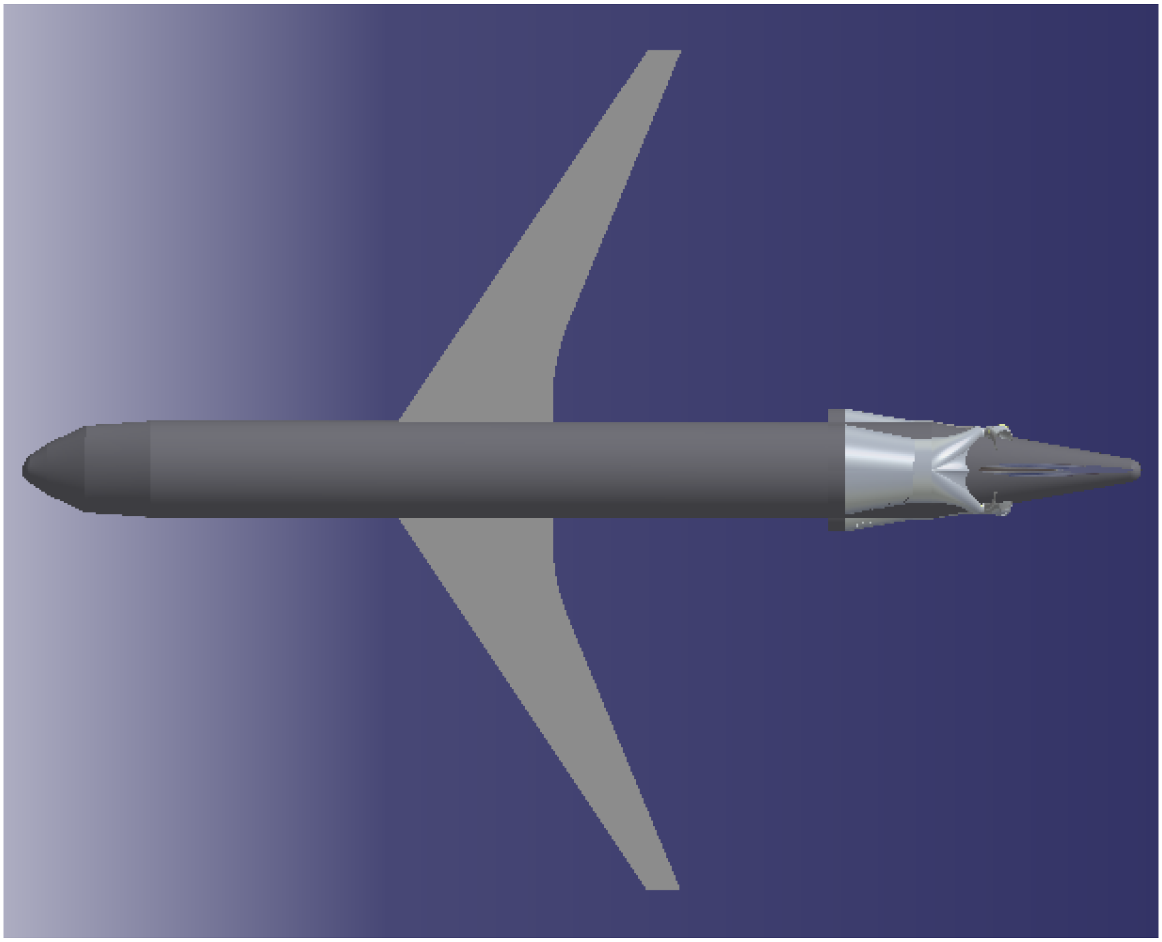

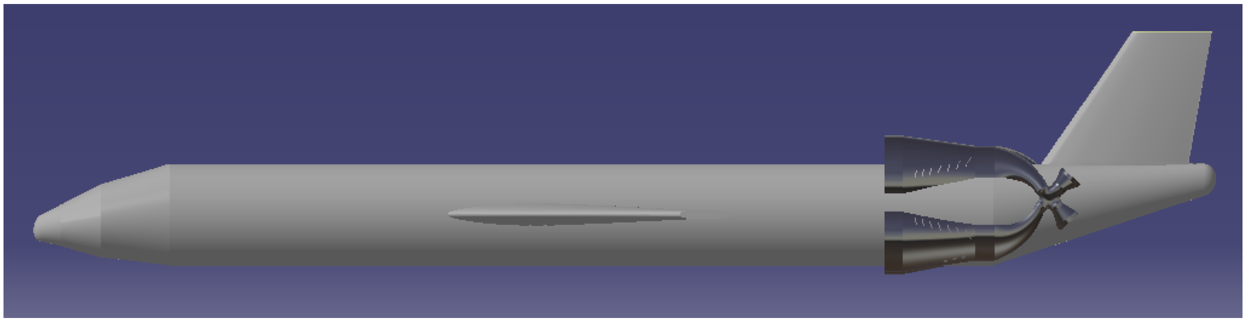

ANEX VII

AUTODESK INVENTOR THREE-DIMENSIONAL MODEL

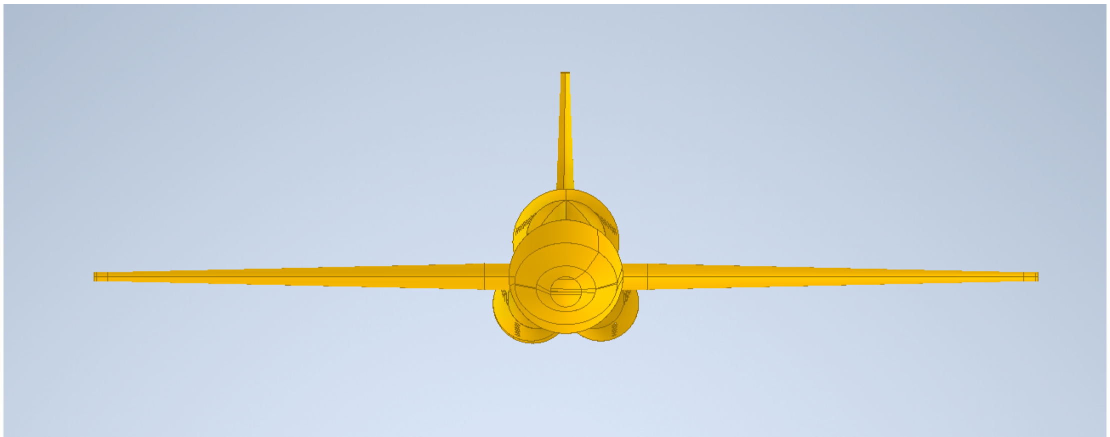

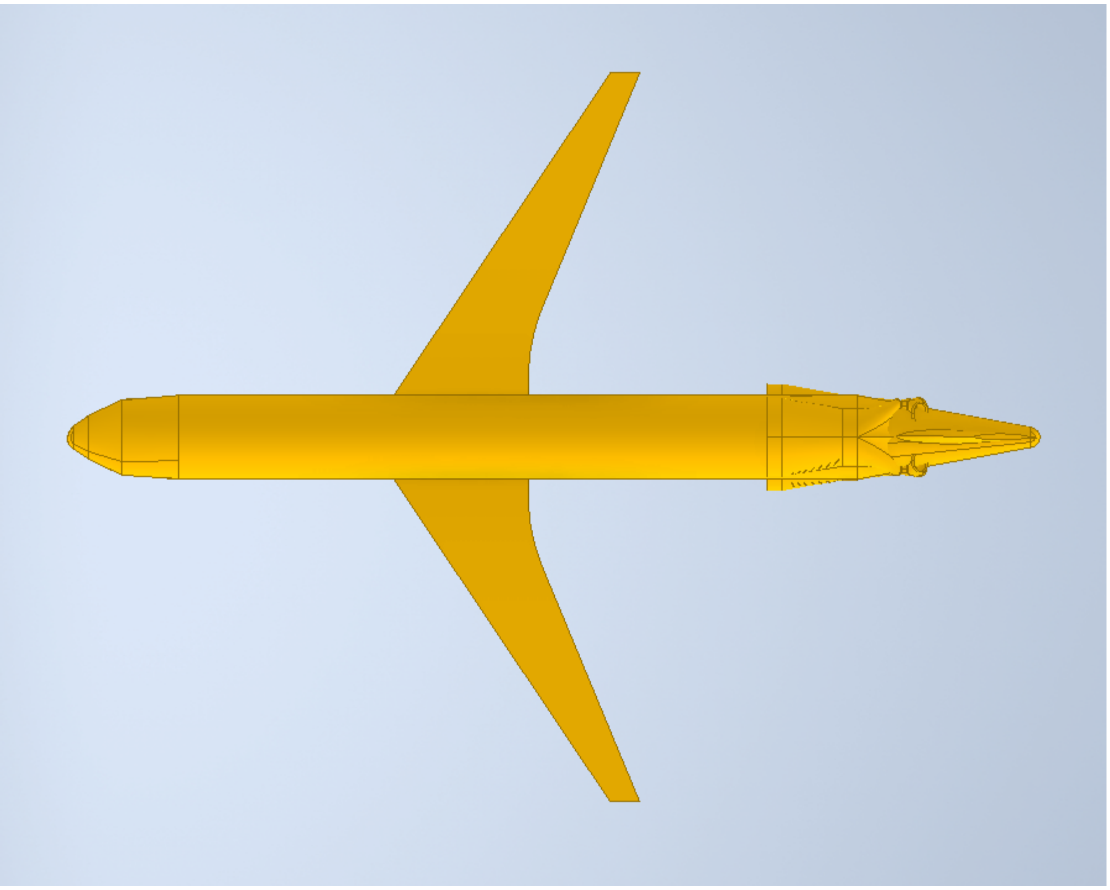

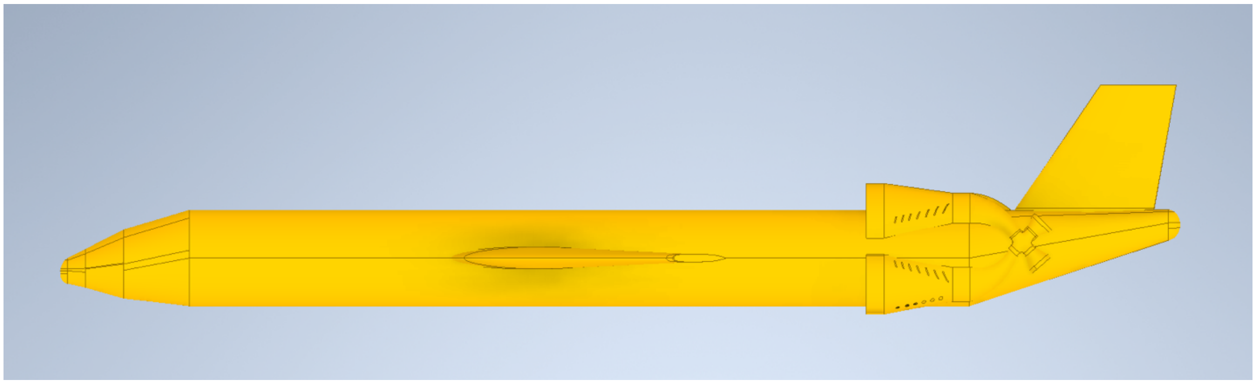

ANEX VIII

UPPER VIEW PLANE CUT LOCATIONS

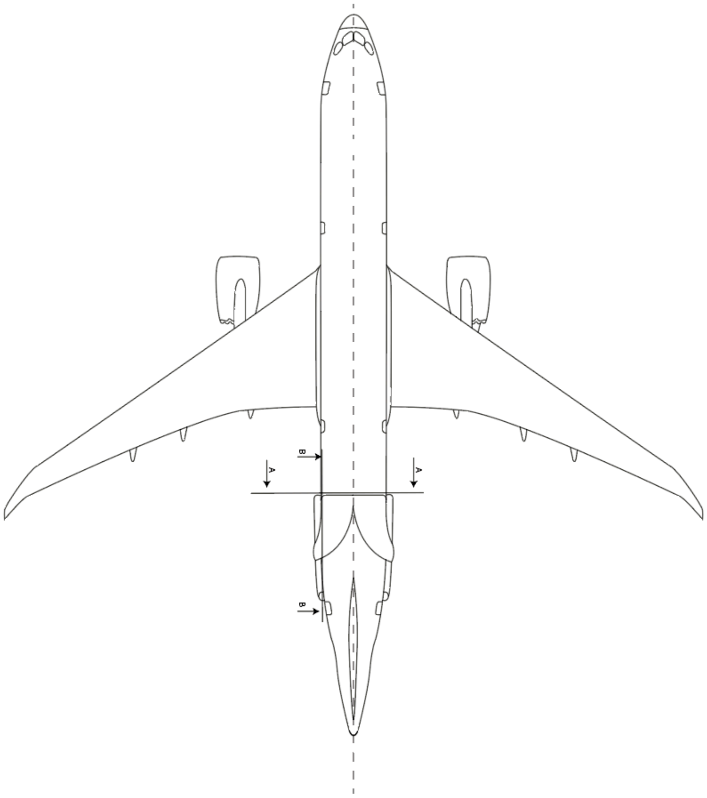

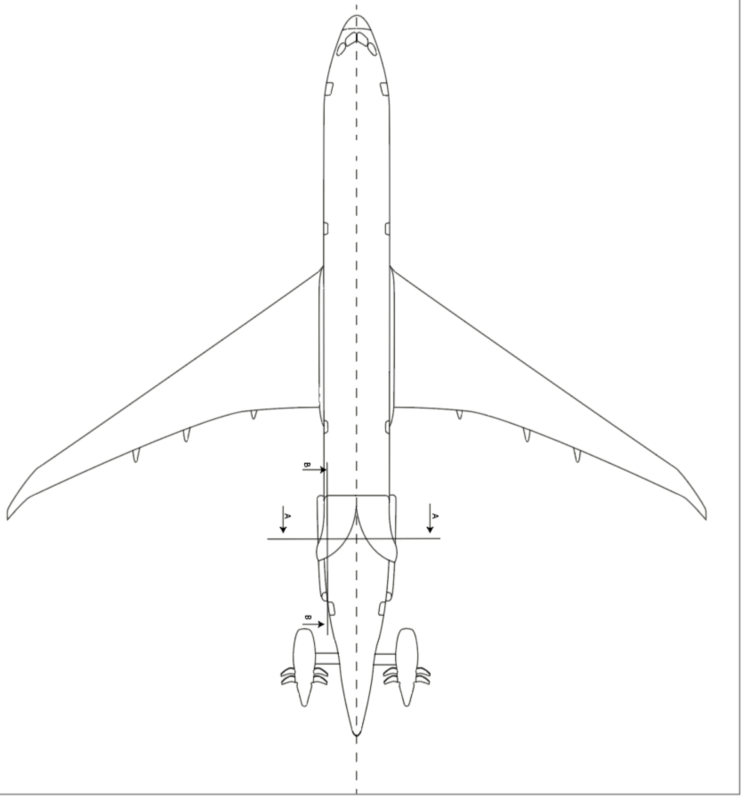

Universidad Europea de Madrid		Degree in Aerospace Engineering	
Final Project Degree		Boeing 787-9 cut plans location	
Engineering Plan nº		Date	
03		09/06/2024	
Author & Project Director			
Carlos de la Calle Merchán			

ANEX IX

BOEING 787-9 WITH CONVENTIONAL CONFIGURATION (INCLUDING THE HORIZONTAL STABILIZER) AT CRUISE

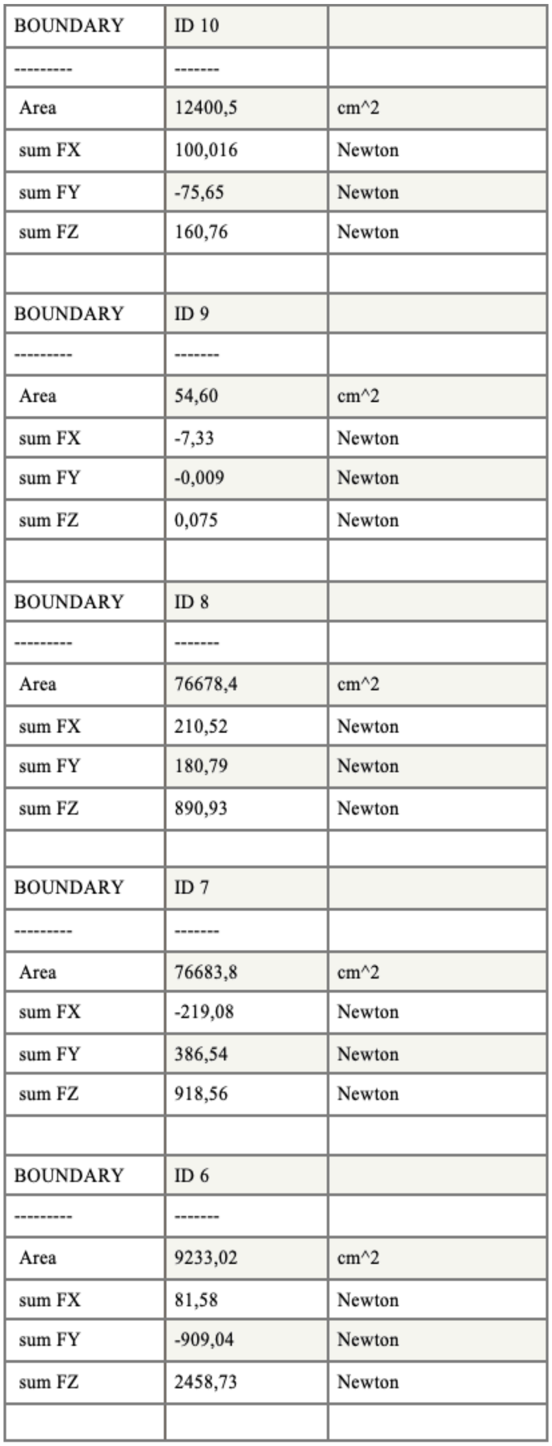

BOUNDARY	ID 10	
---------	-------	
Area	12400,5	cm^2
sum FX	100,016	Newton
sum FY	-75,65	Newton
sum FZ	160,76	Newton
BOUNDARY	ID 9	
---------	-------	
Area	54,60	cm^2
sum FX	-7,33	Newton
sum FY	-0,009	Newton
sum FZ	0,075	Newton
BOUNDARY	ID 8	
---------	-------	
Area	76678,4	cm^2
sum FX	210,52	Newton
sum FY	180,79	Newton
sum FZ	890,93	Newton
BOUNDARY	ID 7	
---------	-------	
Area	76683,8	cm^2
sum FX	-219,08	Newton
sum FY	386,54	Newton
sum FZ	918,56	Newton
BOUNDARY	ID 6	
---------	-------	
Area	9233,02	cm^2
sum FX	81,58	Newton
sum FY	-909,04	Newton
sum FZ	2458,73	Newton

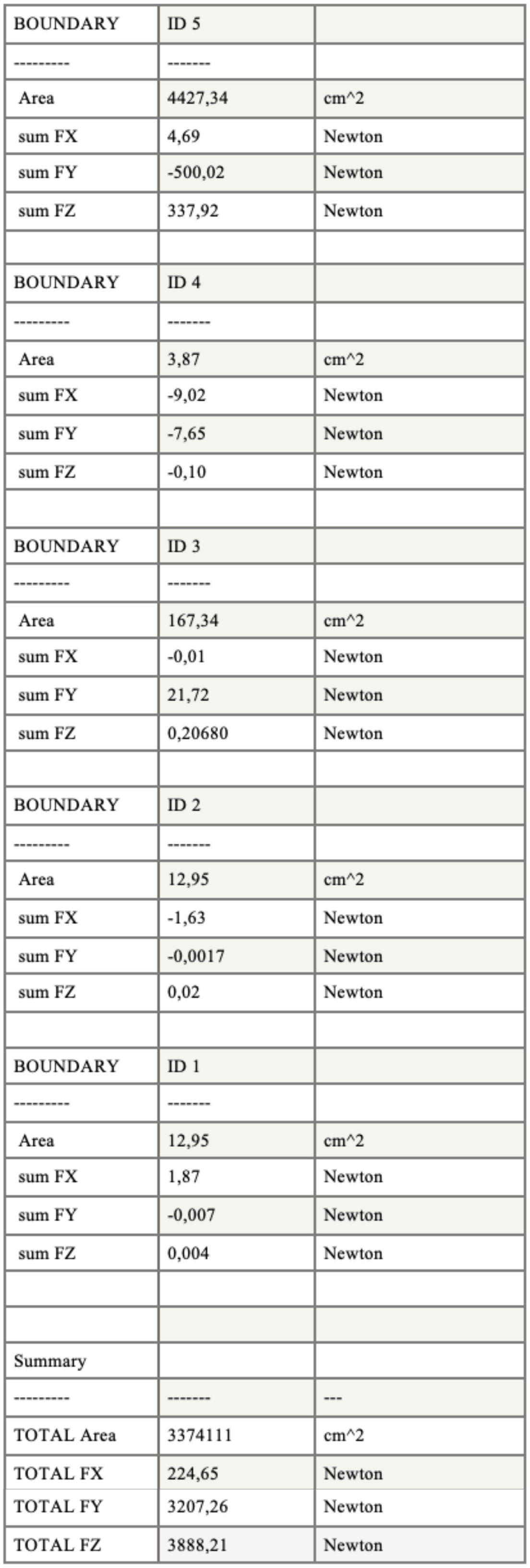

BOUNDARY	ID 5	
---------	-------	
Area	4427,34	cm^2
sum FX	4,69	Newton
sum FY	-500,02	Newton
sum FZ	337,92	Newton
BOUNDARY	ID 4	
---------	-------	
Area	3,87	cm^2
sum FX	-9,02	Newton
sum FY	-7,65	Newton
sum FZ	-0,10	Newton
BOUNDARY	ID 3	
---------	-------	
Area	167,34	cm^2
sum FX	-0,01	Newton
sum FY	21,72	Newton
sum FZ	0,20680	Newton
BOUNDARY	ID 2	
---------	-------	
Area	12,95	cm^2
sum FX	-1,63	Newton
sum FY	-0,0017	Newton
sum FZ	0,02	Newton
BOUNDARY	ID 1	
---------	-------	
Area	12,95	cm^2
sum FX	1,87	Newton
sum FY	-0,007	Newton
sum FZ	0,004	Newton
Summary		
---------	-------	---
TOTAL Area	3374111	cm^2
TOTAL FX	224,65	Newton
TOTAL FY	3207,26	Newton
TOTAL FZ	3888,21	Newton

ANEX X

BOEING 787-9 WITH LIFTING SYSTEM AT CRUISE

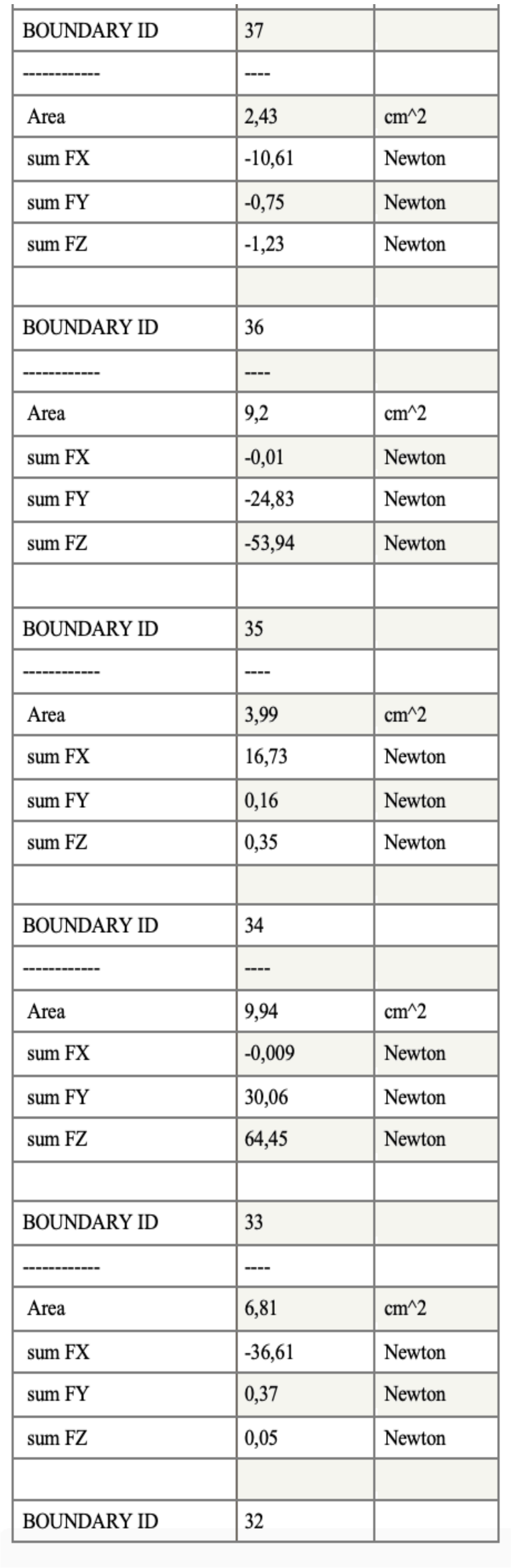

BOUNDARY ID	37	
------------	----	
Area	2,43	cm^2
sum FX	-10,61	Newton
sum FY	-0,75	Newton
sum FZ	-1,23	Newton
BOUNDARY ID	36	
------------	----	
Area	9,2	cm^2
sum FX	-0,01	Newton
sum FY	-24,83	Newton
sum FZ	-53,94	Newton
BOUNDARY ID	35	
------------	----	
Area	3,99	cm^2
sum FX	16,73	Newton
sum FY	0,16	Newton
sum FZ	0,35	Newton
BOUNDARY ID	34	
------------	----	
Area	9,94	cm^2
sum FX	-0,009	Newton
sum FY	30,06	Newton
sum FZ	64,45	Newton
BOUNDARY ID	33	
------------	----	
Area	6,81	cm^2
sum FX	-36,61	Newton
sum FY	0,37	Newton
sum FZ	0,05	Newton
BOUNDARY ID	32	

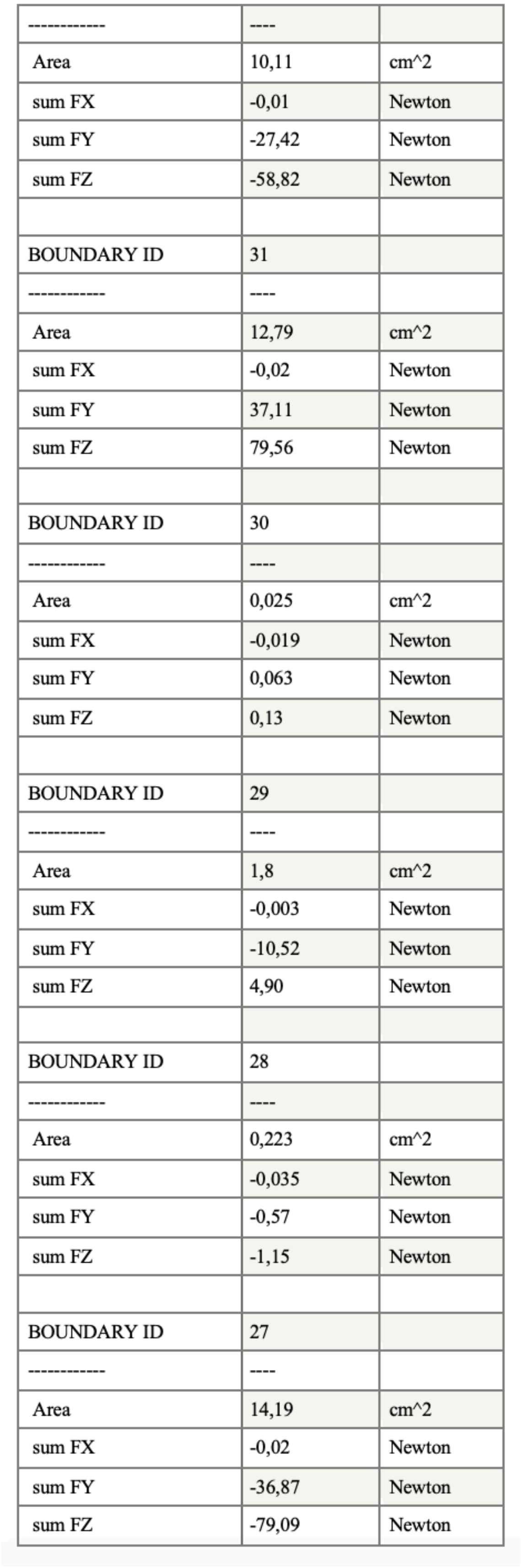

------------	----	
Area	10,11	cm^2
sum FX	-0,01	Newton
sum FY	-27,42	Newton
sum FZ	-58,82	Newton
BOUNDARY ID	31	
------------	----	
Area	12,79	cm^2
sum FX	-0,02	Newton
sum FY	37,11	Newton
sum FZ	79,56	Newton
BOUNDARY ID	30	
------------	----	
Area	0,025	cm^2
sum FX	-0,019	Newton
sum FY	0,063	Newton
sum FZ	0,13	Newton
BOUNDARY ID	29	
------------	----	
Area	1,8	cm^2
sum FX	-0,003	Newton
sum FY	-10,52	Newton
sum FZ	4,90	Newton
BOUNDARY ID	28	
------------	----	
Area	0,223	cm^2
sum FX	-0,035	Newton
sum FY	-0,57	Newton
sum FZ	-1,15	Newton
BOUNDARY ID	27	
------------	----	
Area	14,19	cm^2
sum FX	-0,02	Newton
sum FY	-36,87	Newton
sum FZ	-79,09	Newton

BOUNDARY ID	26	
------------	----	
Area	4,57	cm^2
sum FX	18,47	Newton
sum FY	0,26	Newton
sum FZ	0,42	Newton
BOUNDARY ID	25	
------------	----	
Area	18,49	cm^2
sum FX	-0,017	Newton
sum FY	56,76	Newton
sum FZ	121,75	Newton
BOUNDARY ID	24	
------------	----	
Area	6,26	cm^2
sum FX	-30,75	Newton
sum FY	-1,04	Newton
sum FZ	-1,78	Newton
BOUNDARY ID	23	
------------	----	
Area	19,39	cm^2
sum FX	-0,01	Newton
sum FY	-54,55	Newton
sum FZ	-117,9	Newton
BOUNDARY ID	22	
------------	----	
Area	4,96	cm^2
sum FX	19,83	Newton
sum FY	0,21	Newton
sum FZ	0,41	Newton
BOUNDARY ID	21	
------------	----	
Area	22,61	cm^2
sum FX	-0,18	Newton
sum FY	70,46	Newton
sum FZ	151,1	Newton
BOUNDARY ID	20	
------------	----	
Area	12,08	cm^2
sum FX	-62,74	Newton
sum FY	-1,74	Newton
sum FZ	-1,92	Newton
BOUNDARY ID	19	
------------	----	
Area	23,88	cm^2
sum FX	-0,11	Newton
sum FY	-68,95	Newton
sum FZ	-147,98	Newton
BOUNDARY ID	18	
------------	----	
Area	5,34	cm^2
sum FX	21,12	Newton
sum FY	0,21	Newton
sum FZ	0,449	Newton
BOUNDARY ID	17	
------------	----	
Area	2,01	cm^2
sum FX	0,93	Newton
sum FY	0,056	Newton
sum FZ	-0,15	Newton
BOUNDARY ID	16	
------------	----	cm^2
Area	2,98	Newton
sum FX	0,93	Newton
sum FY	0,055	Newton
sum FZ	-0,15	
BOUNDARY ID	15	
------------	----	

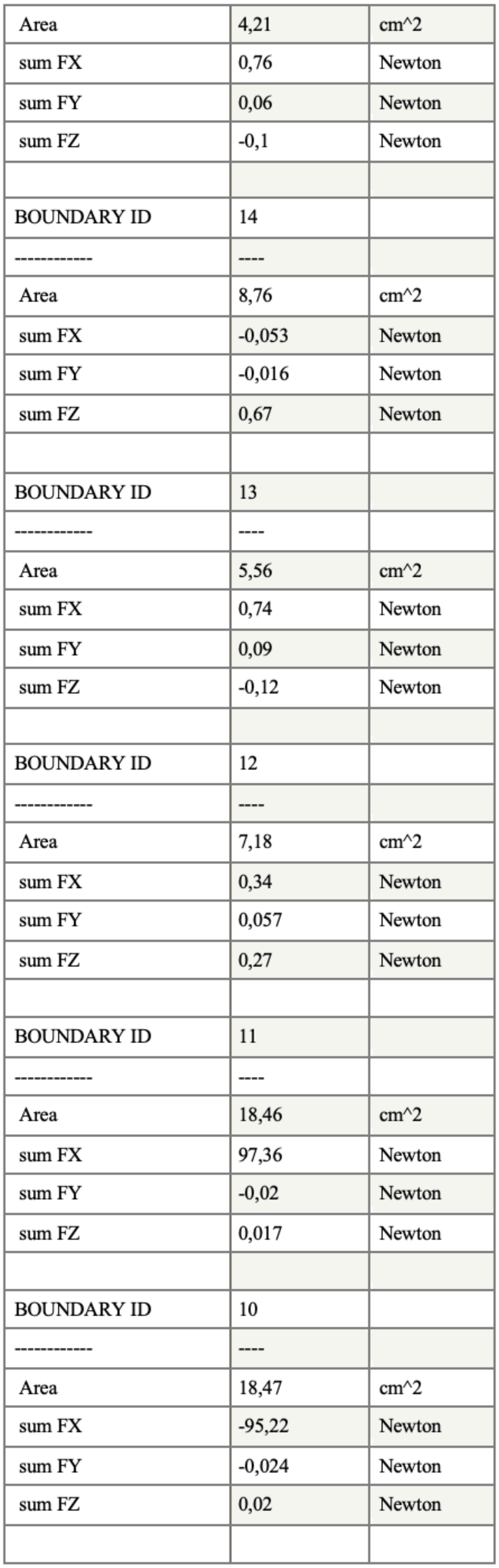

Area	4,21	cm^2
sum FX	0,76	Newton
sum FY	0,06	Newton
sum FZ	-0,1	Newton
BOUNDARY ID	14	
------------	----	
Area	8,76	cm^2
sum FX	-0,053	Newton
sum FY	-0,016	Newton
sum FZ	0,67	Newton
BOUNDARY ID	13	
------------	----	
Area	5,56	cm^2
sum FX	0,74	Newton
sum FY	0,09	Newton
sum FZ	-0,12	Newton
BOUNDARY ID	12	
------------	----	
Area	7,18	cm^2
sum FX	0,34	Newton
sum FY	0,057	Newton
sum FZ	0,27	Newton
BOUNDARY ID	11	
------------	----	
Area	18,46	cm^2
sum FX	97,36	Newton
sum FY	-0,02	Newton
sum FZ	0,017	Newton
BOUNDARY ID	10	
------------	----	
Area	18,47	cm^2
sum FX	-95,22	Newton
sum FY	-0,024	Newton
sum FZ	0,02	Newton

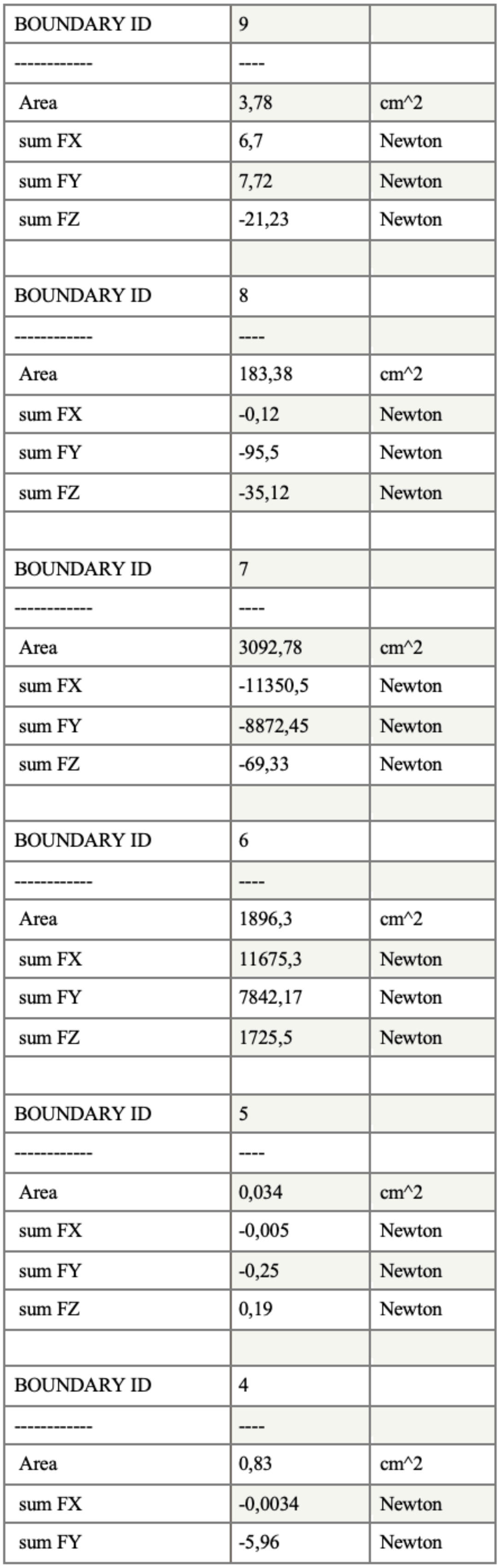

BOUNDARY ID	9	
------------	----	
Area	3,78	cm^2
sum FX	6,7	Newton
sum FY	7,72	Newton
sum FZ	-21,23	Newton
BOUNDARY ID	8	
------------	----	
Area	183,38	cm^2
sum FX	-0,12	Newton
sum FY	-95,5	Newton
sum FZ	-35,12	Newton
BOUNDARY ID	7	
------------	----	
Area	3092,78	cm^2
sum FX	-11350,5	Newton
sum FY	-8872,45	Newton
sum FZ	-69,33	Newton
BOUNDARY ID	6	
------------	----	
Area	1896,3	cm^2
sum FX	11675,3	Newton
sum FY	7842,17	Newton
sum FZ	1725,5	Newton
BOUNDARY ID	5	
------------	----	
Area	0,034	cm^2
sum FX	-0,005	Newton
sum FY	-0,25	Newton
sum FZ	0,19	Newton
BOUNDARY ID	4	
------------	----	
Area	0,83	cm^2
sum FX	-0,0034	Newton
sum FY	-5,96	Newton

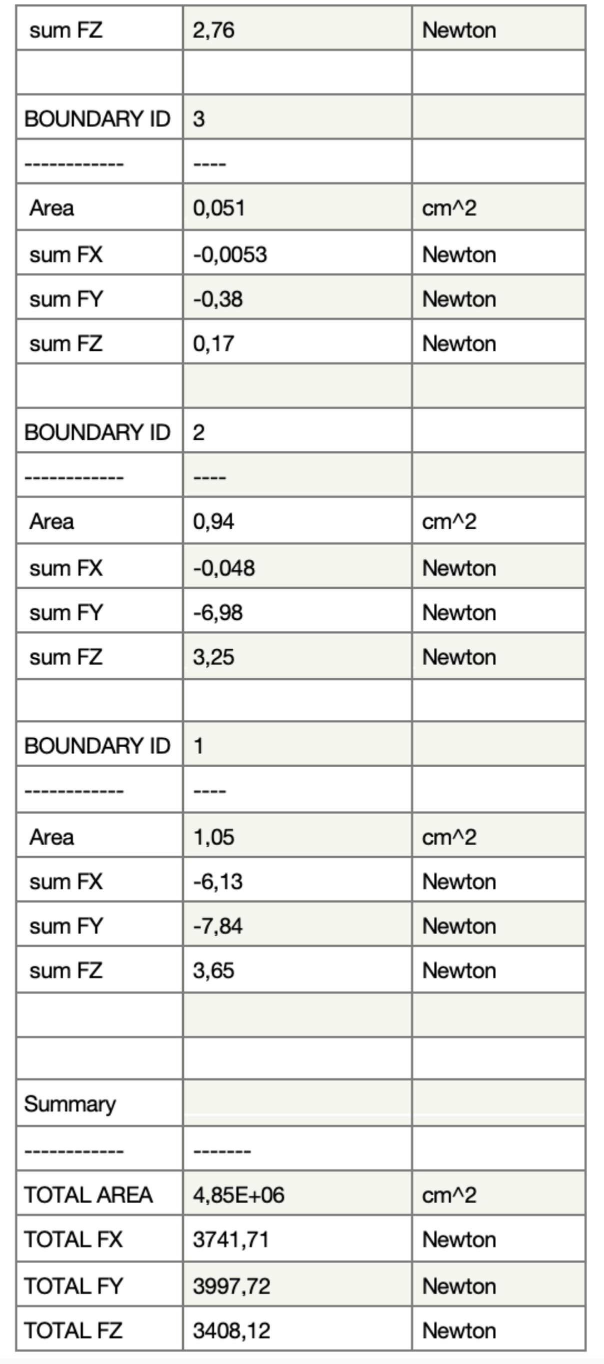

sum FZ	2,76	Newton
BOUNDARY ID	3	
------------	----	
Area	0,051	cm^2
sum FX	-0,0053	Newton
sum FY	-0,38	Newton
sum FZ	0,17	Newton
BOUNDARY ID	2	
------------	----	
Area	0,94	cm^2
sum FX	-0,048	Newton
sum FY	-6,98	Newton
sum FZ	3,25	Newton
BOUNDARY ID	1	
------------	----	
Area	1,05	cm^2
sum FX	-6,13	Newton
sum FY	-7,84	Newton
sum FZ	3,65	Newton
Summary		
------------	-------	
TOTAL AREA	4,85E+06	cm^2
TOTAL FX	3741,71	Newton
TOTAL FY	3997,72	Newton
TOTAL FZ	3408,12	Newton

ANEX XI

BOEING 787-9 WITH LIFTING SYSTEM CONFIGURATION GENERTING LIFT AT CRUISE

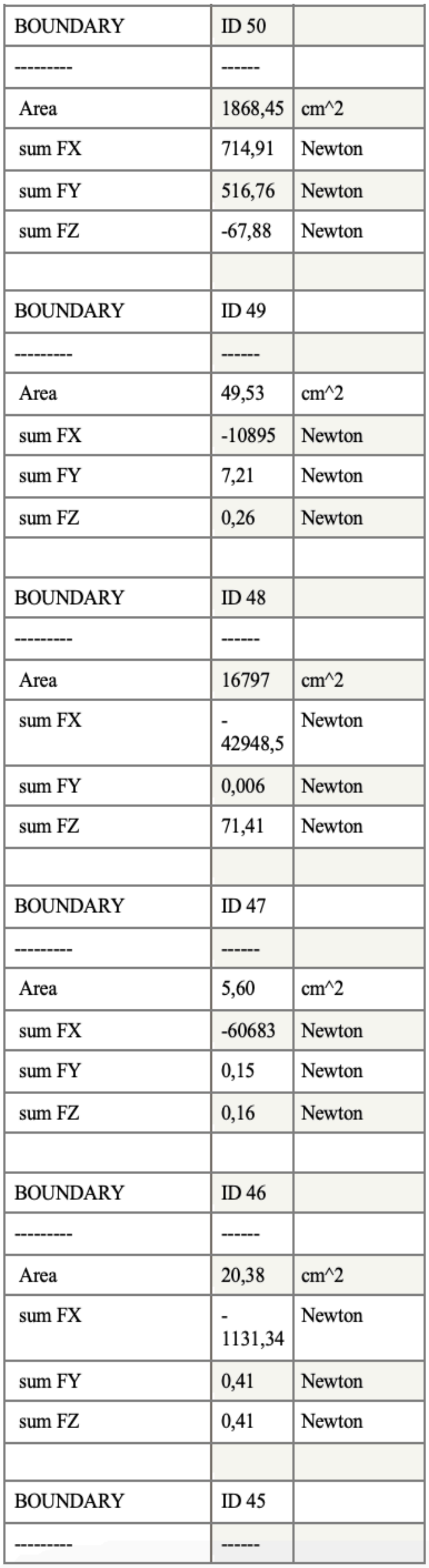

BOUNDARY	ID 50	
---------	------	
Area	1868,45	cm^2
sum FX	714,91	Newton
sum FY	516,76	Newton
sum FZ	-67,88	Newton
BOUNDARY	ID 49	
---------	------	
Area	49,53	cm^2
sum FX	-10895	Newton
sum FY	7,21	Newton
sum FZ	0,26	Newton
BOUNDARY	ID 48	
---------	------	
Area	16797	cm^2
sum FX	-42948,5	Newton
sum FY	0,006	Newton
sum FZ	71,41	Newton
BOUNDARY	ID 47	
---------	------	
Area	5,60	cm^2
sum FX	-60683	Newton
sum FY	0,15	Newton
sum FZ	0,16	Newton
BOUNDARY	ID 46	
---------	------	
Area	20,38	cm^2
sum FX	-1131,34	Newton
sum FY	0,41	Newton
sum FZ	0,41	Newton
BOUNDARY	ID 45	
---------	------	

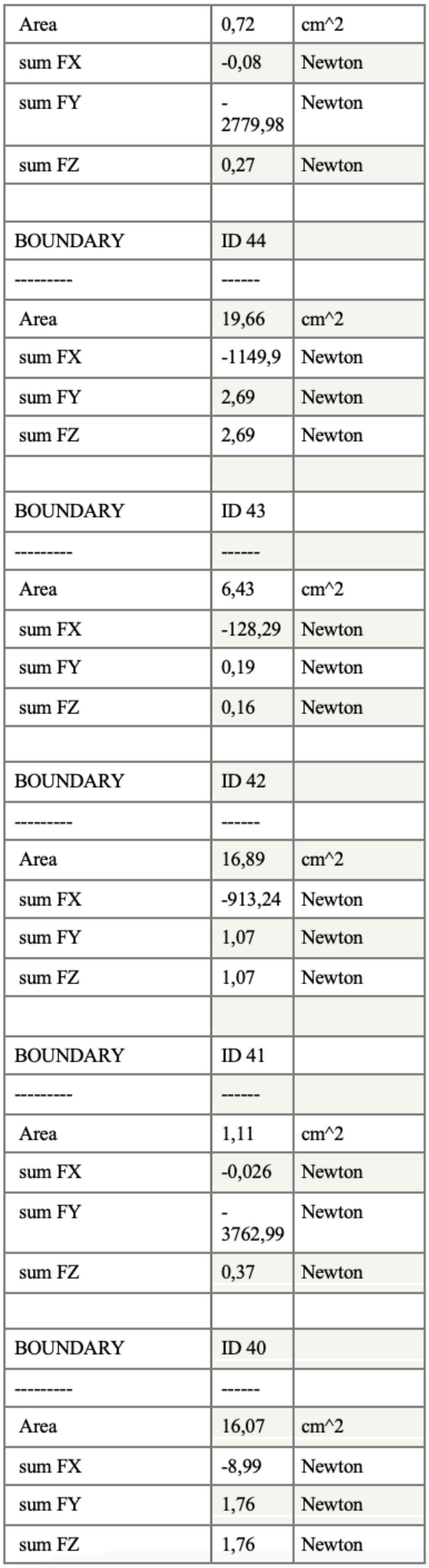

Area	0,72	cm^2
sum FX	-0,08	Newton
sum FY	-2779,98	Newton
sum FZ	0,27	Newton
BOUNDARY	ID 44	
---------	------	
Area	19,66	cm^2
sum FX	-1149,9	Newton
sum FY	2,69	Newton
sum FZ	2,69	Newton
BOUNDARY	ID 43	
---------	------	
Area	6,43	cm^2
sum FX	-128,29	Newton
sum FY	0,19	Newton
sum FZ	0,16	Newton
BOUNDARY	ID 42	
---------	------	
Area	16,89	cm^2
sum FX	-913,24	Newton
sum FY	1,07	Newton
sum FZ	1,07	Newton
BOUNDARY	ID 41	
---------	------	
Area	1,11	cm^2
sum FX	-0,026	Newton
sum FY	-3762,99	Newton
sum FZ	0,37	Newton
BOUNDARY	ID 40	
---------	------	
Area	16,07	cm^2
sum FX	-8,99	Newton
sum FY	1,76	Newton
sum FZ	1,76	Newton

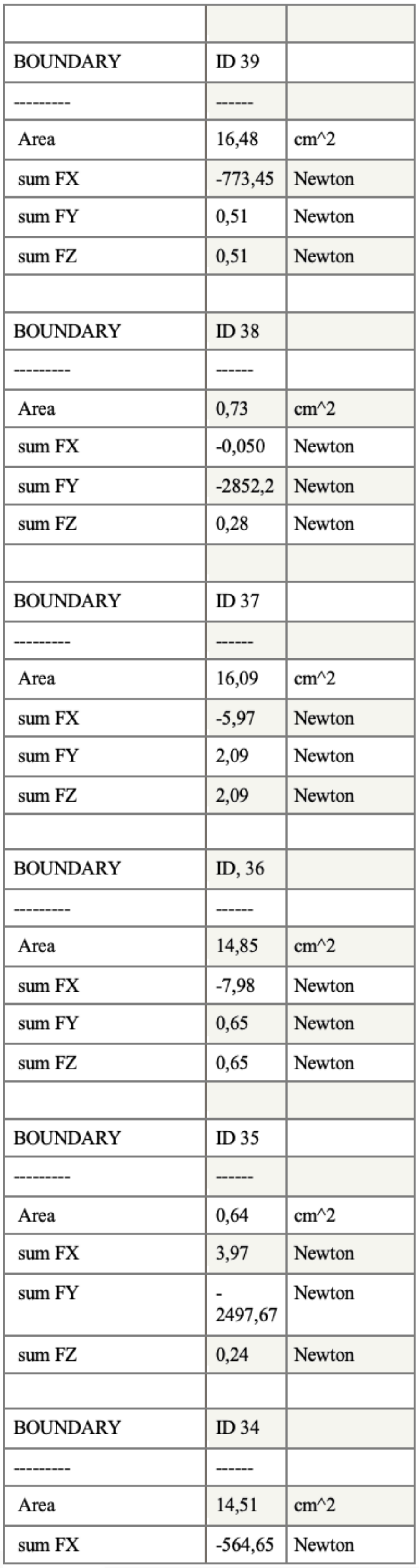

BOUNDARY	ID 39	
---------	------	
Area	16,48	cm^2
sum FX	-773,45	Newton
sum FY	0,51	Newton
sum FZ	0,51	Newton
BOUNDARY	ID 38	
---------	------	
Area	0,73	cm^2
sum FX	-0,050	Newton
sum FY	-2852,2	Newton
sum FZ	0,28	Newton
BOUNDARY	ID 37	
---------	------	
Area	16,09	cm^2
sum FX	-5,97	Newton
sum FY	2,09	Newton
sum FZ	2,09	Newton
BOUNDARY	ID, 36	
---------	------	
Area	14,85	cm^2
sum FX	-7,98	Newton
sum FY	0,65	Newton
sum FZ	0,65	Newton
BOUNDARY	ID 35	
---------	------	
Area	0,64	cm^2
sum FX	3,97	Newton
sum FY	-2497,67	Newton
sum FZ	0,24	Newton
BOUNDARY	ID 34	
---------	------	
Area	14,51	cm^2
sum FX	-564,65	Newton

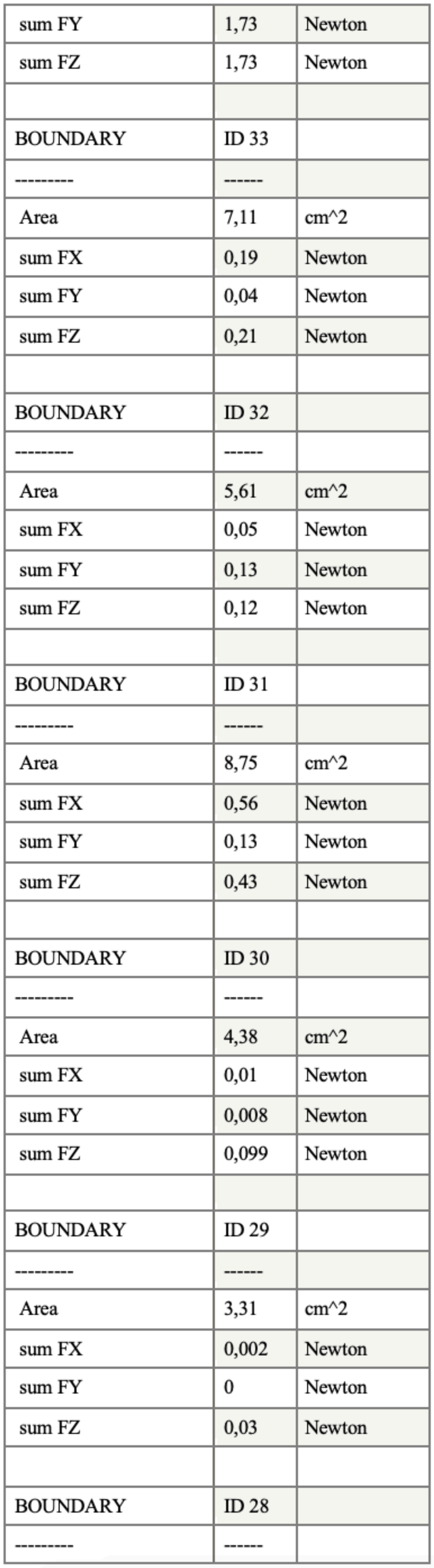

sum FY	1,73	Newton
sum FZ	1,73	Newton
BOUNDARY	ID 33	
---------	------	
Area	7,11	cm^2
sum FX	0,19	Newton
sum FY	0,04	Newton
sum FZ	0,21	Newton
BOUNDARY	ID 32	
---------	------	
Area	5,61	cm^2
sum FX	0,05	Newton
sum FY	0,13	Newton
sum FZ	0,12	Newton
BOUNDARY	ID 31	
---------	------	
Area	8,75	cm^2
sum FX	0,56	Newton
sum FY	0,13	Newton
sum FZ	0,43	Newton
BOUNDARY	ID 30	
---------	------	
Area	4,38	cm^2
sum FX	0,01	Newton
sum FY	0,008	Newton
sum FZ	0,099	Newton
BOUNDARY	ID 29	
---------	------	
Area	3,31	cm^2
sum FX	0,002	Newton
sum FY	0	Newton
sum FZ	0,03	Newton
BOUNDARY	ID 28	
---------	------	

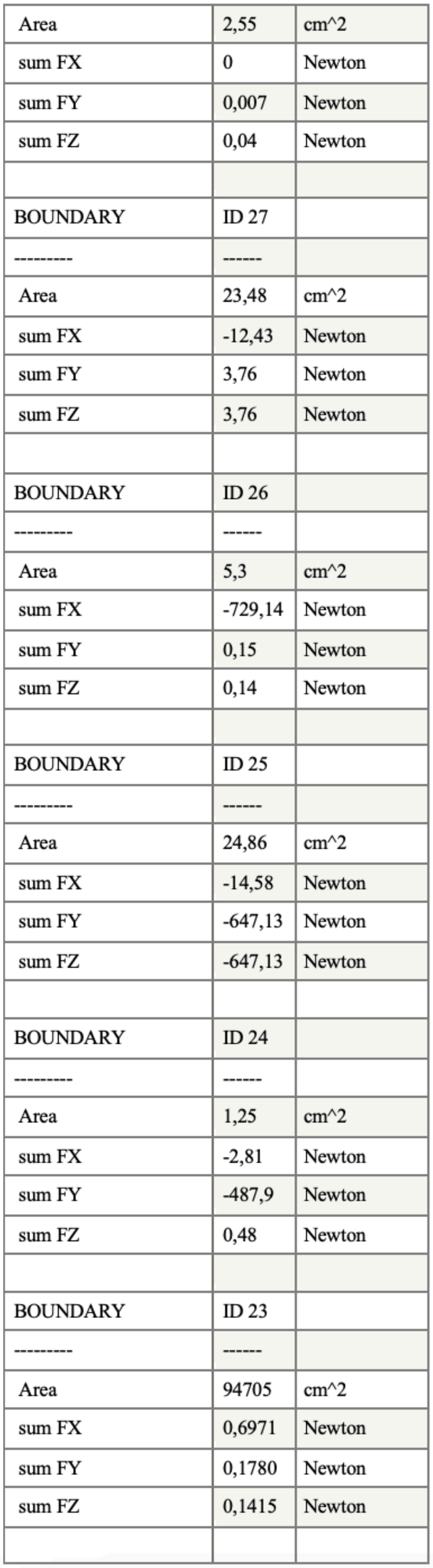

Area	2,55	cm^2
sum FX	0	Newton
sum FY	0,007	Newton
sum FZ	0,04	Newton
BOUNDARY	ID 27	
---------	------	
Area	23,48	cm^2
sum FX	-12,43	Newton
sum FY	3,76	Newton
sum FZ	3,76	Newton
BOUNDARY	ID 26	
---------	------	
Area	5,3	cm^2
sum FX	-729,14	Newton
sum FY	0,15	Newton
sum FZ	0,14	Newton
BOUNDARY	ID 25	
---------	------	
Area	24,86	cm^2
sum FX	-14,58	Newton
sum FY	-647,13	Newton
sum FZ	-647,13	Newton
BOUNDARY	ID 24	
---------	------	
Area	1,25	cm^2
sum FX	-2,81	Newton
sum FY	-487,9	Newton
sum FZ	0,48	Newton
BOUNDARY	ID 23	
---------	------	
Area	94705	cm^2
sum FX	0,6971	Newton
sum FY	0,1780	Newton
sum FZ	0,1415	Newton

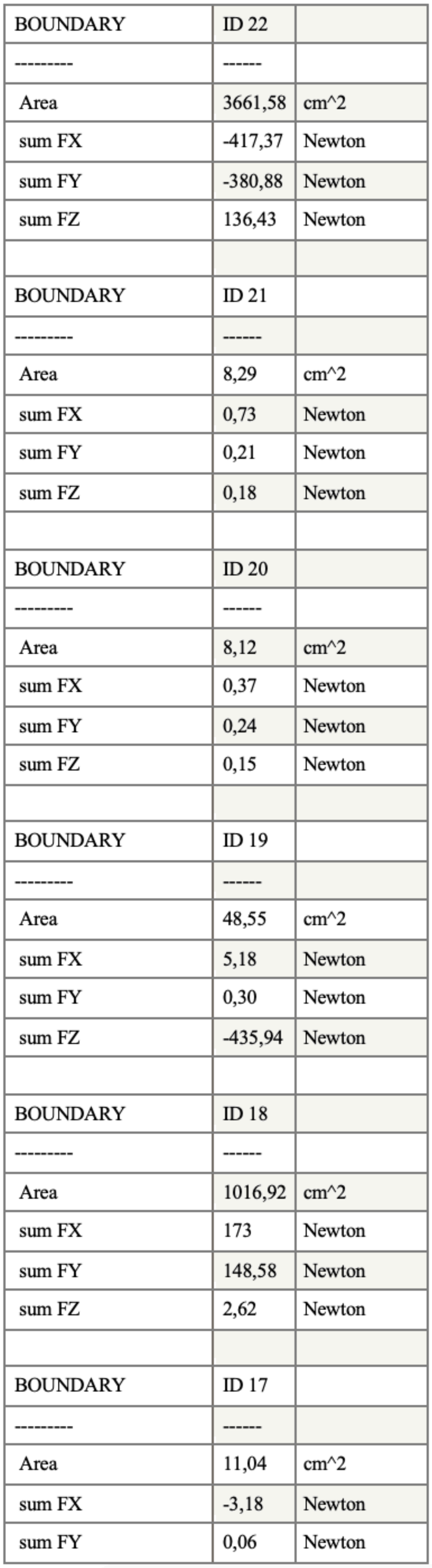

BOUNDARY	ID 22	
---------	------	
Area	3661,58	cm^2
sum FX	-417,37	Newton
sum FY	-380,88	Newton
sum FZ	136,43	Newton
BOUNDARY	ID 21	
---------	------	
Area	8,29	cm^2
sum FX	0,73	Newton
sum FY	0,21	Newton
sum FZ	0,18	Newton
BOUNDARY	ID 20	
---------	------	
Area	8,12	cm^2
sum FX	0,37	Newton
sum FY	0,24	Newton
sum FZ	0,15	Newton
BOUNDARY	ID 19	
---------	------	
Area	48,55	cm^2
sum FX	5,18	Newton
sum FY	0,30	Newton
sum FZ	-435,94	Newton
BOUNDARY	ID 18	
---------	------	
Area	1016,92	cm^2
sum FX	173	Newton
sum FY	148,58	Newton
sum FZ	2,62	Newton
BOUNDARY	ID 17	
---------	------	
Area	11,04	cm^2
sum FX	-3,18	Newton
sum FY	0,06	Newton

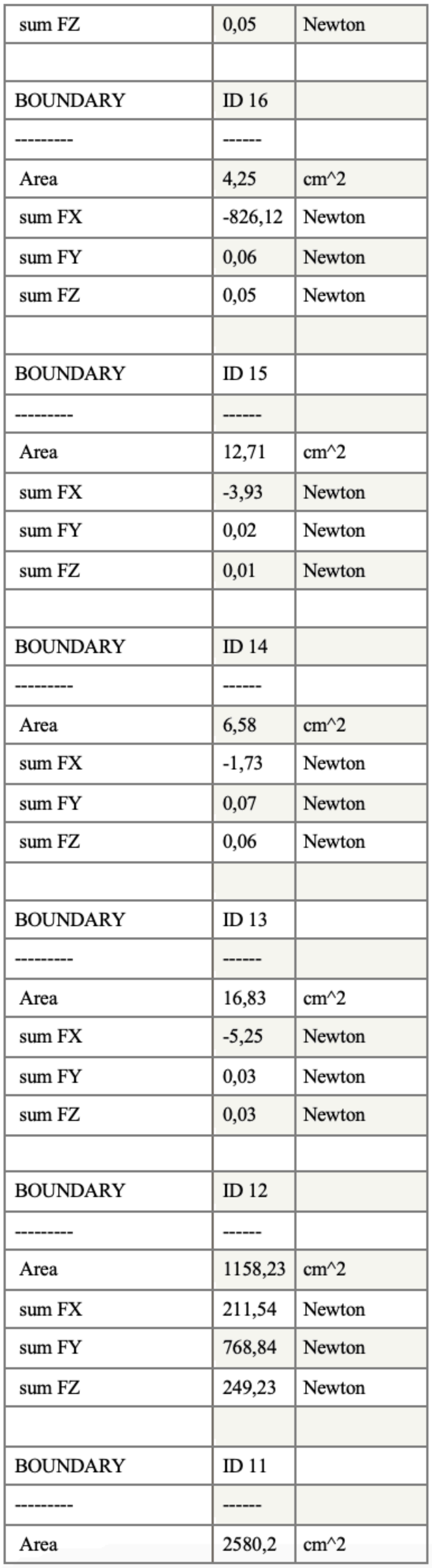

sum FZ	0,05	Newton
BOUNDARY	ID 16	
---------	------	
Area	4,25	cm^2
sum FX	-826,12	Newton
sum FY	0,06	Newton
sum FZ	0,05	Newton
BOUNDARY	ID 15	
---------	------	
Area	12,71	cm^2
sum FX	-3,93	Newton
sum FY	0,02	Newton
sum FZ	0,01	Newton
BOUNDARY	ID 14	
---------	------	
Area	6,58	cm^2
sum FX	-1,73	Newton
sum FY	0,07	Newton
sum FZ	0,06	Newton
BOUNDARY	ID 13	
---------	------	
Area	16,83	cm^2
sum FX	-5,25	Newton
sum FY	0,03	Newton
sum FZ	0,03	Newton
BOUNDARY	ID 12	
---------	------	
Area	1158,23	cm^2
sum FX	211,54	Newton
sum FY	768,84	Newton
sum FZ	249,23	Newton
BOUNDARY	ID 11	
---------	------	
Area	2580,2	cm^2

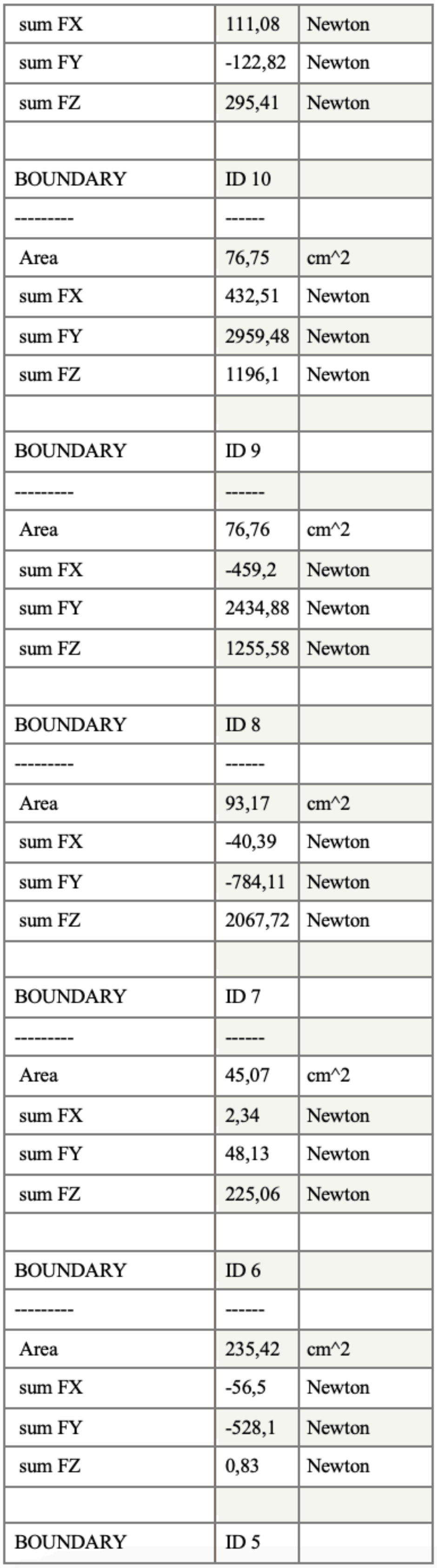

sum FX	111,08	Newton
sum FY	-122,82	Newton
sum FZ	295,41	Newton
BOUNDARY	ID 10	
---------	------	
Area	76,75	cm^2
sum FX	432,51	Newton
sum FY	2959,48	Newton
sum FZ	1196,1	Newton
BOUNDARY	ID 9	
---------	------	
Area	76,76	cm^2
sum FX	-459,2	Newton
sum FY	2434,88	Newton
sum FZ	1255,58	Newton
BOUNDARY	ID 8	
---------	------	
Area	93,17	cm^2
sum FX	-40,39	Newton
sum FY	-784,11	Newton
sum FZ	2067,72	Newton
BOUNDARY	ID 7	
---------	------	
Area	45,07	cm^2
sum FX	2,34	Newton
sum FY	48,13	Newton
sum FZ	225,06	Newton
BOUNDARY	ID 6	
---------	------	
Area	235,42	cm^2
sum FX	-56,5	Newton
sum FY	-528,1	Newton
sum FZ	0,83	Newton
BOUNDARY	ID 5	

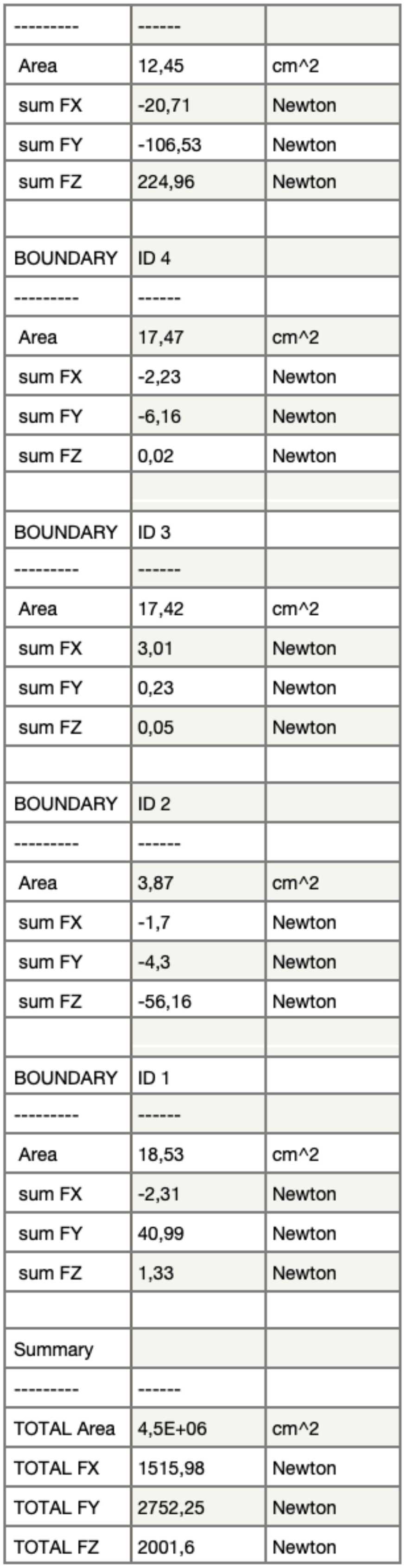

---------	------	
Area	12,45	cm^2
sum FX	-20,71	Newton
sum FY	-106,53	Newton
sum FZ	224,96	Newton
BOUNDARY	ID 4	
---------	------	
Area	17,47	cm^2
sum FX	-2,23	Newton
sum FY	-6,16	Newton
sum FZ	0,02	Newton
BOUNDARY	ID 3	
---------	------	
Area	17,42	cm^2
sum FX	3,01	Newton
sum FY	0,23	Newton
sum FZ	0,05	Newton
BOUNDARY	ID 2	
---------	------	
Area	3,87	cm^2
sum FX	-1,7	Newton
sum FY	-4,3	Newton
sum FZ	-56,16	Newton
BOUNDARY	ID 1	
---------	------	
Area	18,53	cm^2
sum FX	-2,31	Newton
sum FY	40,99	Newton
sum FZ	1,33	Newton
Summary		
---------	------	
TOTAL Area	4,5E+06	cm^2
TOTAL FX	1515,98	Newton
TOTAL FY	2752,25	Newton
TOTAL FZ	2001,6	Newton

ANEX XII

BOEING 787-9 WITH LIFTING SYSTEM CONFIGURATION GENERATING LIFT AT TAKE-OFF

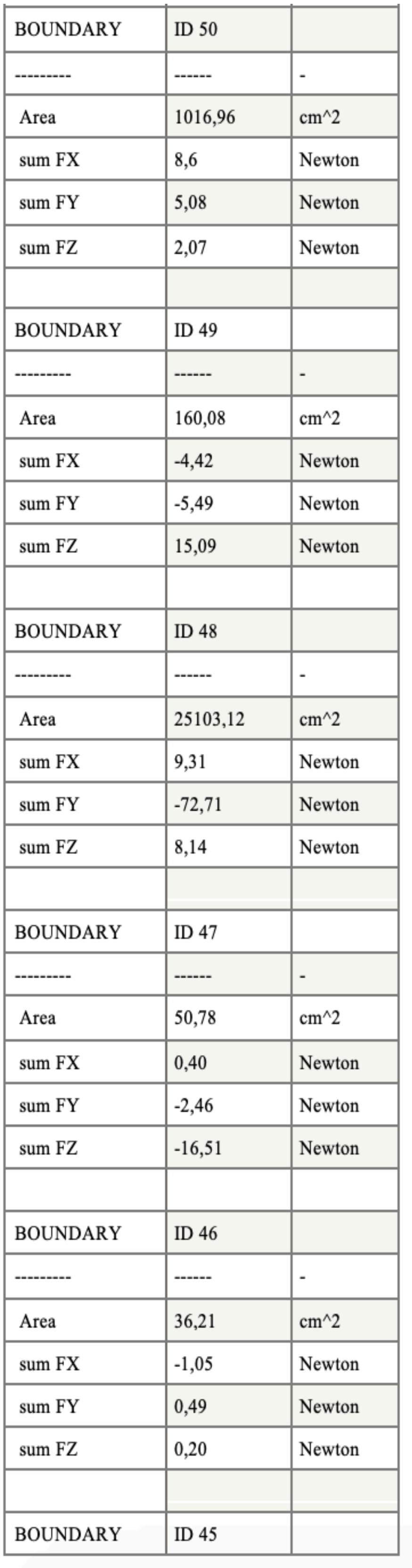

BOUNDARY	ID 50	
---------	------	-
Area	1016,96	cm^2
sum FX	8,6	Newton
sum FY	5,08	Newton
sum FZ	2,07	Newton
BOUNDARY	ID 49	
---------	------	-
Area	160,08	cm^2
sum FX	-4,42	Newton
sum FY	-5,49	Newton
sum FZ	15,09	Newton
BOUNDARY	ID 48	
---------	------	-
Area	25103,12	cm^2
sum FX	9,31	Newton
sum FY	-72,71	Newton
sum FZ	8,14	Newton
BOUNDARY	ID 47	
---------	------	-
Area	50,78	cm^2
sum FX	0,40	Newton
sum FY	-2,46	Newton
sum FZ	-16,51	Newton
BOUNDARY	ID 46	
---------	------	-
Area	36,21	cm^2
sum FX	-1,05	Newton
sum FY	0,49	Newton
sum FZ	0,20	Newton
BOUNDARY	ID 45	

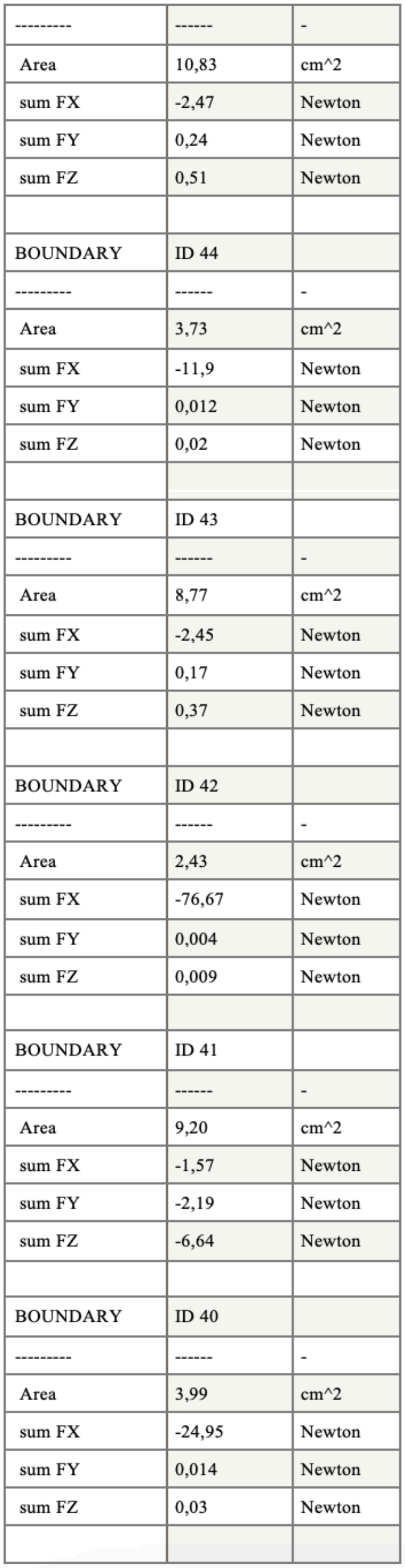

---------	------	-
Area	10,83	cm^2
sum FX	-2,47	Newton
sum FY	0,24	Newton
sum FZ	0,51	Newton
BOUNDARY	ID 44	
---------	------	-
Area	3,73	cm^2
sum FX	-11,9	Newton
sum FY	0,012	Newton
sum FZ	0,02	Newton
BOUNDARY	ID 43	
---------	------	-
Area	8,77	cm^2
sum FX	-2,45	Newton
sum FY	0,17	Newton
sum FZ	0,37	Newton
BOUNDARY	ID 42	
---------	------	-
Area	2,43	cm^2
sum FX	-76,67	Newton
sum FY	0,004	Newton
sum FZ	0,009	Newton
BOUNDARY	ID 41	
---------	------	-
Area	9,20	cm^2
sum FX	-1,57	Newton
sum FY	-2,19	Newton
sum FZ	-6,64	Newton
BOUNDARY	ID 40	
---------	------	-
Area	3,99	cm^2
sum FX	-24,95	Newton
sum FY	0,014	Newton
sum FZ	0,03	Newton

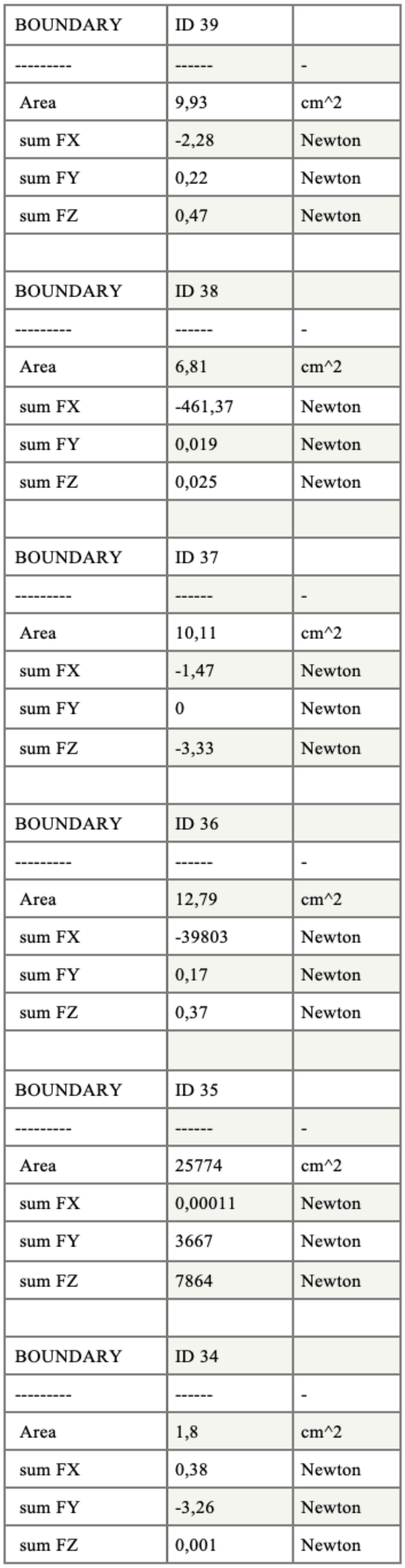

BOUNDARY	ID 39	
---------	------	-
Area	9,93	cm^2
sum FX	-2,28	Newton
sum FY	0,22	Newton
sum FZ	0,47	Newton
BOUNDARY	ID 38	
---------	------	-
Area	6,81	cm^2
sum FX	-461,37	Newton
sum FY	0,019	Newton
sum FZ	0,025	Newton
BOUNDARY	ID 37	
---------	------	-
Area	10,11	cm^2
sum FX	-1,47	Newton
sum FY	0	Newton
sum FZ	-3,33	Newton
BOUNDARY	ID 36	
---------	------	-
Area	12,79	cm^2
sum FX	-39803	Newton
sum FY	0,17	Newton
sum FZ	0,37	Newton
BOUNDARY	ID 35	
---------	------	-
Area	25774	cm^2
sum FX	0,00011	Newton
sum FY	3667	Newton
sum FZ	7864	Newton
BOUNDARY	ID 34	
---------	------	-
Area	1,8	cm^2
sum FX	0,38	Newton
sum FY	-3,26	Newton
sum FZ	0,001	Newton

BOUNDARY	ID 33	
---------	------	-
Area	0,22	cm^2
sum FX	0,001	Newton
sum FY	0,003	Newton
sum FZ	0,006	Newton
BOUNDARY	ID 32	
---------	------	-
Area	14,19	cm^2
sum FX	-2,61	Newton
sum FY	0,11	Newton
sum FZ	0,25	Newton
BOUNDARY	ID 31	
---------	------	-
Area	4,57	cm^2
sum FX	-7318,3	Newton
sum FY	0,017	Newton
sum FZ	0,03	Newton
BOUNDARY	ID, 30	
---------	------	-
Area	18,49	cm^2
sum FX	-3,33	Newton
sum FY	0,43	Newton
sum FZ	0,93	Newton
BOUNDARY	ID 29	
---------	------	-
Area	6,26	cm^2
sum FX	-360,56	Newton
sum FY	0,008	Newton
sum FZ	0,003	Newton
BOUNDARY	ID 28	
---------	------	-
Area	19,39	cm^
sum FX	-2,28	2870
sum FY	-908,72	872
sum FZ	-195,5	965
BOUNDARY	ID 27	
---------	------	-
Area	4,96	cm^2
sum FX	-89,82	Newton
sum FY	0,016	Newton
sum FZ	0,034	Newton
BOUNDARY	ID 26	
---------	------	-
Area	22,61	cm^2
sum FX	-3,79	Newton
sum FY	0,62	Newton
sum FZ	1,33	Newton
BOUNDARY	ID 25	
---------	------	-
Area	12,04	cm^2
sum FX	-854,21	Newton
sum FY	0,007	Newton
sum FZ	0,0006	Newton
BOUNDARY	ID 24	
---------	------	-
Area	23,88	cm^2
sum FX	-1,91	Newton
sum FY	-257,32	Newton
sum FZ	-554,6	Newton
BOUNDARY	ID 23	
---------	------	-
Area	5,35	cm^2
sum FX	-91,79	Newton
sum FY	0,018	Newton
sum FZ	0,039	Newton
BOUNDARY	ID 22	
---------	------	-
Area	2,18	cm^2
sum FX	0,011	Newton
sum FY	-1,42	Newton
sum FZ	0,003	Newton
BOUNDARY	ID 21	
---------	------	-
Area	2,98	cm^2
sum FX	0,016	Newton
sum FY	-2,85	Newton
sum FZ	0,007	Newton
BOUNDARY	ID 20	
---------	------	-
Area	4,21	cm^2
sum FX	0,010	Newton
sum FY	-2,52	Newton
sum FZ	0,01	Newton
BOUNDARY	ID 19	
---------	------	-
Area	8,76	cm^2
sum FX	0,03	Newton
sum FY	-31,9	Newton
sum FZ	0,09	Newton
BOUNDARY	ID 18	
---------	------	-
Area	5,58	cm^2
sum FX	0,024	Newton
sum FY	0,001	Newton
sum FZ	0,016	Newton
BOUNDARY	ID 17	
---------	------	-
Area	7,18	cm^2
sum FX	0,024	Newton
sum FY	-4,36	Newton
sum FZ	0,045	Newton
BOUNDARY	ID 16	
---------	------	-
Area	0,34	cm^2

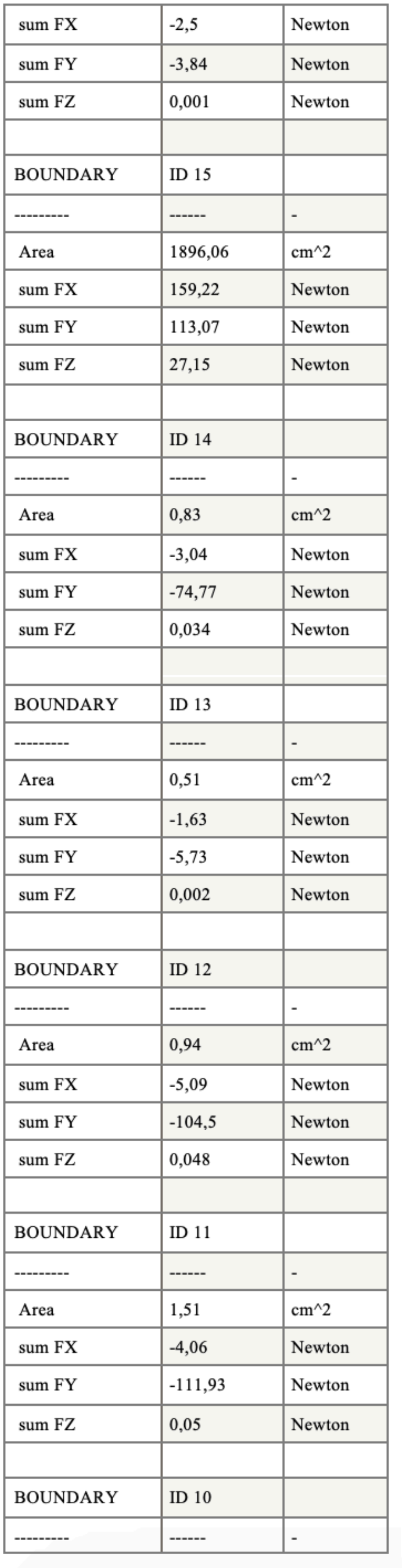

sum FX	-2,5	Newton
sum FY	-3,84	Newton
sum FZ	0,001	Newton
BOUNDARY	ID 15	
---------	------	-
Area	1896,06	cm^2
sum FX	159,22	Newton
sum FY	113,07	Newton
sum FZ	27,15	Newton
BOUNDARY	ID 14	
---------	------	-
Area	0,83	cm^2
sum FX	-3,04	Newton
sum FY	-74,77	Newton
sum FZ	0,034	Newton
BOUNDARY	ID 13	
---------	------	-
Area	0,51	cm^2
sum FX	-1,63	Newton
sum FY	-5,73	Newton
sum FZ	0,002	Newton
BOUNDARY	ID 12	
---------	------	-
Area	0,94	cm^2
sum FX	-5,09	Newton
sum FY	-104,5	Newton
sum FZ	0,048	Newton
BOUNDARY	ID 11	
---------	------	-
Area	1,51	cm^2
sum FX	-4,06	Newton
sum FY	-111,93	Newton
sum FZ	0,05	Newton
BOUNDARY	ID 10	
---------	------	-

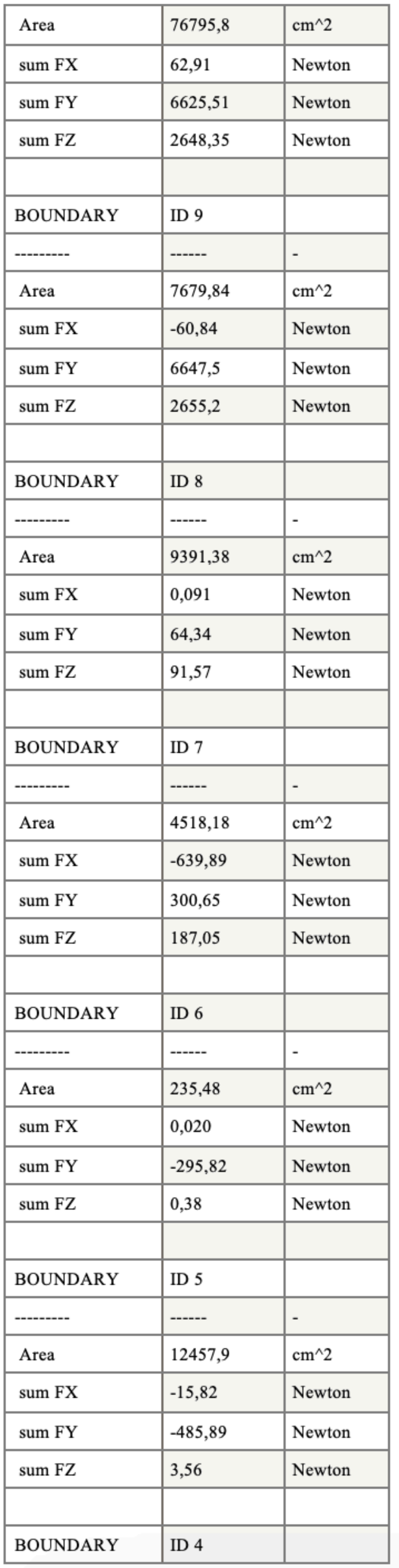

Area	76795,8	cm^2
sum FX	62,91	Newton
sum FY	6625,51	Newton
sum FZ	2648,35	Newton
BOUNDARY	ID 9	
---------	------	-
Area	7679,84	cm^2
sum FX	-60,84	Newton
sum FY	6647,5	Newton
sum FZ	2655,2	Newton
BOUNDARY	ID 8	
---------	------	-
Area	9391,38	cm^2
sum FX	0,091	Newton
sum FY	64,34	Newton
sum FZ	91,57	Newton
BOUNDARY	ID 7	
---------	------	-
Area	4518,18	cm^2
sum FX	-639,89	Newton
sum FY	300,65	Newton
sum FZ	187,05	Newton
BOUNDARY	ID 6	
---------	------	-
Area	235,48	cm^2
sum FX	0,020	Newton
sum FY	-295,82	Newton
sum FZ	0,38	Newton
BOUNDARY	ID 5	
---------	------	-
Area	12457,9	cm^2
sum FX	-15,82	Newton
sum FY	-485,89	Newton
sum FZ	3,56	Newton
BOUNDARY	ID 4	

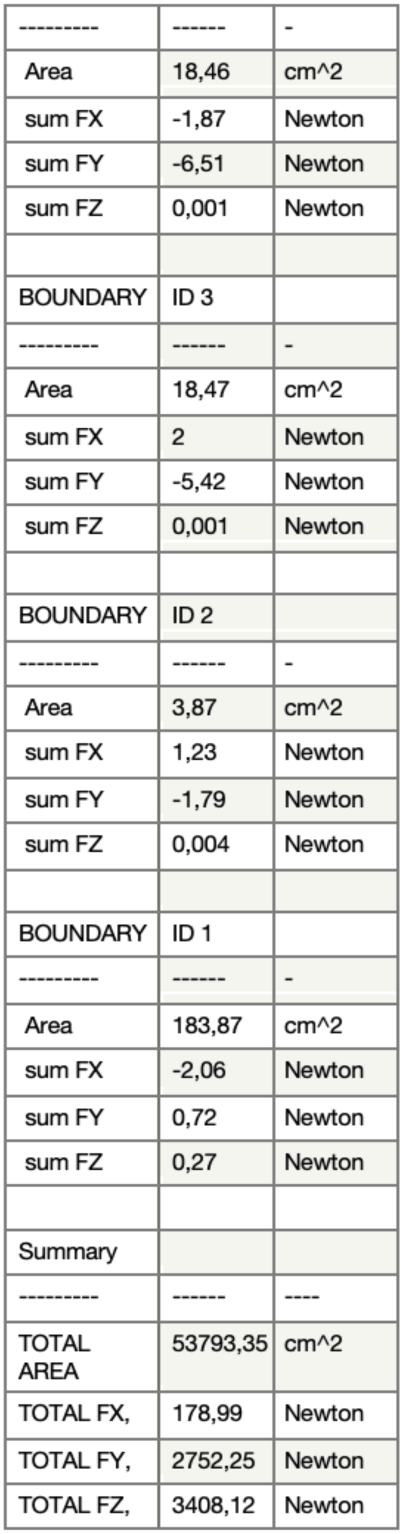

---------	------	-
Area	18,46	cm^2
sum FX	-1,87	Newton
sum FY	-6,51	Newton
sum FZ	0,001	Newton
BOUNDARY	ID 3	
---------	------	-
Area	18,47	cm^2
sum FX	2	Newton
sum FY	-5,42	Newton
sum FZ	0,001	Newton
BOUNDARY	ID 2	
---------	------	-
Area	3,87	cm^2
sum FX	1,23	Newton
sum FY	-1,79	Newton
sum FZ	0,004	Newton
BOUNDARY	ID 1	
---------	------	-
Area	183,87	cm^2
sum FX	-2,06	Newton
sum FY	0,72	Newton
sum FZ	0,27	Newton
Summary		
---------	------	----
TOTAL AREA	53793,35	cm^2
TOTAL FX,	178,99	Newton
TOTAL FY,	2752,25	Newton
TOTAL FZ,	3408,12	Newton

ANEX XIII

BOEING 787-9 WITHOUT LIFTING SYSTEM & HORIZONTAL STABILIZER WHILE CRUISE

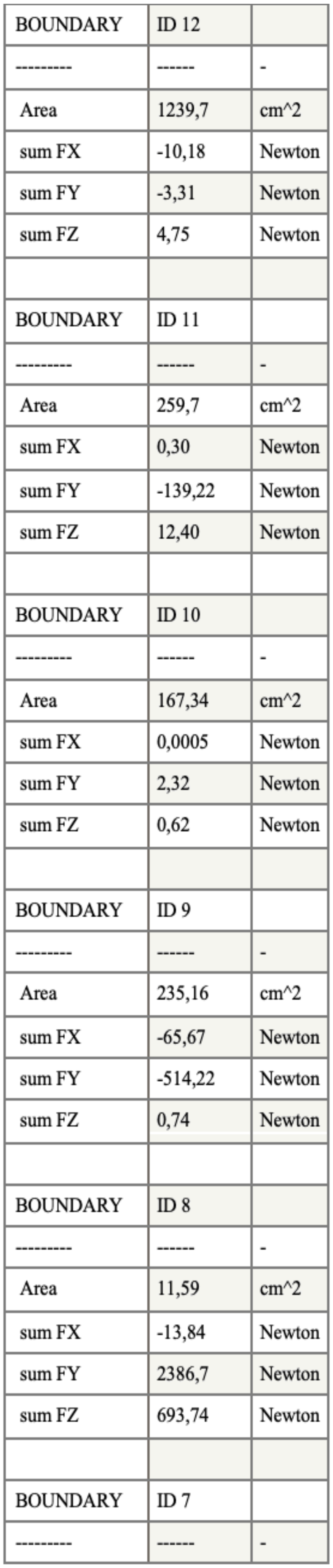

BOUNDARY	ID 12	
---------	------	-
Area	1239,7	cm^2
sum FX	-10,18	Newton
sum FY	-3,31	Newton
sum FZ	4,75	Newton
BOUNDARY	ID 11	
---------	------	-
Area	259,7	cm^2
sum FX	0,30	Newton
sum FY	-139,22	Newton
sum FZ	12,40	Newton
BOUNDARY	ID 10	
---------	------	-
Area	167,34	cm^2
sum FX	0,0005	Newton
sum FY	2,32	Newton
sum FZ	0,62	Newton
BOUNDARY	ID 9	
---------	------	-
Area	235,16	cm^2
sum FX	-65,67	Newton
sum FY	-514,22	Newton
sum FZ	0,74	Newton
BOUNDARY	ID 8	
---------	------	-
Area	11,59	cm^2
sum FX	-13,84	Newton
sum FY	2386,7	Newton
sum FZ	693,74	Newton
BOUNDARY	ID 7	
---------	------	-

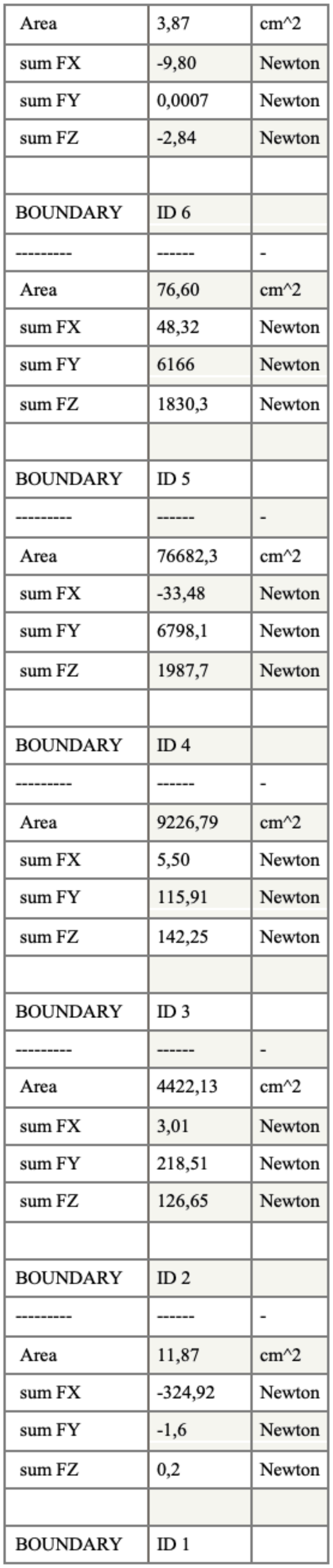

Area	3,87	cm^2
sum FX	-9,80	Newton
sum FY	0,0007	Newton
sum FZ	-2,84	Newton
BOUNDARY	ID 6	
---------	------	-
Area	76,60	cm^2
sum FX	48,32	Newton
sum FY	6166	Newton
sum FZ	1830,3	Newton
BOUNDARY	ID 5	
---------	------	-
Area	76682,3	cm^2
sum FX	-33,48	Newton
sum FY	6798,1	Newton
sum FZ	1987,7	Newton
BOUNDARY	ID 4	
---------	------	-
Area	9226,79	cm^2
sum FX	5,50	Newton
sum FY	115,91	Newton
sum FZ	142,25	Newton
BOUNDARY	ID 3	
---------	------	-
Area	4422,13	cm^2
sum FX	3,01	Newton
sum FY	218,51	Newton
sum FZ	126,65	Newton
BOUNDARY	ID 2	
---------	------	-
Area	11,87	cm^2
sum FX	-324,92	Newton
sum FY	-1,6	Newton
sum FZ	0,2	Newton
BOUNDARY	ID 1	

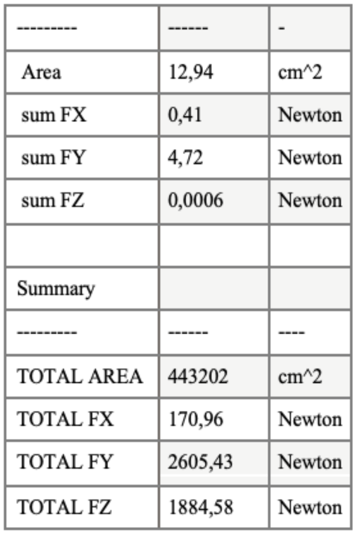

---------	------	-
Area	12,94	cm^2
sum FX	0,41	Newton
sum FY	4,72	Newton
sum FZ	0,0006	Newton
Summary		
---------	------	----
TOTAL AREA	443202	cm^2
TOTAL FX	170,96	Newton
TOTAL FY	2605,43	Newton
TOTAL FZ	1884,58	Newton

ANEX XIV

BOEING 787-9 WITH LIFTING SYSTEM CONFIGURATION ("DRS OPEN") WHILE CRUISE

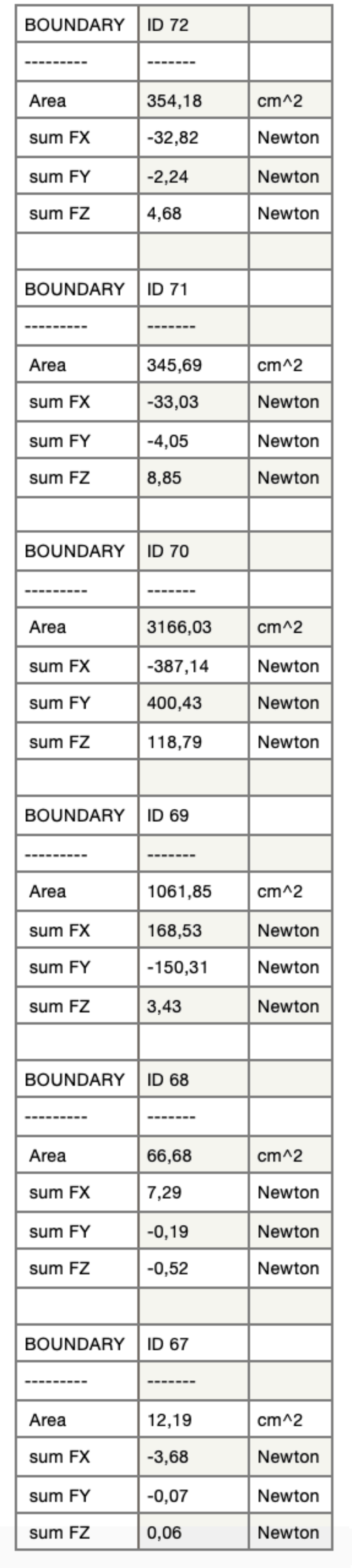

BOUNDARY	ID 72	
---------	-------	
Area	354,18	cm^2
sum FX	-32,82	Newton
sum FY	-2,24	Newton
sum FZ	4,68	Newton
BOUNDARY	ID 71	
---------	-------	
Area	345,69	cm^2
sum FX	-33,03	Newton
sum FY	-4,05	Newton
sum FZ	8,85	Newton
BOUNDARY	ID 70	
---------	-------	
Area	3166,03	cm^2
sum FX	-387,14	Newton
sum FY	400,43	Newton
sum FZ	118,79	Newton
BOUNDARY	ID 69	
---------	-------	
Area	1061,85	cm^2
sum FX	168,53	Newton
sum FY	-150,31	Newton
sum FZ	3,43	Newton
BOUNDARY	ID 68	
---------	-------	
Area	66,68	cm^2
sum FX	7,29	Newton
sum FY	-0,19	Newton
sum FZ	-0,52	Newton
BOUNDARY	ID 67	
---------	-------	
Area	12,19	cm^2
sum FX	-3,68	Newton
sum FY	-0,07	Newton
sum FZ	0,06	Newton

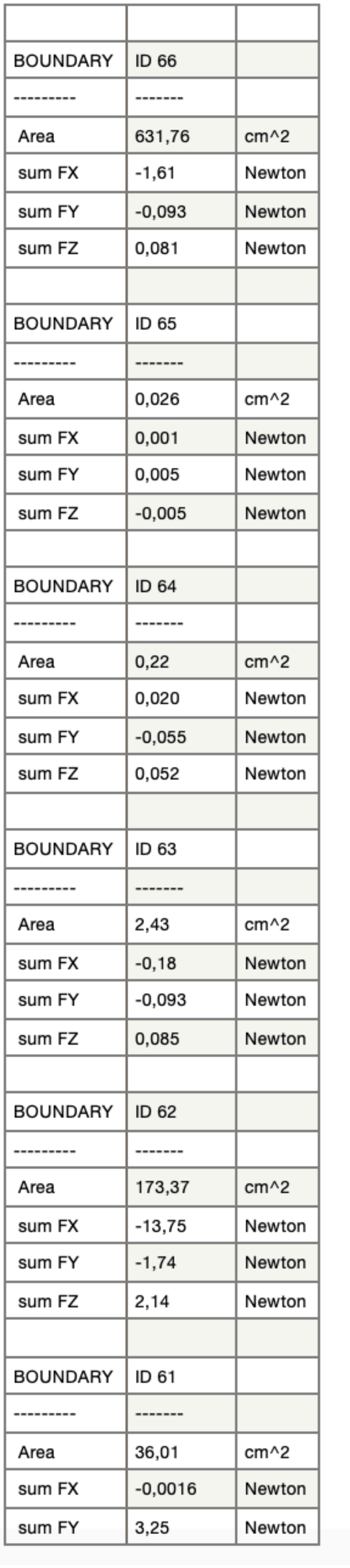

BOUNDARY	ID 66	
---------	-------	
Area	631,76	cm^2
sum FX	-1,61	Newton
sum FY	-0,093	Newton
sum FZ	0,081	Newton
BOUNDARY	ID 65	
---------	-------	
Area	0,026	cm^2
sum FX	0,001	Newton
sum FY	0,005	Newton
sum FZ	-0,005	Newton
BOUNDARY	ID 64	
---------	-------	
Area	0,22	cm^2
sum FX	0,020	Newton
sum FY	-0,055	Newton
sum FZ	0,052	Newton
BOUNDARY	ID 63	
---------	-------	
Area	2,43	cm^2
sum FX	-0,18	Newton
sum FY	-0,093	Newton
sum FZ	0,085	Newton
BOUNDARY	ID 62	
---------	-------	
Area	173,37	cm^2
sum FX	-13,75	Newton
sum FY	-1,74	Newton
sum FZ	2,14	Newton
BOUNDARY	ID 61	
---------	-------	
Area	36,01	cm^2
sum FX	-0,0016	Newton
sum FY	3,25	Newton

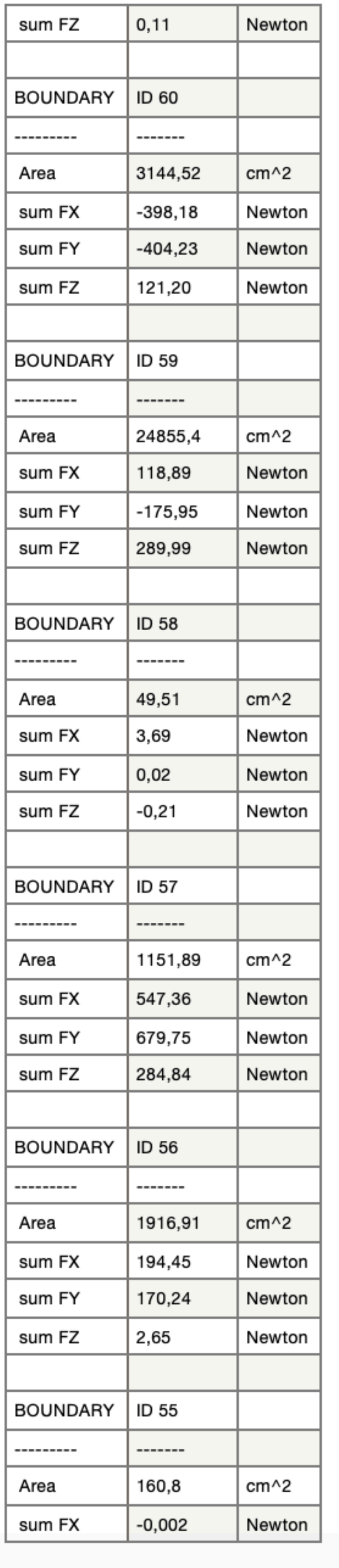

sum FZ	0,11	Newton
BOUNDARY	ID 60	
---------	-------	
Area	3144,52	cm^2
sum FX	-398,18	Newton
sum FY	-404,23	Newton
sum FZ	121,20	Newton
BOUNDARY	ID 59	
---------	-------	
Area	24855,4	cm^2
sum FX	118,89	Newton
sum FY	-175,95	Newton
sum FZ	289,99	Newton
BOUNDARY	ID 58	
---------	-------	
Area	49,51	cm^2
sum FX	3,69	Newton
sum FY	0,02	Newton
sum FZ	-0,21	Newton
BOUNDARY	ID 57	
---------	-------	
Area	1151,89	cm^2
sum FX	547,36	Newton
sum FY	679,75	Newton
sum FZ	284,84	Newton
BOUNDARY	ID 56	
---------	-------	
Area	1916,91	cm^2
sum FX	194,45	Newton
sum FY	170,24	Newton
sum FZ	2,65	Newton
BOUNDARY	ID 55	
---------	-------	
Area	160,8	cm^2
sum FX	-0,002	Newton

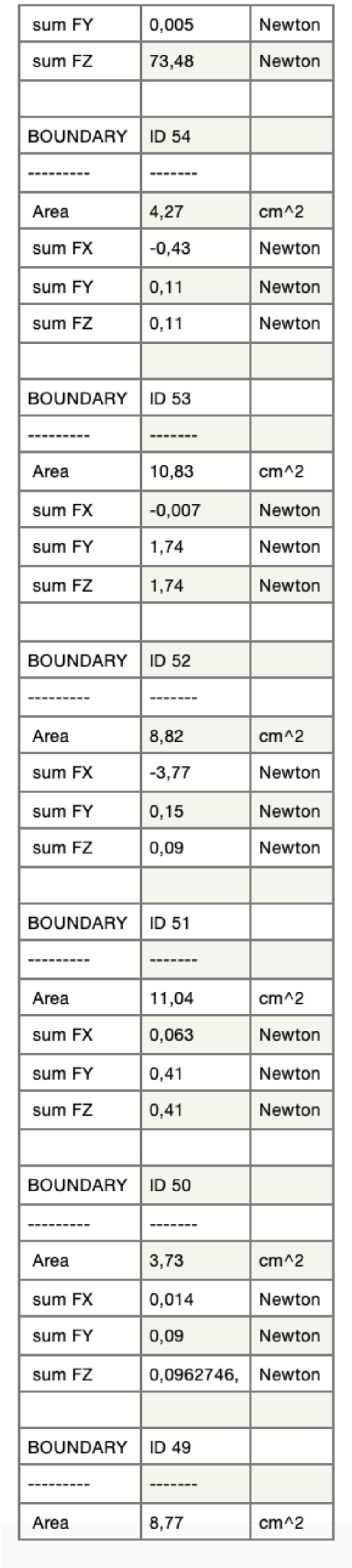

sum FY	0,005	Newton
sum FZ	73,48	Newton
BOUNDARY	ID 54	
---------	-------	
Area	4,27	cm^2
sum FX	-0,43	Newton
sum FY	0,11	Newton
sum FZ	0,11	Newton
BOUNDARY	ID 53	
---------	-------	
Area	10,83	cm^2
sum FX	-0,007	Newton
sum FY	1,74	Newton
sum FZ	1,74	Newton
BOUNDARY	ID 52	
---------	-------	
Area	8,82	cm^2
sum FX	-3,77	Newton
sum FY	0,15	Newton
sum FZ	0,09	Newton
BOUNDARY	ID 51	
---------	-------	
Area	11,04	cm^2
sum FX	0,063	Newton
sum FY	0,41	Newton
sum FZ	0,41	Newton
BOUNDARY	ID 50	
---------	-------	
Area	3,73	cm^2
sum FX	0,014	Newton
sum FY	0,09	Newton
sum FZ	0,0962746,	Newton
BOUNDARY	ID 49	
---------	-------	
Area	8,77	cm^2

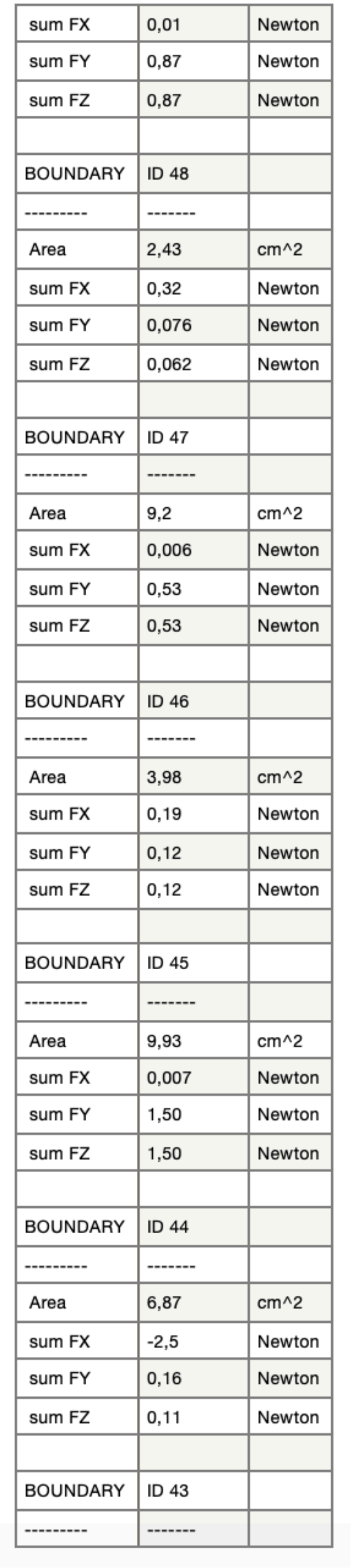

sum FX	0,01	Newton
sum FY	0,87	Newton
sum FZ	0,87	Newton
BOUNDARY	ID 48	
---------	-------	
Area	2,43	cm^2
sum FX	0,32	Newton
sum FY	0,076	Newton
sum FZ	0,062	Newton
BOUNDARY	ID 47	
---------	-------	
Area	9,2	cm^2
sum FX	0,006	Newton
sum FY	0,53	Newton
sum FZ	0,53	Newton
BOUNDARY	ID 46	
---------	-------	
Area	3,98	cm^2
sum FX	0,19	Newton
sum FY	0,12	Newton
sum FZ	0,12	Newton
BOUNDARY	ID 45	
---------	-------	
Area	9,93	cm^2
sum FX	0,007	Newton
sum FY	1,50	Newton
sum FZ	1,50	Newton
BOUNDARY	ID 44	
---------	-------	
Area	6,87	cm^2
sum FX	-2,5	Newton
sum FY	0,16	Newton
sum FZ	0,11	Newton
BOUNDARY	ID 43	
---------	-------	

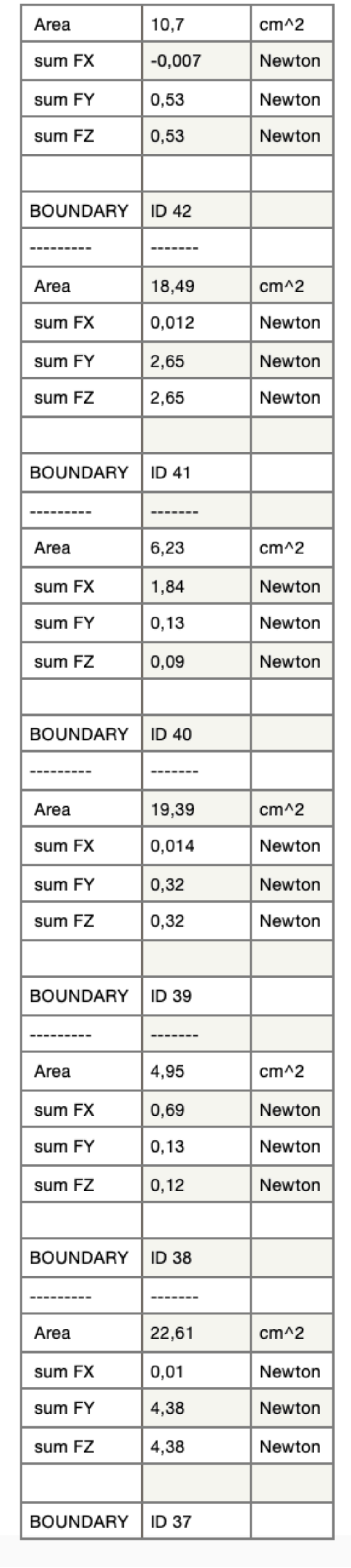

Area	10,7	cm^2
sum FX	-0,007	Newton
sum FY	0,53	Newton
sum FZ	0,53	Newton
BOUNDARY	ID 42	
---------	-------	
Area	18,49	cm^2
sum FX	0,012	Newton
sum FY	2,65	Newton
sum FZ	2,65	Newton
BOUNDARY	ID 41	
---------	-------	
Area	6,23	cm^2
sum FX	1,84	Newton
sum FY	0,13	Newton
sum FZ	0,09	Newton
BOUNDARY	ID 40	
---------	-------	
Area	19,39	cm^2
sum FX	0,014	Newton
sum FY	0,32	Newton
sum FZ	0,32	Newton
BOUNDARY	ID 39	
---------	-------	
Area	4,95	cm^2
sum FX	0,69	Newton
sum FY	0,13	Newton
sum FZ	0,12	Newton
BOUNDARY	ID 38	
---------	-------	
Area	22,61	cm^2
sum FX	0,01	Newton
sum FY	4,38	Newton
sum FZ	4,38	Newton
BOUNDARY	ID 37	

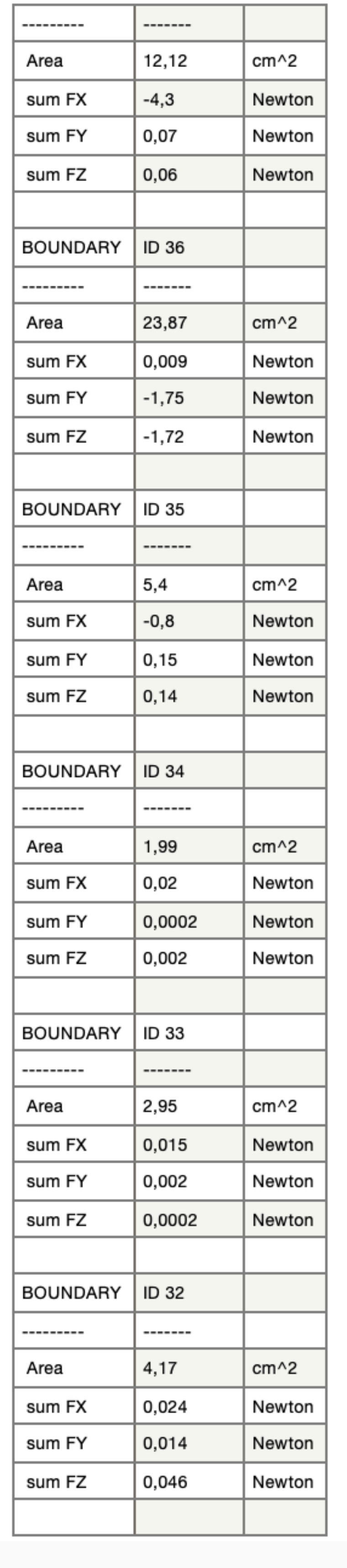

---------	-------	
Area	12,12	cm^2
sum FX	-4,3	Newton
sum FY	0,07	Newton
sum FZ	0,06	Newton
BOUNDARY	ID 36	
---------	-------	
Area	23,87	cm^2
sum FX	0,009	Newton
sum FY	-1,75	Newton
sum FZ	-1,72	Newton
BOUNDARY	ID 35	
---------	-------	
Area	5,4	cm^2
sum FX	-0,8	Newton
sum FY	0,15	Newton
sum FZ	0,14	Newton
BOUNDARY	ID 34	
---------	-------	
Area	1,99	cm^2
sum FX	0,02	Newton
sum FY	0,0002	Newton
sum FZ	0,002	Newton
BOUNDARY	ID 33	
---------	-------	
Area	2,95	cm^2
sum FX	0,015	Newton
sum FY	0,002	Newton
sum FZ	0,0002	Newton
BOUNDARY	ID 32	
---------	-------	
Area	4,17	cm^2
sum FX	0,024	Newton
sum FY	0,014	Newton
sum FZ	0,046	Newton

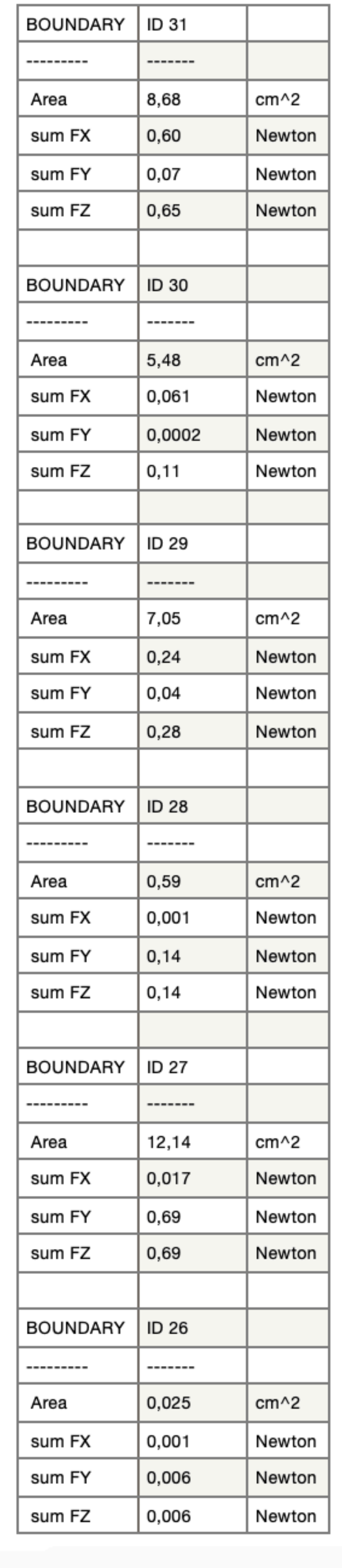

BOUNDARY	ID 31	
---------	-------	
Area	8,68	cm^2
sum FX	0,60	Newton
sum FY	0,07	Newton
sum FZ	0,65	Newton
BOUNDARY	ID 30	
---------	-------	
Area	5,48	cm^2
sum FX	0,061	Newton
sum FY	0,0002	Newton
sum FZ	0,11	Newton
BOUNDARY	ID 29	
---------	-------	
Area	7,05	cm^2
sum FX	0,24	Newton
sum FY	0,04	Newton
sum FZ	0,28	Newton
BOUNDARY	ID 28	
---------	-------	
Area	0,59	cm^2
sum FX	0,001	Newton
sum FY	0,14	Newton
sum FZ	0,14	Newton
BOUNDARY	ID 27	
---------	-------	
Area	12,14	cm^2
sum FX	0,017	Newton
sum FY	0,69	Newton
sum FZ	0,69	Newton
BOUNDARY	ID 26	
---------	-------	
Area	0,025	cm^2
sum FX	0,001	Newton
sum FY	0,006	Newton
sum FZ	0,006	Newton

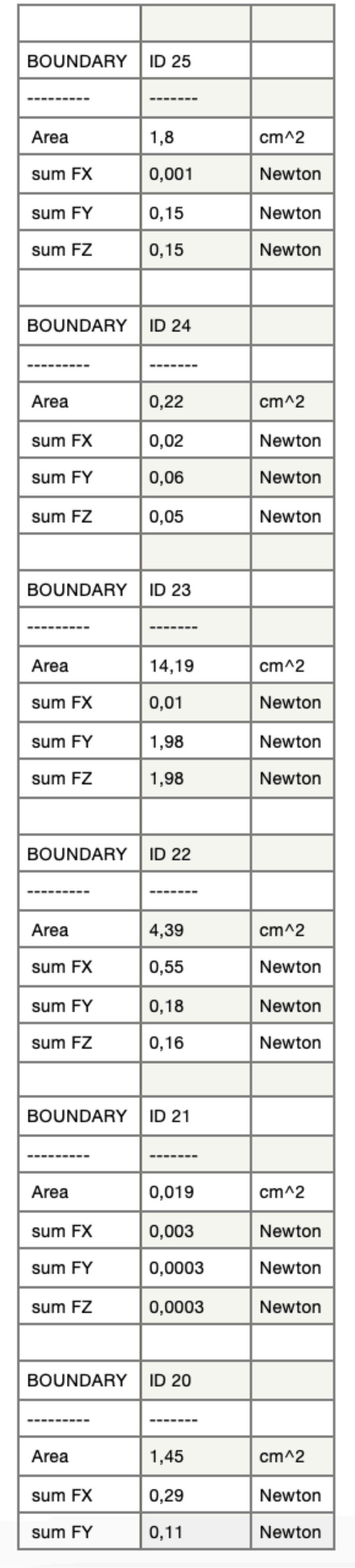

BOUNDARY	ID 25	
---------	-------	
Area	1,8	cm^2
sum FX	0,001	Newton
sum FY	0,15	Newton
sum FZ	0,15	Newton
BOUNDARY	ID 24	
---------	-------	
Area	0,22	cm^2
sum FX	0,02	Newton
sum FY	0,06	Newton
sum FZ	0,05	Newton
BOUNDARY	ID 23	
---------	-------	
Area	14,19	cm^2
sum FX	0,01	Newton
sum FY	1,98	Newton
sum FZ	1,98	Newton
BOUNDARY	ID 22	
---------	-------	
Area	4,39	cm^2
sum FX	0,55	Newton
sum FY	0,18	Newton
sum FZ	0,16	Newton
BOUNDARY	ID 21	
---------	-------	
Area	0,019	cm^2
sum FX	0,003	Newton
sum FY	0,0003	Newton
sum FZ	0,0003	Newton
BOUNDARY	ID 20	
---------	-------	
Area	1,45	cm^2
sum FX	0,29	Newton
sum FY	0,11	Newton

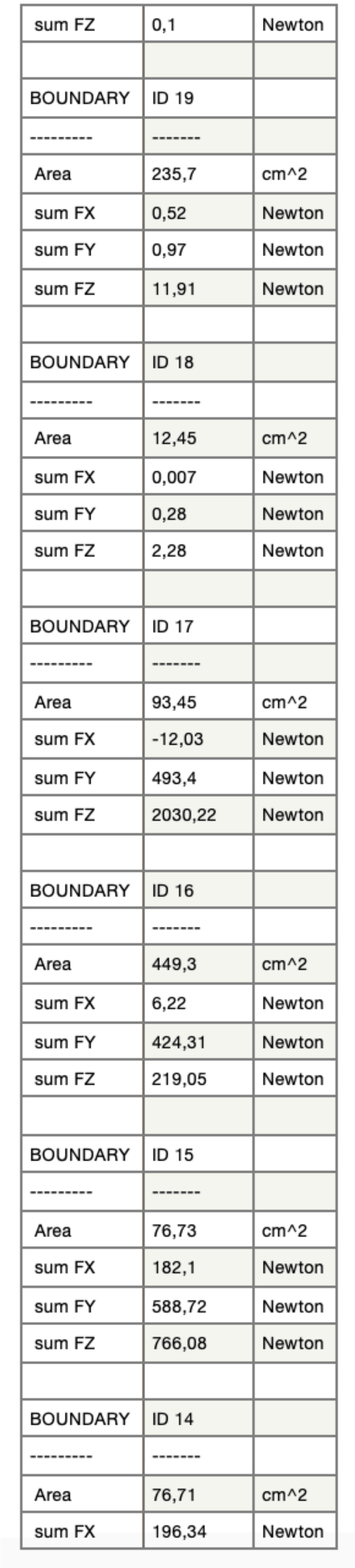

sum FZ	0,1	Newton
BOUNDARY	ID 19	
---------	-------	
Area	235,7	cm^2
sum FX	0,52	Newton
sum FY	0,97	Newton
sum FZ	11,91	Newton
BOUNDARY	ID 18	
---------	-------	
Area	12,45	cm^2
sum FX	0,007	Newton
sum FY	0,28	Newton
sum FZ	2,28	Newton
BOUNDARY	ID 17	
---------	-------	
Area	93,45	cm^2
sum FX	-12,03	Newton
sum FY	493,4	Newton
sum FZ	2030,22	Newton
BOUNDARY	ID 16	
---------	-------	
Area	449,3	cm^2
sum FX	6,22	Newton
sum FY	424,31	Newton
sum FZ	219,05	Newton
BOUNDARY	ID 15	
---------	-------	
Area	76,73	cm^2
sum FX	182,1	Newton
sum FY	588,72	Newton
sum FZ	766,08	Newton
BOUNDARY	ID 14	
---------	-------	
Area	76,71	cm^2
sum FX	196,34	Newton

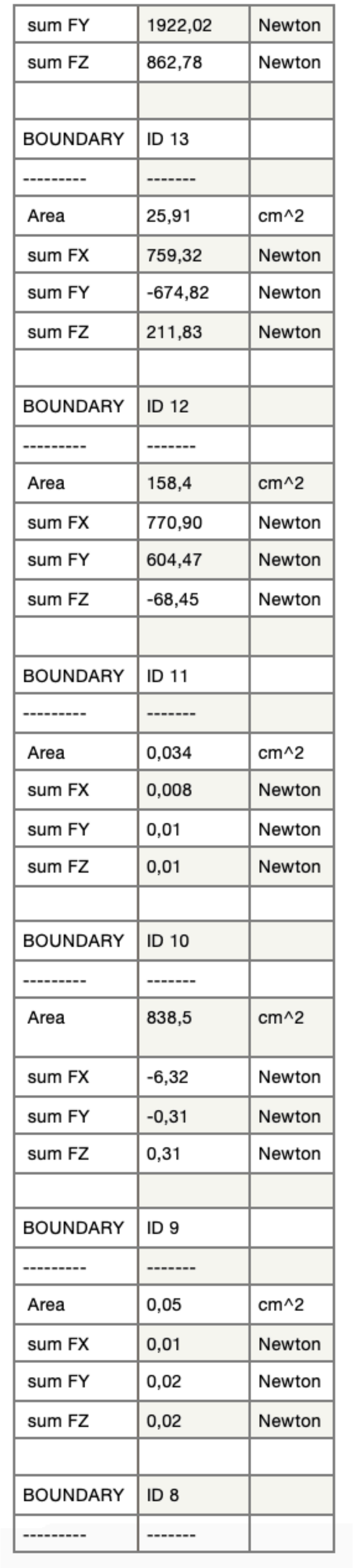

sum FY	1922,02	Newton
sum FZ	862,78	Newton
BOUNDARY	ID 13	
---------	-------	
Area	25,91	cm^2
sum FX	759,32	Newton
sum FY	-674,82	Newton
sum FZ	211,83	Newton
BOUNDARY	ID 12	
---------	-------	
Area	158,4	cm^2
sum FX	770,90	Newton
sum FY	604,47	Newton
sum FZ	-68,45	Newton
BOUNDARY	ID 11	
---------	-------	
Area	0,034	cm^2
sum FX	0,008	Newton
sum FY	0,01	Newton
sum FZ	0,01	Newton
BOUNDARY	ID 10	
---------	-------	
Area	838,5	cm^2
sum FX	-6,32	Newton
sum FY	-0,31	Newton
sum FZ	0,31	Newton
BOUNDARY	ID 9	
---------	-------	
Area	0,05	cm^2
sum FX	0,01	Newton
sum FY	0,02	Newton
sum FZ	0,02	Newton
BOUNDARY	ID 8	
---------	-------	

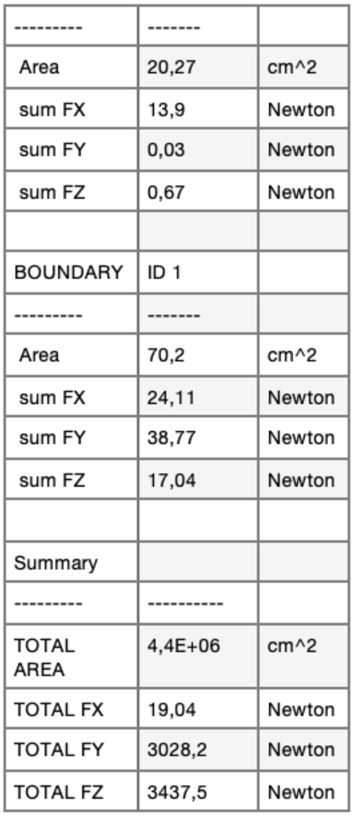

---------	-------	
Area	20,27	cm^2
sum FX	13,9	Newton
sum FY	0,03	Newton
sum FZ	0,67	Newton
BOUNDARY	ID 1	
---------	-------	
Area	70,2	cm^2
sum FX	24,11	Newton
sum FY	38,77	Newton
sum FZ	17,04	Newton
Summary		
---------	----------	
TOTAL AREA	4,4E+06	cm^2
TOTAL FX	19,04	Newton
TOTAL FY	3028,2	Newton
TOTAL FZ	3437,5	Newton

ANEX XV

BOEING 787-9 WITHOUT LIFTING SYSTEM & HORIZONTAL STABILIZER DURING TAKE-OFF

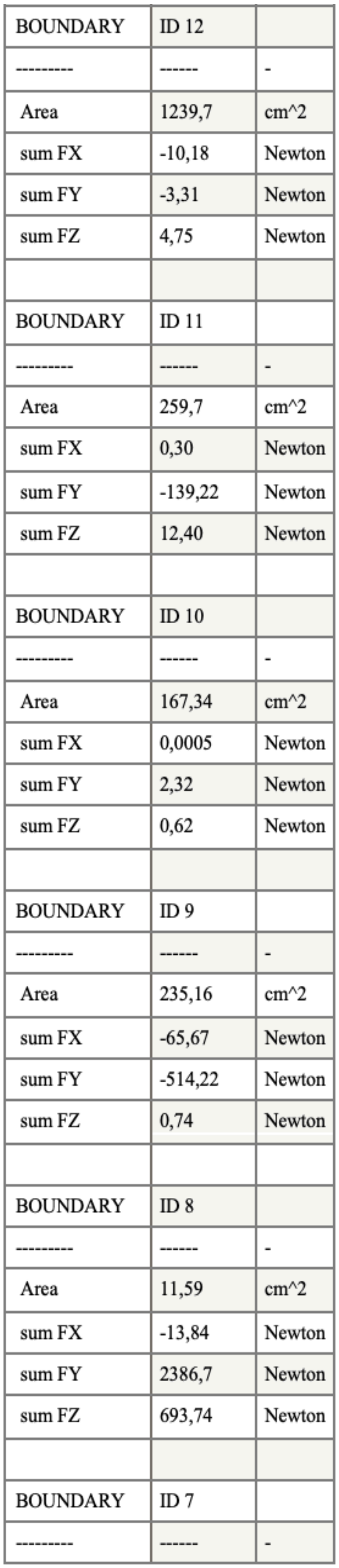

BOUNDARY	ID 12	
---------	------	-
Area	1239,7	cm^2
sum FX	-10,18	Newton
sum FY	-3,31	Newton
sum FZ	4,75	Newton
BOUNDARY	ID 11	
---------	------	-
Area	259,7	cm^2
sum FX	0,30	Newton
sum FY	-139,22	Newton
sum FZ	12,40	Newton
BOUNDARY	ID 10	
---------	------	-
Area	167,34	cm^2
sum FX	0,0005	Newton
sum FY	2,32	Newton
sum FZ	0,62	Newton
BOUNDARY	ID 9	
---------	------	-
Area	235,16	cm^2
sum FX	-65,67	Newton
sum FY	-514,22	Newton
sum FZ	0,74	Newton
BOUNDARY	ID 8	
---------	------	-
Area	11,59	cm^2
sum FX	-13,84	Newton
sum FY	2386,7	Newton
sum FZ	693,74	Newton
BOUNDARY	ID 7	
---------	------	-

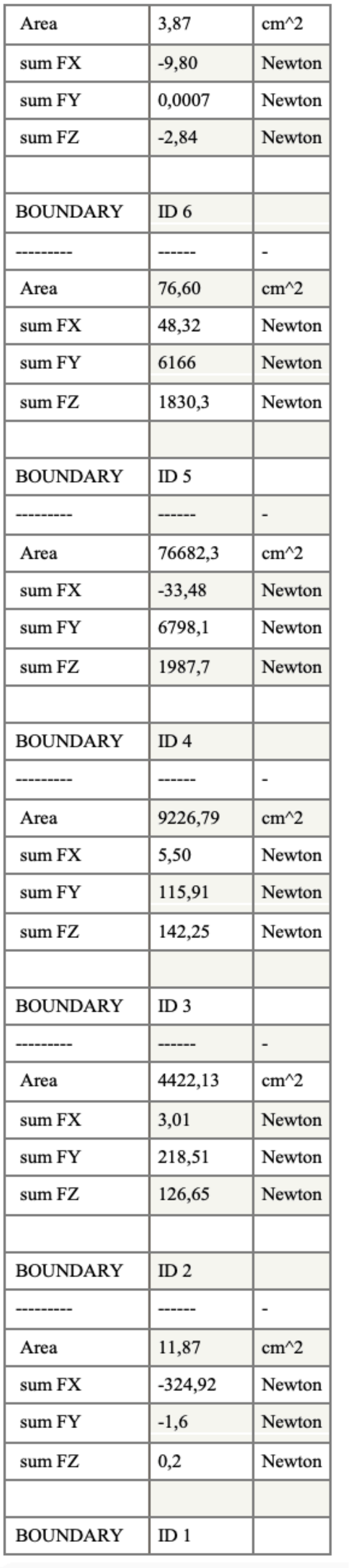

Area	3,87	cm^2
sum FX	-9,80	Newton
sum FY	0,0007	Newton
sum FZ	-2,84	Newton
BOUNDARY	ID 6	
---------	------	-
Area	76,60	cm^2
sum FX	48,32	Newton
sum FY	6166	Newton
sum FZ	1830,3	Newton
BOUNDARY	ID 5	
---------	------	-
Area	76682,3	cm^2
sum FX	-33,48	Newton
sum FY	6798,1	Newton
sum FZ	1987,7	Newton
BOUNDARY	ID 4	
---------	------	-
Area	9226,79	cm^2
sum FX	5,50	Newton
sum FY	115,91	Newton
sum FZ	142,25	Newton
BOUNDARY	ID 3	
---------	------	-
Area	4422,13	cm^2
sum FX	3,01	Newton
sum FY	218,51	Newton
sum FZ	126,65	Newton
BOUNDARY	ID 2	
---------	------	-
Area	11,87	cm^2
sum FX	-324,92	Newton
sum FY	-1,6	Newton
sum FZ	0,2	Newton
BOUNDARY	ID 1	

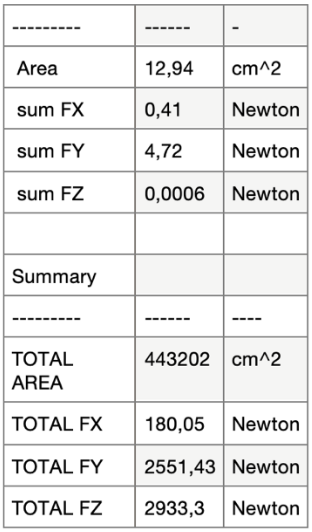

---------	------	-
Area	12,94	cm^2
sum FX	0,41	Newton
sum FY	4,72	Newton
sum FZ	0,0006	Newton
Summary		
---------	------	----
TOTAL AREA	443202	cm^2
TOTAL FX	180,05	Newton
TOTAL FY	2551,43	Newton
TOTAL FZ	2933,3	Newton

ANEX XVI

BOEING 787-9 WITH CONVENTIONAL CONFIGURATION (INCLUDING HORIZONTAL STABILIZER)

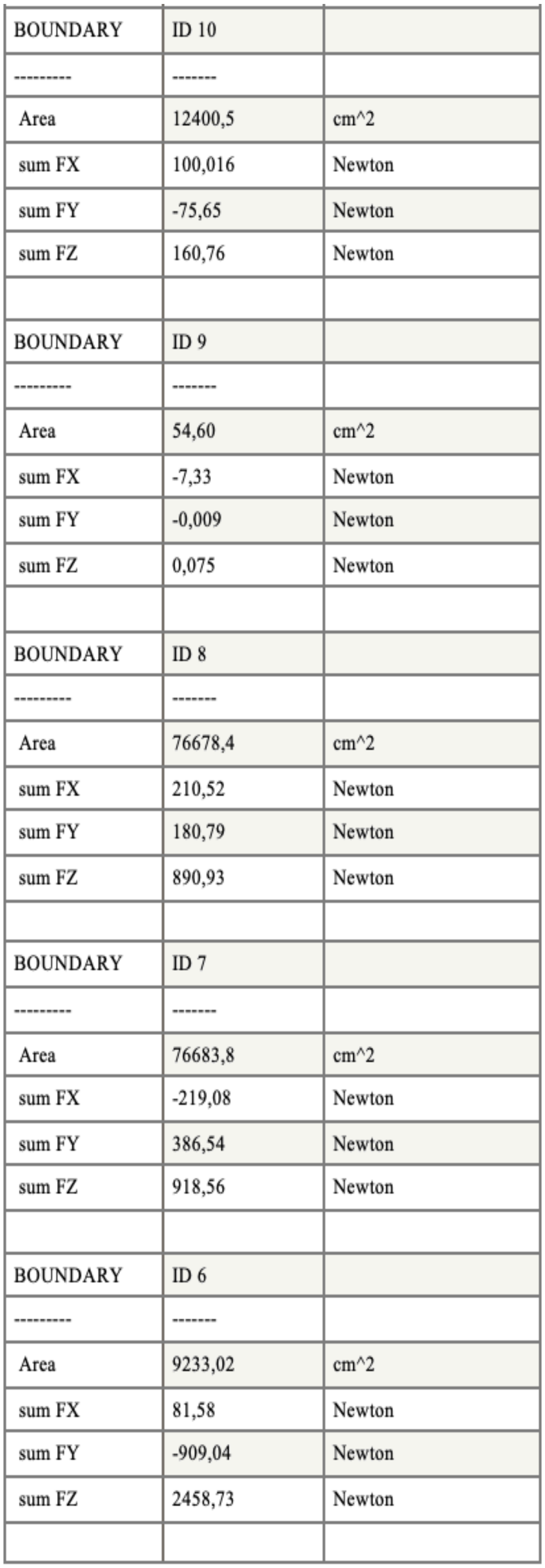

BOUNDARY	ID 10	
---------	-------	
Area	12400,5	cm^2
sum FX	100,016	Newton
sum FY	-75,65	Newton
sum FZ	160,76	Newton
BOUNDARY	ID 9	
---------	-------	
Area	54,60	cm^2
sum FX	-7,33	Newton
sum FY	-0,009	Newton
sum FZ	0,075	Newton
BOUNDARY	ID 8	
---------	-------	
Area	76678,4	cm^2
sum FX	210,52	Newton
sum FY	180,79	Newton
sum FZ	890,93	Newton
BOUNDARY	ID 7	
---------	-------	
Area	76683,8	cm^2
sum FX	-219,08	Newton
sum FY	386,54	Newton
sum FZ	918,56	Newton
BOUNDARY	ID 6	
---------	-------	
Area	9233,02	cm^2
sum FX	81,58	Newton
sum FY	-909,04	Newton
sum FZ	2458,73	Newton

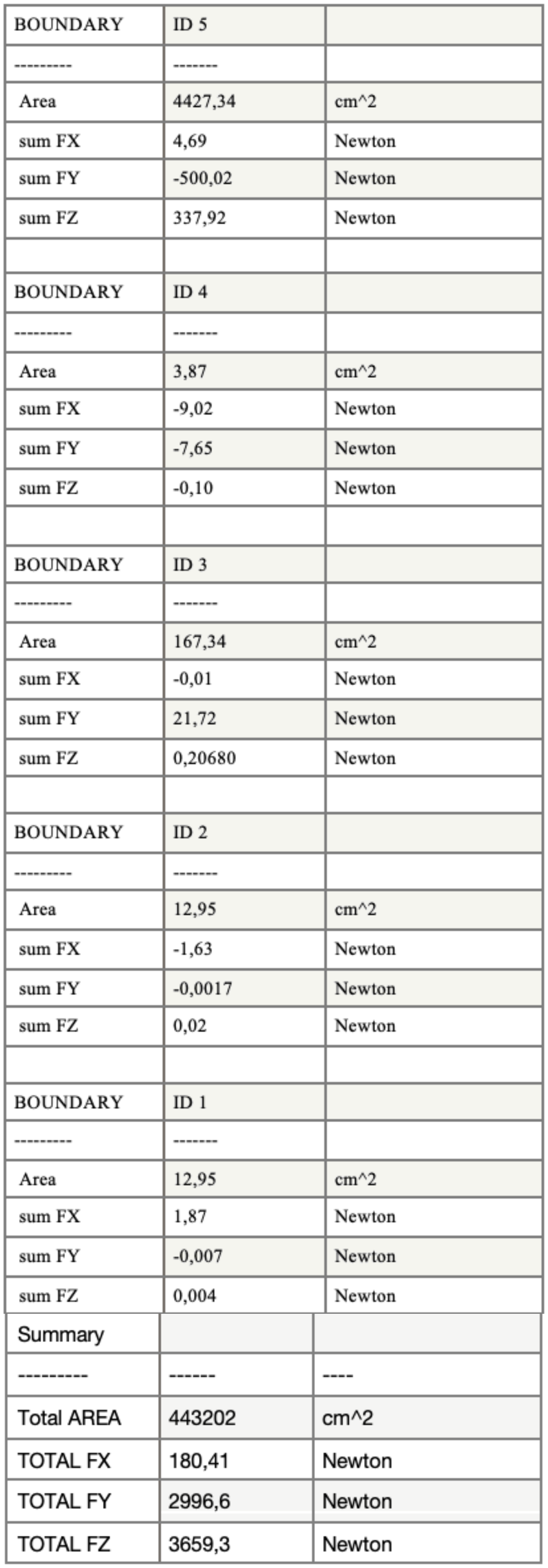

BOUNDARY	ID 5	
---------	-------	
Area	4427,34	cm^2
sum FX	4,69	Newton
sum FY	-500,02	Newton
sum FZ	337,92	Newton
BOUNDARY	ID 4	
---------	-------	
Area	3,87	cm^2
sum FX	-9,02	Newton
sum FY	-7,65	Newton
sum FZ	-0,10	Newton
BOUNDARY	ID 3	
---------	-------	
Area	167,34	cm^2
sum FX	-0,01	Newton
sum FY	21,72	Newton
sum FZ	0,20680	Newton
BOUNDARY	ID 2	
---------	-------	
Area	12,95	cm^2
sum FX	-1,63	Newton
sum FY	-0,0017	Newton
sum FZ	0,02	Newton
BOUNDARY	ID 1	
---------	-------	
Area	12,95	cm^2
sum FX	1,87	Newton
sum FY	-0,007	Newton
sum FZ	0,004	Newton
Summary		
---------	------	----
Total AREA	443202	cm^2
TOTAL FX	180,41	Newton
TOTAL FY	2996,6	Newton
TOTAL FZ	3659,3	Newton

ANEX XVII

LINEAL ACTUATORS SPECIFICATIONS

DC Motor Acme Screw

Up to 165 lb. (734 N) Rated Load
Up to 1.75 in. (45 mm)/sec. Travel Speed

M-Track 1 compact units are completely self-contained and sealed to allow use in small spaces without sacrificing power or capability. The load and length capabilities provide solutions for a diverse range of intermittent duty applications.

Functionally, M-Track 1 actuators are easily interchanged with comparable size hydraulic or pneumatic cylinders on intermittent duty applications. The actuator provides consistent, repeatable performance even for applications with operating conditions including temperature extremes, high humidity, or significant dust.

Features

- **An Acme Screw** drive delivers up to 165 pounds (734 N) of force at a minimum extension rate of 0.25 inches (6.35 millimeters) per second.
- **The anodized aluminum alloy** housing resists corrosion and provides protection from dirt, dust and humidity.
- **Temperature operating range** of –20° F to +150° F (-26° to +65° C). –40° F to +185° F (-40° to +80° C) available.
- **Standard stroke lengths** of 1, 2, 4, 6, 8, 10, 12 inches (50, 100, 150, 200, 254, 300 millimeters) are available.*
- **Internal limit switches** automatically shut off the unit at end of stroke.
- **Optional potentiometer** can provide positional location feedback.
- **IP69K Static, IP65 Dynamic**
- **Temporary Immersion** with protective boot (see page 10).
- **Rod is non rotating** during operation, can be rotated for mounting purposes.

Typical Applications

Light load and short distance applications such as:

- **Valve and vent** adjustments
- **Light weight** tilt or lift positioning
- **Vise and clamp** operations

Specifications

Load Capacity	25 lbs. (111 N)	50 lbs. (222 N)	100 lbs. (445 N)	165 lbs. (734 N)
Speed at Full Load	1.75 in. (45 mm)/sec	0.80 in. (20 mm)/sec	0.45 in. (11 mm)/sec	0.25 in. (6 mm)/sec
Input Voltage	12 or 24 volt DC for all models			
Static Load Capacity	300 lbs. (135 N) for all models			
Stroke Length	1, 2, 4, 6, 8, 10 and 12 in. (50, 100, 150, 200, 254, 300 mm) for all models*			
Clevis Ends	.25 in. (6.4 mm) diameter			
Duty Cycle	25% for all models			
Operation Temperature Range	-20° F to +150° F (-26° to + 65° C) for all models, -40° F to +185° F (-40° C to +80° C) available			
Environment	IP65 Dynamic, IP69K and Temporary Immersion with Protective Boot			
Limit Switch	Fixed end of stroke limit switches standard for all units			
Potentiometer	Linear membrane potentiometer optional on all units			

Dimensions

		in.	mm	in.	mm	in.	mm	in.	mm	in.	mm	in.	mm
M-Track	**Stroke**	2	50	4	100	6	150	8	200	10	254	12	300
	A (w/o POT)	6.22	158.0	8.23	209.0	10.24	260.1	12.24	310.9	14.25	362.0	16.26	413.0
	A (POT)	7.55	191.8	9.57	243.1	11.57	293.9	13.58	344.9	15.58	395.7	17.58	446.5

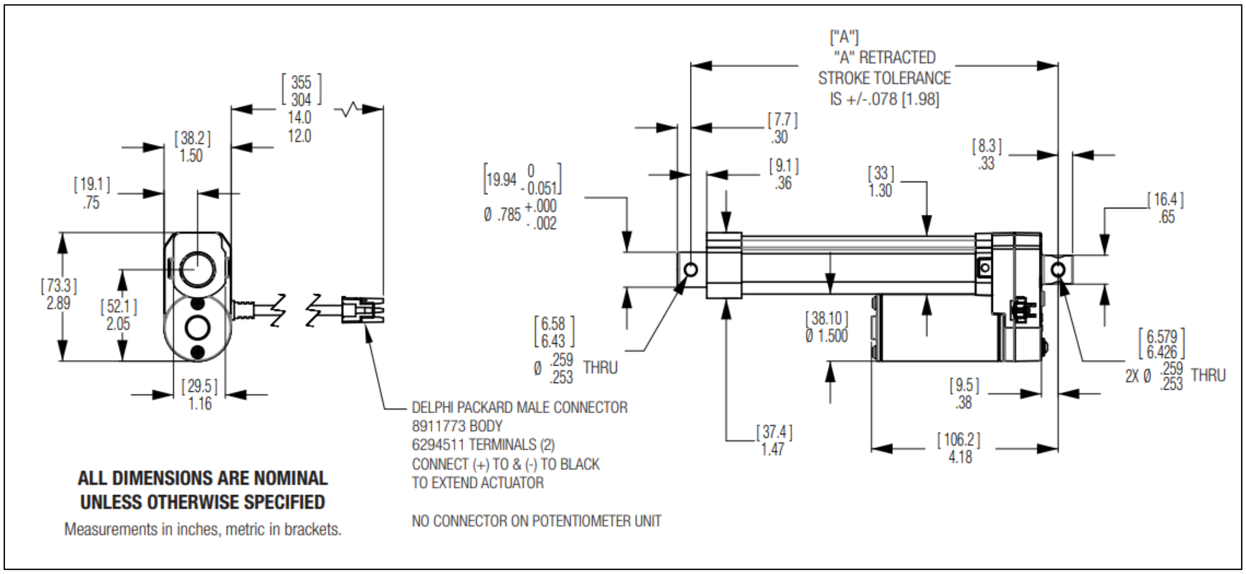

DELPHI PACKARD MALE CONNECTOR
8911773 BODY
6294511 TERMINALS (2)
CONNECT (+) TO & (-) TO BLACK
TO EXTEND ACTUATOR

NO CONNECTOR ON POTENTIOMETER UNIT

**ALL DIMENSIONS ARE NOMINAL
UNLESS OTHERWISE SPECIFIED**
Measurements in inches, metric in brackets.

ANEX XVIII

RADIAL ACTUATORS SPECIFICATIONS

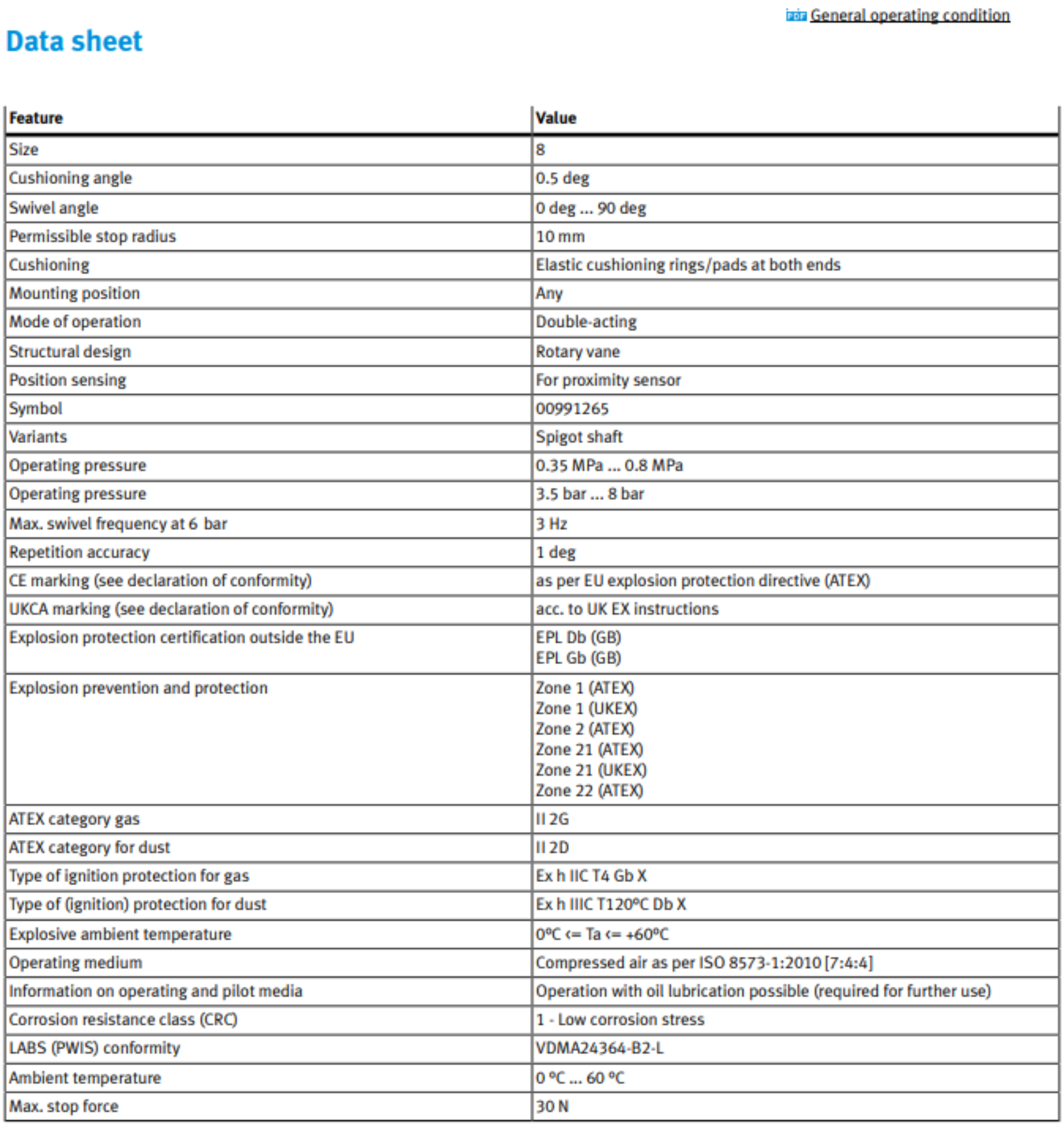

General operating condition

Data sheet

Feature	Value
Size	8
Cushioning angle	0.5 deg
Swivel angle	0 deg ... 90 deg
Permissible stop radius	10 mm
Cushioning	Elastic cushioning rings/pads at both ends
Mounting position	Any
Mode of operation	Double-acting
Structural design	Rotary vane
Position sensing	For proximity sensor
Symbol	00991265
Variants	Spigot shaft
Operating pressure	0.35 MPa ... 0.8 MPa
Operating pressure	3.5 bar ... 8 bar
Max. swivel frequency at 6 bar	3 Hz
Repetition accuracy	1 deg
CE marking (see declaration of conformity)	as per EU explosion protection directive (ATEX)
UKCA marking (see declaration of conformity)	acc. to UK EX instructions
Explosion protection certification outside the EU	EPL Db (GB) EPL Gb (GB)
Explosion prevention and protection	Zone 1 (ATEX) Zone 1 (UKEX) Zone 2 (ATEX) Zone 21 (ATEX) Zone 21 (UKEX) Zone 22 (ATEX)
ATEX category gas	II 2G
ATEX category for dust	II 2D
Type of ignition protection for gas	Ex h IIC T4 Gb X
Type of (ignition) protection for dust	Ex h IIIC T120°C Db X
Explosive ambient temperature	0°C <= Ta <= +60°C
Operating medium	Compressed air as per ISO 8573-1:2010 [7:4:4]
Information on operating and pilot media	Operation with oil lubrication possible (required for further use)
Corrosion resistance class (CRC)	1 - Low corrosion stress
LABS (PWIS) conformity	VDMA24364-B2-L
Ambient temperature	0 °C ... 60 °C
Max. stop force	30 N

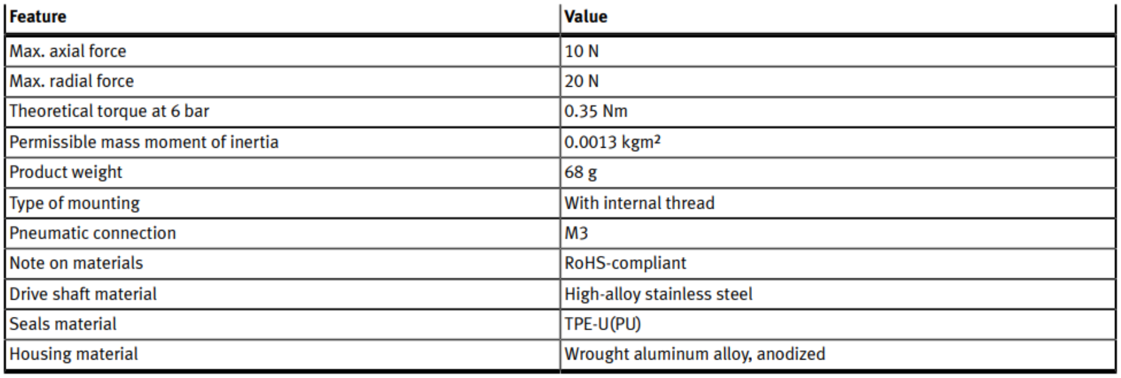

Feature	Value
Max. axial force	10 N
Max. radial force	20 N
Theoretical torque at 6 bar	0.35 Nm
Permissible mass moment of inertia	0.0013 kgm²
Product weight	68 g
Type of mounting	With internal thread
Pneumatic connection	M3
Note on materials	RoHS-compliant
Drive shaft material	High-alloy stainless steel
Seals material	TPE-U(PU)
Housing material	Wrought aluminum alloy, anodized

ANEX XIX

CFRP SANDWHICH MATERIAL SPECIFICATIONS

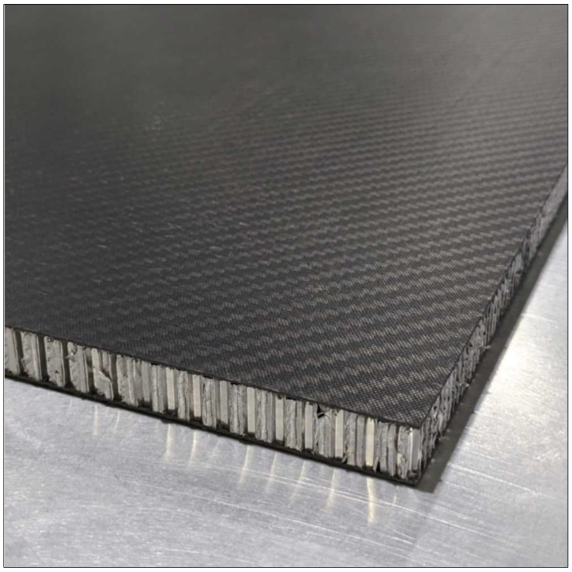

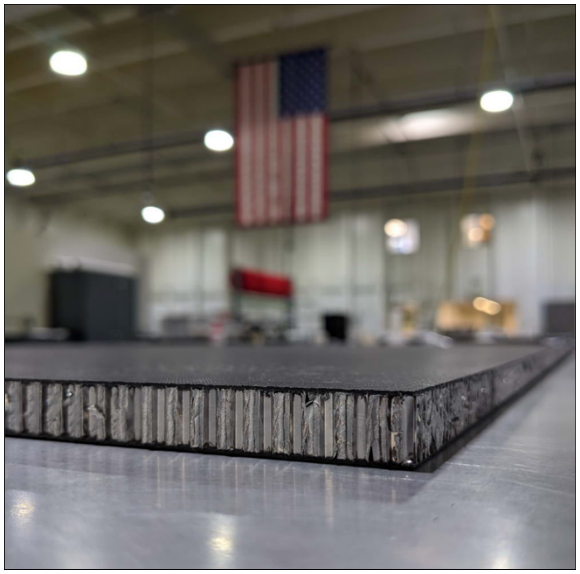

P/N	904-44
WT.	3.434 kg
Color	Black
Core Thickness	1.168 cm
Core Thickness V2	0.460"
Materials	Carbon Fiber Skins / Aluminum Honeycomb Core
Panel Thickness	1.27 cm
Plate Finish	Matte / Matte
Length x Width	48" x 48" / 1219.2mm x 1219.2mm
Skin Thickness	0.020000
Skin Thickness V2	0.02" (2 Plies)

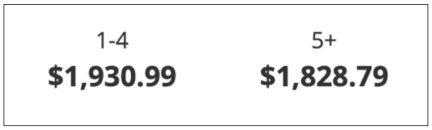

1-4	5+
$1,930.99	**$1,828.79**

ANEX XX

FUEL PRICES AT LOS ANGELES AIRPORT

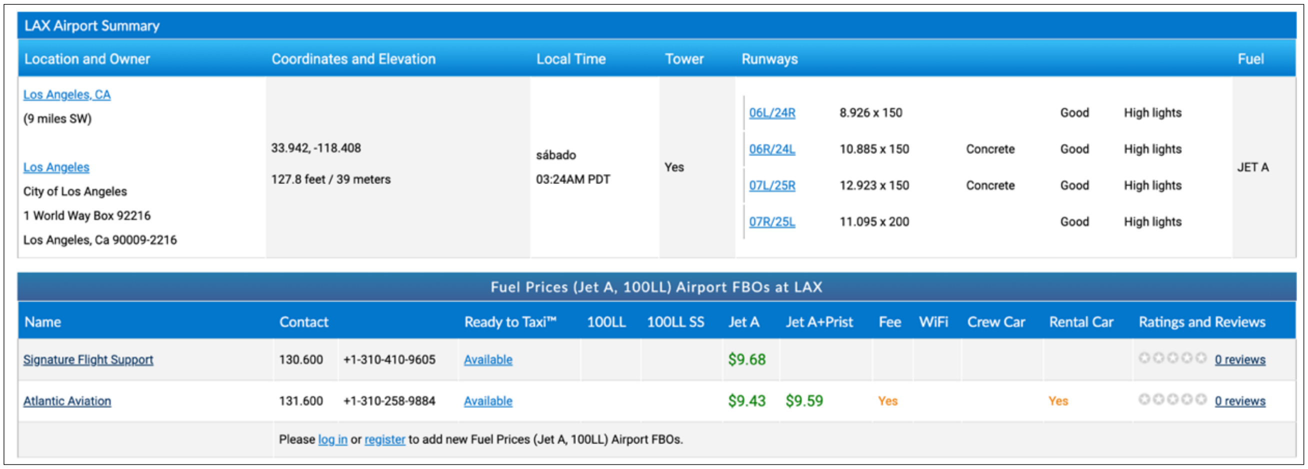

LAX Airport Summary

Location and Owner	Coordinates and Elevation	Local Time	Tower	Runways					Fuel
Los Angeles, CA (9 miles SW) Los Angeles City of Los Angeles 1 World Way Box 92216 Los Angeles, Ca 90009-2216	33.942, -118.408 127.8 feet / 39 meters	sábado 03:24AM PDT	Yes	06L/24R	8.926 x 150		Good	High lights	JET A
				06R/24L	10.885 x 150	Concrete	Good	High lights	
				07L/25R	12.923 x 150	Concrete	Good	High lights	
				07R/25L	11.095 x 200		Good	High lights	

Fuel Prices (Jet A, 100LL) Airport FBOs at LAX

Name	Contact		Ready to Taxi™	100LL	100LL SS	Jet A	Jet A+Prist	Fee	WiFi	Crew Car	Rental Car	Ratings and Reviews
Signature Flight Support	130.600	+1-310-410-9605	Available			$9.68						○○○○○ 0 reviews
Atlantic Aviation	131.600	+1-310-258-9884	Available			$9.43	$9.59	Yes			Yes	○○○○○ 0 reviews
	Please log in or register to add new Fuel Prices (Jet A, 100LL) Airport FBOs.											

REFERENCES

1. [1] Boeing 787-9 Fuel tanks distribution. [Image]. *Modern Airliners - Boeing 787 Dreamliner*. (2022, 19 diciembre). Modern Airliners. https://www.modernairliners.com/boeing-787

2. [2] Airbus A330 Fuel tanks distribution. [Image]. *A330 Fuel System – AeroPeep – Aircraft and Engineering Forum*. (2020, 5 noviembre). Aeropeep – Aircraft and Engineering Forum. https://aeropeep.com/a330-fuel-system/

3. [3] Boeing 787 Dreamliner. [Image]. Boreadas, J. (2020, 23 julio). *Boeing 787 Dreamliner, el avión más moderno del mundo*. Eas BCN. https://easbcn.com/boeing-787-dreamliner-el-avion-mas-moderno-del-mundo/

4. [4] Boeing 787-9 specifications. Wikipedia contributors. (2024, 16 mayo). *Boeing 787 Dreamliner*. Wikipedia. https://en.wikipedia.org/wiki/Boeing_787_Dreamliner

5. [5] Airbus A350-900 specifications. colaboradores de Wikipedia. (2024, 15 mayo). *Airbus A350*. Wikipedia, la Enciclopedia Libre. https://es.wikipedia.org/wiki/Airbus_A350

6. [6] Bernoulli Principle. [Image]. Orr, B. (2021, 25 mayo). *Bernoulli's Principle*. HVAC School. https://hvacrschool.com/bernoullis-principal/

7. [7] Airfoil generating downforce. [Image]. *I need help with analyzing my results - FSAE wing*. (2019, 28 noviembre). SimScale CAE Forum. https://www.simscale.com/forum/t/i-need-help-with-analyzing-my-results-fsae-wing/87008

8. [8] Airfoil generating lift. [Image]. Skill-Lync. (2023, 16 febrero). *Analysis of NACA0012 Airfoil for Different Angle of Attacks - Student Projects*. Skill-Lync. https://skill-lync.com/student-projects/analysis-of-naca0012-airfoil-for-different-angle-of-attacks

9. [9] Bernoulli Principle. [Image]. Limited, A. (s. f.). *Bernoulli equation hi-res stock photography and images - Alamy*. Alamy. https://www.alamy.com/stock-photo/bernoulli-equation.html?sortBy=relevant

10. [10] Mass Conservation Principle. [Image]. Conservation of Mass: Continuity Equation. (2022). En *INTRODUCTION TO AEROSPACE FLIGHT VEHICLES*. https://doi.org/10.15394/eaglepub.2022.1066.n16

11. [11] Red Bull F1 car rear wing with DRS open. [Image]. Smith, L., & Coleman, M. (2023, 21 septiembre). Does F1's flexi-wing rule change explain Red Bull's Singapore stumble? Mailbag. *The Athletic*. https://www.nytimes.com/athletic/4884392/2023/09/21/f1-red-bull-flexi-wing-rule/

12. [12] Red Bull F1 car rear wing with DRS closed. GPBlog. (2023, 25 marzo). Red Bull Racing tiene un truco para mejorar el DRS. *GPblog.com*. https://www.gpblog.com/es/noticias/190959/red-bull-racing-tiene-un-truco-para-mejorar-el-drs.html

13. [13] NACA 0012 Airfoil. [Image]. *NACA 0012 AIRFOILS (n0012-il)*. (s. f.). http://airfoiltools.com/airfoil/details?airfoil=n0012-il

14. [14] RAE 2822 Airfoil. [Image]. *RAE 2822 AIRFOIL (rae2822-il)*. (s. f.). http://airfoiltools.com/airfoil/details?airfoil=rae2822-il

15. [15] Internal Structure of a section of a commercial aircraft. [Image]. *22.14. 55 Empennage/Stabilizers - Abbott Aerospace UK Ltd*. (2019, 20 noviembre). Abbott Aerospace UK Ltd. https://www.abbottaerospace.com/aa-sb-001/22-aircraft-specific-design-features-and-design-methods/22-14-55-empennage-stabilizers/

16. [16] Coanda Effect. [Image]. colaboradores de Wikipedia. (2024a, mayo 2). *Efecto coandă*. Wikipedia, la Enciclopedia Libre. https://es.wikipedia.org/wiki/Efecto_Coand%C4%83

17. [17] Ferrari F1 2023 Air Intakes. [Image]. F. (2023b, febrero 14). TECHNICAL ANALYSIS: Ferrari's 2023 SF-23 – A complete redesign or subtle evolution? | Formula 1®. *Formula 1® - The Official F1® Website*. https://www.formula1.com/en/latest/article/tech-analysis-ferraris-2023-sf-23-a-complete-redesign-or-subtle-evolution.7qUstZ2bHNORVuddhNCb06

18. [18] CFRP Sandwich structure with Aluminum core. [Image]. Wu, Y., Liu, Q., Fu, J., Li, Q., & Hui, D. (2017). Dynamic crash responses of bio-inspired aluminum honeycomb sandwich structures with CFRP panels. *Composites. Part B, Engineering*, *121*, 122-133. https://doi.org/10.1016/j.compositesb.2017.03.030

19. [19] Lineal Actuators. [Image]. Actuators, L. A. L. A. L. A. L. A. L. A. L. (2023, 28 agosto). *Linear actuators Linear actuators Linear actuators linear actuators Linear actuators linear actuators*. ETI Systems. https://etisystems.com/linear-actuators/

20. [20] Radial Actuators. [Image]. *Rotary Actuator MCRC|Mindman Pneumatics*. (s. f.). https://www.mindman.com.tw/product-MCRC.html

21. [21] Adverse pressure gradient. [Image]. Karavadiya, D. (2024, 10 abril). *Learn about pressure gradient in CFD | Divykumar Karavadiya posted on the topic | LinkedIn*. https://www.linkedin.com/posts/divykumar-karavadiya-a60a88190_fluiddynamics-pressuregredients-engineering-activity-7183762167232446465-p_AO

22. [22] Materials used for the composition of the Boeing 787-9. Griffiths, B. (2018, 31 mayo). Boeing sets pace for composite usage in large civil aircraft. *Gardner Business Media, Inc*. https://www.compositesworld.com/articles/boeing-sets-pace-for-composite-usage-in-large-civil-aircraft

23. [23] Volume coefficients. [Table]. Daniel Webster College & Mohammad Sadraey. *Tail Design*. Chapter 6. (2016). http://aero.us.es/adesign/Slides/Extra/Stability/Design_Tail/Chapter%206.%20Tail%20Design.pdf

24. [24] Distance between aerodynamic centers & gravity centers. [Image]. Daniel Webster College & Mohammad Sadraey. *Tail Design*. Chapter 6. (2016). http://aero.us.es/adesign/Slides/Extra/Stability/Design_Tail/Chapter%206.%20Tail%20Design.pdf

25. [25] Sustainable development goals for 2030. [Image]. colaboradores de Wikipedia. (s. f.). *Archivo: Sustainable Development Goals.svg - Wikipedia, la enciclopedia libre*. https://es.m.wikipedia.org/wiki/Archivo:Sustainable_Development_Goals.svg

26. [26] Flight route from Los Angeles- London Heathrow. [Image]. *A map from the Great Circle Mapper*. (s. f.). Great Circle Mapper. http://www.gcmap.com/mapui?P=lhr-lax

27. [27] Boeing 787-9 general information. Colaboradores de Wikipedia. (2024, 26 enero). *Boeing 787*. Wikipedia, la enciclopedia libre. https://es.wikipedia.org/wiki/Boeing_787#787-9

28. [28] Boeing 787-9 general information. *787 Dreamliner by design*. (s. f.). https://www.boeing.com/commercial/787/by-design

29. [29] Downwash definition. *Welcome to How Things Fly*. (s. f.). https://howthingsfly.si.edu/ask-an-explainer/what-downwash

30. [30] Bernoulli Principle explanation. Wikipedia contributors. (2024a, mayo 13). *Bernoulli's principle*. Wikipedia. https://en.wikipedia.org/wiki/Bernoulli%27s_principle

31. [31] Bernoulli Principle explanation. Libretexts. (2022, 14 diciembre). *14.8: Bernoulli's Equation*. Physics LibreTexts. https://phys.libretexts.org/Bookshelves/University_Physics/University_Physics_(OpenSt

ax)/Book%3A_University_Physics_I_-_Mechanics_Sound_Oscillations_and_Waves_(OpenStax)/14%3A_Fluid_Mechanics/14.08%3A_Bernoullis_Equation

32. [32] Mass Conservation Principle. Zhao, D., Han, N., Goh, E., Cater, J., & Reinecke, A. (2019). Aeroacoustics of wind turbines. En *Elsevier eBooks* (pp. 463-491). https://doi.org/10.1016/b978-0-12-817135-6.00008-9

33. [33] Mass Conservation Principle. The Editors of Encyclopaedia Britannica. (2006, 1 junio). *Conservation of mass | Law of Conservation, Matter & Energy*. Encyclopedia Britannica. https://www.britannica.com/science/conservation-of-mass

34. [34] Drag Reduction System information. Coleman, M. (2024, 11 marzo). What is DRS and why does the device raise criticism? *The Athletic*. https://www.nytimes.com/athletic/4266856/2024/02/23/formula-one-f1-drs-explained/

35. [35] Materials used for the Boeing 787 manufacturing. Jared, B. H. (2022). Metal additive manufacturing. En *Elsevier eBooks* (pp. 247-298). https://doi.org/10.1016/b978-0-323-95062-6.00005-x

36. [36] Composite materials manufacturing processes. Pirancomposite. (2023, 26 septiembre). Composite manufacturing Process | Piran Advanced Composites. *Piran Advanced Composites*. https://pirancomposites.com/news/composite-manufacturing-process/

37. [37] Prepeg storage process. *Prepreg and b-stage Transportation and Storage Guidelines*. (2021, enero). Norplex Micarta. https://www.norplex-micarta.com/wp-content/uploads/2021/02/Prepreg_Transportation_Storage.pdf

38. [38] Aircraft's internal structure components. Anatomy of Aircraft & Spacecraft. (2023). En *ANATOMY OF AIRCRAFT & SPACECRAFT*. https://doi.org/10.15394/eaglepub.2022.1066.n3

39. [39] Wingtip vortices explanation. Wikipedia contributors. (2024a, abril 30). *Wingtip vortices*. Wikipedia. https://en.wikipedia.org/wiki/Wingtip_vortices

40. [40] Coanda Effect explanation. Rapchak, L., Rapchak, L., & Flow, N. (2023, 27 febrero). *Definition of the Coanda Effect*. Nex Flow Air Products Corp. https://www.nexflow.com/blog/definition-coanda-effect/#:~:text=The%20Coanda%20Effect%20was%20discovered,stream%20is%20not%20too%20sharp.

41. [41] Coanda Effect explanation. Wikipedia contributors. (2024a, febrero 1). *Coandă effect*. Wikipedia. https://en.wikipedia.org/wiki/Coand%C4%83_effect

42. [42] Formula 1 Air Intakes. Wojtaszczyk, A. D. (2022, 24 febrero). Mercedes también presenta branquias en el W13 de Russell. *Car And Driver*. https://www.caranddriver.com/es/formula-1/a39202167/f1-mercedes-branquias-w13/

43. [43] Turbulator explanation. *Turbulators*. (s. f.). https://www.mh-aerotools.de/airfoils/turbulat.htm

44. [44] Drain holes explanation. Craig, V. A. P. B. P. A. (2018, 7 julio). *The Drain Hole - StudentPilot.com*. StudentPilot.com. https://studentpilot.com/2001/07/09/the-drain-hole/

45. [45] Aircraft exit Passenger door information. *Aircraft Door & Emergency Exit Types and Role Considerations*. (2021, mayo). https://sassofia.com/wp-content/uploads/2022/05/Aircraft-Door-Emergency-Exit-Types-and-Role-Considerations.pdf

46. [46] Importance of aluminum honeycomb in CFRP material. Germana. (2022, 14 julio). Aluminum honeycomb panels: why choose them? *Italcoat Srl -Surface treatment and lacquering of aluminum coils*. https://www.italcoat.com/blog/aluminum-honeycomb-panels-why-choose-them/#:~:text=The%20main%20advantages%20are%3A,easier%20manufacturing%20of%20the%20material

47. [47] CFRP with aluminum core specifications. *Sandwich Panel - Carbon Fiber Skin with Aluminum Honeycomb Core*. (s. f.). https://www.rockwestcomposites.com/twill-aluminum-sandwich

48. [48] Corrosion avoidance due to composite materials. Composites Fibreglass International. (2023, 26 julio). *Maintenance and Durability of Composite Materials*. https://cfint.com.au/maintenance-and-durability-of-composite-materials/#:~:text=Composite%20materials%20are%20a%20great,materials%20like%20steel%20and%20aluminium.

49. [49] Symmetric airfoils information. *Exploring the Aerodynamics of Symmetrical Airfoil*. (s. f.). https://resources.system-analysis.cadence.com/blog/msa2022-exploring-the-aerodynamics-of-symmetrical-airfoil#:~:text=In%20the%20case%20of%20the,change%20in%20angle%20of%20attack.

50. [50] Asymmetric airfoils information. *Effect of Shape on Lift*. (s. f.). https://www.grc.nasa.gov/www/k-12/VirtualAero/BottleRocket/airplane/shape.html

51. [51] Transonic airfoils information. *RAE2822 Transonic Airfoil*. (s. f.). https://www.grc.nasa.gov/www/wind/valid/raetaf/raetaf.html

52. [52] Control volume explanation. Wikipedia contributors. (2023, 4 octubre). *Control volume*. Wikipedia. https://en.wikipedia.org/wiki/Control_volume

53. [53] Wingtip vortices information. Wikipedia contributors. (2024c, abril 30). *Wingtip vortices*. Wikipedia. https://en.wikipedia.org/wiki/Wingtip_vortices

54. [54] Boeing 787-9 cruise speed. colaboradores de Wikipedia. (2024b, mayo 11). *Boeing 787*. Wikipedia, la Enciclopedia Libre. https://es.wikipedia.org/wiki/Boeing_787

55. [55] SST-K omega turbulence model general information. *Menter Shear Stress Transport model*. (s. f.). https://turbmodels.larc.nasa.gov/sst.html

56. [56] SST-K omega turbulence model main equations. *SST k-omega model -- CFD-Wiki, the free CFD reference*. (s. f.). https://www.cfd-online.com/Wiki/SST_k-omega_model

57. [57] Aerodynamic forces. *Aerodynamic forces*. (s. f.). https://www.grc.nasa.gov/www/k-12/VirtualAero/BottleRocket/airplane/presar.html

58. [58] Velocity gradient. McGinty, B. (s. f.). *Velocity gradients*. https://www.continuummechanics.org/velocitygradient.html

59. [59] Boundary layer information. *Boundary layer*. (s. f.). https://www.grc.nasa.gov/www/k-12/BGP/boundlay.html

60. [60] Reynolds number. *Reynolds Number*. (s. f.). https://www.grc.nasa.gov/www/k-12/airplane/reynolds.html

61. [61] Laminar & turbulent flow. Ramos, L. (2023, 9 diciembre). *Laminar or Turbulent Flow*. CRUMA. https://cruma.es/en/flujo-laminar-o-turbulento/

62. [62] Boundary layer detachment. Wikipedia contributors. (2024b, abril 17). *Flow separation*. Wikipedia. https://en.wikipedia.org/wiki/Flow_separation#:~:text=The%20boundary%20layer%20separates%20when,forms%20of%20eddies%20and%20vortices.

63. [63] Adverse pressure gradient. Wikipedia contributors. (2022, 9 noviembre). *Adverse pressure gradient*. Wikipedia. https://en.wikipedia.org/wiki/Adverse_pressure_gradient

64. [64] Adverse pressure gradient. Tu, J., Yeoh, G., & Liu, C. (2018). CFD case studies. En *Elsevier eBooks* (pp. e1-e122). https://doi.org/10.1016/b978-0-08-101127-0.00020-9

65. [65] Stagnation point. Wikipedia contributors. (2023b, diciembre 6). *Stagnation point flow*. Wikipedia. https://en.wikipedia.org/wiki/Stagnation_point_flow

66. [66] Suction peak. *What is suction peak?* (s. f.). Aviation Stack Exchange. https://aviation.stackexchange.com/questions/73228/what-is-suction-peak

67. [67] Parasite drag. *Parasite drag*. (2022, 19 junio). SKYbrary Aviation Safety. https://skybrary.aero/articles/parasite-drag

68. [68] Wake in aerodynamics. Wikipedia contributors. (2024b, marzo 20). *Wake (physics)*. Wikipedia. https://en.wikipedia.org/wiki/Wake_(physics)

69. [69] Dihedral angle. Wikipedia contributors. (2024b, febrero 28). *Dihedral angle*. Wikipedia. https://en.wikipedia.org/wiki/Dihedral_angle#:~:text=A%20dihedral%20angle%20is%20the,line%20as%20a%20common%20edge.

70. [70] Carbon fiber selected. *Sandwich Panel - Carbon Fiber Skin with Aluminum Honeycomb Core*. (s. f.-b). https://www.rockwestcomposites.com/twill-aluminum-sandwich

71. [71] Lineal actuators speficiations. Actuators, L. A. L. A. L. A. L. A. L. A. L. (2023, 28 agosto). *Linear actuators Linear actuators Linear actuators linear actuators Linear actuators linear actuators*. ETI Systems. https://etisystems.com/linear-actuators/

72. [72] Radial actuators specifications. *Rotary Actuator MCRC|Mindman Pneumatics*. (s. f.). https://www.mindman.com.tw/product-MCRC.html

73. [73] Boeing 787-9 material composition. Jared, B. H. (2022b). Metal additive manufacturing. En *Elsevier eBooks* (pp. 247-298). https://doi.org/10.1016/b978-0-323-95062-6.00005-x

74. [74] Rudder at the vertical stabilizer. *Rudder - Yaw*. (s. f.). https://www.grc.nasa.gov/www/k-12/VirtualAero/BottleRocket/airplane/rud.html

75. [75] Crosswind explanation. Wikipedia contributors. (2024b, febrero 10). *Crosswind*. Wikipedia.
https://en.wikipedia.org/wiki/Crosswind

76. [76] IATA and air traffic control. *Global Outlook for Air Transport Times of Turbulence*. (2022, junio).
https://www.iata.org/en/iata-repository/publications/economic-reports/airline-industry-economic-performance---june-2022---report/

77. [77] Agenda 2030 information. *Transformar nuestro mundo: la Agenda 2030 para el Desarrollo Sostenible | Department of Economic and Social Affairs*. (s. f.). https://sdgs.un.org/es/2030agenda

78. [78] Sustainable Development Goals. *THE 17 GOALS | Sustainable Development*. (s. f.). https://sdgs.un.org/goals

79. [79] Materials used for horizontal stabilizer manufacturing. Gao, Y., An, G., & Zhi, C. (2021). Airworthiness verification test of the flight control system. En *Elsevier eBooks* (pp. 631-672).
https://doi.org/10.1016/b978-0-12-822990-3.00009-7

80. [80] Los Angeles- London Heathrow flight distance. *A map from the Great Circle Mapper*. (s. f.). Great Circle Mapper.
http://www.gcmap.com/mapui?P=lhr-lax

81. [81] Rolls Royce Trent 1000 specifications. colaboradores de Wikipedia. (2020, 23 noviembre). Rolls-Royce Trent 1000. Wikipedia, la Enciclopedia Libre. https://es.wikipedia.org/wiki/Rolls-Royce_Trent_1000

82. [82] Rolls Royce Trent 1000 specifications. *Trent 1000*. (s. f.).
https://www.rolls-royce.com/products-and-services/civil-aerospace/widebody/trent-1000.aspx#/

83. [83] Weight of the Boeing 787-9. Wikipedia contributors. (2024j, mayo 16). *Boeing 787 Dreamliner*. Wikipedia.
https://en.wikipedia.org/wiki/Boeing_787_Dreamliner

84. [84] Wikipedia contributors. (2024e, abril 7). *Range (aeronautics)*. Wikipedia.
https://en.wikipedia.org/wiki/Range_(aeronautics)

85. [85] Lift over drag ratio estimation. *Physics and Astronomy Outreach Program at the University of British Columbia*. (2010, julio).
https://phas.ubc.ca/~james/teaching/phys333/module4_lesson2.pdf

86. Boeing 787-9 fuel consumption. *What is the fuel burn of a 787-9 on a ferry flight?* (s. f.). Aviation Stack Exchange. https://aviation.stackexchange.com/questions/95519/what-is-the-fuel-burn-of-a-787-9-on-a-ferry-flight

87. [87] Aircraft fuel Price. *Jet Center Los Angeles FBO Info & Fuel Prices at Hawthorne Municipal (KHHR) - FlightAware*. (s. f.). FlightAware. https://www.flightaware.com/resources/airport/KHHR/services/FBO/Jet_Center_Los_Angeles

88. [88] General Electric GE36 propfan. Wikipedia contributors. (2023b, noviembre 24). *General Electric GE36*. Wikipedia. https://en.wikipedia.org/wiki/General_Electric_GE36

89. [89] Volume coefficient estimation. Daniel Webster College & Mohammad Sadraey. *Tail Design*. Chapter 6. (2016). http://aero.us.es/adesign/Slides/Extra/Stability/Design_Tail/Chapter%206.%20Tail%20Design.pdf

90. [90] Lift over drag ratio in propfan engines. *Aerodynamic and Propeller Performance Characteristics of a Propfan-Powered, Semispan Model*. (1985, diciembre). NASA Technical Memorandum. https://ntrs.nasa.gov/api/citations/19880004710/downloads/19880004710.pdf

91. [91] IATA calculator. *ICAO Carbon Emissions Calculator (ICEC)*. (s. f.). https://www.icao.int/environmental-protection/Carbonoffset/Pages/default.aspx